

The University of Maine

DigitalCommons@UMaine

Electronic Theses and Dissertations

Fogler Library

Summer 8-16-2024

Cranial Thinning in High-risk Alcohol Users: a Postmortem Computed Tomography Study

Jamie A. Wren

University of Maine, jamie.a.wren@maine.edu

Follow this and additional works at: <https://digitalcommons.library.umaine.edu/etd>



Part of the [Medicine and Health Sciences Commons](#)

Recommended Citation

Wren, Jamie A., "Cranial Thinning in High-risk Alcohol Users: a Postmortem Computed Tomography Study" (2024). *Electronic Theses and Dissertations*. 4066.

<https://digitalcommons.library.umaine.edu/etd/4066>

This Open-Access Dissertation is brought to you for free and open access by DigitalCommons@UMaine. It has been accepted for inclusion in Electronic Theses and Dissertations by an authorized administrator of DigitalCommons@UMaine. For more information, please contact um.library.technical.services@maine.edu.

**CRANIAL THINNING IN HIGH-RISK ALCOHOL USERS: A POSTMORTEM
COMPUTED TOMOGRAPHY STUDY**

By

Jamie Allen Wren

B.A. University of Maine, 2012

M.P.H. University of New England, 2015

A DISSERTATION

Submitted in Partial Fulfillment of the

Requirements for the Degree of

Doctor of Philosophy

(in Interdisciplinary Studies - Biomedical Anthropology)

The Graduate School

The University of Maine

August 2024

Advisory Committee:

Marcella H. Sorg, Research Professor of Anthropology, Climate Change, and Public Policy, University of Maine, Advisor

Kathleen Becker, Associate Graduate Faculty, Graduate School of Biomedical Sciences and Engineering, University of Maine; Assistant Professor of Biomedical Science, University of New England

Robert Lehnhard, Professor of Kinesiology, University of Maine

Heather Edgar, Professor of Anthropology, University of New Mexico

Leslie Eisenberg, Honorary Fellow, Department of Anthropology, and Senior Research Fellow, Center for Healthy Minds, University of Wisconsin-Madison

Mark Flomenbaum, Chief Medical Examiner, State of Maine (ret.)

© 2024 Jamie A. Wren

All Rights Reserved

CRANIAL THINNING IN HIGH-RISK ALCOHOL USERS: A POSTMORTEM COMPUTED TOMOGRAPHY STUDY

By Jamie Allen Wren

Dissertation Advisor: Dr. Marcella H. Sorg

An Abstract of the Dissertation Presented
in Partial Fulfillment of the Requirements
for the Degree of Doctor of Philosophy
(Interdisciplinary Studies- Biomedical Anthropology)
August 2024

There is substantial evidence demonstrating chronic, heavy intake (e.g. >5 drinks per day for men) is detrimental to human bone, often leading to osteopenia and secondary osteoporosis. A review of relevant literature from the 1950s to the present did not reveal any studies examining the impact of heavy alcohol use on the human cranium. The aim of this dissertation is to help address this research gap.

One hundred and forty-four post-mortem computed tomography (PMCT) scans were selected from deaths investigated by the New Mexico Office of the Medical Investigator. Deidentified PMCT scans were provided by the New Mexico Decedent Image Database. The study sample is comprised of normal-weight men, aged 21-55, with a known drinking status (low-risk or high-risk).

Based on prior case observations, eight cranial sites were selected for study. Twenty-millimeter bilateral segments were created on the orbital roof, lateral frontal, temporal squamous, and cerebellar fossa of the occiput. Segments were assessed for minimum thickness and radiological markers of bone quality.

Results indicate that high-risk alcohol users have significantly thinner crania than low-risk alcohol users at all sites except for the lateral frontal. Radiodensity measurements of the

segments revealed areas of significantly lower and, paradoxically, higher radiodensities in high-risk alcohol users compared to low-risk alcohol users.

Findings from this study have potential applications in the fields of medicolegal death investigation, forensic anthropology, and clinical medicine. Medicolegal death investigators might better understand and explain fatalities among individuals with a known history of heavy alcohol use when blunt force trauma of the head contributes to their death, leading to better documentation and public health statistics surrounding these deaths. Clinically, appreciating that a patient who exhibits high-risk alcohol use behavior may be at risk for cranial thinning and osteoporosis could afford providers with an opportunity to treat secondary cranial osteoporosis and/or do targeted head injury prevention education with this population (e.g., helmet safety and fall prevention).

These findings may provide forensic anthropologists with an additional differential diagnosis in cases where cranial thinning is present. As in medicolegal death investigation, this finding may also help forensic anthropologists better interpret perimortem cranial blunt force trauma in high-risk alcohol users. Lastly, a further appreciation of alcohol's systemic skeletal effects can help forensic anthropologists better interpret age and antemortem trauma in individuals known to use alcohol heavily.

DEDICATION

For Tom, who knew I could.

And for Nancy, who knew I would.

ACKNOWLEDGEMENTS

This section is long, but this has truly taken a village and I would not have finished without the support of *all* those below.

First and foremost, above all else, I need to thank my husband, Tom. He is my biggest supporter, not only over the very long course of this dissertation but in every aspect of our lives. Thank you for everything you do- making sure there was actual food in the house, ensuring that I rest when I didn't think I needed to, and for always, always surprising me and keeping me laughing. Your confidence in me kept me going when I didn't think I could. Thank you for being a methodological sounding board, lending your R wizardry, and patiently and calmly listening as I (neither patiently nor calmly) worked through problems and hurdles. This dissertation, and everything else, wouldn't be possible without you.

To my parents, I can't thank you enough for all the support and opportunities you've provided me over the years and for your patience and understanding of my role as a perpetual student. A huge thank you goes to my sister, Morgan, who dragged me through my first college research paper, and helped me realize that college wasn't as scary as I had assumed. Thank you to Auntie for all the popovers and molasses cookies and to Papere for all the chicken soup and gossip. Thank you to Mimi, who, when I was young, showed me you could see the outline of the bones in your hands with a simple flashlight, sparking a lifelong fascination with radiology. Thank you to my godmother, Anne Lucey, for always encouraging my education, even if I didn't go to law school...

To all my co-workers at the Margaret Chase Smith Policy Center and the University of Maine, thank you for all your support and comradery over the past 14 years. Thanks go to the director of the Policy Center, Dr. Jonathan Rubin, for his support during the final stretch of this

project; it enabled me to complete this dissertation. Thank you to my co-workers Susan Kinney, Marissa Kinney, Andrew Fournier, Alexis Johnson, Joanna Rosebush, and Janene LaChance for being so wonderful and making what we do possible. You all carried more than your fair share while I completed this project. Thank you to Dr. Mary Mahoney-O'Neil for being such a tour de force of positivity and encouragement. Special thank yous to Jennifer Bonnet and Melanie Spencer for being such integral parts of my UMaine community.

To Megan Bailey and Susan D'Angelo, thank you for everything you have done and continue to do for me, especially for putting up with the daily barrage of text messages giving unsolicited play-by-play updates of all the ups and downs. A truly heartfelt and special thank you to Eva McLaughlin for your friendship and counsel over the years. Your kindness has forever affected me, and I am where I am today because of you. I am forever in each of your debt and eternally grateful for your friendship.

I want to thank the members of my dissertation committee, past and present: Dr. Kathleen Becker for always being up for a quick Zoom to talk through successes and hurdles and always checking in to make sure I was taking care of myself; Dr. Heather Edgar for her guidance in the planning of this study, allowing me access to the New Mexico Decedent Image Database, suggesting 3D Slicer to me, and for all her thoughtful feedback; Dr. Leslie Eisenberg for keeping me on my toes and for always pushing/helping me to go just a bit farther; Dr. Mark Flomenbaum for helping me think more critically about the physiology at play in alcohol-related bone disease as well as his many excellent lessons over the years, especially in photography; Dr. Robert Lehnhard for his wisdom, life lessons, and unconditional support; and finally, Dr. Deborah Saber for all her support and absolute, unyielding confidence in me. Thank you to the entire committee

for your constant encouragement and excellent feedback on the drafts of this work. You have all made it, and me, better.

Most importantly, thank you to my committee chair, mentor, and friend of the last 15+ years, Dr. Marci Sorg. Thank you for the time, energy, resources, and patience you have invested in me. Thank you for all the life lessons and for teaching me the importance of showing up. I'll never be able to repay it all. To quote the awkward wisdom tooth, "I'm impacted!"

Thanks to Dr. Cliff Rosen for his guidance on several aspects of this project, Dr. William Halteman for his help with the statistical analyses, and Dr. David Warner for his help with the radiological aspects of this study.

Thank you to New Mexico Office of the Medical Investigator and the University of New Mexico for granting me access to the New Mexico Decedent Image Database.

Thank you to everyone at the Offices of Chief Medical Examiner in Maine and New Hampshire for your camaraderie over the years. In particular, I'd like to thank Dr. Tom Andrew, who first inspired this project. Thank you also to everyone at the New England Seminar in Forensic Sciences for your warm welcome all those years ago and for your continued friendship and encouragement.

Thank you to all my "Sorg Siblings" and all my friends in the Anthropology Department, past and present.

Finally, to my friends, listed in no particular order: Chad and Mo Libby, Emily Yenco, Jeremiah Miner, Hannah Hudson, Jessie Whelpley, my colleague Paul Pluta, Sierran Lucey, Andrea Steward and Jordan Henry, the Rampe Family, Jacob Baker and Jessica Bishop (and Dot), Ashley Hannigan, Kendra Glueck, Jaime Jarvis, Andrew Dana, Alexander Rezk, Beth Kevit, Taylor Slemmer, and again, Joanna Rosebush, Marissa Kinney, Andrew Fournier, Janene

LaChance, Susan Kinney, Susan D'Angelo, Megan Bailey, and Eva McLaughlin. Thank you for listening, for your constant encouragement, for sending animal pictures and care packages, and for just generally being there. It has meant the world to me.

(If I've forgotten anyone, please know that I'm equally thankful for you and mortified that I missed you.)

TABLE OF CONTENTS

DEDICATION	III
ACKNOWLEDGEMENTS	IV
DISCLAIMER	xiv
LIST OF TABLES	xv
LIST OF FIGURES	xx
LIST OF EQUATIONS.....	xxii
Chapter	
1. INTRODUCTION	1
INTRODUCTION	1
IMPORTANCE OF THE RESEARCH	2
DEVELOPMENT OF THE RESEARCH QUESTION.....	3
DEFINITIONS AND TERMINOLOGY REGARDING ALCOHOL USE.....	7
REVIEW OF RELEVANT LITERATURE.....	8
Overview of Skeletal Biology and Relevant Physiology.....	9
Osteoblasts	9
Osteoclasts	10
Osteocytes.....	11
Bone Lining Cells	12

Skeletal Remodeling	13
Dysregulation/Uncoupling.....	14
Overview of the General Epidemiology, Pathophysiology, and Diagnosis of Osteoporosis	15
Type I Osteoporosis	16
Type II Osteoporosis.....	17
Diagnosis of Osteoporosis	18
Dual Energy X-ray Absorptiometry	18
Computed Tomography.....	18
Summary of General Epidemiology, Pathophysiology, and Diagnosis of Osteoporosis.....	23
Overview of Cranial Osteoporosis and Other Cranial Pathology.....	23
Cranial Osteoporosis.....	23
Cranial Pathology.....	25
Summary of Cranial Osteoporosis and Cranial Pathology	35
Overview of Cranial Thickness	35
Utility of Measuring Cranial Thickness via Computed Tomography.....	35
Standard References for Cranial Thickness	37
Cranial Thickness and Substance and Alcohol Use	40
Summary of Cranial Thickness Research	41
Alcohol’s Protective Effect on Bone.....	42
Alcohol’s Negative Effects on Bone.....	43
Reversal of Alcohol’s Effects.....	60

Summary Alcohol Use and Bone	61
Radiography in Forensic Anthropology	61
Radiography in Forensic Anthropology	62
Development of the Biological Profile	65
Identification	68
Evaluating Trauma	69
Assessing Taphonomic Change	69
Summary of Imaging in Forensic Anthropology	70
Conclusions	70
ORGANIZATION OF THE CHAPTERS	71
2. METHODOLOGY	72
INTRODUCTION	72
NEW MEXICO DECEDENT IMAGE DATABASE	72
DETERMINATION OF EFFECT SIZE, SAMPLE SIZE, AND SAMPLE SELECTION	73
Sample Selection	75
COMPUTED TOMOGRAPHY SETTINGS	76
DATA COLLECTION	77
3D SLICER	78
Pre-Segmentation Scan Processing	79
Determination of Segment Location	79
Segment Selection	80

Slicer Statistics.....	85
Measurement of Minimum Thickness	85
STATISTICAL ANALYSES	90
3. RESULTS.....	92
INTRODUCTION	92
SAMPLE OVERVIEW.....	92
HYPOTHESIS 1	96
One-Tail T-Tests for Independent Samples.....	97
Analysis of Covariance	100
Summary of Hypothesis One	107
HYPOTHESIS TWO	109
One-Tail T-Tests for Independent Samples.....	109
Analysis of Covariance	112
Summary of Hypothesis Two.....	112
HYPOTHESIS 3A	113
One-Tail T-Tests for Independent Samples.....	113
Analysis of Covariance	117
Summary of Hypothesis 3a.....	118
HYPOTHESIS 3B.....	119
One-Tail T-Tests for Independent Samples.....	119

Analysis of Covariance	122
Summary of Hypothesis 3b.....	123
HYPOTHESIS 3C.....	124
One-Tail T-Tests for Independent Samples.....	124
Analysis of Covariance	127
Pearson’s Correlation Coefficients	128
Summary of Hypothesis 3c.....	129
HYPOTHESIS 3D	130
One-Tail T-Tests for Independent Samples.....	130
Analysis of Covariance	133
Summary of Hypothesis 3d.....	134
INTRAOBSERVER ERROR	135
Interpretation of Interclass Correlation Coefficients	139
CONCLUSIONS.....	140
4. DISCUSSION.....	142
LIMITATIONS OF THE RESEARCH DESIGN AND METHODOLOGY	142
Limitations of the Research Design.....	142
Limitations of the Methodology	143
Body Mass Index	143
Nutritional Status	144

Scan resolution.....	144
Hounsfield Units.....	144
Segment Selection and Reporting.....	145
Replicability.....	146
PATHOPHYSIOLOGY OF ALCOHOL-INDUCED BONE DISEASE	146
IMPORTANCE TO MEDICOLEGAL DEATH INVESTIGATION AND PUBLIC HEALTH	148
IMPORTANCE TO FORENSIC ANTHROPOLOGY	149
IMPORTANCE TO CLINICAL COMMUNITIES	151
SEGMENT VOLUME	151
COMPUTED TOMOGRAPHY IN FORENSIC CASEWORK AND RESEARCH.....	151
ALCOHOL-INDUCED BONE DISEASE AND HOUNSFIELD UNITS	153
SUMMARY	154
5. CONCLUSIONS	156
INTRODUCTION	156
FUTURE RESEARCH.....	156
FINAL REMARKS	157
REFERENCES	158
APPENDIX A PERMISSION TO USE PHOTOGRAPHS.....	178
APPENDIX B ANALYSIS OF COVARIANCE AND PEARSON CORRELATION TABLES.....	180

DISCLAIMER

This dissertation contains photographic and radiographic depictions of human remains.

LIST OF TABLES

TABLE 1 US STANDARD DRINK BY GRAMS OF ALCOHOL, SERVING EQUIVALENT, AND ALCOHOL BY VOLUME	7
TABLE 2 COMMONLY ACCEPTED VALUES ASSOCIATED WITH HOUNSFIELD UNITS	19
TABLE 3 COMPARISON OF THE SKELETAL FEATURES, ETIOLOGY, RADIOGRAPHIC SIGNS, AND HISTOLOGICAL SIGNS OF COMMON PATHOLOGICAL CONDITIONS THAT MAY CAUSE THINNING OR POROSITY OF THE CRANIUM	31
TABLE 4 MEASUREMENTS OF CRANIAL THICKNESS REPORTED IN RECENT LITERATURE.....	38
TABLE 5 ELECTROLYTES AND THEIR ROLE IN HUMAN HEALTH, SKELETAL BIOLOGY, AND DISRUPTIONS DUE TO ALCOHOL	45
TABLE 6 SELECTED HORMONES AND THEIR ROLE IN HUMAN HEALTH, SKELETAL BIOLOGY, AND EFFECTS DUE TO ALCOHOL	48
TABLE 7 SELECTED VITAMINS AND NUTRIENTS AND THEIR ROLE IN HUMAN HEALTH, SKELETAL BIOLOGY, AND DISRUPTIONS DUE TO ALCOHOL	51
TABLE 8 SELECTED METALS AND THEIR ROLE IN HUMAN HEALTH, SKELETAL BIOLOGY, AND DISRUPTIONS DUE TO ALCOHOL	55
TABLE 9 SELECTED CYTOKINES AND THEIR ROLE IN HUMAN HEALTH, SKELETAL BIOLOGY, AND DISRUPTIONS DUE TO ALCOHOL	58
TABLE 10 ADULT COMPUTED TOMOGRAPHY SCAN PROTOCOL FOR THE NEW MEXICO OFFICE OF THE MEDICAL INVESTIGATOR FOR NON-DECOMPOSED CASES	76
TABLE 11 DECOMPOSED ADULT COMPUTED TOMOGRAPHY PROTOCOL FOR THE NEW MEXICO OFFICE OF THE MEDICAL INVESTIGATOR.....	77
TABLE 12 LEVEL OF AGREEMENT AND RELIABILITY AND ASSOCIATED INTERCLASS CORRELATION COEFFICIENT	78
TABLE 13 SEGMENT LOCATION	80
TABLE 14 VARIABLE DEFINITION.....	85
TABLE 15 NUMBER OF DECEDENTS IN EACH ALCOHOL USE RISK GROUP	93
TABLE 16 REPORTED CAUSES OF DEATH FOR HIGH-RISK ALCOHOL USERS	93

TABLE 17 REPORTED CAUSES OF DEATH FOR LOW-RISK ALCOHOL USERS.....	94
TABLE 18 DECEDENT POPULATION AFFINITY BY RISK GROUP	94
TABLE 19 AVERAGE AGE AND BODY MASS INDEX FOR THE HIGH-RISK AND LOW-RISK ALCOHOL USER GROUPS	95
TABLE 20 NUMBER OF INDIVIDUALS ANALYZED FOR MINIMUM SEGMENT THICKNESS BY SEGMENT AND RISK GROUP.....	96
TABLE 21 AVERAGE MINIMUM SEGMENT THICKNESS IN MILLIMETERS AS WELL AS BETWEEN-GROUP DIFFERENCES AND ONE-TAIL P-VALUES FOR EACH SEGMENT AND RISK GROUP	97
TABLE 22 RESULTS OF ANALYSIS OF COVARIANCES FOR MINIMUM SEGMENT THICKNESS CONTROLLING FOR DECEDENT AGE AND POPULATION AFFINITY	100
TABLE 23 CLASSIFICATION OF RISK GROUP MEMBERSHIP BASED ON THE 50TH PERCENTILE VALUE FOR MINIMUM SEGMENT THICKNESS.....	102
TABLE 24 FIFTIETH PERCENTILE CRANIAL THICKNESS MEASUREMENTS, SENSITIVITY, AND POSITIVE PREDICTIVE VALUE OF THE MODEL FOR EACH SEGMENT	103
TABLE 25 AVERAGE MINIMUM SEGMENT VOLUME IN MILLIMETERS CUBED AS WELL AS BETWEEN-GROUP DIFFERENCES AND ONE-TAIL P-VALUES FOR EACH SEGMENT AND RISK GROUP	109
TABLE 26 RESULTS OF ANALYSIS OF COVARIANCES FOR SEGMENT VOLUME CONTROLLING FOR DECEDENT AGE AND POPULATION AFFINITY	112
TABLE 27 AVERAGE MINIMUM HOUNSFIELD UNITS DETECTED AS WELL AS BETWEEN-GROUP DIFFERENCES AND ONE-TAIL P-VALUES BY SEGMENT AND RISK GROUP	113
TABLE 28 RESULTS OF ANALYSIS OF COVARIANCES FOR MINIMUM HOUNSFIELD UNITS CONTROLLING FOR DECEDENT AGE AND POPULATION AFFINITY.....	117
TABLE 29 AVERAGE MAXIMUM HOUNSFIELD UNITS DETECTED, BETWEEN-GROUP DIFFERENCES, AND ONE-TAIL P-VALUES BY SEGMENT AND RISK GROUP	119
TABLE 30 RESULTS OF ANALYSIS OF COVARIANCES FOR MAXIMUM HOUNSFIELD UNITS CONTROLLING FOR DECEDENT AGE AND POPULATION AFFINITY	122
TABLE 31 AVERAGE MEAN HOUNSFIELD UNITS DETECTED AS WELL AS BETWEEN-GROUP DIFFERENCES AND ONE-TAIL P-VALUES BY SEGMENT AND RISK GROUP	124

TABLE 32 RESULTS OF ANALYSIS OF COVARIANCES FOR MEAN HOUNSFIELD UNITS CONTROLLING FOR DECEDENT AGE AND POPULATION AFFINITY.....	127
TABLE 33 PEARSON'S CORRELATION COEFFICIENTS BETWEEN MINIMUM SEGMENT THICKNESS AND MEAN HOUNSFIELD UNITS	128
TABLE 34 PEARSON'S CORRELATION COEFFICIENTS FOR SEGMENT VOLUME AND MEAN HOUNSFIELD UNITS.....	129
TABLE 35 AVERAGE MEDIAN HOUNSFIELD UNITS DETECTED AS WELL AS BETWEEN-GROUP DIFFERENCES AND ONE-TAIL P-VALUES BY SEGMENT AND RISK GROUP	130
TABLE 36 RESULTS OF ANALYSIS OF COVARIANCES FOR MEDIAN HOUNSFIELD UNITS CONTROLLING FOR DECEDENT AGE AND POPULATION AFFINITY	133
TABLE 37 LEVEL OF AGREEMENT FOR INTERCLASS COEFFICIENTS	135
TABLE 38 INTERCLASS CORRELATION COEFFICIENT FOR MINIMUM SEGMENT THICKNESS	136
TABLE 39 INTERCLASS CORRELATION COEFFICIENTS FOR SEGMENT VOLUME	136
TABLE 40 INTERCLASS CORRELATION COEFFICIENTS FOR MINIMUM HOUNSFIELD UNITS.....	137
TABLE 41 INTERCLASS CORRELATION COEFFICIENTS FOR MAXIMUM HOUNSFIELD UNITS.....	138
TABLE 42 INTERCLASS CORRELATION COEFFICIENTS FOR MEAN HOUNSFIELD UNITS.....	138
TABLE 43 INTERCLASS CORRELATION COEFFICIENTS FOR MEDIAN HOUNSFIELD UNITS	139
TABLE 44 HOUNSFIELD UNITS IN HIGH-RISK ALCOHOL USERS COMPARED TO HOUNSFIELD UNITS OF LOW-RISK USERS BY SEGMENT	153
TABLE 45 ANALYSIS OF COVARIANCE FOR MINIMUM SEGMENT THICKNESS CONTROLLING FOR DECEDENT AGE	181
TABLE 46 ANALYSIS OF COVARIANCE FOR MINIMUM SEGMENT THICKNESS CONTROLLING FOR DECEDENT POPULATION AFFINITY	183
TABLE 47 ANALYSIS OF COVARIANCE FOR SEGMENT VOLUME CONTROLLING FOR DECEDENT AGE	185
TABLE 48 ANALYSIS OF COVARIANCE FOR SEGMENT VOLUME CONTROLLING FOR DECEDENT POPULATION AFFINITY	187

TABLE 49 ANALYSIS OF COVARIANCE FOR MINIMUM HOUNSFIELD UNITS CONTROLLING FOR DECEDENT AGE	189
TABLE 50 ANALYSIS OF COVARIANCE FOR MINIMUM HOUNSFIELD UNITS CONTROLLING FOR DECEDENT POPULATION AFFINITY	191
TABLE 51 ANALYSIS OF COVARIANCE FOR MAXIMUM HOUNSFIELD UNITS CONTROLLING FOR DECEDENT AGE	193
TABLE 52 ANALYSIS OF COVARIANCE FOR MAXIMUM HOUNSFIELD UNITS CONTROLLING FOR DECEDENT POPULATION AFFINITY	195
TABLE 53 ANALYSIS OF COVARIANCE FOR MEAN HOUNSFIELD UNITS CONTROLLING FOR DECEDENT AGE	197
TABLE 54 ANALYSIS OF COVARIANCE FOR MEAN HOUNSFIELD UNITS CONTROLLING FOR DECEDENT POPULATION AFFINITY	199
TABLE 55 ANALYSIS OF COVARIANCE FOR MEDIAN HOUNSFIELD UNITS CONTROLLING FOR DECEDENT POPULATION AFFINITY	201
TABLE 56 ANALYSIS OF COVARIANCE FOR MEDIAN HOUNSFIELD UNITS CONTROLLING FOR DECEDENT POPULATION AFFINITY	203
TABLE 57 TWO-TAILED PEARSON'S CORRELATION COEFFICIENTS FOR THE LEFT CRUCIFORM BY RISK-GROUP	205
TABLE 58 TWO-TAILED PEARSON'S CORRELATION COEFFICIENTS FOR THE LEFT FRONTAL BY RISK-GROUP	207
TABLE 59 TWO-TAILED PEARSON'S CORRELATION COEFFICIENTS FOR THE LEFT ORBIT BY RISK-GROUP	209
TABLE 60 TWO-TAILED PEARSON'S CORRELATION COEFFICIENTS FOR THE LEFT TEMPORAL BY RISK-GROUP	211
TABLE 61 TWO-TAILED PEARSON'S CORRELATION COEFFICIENTS FOR THE RIGHT CRUCIFORM BY RISK-GROUP	213
TABLE 62 TWO-TAILED PEARSON'S CORRELATION COEFFICIENTS FOR THE RIGHT FRONTAL BY RISK-GROUP	215
TABLE 63 TWO-TAILED PEARSON'S CORRELATION COEFFICIENTS FOR THE RIGHT ORBIT BY RISK-GROUP	217

TABLE 64 TWO-TAILED PEARSON'S CORRELATION COEFFICIENTS FOR THE
RIGHT TEMPORAL BY RISK-GROUP 219

LIST OF FIGURES

FIGURE 1 ORBITAL THINNING OBSERVED IN AN INDIVIDUAL WITH A HISTORY OF SEVERE ALCOHOL USE DISORDER.....	4
FIGURE 2 TYPICAL ORBITAL ROOF THICKNESS.....	4
FIGURE 3 LATERAL FRONTAL AND TEMPORAL THINNING SEEN IN AN INDIVIDUAL WITH A HISTORY OF SEVERE ALCOHOL USE DISORDER. NOTE THE VESSEL EROSION THROUGH THE OUTER TABLE OF THE TEMPORAL CORTEX.	5
FIGURE 4 TYPICAL LATERAL FRONTAL AND TEMPORAL THICKNESS	5
FIGURE 5 OCCIPITAL THINNING SEEN IN THE CEREBELLAR FOSSAE IN AN INDIVIDUAL WITH A HISTORY OF SEVERE ALCOHOL USE DISORDER.....	6
FIGURE 6 TYPICAL OCCIPITAL CEREBELLAR FOSSAE THICKNESS.....	6
FIGURE 7 LOCAL HOUNSFIELD UNITS AND CORRELATIONS WITH BONE DENSITY REPORTED IN RECENT LITERATURE BY ANATOMIC LOCATION	22
FIGURE 8 INFERIOR VIEW OF THE CRANIUM SHOWING PLACEMENT OF THE ORBITAL SEGMENTS. ANTERIOR IS UP. SECTIONING CREATED VIRTUALLY IN 3D SLICER.	82
FIGURE 9 LATERAL VIEW OF A DECEDENT SHOWING PLACEMENT OF THE FRONTAL AND TEMPORAL SEGMENTS	83
FIGURE 10 ENDOCRANIAL VIEW OF THE CRANIUM SHOWING PLACEMENT OF THE CEREBELLAR FOSSAE SEGMENTS	84
FIGURE 11 CORONAL VIEW OF THE LEFT FRONTAL SEGMENT.....	87
FIGURE 12 SAME SLICE AS FIGURE 8, WITH THE FRONTAL SEGMENT HIDDEN.....	88
FIGURE 13 LEFT FRONTAL SEGMENT HIDDEN, WITH MINIMUM SEGMENT THICKNESS MEASURED.....	89
FIGURE 14 FRONTAL SEGMENT DISPLAYED SHOWING MINIMUM SEGMENT THICKNESS	90
FIGURE 15 RANGE OF MINIMUM THICKNESS BY SEGMENT AND RISK GROUP.....	98
FIGURE 16 PREDICTED PROBABILITY OF GROUP MEMBERSHIP FOR THE LEFT CEREBELLAR FOSSA	103

FIGURE 17 PREDICTED PROBABILITY OF GROUP MEMBERSHIP FOR THE LEFT FRONTAL.....	104
FIGURE 18 PREDICTED PROBABILITY OF GROUP MEMBERSHIP FOR THE LEFT ORBIT.....	104
FIGURE 19 PREDICTED PROBABILITY OF GROUP MEMBERSHIP FOR THE LEFT TEMPORAL	105
FIGURE 20 PREDICTED PROBABILITY OF GROUP MEMBERSHIP FOR THE RIGHT CEREBELLAR FOSSA	105
FIGURE 21 PREDICTED PROBABILITY OF GROUP MEMBERSHIP FOR THE RIGHT FRONTAL.....	106
FIGURE 22 PREDICTED PROBABILITY OF GROUP MEMBERSHIP FOR THE RIGHT ORBIT	106
FIGURE 23 PREDICTED PROBABILITY OF GROUP MEMBERSHIP FOR THE RIGHT TEMPORAL	107
FIGURE 24 RANGE OF SEGMENT VOLUME BY SEGMENT AND RISK GROUP	110
FIGURE 25 RANGE OF MINIMUM HOUNSFIELD UNITS BY SEGMENT AND RISK GROUP.....	115
FIGURE 26 RANGE OF MAXIMUM HOUNSFIELD UNITS BY SEGMENT AND RISK GROUP	120
FIGURE 27 RANGE OF MEAN HOUNSFIELD UNITS BY SEGMENT AND RISK GROUP	125
FIGURE 28 RANGE OF MEDIAN HOUNSFIELD UNITS BY SEGMENT AND RISK GROUP	131

LIST OF EQUATIONS

EQUATION 1 COHEN'S D FOR CALCULATION OF ESTIMATED STUDY EFFECT SIZE	73
EQUATION 2 CALCULATION OF S_{POOLED} FOR COHEN'S D.....	74
EQUATION 3 CALCULATION OF COHEN'S D TO DETERMINE ESTIMATED EFFECT SIZE	74
EQUATION 4 EQUATION TO DETERMINE SUBSAMPLE NEEDED FOR RELIABILITY TESTING.....	77
EQUATION 5 CALCULATION TO DETERMINE SUBSAMPLE NEEDED FOR RELIABILITY TESTING.....	78
EQUATION 6 EQUATION FOR BONFERRONI'S CORRECTION	91
EQUATION 7 CALCULATION OF BONFERRONI CORRECTION	91

CHAPTER 1

INTRODUCTION

Introduction

Individuals who are acutely intoxicated with ethanol and who also suffer health conditions related to long-term heavy ethanol consumption are well represented in medicolegal populations. For example, in the United States, there were over 12,000 deaths between 2018 and 2022 solely attributable to acute alcohol intoxication (CDC WONDER, 2024). This number does not account for cases where alcohol was present in combination with other drugs or where long-term alcohol use was the underlying or a contributing cause of death or was present as an additional finding. Further, in the United States, it is estimated that 1 in 10 individuals over the age of 18 meet the criteria for alcohol use disorder (SAMSHA, 2018). As such, it is prudent that forensic anthropologists have an appreciation for the negative skeletal effects that alcohol use can have.

There exists a well-documented link between excessive ethanol consumption and negative skeletal effects (See for example: Alvisa-Negrin et al., 2009; Bikle et al., 1993; Cheraghi et al., Gaddini et al. 2016; Maurel et al., 2012a and 2012b; Maddalozzo et al., 2009; Peris et al., 1994; Tucker et al., 2009). Grossly, heavy alcohol use can cause a reduction in bone formation and an increase in bone resorption, leading to global cortical thinning, decreased bone density, increased risk of pathological fracture, and poor fracture healing. Studies on the negative skeletal effects of heavy alcohol consumption have mainly focused on serum markers of bone turnover and/or the bone mineral density of anatomic areas that have the greatest impact on clinical morbidity in humans, such as the hip, wrist, and spine (for example, González-Reimers

et al., 2015; Spencer et al., 1986; Sripanyakorn et al., 2009). Little to no attention has been paid to the potential negative skeletal effects that heavy alcohol use could exert on the cranium.

This dissertation aims to begin addressing this knowledge gap by examining cranial thickness and radiodensity among heavy alcohol users using postmortem computed tomography scans from the New Mexico Decedent Image Database. The New Mexico Decedent Image Database (NMDID) pairs computed tomography scans of a forensic sample from the American Southwest with up to 69 variables containing information on an individual's cause of death, underlying health conditions, hobbies, dietary habits, and lifestyle, including their level of alcohol use (Edgar et al., 2020). NMDID was selected for this study because of its unique ability to examine cranial thinning in the context of high-risk alcohol use.

Importance of the Research

This study has potential applications in medicolegal death investigation, forensic anthropology, and clinical medicine. If cranial thinning indeed can occur in the setting of heavy alcohol use, medicolegal death investigators might better understand and explain fatalities among individuals with a known history of heavy alcohol use when blunt force trauma of the head contributes to their death. Furthermore, recognition of the role heavy alcohol use can have in these deaths may increase the documentation of alcohol use/alcohol use disorder on the death certificate, leading to better public health statistics and a better understanding of the far-reaching effects of alcohol.

If cranial thinning can occur in the setting of heavy alcohol use, it would give forensic anthropologists an additional differential diagnosis in cases where cranial thinning is present. As in medicolegal death investigation, this finding may also help forensic anthropologists better

interpret perimortem cranial blunt force trauma in heavy alcohol users. Lastly, a further appreciation of alcohol's systemic skeletal effects can help forensic anthropologists better interpret age and antemortem trauma in individuals known to use alcohol heavily.

Clinically, a finding of thinner crania among high-risk alcohol users could allow providers to do targeted head injury prevention education (e.g. helmet safety, fall prevention) with individuals who report heavy alcohol use. Appreciating the negative effects impact of heavy alcohol use may also give clinicians the opportunity to treat secondary cranial osteoporosis in this population.

Development of the Research Question

The impetus for this study was a series of forensic anthropology cases from northern New England in which extreme cranial thinning was observed in individuals with a known alcohol use disorder. A cursory literature review was performed to find an explanatory link between cranial thinning and alcohol use. Therefore, this research question was formulated to assess whether such a connection exists.

Figures 1, 3, and 5 are examples of the cranial thinning observed in the series of forensic cases among individuals with a known alcohol use disorder. Figures 2, 4, and 6 are examples of a cranium with typical thickness. All pictures were taken by the author and used with the permission of the consulting forensic anthropologist and the respective Office of Chief Medical Examiner (see Appendix 1).



Figure 1 Orbital thinning observed in an individual with a history of severe alcohol use disorder.



Figure 2 Typical orbital roof thickness



Figure 3 Lateral Frontal and Temporal thinning seen in an individual with a history of severe alcohol use disorder. Note the vessel erosion through the outer table of the temporal cortex.



Figure 4 Typical lateral frontal and temporal thickness



Figure 5 Occipital thinning seen in the cerebellar fossae in an individual with a history of severe alcohol use disorder.



Figure 6 Typical Occipital cerebellar fossae thickness

Definitions and Terminology Regarding Alcohol Use

For men, heavy drinking is defined as the consumption of >5 standard drinkers in a day or more than 15 standard drinks per week (NIAAA, 2024). For women, the threshold is much lower, with heavy drinking defined as consuming >4 standard drinkers per day or more than 8 in a week (NIAAA, 2024). Table 1 lists the United States’ definition of a standard drink. The New Mexico Decedent Image Database uses modified NIAAA definitions of drinking to code the decedent’s drinking status.

In this dissertation, the terms “heavy alcohol use” and “high-risk alcohol use” both refer to the consumption of greater than five standard drinks per day or 15 standard drinks in a week.

Table 1 US standard drink by grams of alcohol, serving equivalent, and alcohol by volume^a

Number of Standard Drinks	Grams of Alcohol	Equivalent to	Alcohol By Volume (ABV)
1 Standard Drink	14 grams	12 oz of beer 4 oz of wine 1.5 oz of spirits	~5% ABV ~12% ABV ~40% ABV

Table References: National Institute of Alcohol Abuse and Alcoholism (2024)^a

Hypotheses

As mentioned, little to no research exists regarding the impact of heavy, i.e., high-risk, alcohol use on the human cranium. Based on the known negative effects heavy alcohol use has on human bone in anatomic areas at risk for pathological fracture, it follows that the cranium would also be negatively affected. Combined with observations from forensic cases, the central hypotheses of this study are that:

- 1) Cranial bone is thinner in high-risk alcohol users than in low-risk alcohol users when measured at the orbital roof, lateral frontal, cerebellar fossa of the occiput, and the temporal squamous.
- 2) Cranial segments taken from high-risk alcohol users have less volume than those taken from low-risk alcohol users.
- 3) The composition of cranial bone in high-risk alcohol users is different than that of low-risk alcohol users in the following ways:
 - a. The Minimum Hounsfield unit is lower in high-risk users than low-risk users.
 - b. The Maximum Hounsfield units is greater in high-risk users than in low-risk users.
 - c. Mean Hounsfield units are greater in high-risk users than in low-risk users.
 - d. Median Hounsfield units are greater in high-risk users than in low-risk users.

Review of Relevant Literature

The following literature review provides contextual information necessary to inform the basis of this work and demonstrates the gaps in the literature that this dissertation aims to fill. Searches were performed using Google Scholar to find English language literature from the 1950s to the present, with exceptions for seminal articles from the late 19th and early 20th centuries. The search was conducted thematically on the topics of skeletal biology, alcohol's effect on bone, osteoporosis, cranial pathology, population standards for cranial thickness, the use of Hounsfield units to approximate bone density, and the use of radiography in forensic anthropology. Standard resources, such as textbooks, were use as appropriate.

Overview of Skeletal Biology and Relevant Physiology

Despite a lack of current research on alcohol-induced changes to the bones of the human cranium, the basics of human skeletal biology are well understood. The human skeleton provides structural support for soft tissues and plays a major role in whole-body homeostasis by acting as a mineral reservoir (Kartsogiannis and Ng, 2004). The human skeleton is composed of four cell types: osteoblasts, osteoclasts, osteocytes, and bone lining cells, all of which work in concert with a myriad of electrolytes, hormones, vitamins and nutrients, metals, and cytokines to maintain skeletal homeostasis (Robling and Bonewald, 2020). Tables 4 through 8 list these components and their effect on skeletal health as well as the impact alcohol has on skeletal homeostasis.

Osteoblasts

Osteoblasts (OB) are the cells primarily responsible for the deposition of new bone in the skeleton during times of remodeling and repair, i.e., maintaining skeletal architecture. They also function to regulate osteoclast differentiation (Neve et al., 2011; Burr and Allen 2019).

OBs are derived from mesenchymal stem cells (MSC) that are found in the bone marrow and the periosteum. Bone marrow-derived MSCs are primarily involved in normal skeletal remodeling, while periosteum-derived MSCs tend to become activated more during injury repair. In addition to generating OB, MSCs serve as the precursors to various other cell lineages such as chondroblasts, adipocytes, and myocytes. The transition of a cell from MSC into the mature osteoblast occurs in four stages: 1) lineage commitment, 2) proliferation, 3) extracellular matrix maturation, and 4) matrix mineralization (Neve et al., 2011; Titorencu et al., 2014).

During Stage 1 of OB maturation, bone morphogenic proteins from mature osteoblasts binds to MCS, transforming it into an osteoprogenitor cell. In Stage 2, the osteoprogenitor cells express Runt-related transcription factor 2 (RUNX2) and type I collagen, allowing them to further proliferate. Stage 3 begins the maturation of the extracellular matrix: parathyroid hormone acts upon the immature osteoblast, causing it to secrete alkaline phosphatase, which combines with extracellular calcium ions to form hydroxyapatite (Ansari et al., 2022; Titorencu et al., 2014). Finally, Stage 4 results in the full maturation of osteoblasts, secreting material necessary for the full mineralization of the extracellular matrix including, Type I and II collagen, and bone sialoprotein. The full mineralization of the matrix traps the majority mature osteoblasts, beginning their transformation into an osteocyte (Titorencu et al., 2014).

Beyond building new bone, osteoblasts help stop bone loss via their regulation of osteoclasts. The primary mechanism by which osteoblast inhibit osteoclasts is through the secretion of osteoprotegerin, which competes with Receptor Activator of Nuclear Factor kappa-B Ligand (RANKL) in binding with Receptor Activator of Nuclear Factor kappa-B (RANK) on the surface of osteoclastic precursor cells (Neve et al., 2011). The RANK-RANKL pathway is the primary mechanism by which osteoclastic precursors cells are driven towards maturing into osteoclasts (Burr and Allen, 2019).

Osteoclasts

Osteoclasts (OCL) are the antagonists of OBs and are responsible for the resorption of bone during remodeling. They are derived from hematopoietic cells, specifically of the monocyte-macrophage lineage. OCLs are large, multi-nucleated cells, and when mature, may exhibit from 3 to 20 nuclei. During bone resorption, OCL's pre-cursor cells are recruited to a

quiescent bone surface by inflammatory cytokines such as Interleukin-6, which stimulates RANKL (Burr and Allen, 2019). Once at the bone surface, their maturation is mediated by RANKL expressed by osteocytes and osteoblasts. During maturation, the OCLs undergo cellular polarization, which allows them to directly form a seal on the bone surface so that H⁺ ions can locally resorb bone (Burr and Allen, 2019).

Unlike osteoblasts, which can continue on as osteocytes, all osteoclasts die by apoptosis when their remodeling/resorption function is completed. While the exact trigger of cellular apoptosis in osteoclasts is not known, *in vitro* studies have shown that high levels of extracellular calcium (such as would be present in resorption pits) can cause cell death (Burr and Allen, 2019). It is reasonable to assume that the osteoclast would die once a critical level of calcium was reached, as otherwise, staying alive could cause OCLs to release an excess of calcium into the bloodstream and cause systemic pathophysiology and damage to the bone.

Osteocytes

Osteocytes comprise approximately 90% of all bone cells, and serve critical functions related to skeletal homeostasis, impacting both osteoblasts and osteoclasts. Arising from mature osteoblasts, osteocytes are not only the longest living bone cell, but one of the longest living cells in the human body, with a potential lifespan reaching into the decades (Robling and Bonewald, 2020).

As discussed above, a mature osteoblast becomes enmeshed within the bony matrix and begins to form an osteocyte during the final stage of matrix mineralization. After an OB is trapped, it begins to generate cellular extensions that expand until they make contact with either another enmeshed OB, or a mature osteocyte. Through their extensive cytoplasmic and canaliculi

networks, osteocytes can detect changes in mechanical loads, and shifts in fluids, ions, and hormones. A major chemical produced by osteocytes is sclerostin. Sclerostin helps the osteocyte exert control over both osteoblasts and osteoclasts. Increased amounts of sclerostin are released when the osteocyte detects limited mechanical load, such as during disuse or microgravity. The increased Sclerostin stimulates RANKL and osteoclastogenesis and also inhibits the differentiation of MSCs into osteoblasts. Conversely, when suppressed, increased osteoblastogenesis occurs. In response to the environmental shifts previously mentioned, the osteocyte can secrete OPG, RANKL, or Sclerostin, thereby exerting control over both osteoblasts and osteoclasts (Burr and Allen, 2019). (Delgado-Calle et al., 2017).

Bone Lining Cells

While most (60-80%) osteoblasts die by apoptosis, approximately 5-20% of them become embedded in the osteoid matrix they have produced and differentiate/mature into osteocytes. The remaining osteoblasts differentiate into bone lining cells (BLC) during remodeling (Burr and Allen, 2019). BLCs are extremely flat and line the surfaces of bone that are not undergoing remodeling. By communicating with osteocytes through gap junction, BLC help to regulate a myriad of functions including hematopoiesis, calcium homeostasis, and bone remodeling (Dall'Ara and Cheong, 2022). BLC help keep the correct contour and shape of the bone by removing extraneous collagen fibrils and are also thought to be able to revert back to osteoblasts when needed, e.g. for fracture repair and remodeling. (Miller, 1989; Matsuo and Otaki, 2012).

Skeletal Remodeling

Remodeling is the process by which skeletal integrity is maintained through the repair of microdamage. Remodeling also plays a key role in the body's ability to maintain calcium homeostasis (Gaddini et al., 2016). The remodeling cycle represents a simple mechanism, with exceedingly complicated components and players. It is thought that microdamage to the skeleton and osteocyte death are triggers of remodeling (Burr and Allen, 2019). The two main types of remodeling are targeted, wherein acute damage to the skeleton is repaired in a focused, hyper-local manner, and stochastic, which occurs randomly with no specific trigger and is thought to play a role in calcium homeostasis. Remodeling can occur on any of the four main bone surfaces (periosteal, endocortical, trabecular, and intracortical, and can be divided into five stages:

- 1) Activation- during this phase, osteoclastic precursors (monocytes) are recruited to the bone surfaces by the activation of inflammatory cytokines, such as IL-6, which activate RANKL, thereby stimulating osteoclastogenesis. This release of inflammatory cytokines is particularly true of targeted remodeling when there is microdamage.
- 2) Resorption- When OCs are mature, they bind to the bone surface and free calcium and collagen from the bone. This process lasts 3 to 6 weeks.
- 3) Reversal- Once OCs are done resorbing bone, OBs are recruited to the site through an unknown mechanism to come in and begin laying down the osteoid matrix.

4) Formation- Generally, this is the phase in which OBs lay down the osteoid matrix, primarily Type 1 collagen, which will serve as the medium upon which mineralization will occur. Mineralization takes place in two distinct phases, the first is over a period of 2-3 weeks and involves the recruitment of calcium and phosphate ions to begin forming the hydroxyapatite crystals. Phase one is responsible for approximately 70% of the re-mineralization. Phase Two mineralization takes place over the course of a year or more and lays down the remainder of the bony crystal.

5) Quiescence- As the name suggests, this is the resting phase of bone remodeling. Those OBs that have not died by apoptosis have become trapped in the osteoid and become osteocytes or have transitioned to bone lining cells. Most skeletal structures are in the Quiescent phase at any given time (Burr and Allen, 2019).

In most instances, a complete remodeling cycle takes approximately 4 to 6 months to complete; however, as discussed above, the newly deposited bone may take upwards of a year to fully mineralize (Burr and Allen, 2019). The rate of remodeling in a healthy individual is predominantly determined by the person's age and genetics. However, several external factors, such as exercise/physical activity, nutrition, and medications, may all influence and alter the actual timeline. For example, Chakkalakal (2005) and Michael and Bengtson (2016) have demonstrated that remodeling is substantially affected in the setting of chronic alcohol use.

Dysregulation/Uncoupling

While the above-described processes are how the skeletal system works in an ideal, homeostatic state, dysregulation does occur with some frequency. Dysregulation of any part of

the bone remodeling cycle can be extremely detrimental and generally leads to one of two skeletal changes: either a net increase in bone mineral density or a net decrease in bone mineral density. Dysregulation leading to a net decrease in bone mineral density can occur in one of three ways: 1) a net increase in the number or survival time of osteoclasts, 2) a net reduction in or early apoptosis of osteoblasts, or 3) a combination of the two, which, can be seen in the setting of long-term, heavy alcohol use (Gaddini et al., 2016; Rosen, 2020). Any condition that creates one of these three scenarios will lead to a net loss of bone, potentially resulting in osteoporosis.

Overview of the General Epidemiology, Pathophysiology, and Diagnosis of Osteoporosis

As previously discussed, severe dysregulation of bone remodeling, favoring a net decrease in bone density, can result in Osteoporosis (Rosen, 2020). Clinically, osteoporosis is defined as a bone mineral density 2.5 standard deviations below that of white women aged 20-29 (Kanis et al., 1994). Osteoporosis significantly impacts the life expectancy and quality of life for millions of Americans each year (National Osteoporosis Foundation, 2018). By 2025, an estimated 3 million pathologic fractures will occur annually in the US, resulting in estimated medical expenditures of over \$25.2 billion (Burge et al., 2007).

The benchmark population may vary, but the World Health Organization uses a population of young, healthy women (Kanis et al., 2008). The use of different reference populations to measure bone density can have drastic effects on the prevalence and diagnosis of Osteoporosis (Kaufman, 2021). For example, Kaufman (2021) found that in older men, when compared to the standard WHO cohort, the rate of osteoporosis was only 2%; however, when compared to a cohort of young men, the rate of osteoporosis increased to 9.4%. Kaufman's findings may well explain why 10 million Americans currently meet the clinical criteria for

osteoporosis, but many remain untreated until they experience an osteoporotic fracture (National Osteoporosis Foundation, 2018).

Pathological fractures are a leading cause of morbidity and mortality in elderly individuals (Rosen, 2020). Commonly, pathologic fractures are seen in the spine, wrist, and hip, and therefore are the areas that are the most commonly analyzed when testing for bone density (Rosen, 2020). Hip fractures are the most common osteoporotic fracture and also the most deadly, with a 20% risk of mortality in the first year after a hip fracture (Rosen, 2020).

Osteoporosis can be classified into two predominant types. Type I, or primary osteoporosis, occurs in aging populations as the result of gonadal insufficiency and is classically seen in postmenopausal women (Rosen, 2020). Type II, or secondary osteoporosis, results indirectly from another condition, either medical, environmental, or behavioral (Rosen, 2020).

Type I Osteoporosis

Type I osteoporosis predominately affects postmenopausal women, with the prevalence increasing significantly with age (Melton, 1995; Rosen, 2020). At age 50, approximately 14% of women would meet the clinical definition of osteoporosis, while by age 80, 70% of women would meet the diagnostic criteria. Men also lose skeletal mass as they age and will eventually reach the same loss as women approximately ten years later (Kaufman, 2021). Risk factors for developing osteoporosis include high and low body mass index, smoking, family history of fracture, being over the age of 65, and alcohol use (Rosen, 2020).

Osteoporosis occurs in aging women and men due to a reduction in gonadal hormones (Rosen, 2020). In women, the effect is particularly profound due to the immediate deprivation of endogenous estrogen. Estrogen, as discussed below, is a critical component of skeletal health as

it promotes osteoblastogenesis and the survival of mature osteoblasts while simultaneously inhibiting osteoclastogenesis by reducing inflammatory cytokines (Li et al., 2020). Similarly, testosterone has been found to have a protective effect on bone by increasing cell death in osteoclasts and inhibiting apoptosis in osteoblasts (Gaddini et al., 2016).

Type II Osteoporosis

Unlike Type I osteoporosis, Type II osteoporosis can affect individuals of any age group because it occurs secondary to a condition that is detrimental to skeletal health. Common conditions which promote the onset of Type II osteoporosis include hematologic disorders, gastrointestinal conditions, long-term glucocorticoid therapy, smoking, liver disease, Type I and Type II diabetes, and severe alcohol use disorder (Gaddini et al., 2016; Rosen, 2020).

Clinicians treating patients with most of the conditions listed would be aware of their patients' risk factors for Type II osteoporosis. Unfortunately, many patients who use alcohol excessively, do not discuss their drinking with their healthcare providers. Hingson et al. (2012) found that only 14% of individuals drinking excessively discussed the risks of doing so with their provider. According to the 2020 National Household Survey on Drug Use and Health, 27.6 million people aged 18 or older in the United States had an alcohol use disorder (Delphin-Rittmon, 2022). This means that nearly twenty-eight million people in the United States alone may be at silent risk for Type II osteoporosis.

Diagnosis of Osteoporosis

Dual Energy X-ray Absorptiometry

The current gold standard for diagnosis of osteoporosis is dual-energy x-ray absorptiometry, or DEXA (previously referred to as DXA). DEXA uses low-dose X-rays with two specific energy wavelengths to measure bone density. As the two energy waves pass through the body, one wave has greater affinity for soft tissue, while the other has a greater affinity for bone (Berger, 2002). Using two different energy waves allows for the density of soft tissue to be assessed independently from that of bone. Density is assessed by measuring the difference between the amount of energy released from the x-ray generator and the amount of energy that reaches the receiver. The greater the energy lost, the more absorbed by the patient's body. Tissue density is highly correlated with the amount of energy that is absorbed, and so less energy that reaches the receiver, the higher density of tissues (i.e. bone) it passed through (Berger, 2002).

In the early days of DEXA, Brismar and Ringertz (1996) examined the impact of including the cranium in measurement of areal bone mineral density. They found that due to the high cortical content of the cranium, which accounted for over 20% of the total areal BMD, T-scores and prediction of future fracture risk were significantly skewed. They therefore concluded that the cranium should be excluded from DEXA scans, and that is still the case today.

Computed Tomography

The first documented use of X-rays to assess osteoporosis was by Lachman and Whelan (1936). Since then, radiography has advanced considerably and in recent years, researchers have recognized the utility of using clinical computed tomography scans (CT scans) to perform opportunistic screenings of bone mineral density (Christensen et al., 2020; Colantonio et al.,

2020; Elarjani et al., 2021; Hendrickson et al., 2018; Lee et al., 2017; Pervaiz et al., 2013; Pickhardt et al., 2013; Romme et al., 2012; Schreiber et al., 2014; Schreiber et al., 2015; Zaidi et al., 2018). Computed tomography is well situated to perform these measurements due to its fundamental mechanics.

First used in a clinical setting in the early 1970's, computed tomography scans essentially perform a rapid series of helical X-rays and then uses various algorithms to amalgamate them, allowing for 3-dimensional reconstruction of the scanned object (Garvin and Stock, 2016; Hounsfield, 1980). Furthermore, CT scans result in a universally used, dimensionless unit, called a Hounsfield Unit (HU). The arbitrary scale of HUs is set so 0 equals the radiodensity of distilled water at 0° Celsius at sea-level, while -1000 equals the radiodensity of air at 0° Celsius at sea level (Hounsfield, 1980). Hounsfield units are derived from the attenuation coefficient of the x-ray beam used by the CT scanner, i.e. how much of the x-ray energy is lost when it passes through an object (National Institute of Biomedical Imaging and Bioengineering, 2022). Table 2 shows common values associated with HU.

Table 2 Commonly accepted values associated with Hounsfield units^a

Substance	Hounsfield Range
Air	-1,000
Fat	-100
Water	0
Soft tissue	30 - 45
Trabecular bone	300 – 800
Cortical bone	>1,000

Table references: Hounsfield (1980)^a

Several of studies have been able to correlate HU values to DEXA T-scores denoting normal, osteopenic, and osteoporotic bone (Buckens et al., 2015; Christensen et al., 2020; Colantonio et al., 2020; Elarjani et al., 2021; Hendrickson et al., 2018; Lee et al., 2017; Na et al.,

2018; Pervaiz et al., 2013; Pickhardt et al., 2013; Romme et al., 2012; Shreiber et al., 2015; Yamada et al., 2007; Zaidi et al., 2018). To correlate HU with DEXA scores, researchers either had to use a phantom calibration, i.e., where an object of known density is scanned and the resulting Hounsfield for additional scans can be calibrated to that density, or had DEXA scans from the patients included in the study with which to compare HU. However, the resulting HU were all dependent on the area of the body and the scan settings of the CT scanner. The range of Hounsfield Units found in each study are displayed in Figure 7.

The threshold for osteoporosis in the spine varies greatly depending on which segment is studied. Na et al. (2018) measured Hounsfield units in the diplöe of the anterior frontal and found that HU <515 was indicative of osteoporosis. Colantonio et al. (2020) found that an HU of <447 was indicative of osteoporosis in the cervical spine. Romme et al. (2012) found that thoracic vertebrae HU <147 was diagnostic of osteoporosis. The most studied area of the spine is the lumbar vertebrae, likely due to its common measurement in DEXA. Various researchers had found that normal bone is represented by HU of 186 to 201, while osteoporotic bone was found to have HU of 99 to 136 (Buckens et al., 2015; Elarjani et al., 2021; Hendrickson et al., 2018; Lee et al., 2017; Pickhardt et al., 2013; Zaidi et al., 2018).

For the upper body, Yamada et al. (2007) found that HU of the humeral head ranging from 93 to 149 indicated normal bone, 77 to 129 indicated osteopenia, and 63 to 121 indicated osteoporosis. The significant overlap between these values indicated that the humeral head is likely a poor area to screen for osteoporosis. Meanwhile, Pervaiz et al. (2013) found that proximal humerus HU of 104-121 indicated normal bone, 93-103 indicated osteopenia, and <92 indicated osteoporosis. These data had much less overlap, suggesting that if the humerus is used,

the proximal portion should be used. Finally, Shreiber et al. (2015) found a HU of <231 was predictive of an increased fracture risk at the distal radius.

In the lower extremities Lee et al. (2017), found that HU of <296 in the femoral head was diagnostic for osteoporosis, while a HU of just 4 was diagnostic for the femoral neck.

Christensen et al. (2020) found a HU of 112 was diagnostic for the proximal femur. Finally, Lee et al. (2017) found that HU <122 of the distal tibia, and <311 for the talus, were diagnosis of OS.

The range of Hounsfield units reported in the literature that denote normal, osteopenic, and osteoporotic bone varies and overlaps throughout the skeleton. This is likely due to the different composition of the areas as well as the different mechanical loads they experience as well as the scan settings of the device used. Unless the scan settings of two studies are identical, caution should be used during comparison.

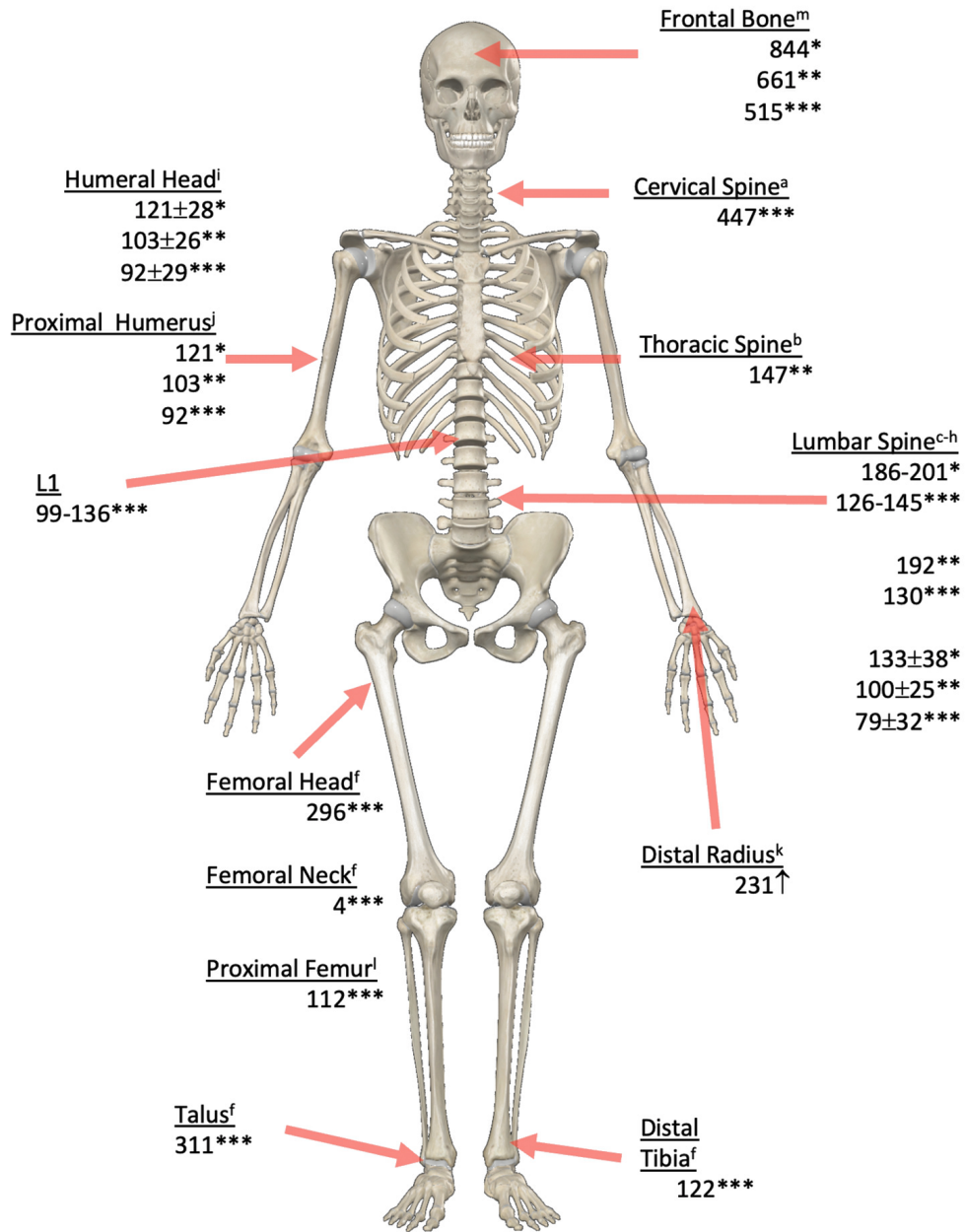


Figure 7 Local Hounsfield units and correlations with bone density reported in recent literature by anatomic location

Figure references: Colantonio et al. (2020)^a, Romme et al. (2012)^b, Buckens et al. (2015)^c, Elarjani et al. (2021)^d, Hendrickson et al. (2018)^e, Lee et al. (2017)^f, Pickhardt et al. (2013)^g, Zaidi et al. (2018)^h, Yamada et al. (2007)ⁱ, Pervaiz et al. (2013)^j, Shreiber et al. (2015)^k, Christensen et al. (2020)^l, Na et al., 2018^m.
 *normal bone, **osteopenia, ***osteoporosis

Summary of General Epidemiology, Pathophysiology, and Diagnosis of Osteoporosis

Millions of Americans are at risk of an osteoporotic fracture, with over 10 million currently undiagnosed. While DEXA remains the gold standard for the diagnosis of osteoporosis, recent studies have found that CT-derived Hounsfield units are an excellent proxy for bone mineral density and are good at predicting osteoporosis and subsequent fracture risk. However, more research is needed as there is no current universally agreed-upon conversion for CT-derived Hounsfield units to DEXA-derived t-scores. Furthermore, the majority of these studies have focused predominantly on the clinically important areas prone to pathologic fracture, with only one study examining cranial osteoporosis via Hounsfield units, but not in the context of injury risk.

Overview of Cranial Osteoporosis and Other Cranial Pathology

Cranial Osteoporosis

Despite the prevalence of high-risk alcohol use in the United States and the well-documented connection between excessive alcohol use and Type II osteoporosis, the research on alcohol-related osteoporosis has focused on the sites at the highest risk for fracture, i.e., the hip, wrist, spine (González-Reimers et al., 2015; Rosen, 2020; Spencer et al., 1986; Sripanyakorn et al., 2009). The impact of heavy alcohol use on the human cranium has largely been overlooked, even though reduced bone quality in the cranium may have significant impacts on morbidity and mortality (Mann et al., 2017; Torimitsu et al., 2014a; Yoganandan et al., 1995).

As early as the 18th century, anatomists and anthropologists have been interested in the thinning of the human cranium (Sandifort, 1783; Anderson, 1882). However, besides Na et al.

(2018), only a handful of studies have directly or indirectly explored the relationship between the cranium and diffuse osteoporosis and thinning via computed tomography (Hatch et al., 2018; Kawashima et al., 2019, Torimitsu et al., 2014a)

Hatch et al., 2018 examined the lateral skull base in order to determine if there was a relationship between Hounsfield units, cerebrospinal fluid leak, and obesity. The authors found no significant difference between the two groups suggesting that obesity does not play a role in the thinning of the skull base (Hatch et al., 2018).

Kawashima et al. (2019) did a retrospective study using a cohort of clinical patients from a large hospital who had both a cranial CT and DEXA performed within 12 months of one another. The normal density and osteoporotic cohorts each were comprised of 29 individuals. The authors of this study used advanced texture analysis¹ to examine 41 different features of the clivus, sphenoid triangles, and mandibular condyles. Results of the texture analysis found statistically significant differences in several of the features measured, indicating that texture analysis may be used to assess cranial osteoporosis (Kawashima et al. 2019). Although apparently promising, this methodology is markedly computationally heavy, and many of the texture analysis features were proprietary to the institution's imaging system.

Finally, Torimitsu et al. (2014a), used a forensic sample of Japanese men and women over the age of 25 to test cranial fracture load by age and sex at four cranial points (the parietal, occipital, and left and right temporals). Prior to fracture testing, each of the 376 samples collected were scanned via computed tomography. Results showed a weak but significant negative correlation between cranial thickness and age in the female sample, which the authors

¹ Texture analysis uses advanced mathematical algorithms to analyze “complex visual patterns with an image that consist of simple sub-patterns with characteristic features that may be evaluated through quantitative analysis”. (Kawashima et al., 2019, pg. 213).

attributed to the possibility of the general decrease in bone density with age seen among women. However, these results were ancillary and not given much discussion in the article. Though this article did mention alcohol, the extent of the discussion of cranial osteoporosis and its (potential) connection to alcohol was limited to, “In future studies, ante-mortem data should be collected taking into account nutrition conditions, history of chronic alcohol use, cigarette smoking, and drug abuse, as well as other external factors” (Torimitsu et al., 2014a, pg. 185e7).

Cranial Pathology

Unlike the dearth of articles examining cranial thinning in systemic osteoporosis and alcohol use, research into other potential causes of cranial this is extensive. Both basic and advanced imaging modalities may be used to assess pathological changes in bone. Research has shown that imaging greatly enhances the differential diagnosis of skeletal pathology, such as rickets, or the developmental pathway of pathological conditions, such as craniosynostosis (Buikstra, 2019; Heuzé et al., 2010).

As shown in Table 3, imaging can be employed to help support the differential/probabilistic diagnosis of those pathological conditions in the cranium. Table 3 compares the skeletal features, etiology, radiographic, and histological signs of conditions that may affect the cranium as well as the populations most commonly affected. Alterations of normal cranial thickness and density may be normal anatomic variants, such as arachnoid granulations or enlarged parietal foramina, or pathological in nature, such as scurvy or porotic hyperostosis. Forensic anthropologists need to appreciate the manifestations of these conditions so that the remains may be properly interpreted.

Alcohol-induced bone disease, a well-known category of Type II osteoporosis, may present in the cranium with abnormally thin cortex, which may or may not include erosion of the outer table by meningeal vessels. The cause of the observed thinning is multifactorial but is common in heavy alcohol users (e.g., those consuming greater than four standard drinks per day), who may not otherwise be at risk for Type I osteoporosis. Radiographically, this may present with abnormally thin cortical bone and reduced trabeculae (Michael & Bengtson, 2016). The physiologic effects of alcohol on bone are discussed in greater detail below.

As opposed to alcohol-induced bone disease, primary (Type I) osteoporosis usually presents in older populations as a result of gonadal insufficiency (Barnsley et al., 2021; Burr and Allen, 2019; Rosen, 2020). Diffusely thin cortical bone, with microfracture and low bone density when measured by dual-energy x-ray absorptiometry, are all radiographic hallmarks of this disease (Barnsley et al., 2021; Burr and Allen, 2019; Rosen, 2020). Compared with alcohol-induced bone disease, wherein histology shows a global reduction of remodeling, histological signs of primary osteoporosis show a loss of trabeculae, particularly those oriented horizontally (Bikel et al., 1993; Marcu et al., 2011).

Perhaps most similar to alcohol-induced changes in the cranium is the previously discussed phenomenon of biparietal thinning. Biparietal thinning presents as unilateral or bilateral focal, ovoid areas of thinning on the parietal. The depression's margins usually slope inward toward the cortex of the endocranium with the thinnest areas of depression towards the center of depression and follow a somewhat predictable progression of ecto-cranial cortical and diploic erosion, with preservation of the endo-cranial surface (Mann and Hunt, 2013). Its etiology is unclear, though senile osteoporosis and genetic and biomechanical causes have been suggested (Mann et al., 2017). Radiographically, these changes appear as extreme, well-

circumscribed areas of radiolucency on the parietals, with occasional evidence of healing fracture. While the etiology of biparietal thinning is not agreed upon, primary osteoporosis, hereditary conditions, and biomechanical factors have all been postulated (Mann et al., 2017). Histological signs can be uncertain, as some cases have reported increased bone turnover, while others have noted a paradoxical lack of osteoclasts (Mann et al., 2017). The incidence of biparietal thinning increases with age and is more common among women, perhaps lending more credence to the etiology being related to senescent osteoporosis (Mann and Hunt, 2013).

Biparietal thinning should not be confused with enlarged parietal foramina, which is a common finding in all populations, though more so among males. Sixty-five percent of the population have foramina >2mm, while only 1:20,000 have foramina >5mm. The enlarged foramina are the result of poor ossification and are easily appreciated radiographically. If the foramina are extremely pronounced, an MRI can be used for the detection of associated soft tissue abnormalities (Mann and Hunt, 2013).

Famously known to affect sailors, in modern cases, scurvy usually appears in individuals experiencing an intentional withholding of proper nutrition. Scorbutic skeletal lesions present as abnormal porosity across the cranium, with particularly pathognomonic lesions observed in the greater wing of the sphenoid (Crist and Sorg, 2014; Waldron, 2009). Cranial bossing on the frontal may also be observed due to an increase in periosteal apposition (Waldron, 2009). Radiographically, scurvy classically presents with a white line of Frankel, i.e., a widened and hyperdense zone of provisional calcification in long bones and evidence of subperiosteal hemorrhage (Sorg et al., 2004; Waldron, 2009). Histologically, thickened calcification zones decreased trabeculae, and new periosteal bone formation can be seen (Waldron, 2009).

Porous cranial lesions, which can present as cribra orbitalia (CO) or porotic hyperostosis (PH), have historically been attributed to anemias, particularly iron deficiency anemia [Brickley, et al., 2020; O'Donnell et al., 2020). Recently, however, there has been a greater appreciation that these lesions may be caused by other illnesses, such as respiratory infections or gastrointestinal disorders, but that they are ultimately a sign of physical stress (O'Donnell et al., 2020; O'Donnell et al., 2023). Cribra orbitalia manifests as small “sieve-like” lesions on the roof of the orbit, while porotic hyperostosis presents as 0.5mm to 2mm porous lesions on the cranial vault accompanied by thickened bone (Mann and Hunt, 2013; O'Donnell et al., 2020). While the two lesions may have some pathogenic overlap, they can be caused by different conditions (e.g., CO may be caused by hypo-or-hyperplastic conditions, whereas PH, by definition, has hypertrophy involved) (Rivera and Mirazón Lahr, 2017). Both manifest in childhood, and the lesions present in adult remains usually show evidence of healing (O'Donnell et al., 2023). Radiographically, computed tomography may be used to appreciate CO and PH as one would macroscopically² (Anderson et al., 2021; O'Donnell et al., 2019; O'Donnell et al., 2020; O'Donnell et al., 2023). While both conditions are fairly common in archaeological populations, their prevalence in contemporary populations is widely unknown, but CO has been reported to be as high as 24% in a pediatric forensic sample from the American Southwest (Mann and Hunt, 2013; O'Donnell, 2020).

Arachnoid depression and pacchionian pits are normal findings on the endocranial surface, arising from granulations that serve to filter and return cerebrospinal fluid. Usually ranging from <2mm-5mm, they are most common in the frontal and parietal regions and present as small depressions with smooth edges (Mann and Hunt, 2013). Rarely do the depressions erode

² Lesions present on computed tomography scans must be larger than the scan resolution to be appreciated (Anderson et al., 2021).

through the outer cortical surface. Radiographically, they appear as well-circumscribed areas of normal bone that show no evidence of lysis or sclerosis. Arachnoid depressions and pacchionian pits occur in all populations and increase in size and frequency with age, though no standard exists for aging an individual based on their appearance (Mann and Hunt, 2013)

When extremely prominent arachnoid depressions are present on the endocranial surface of the frontal, giving the appearance of a so-called “beaten copper appearance,” intracranial hypertension should be kept in mind. Usually, the results of an endocrine disorder, this condition predominately affects older obese women (Degnan and Levi, 2011; Ittyachen and Anand, 2019). Radiographically, this condition appears exactly as it does macroscopically. The endocranial surface has a copper-pounded appearance with prominent depression, particularly in the temporal and sphenoid (Ittyachen and Anand, 2019).

Only causing decreased cortical bone and increased porosity in the very early stages, Paget’s disease is caused by a dysregulation of bone coupling; first increasing bone resorption, then increasing osteoblastic activity, leading to a thickened, heavy skull, quite the opposite of alcohol-induced bone disease. Radiographically, Paget’s disease presents with inflammation and sclerosis of bone and with a thickened cortex. Paget’s is uncommon, with one study finding that it only affected <2% of the population in the United Kingdom (Waldron, 2009)

While temporal thinning may be seen in alcohol-induced bone disease, destruction and erosion of the temporal are common findings in skeletal remains, and when present, mastoiditis should be considered. When the middle ear becomes extremely infected, the infection may spread to the mastoid, destroying the normal organization of the mastoid sinus and eroding the outer cortical layer (Mafee et al., 1985). Radiographically, the disruption of the bony septa of the air cells and erosion of the lateral can be seen. On occasion, osteomyelitis of the petrous may be

present as well. Mastoiditis is a rare condition in modern populations, usually affecting children rather than adults (Mafee et al., 1985).

Finally, classic hyperparathyroidism, in which excessive levels of parathyroid hormone are produced due to benign parathyroid adenomas, significantly increases bone resorption and can have an extreme impact on the cranium (Marcocci et al., 2012). In the cranium, hyperparathyroidism causes diffuse, well-defined, lytic lesions, giving the cranium a distinct “salt and pepper” appearance on radiography due to the alternation areas of normal bone and resorbed areas (Bennett et al., 2020).

Table 3 Comparison of the skeletal features, etiology, radiographic signs, and histological signs of common pathological conditions that may cause thinning or porosity of the cranium

Condition	Skeletal Features	Etiology	Radiographic Signs	Histological Signs	Affected Populations
Alcohol-induced bone disease	Global osteopenia/osteoporosis with thinning of both trabeculae and cortical bone Evident in areas with thin diploe such as scapulae and cranium	Decreased osteoblast function, increased osteoclast function Nutritional deficits leading to electrolyte imbalances Direct effect of alcohol and its metabolites on cortical bone via Haversian System	Abnormally thin cortex and trabeculae Hypothesized lower Hounsfield Units and 3D volume on CT	Global reduction in remodeling, but with increased resorption surfaces and decreased formation surfaces	Chronic, heavy alcohol users, e.g. $\geq 28\text{g/day}$
Primary Osteoporosis	Thinning of trabeculae Abnormally thin cortex Low-velocity fractures in the wrist and hip Collapsed thoracolumbar vertebrae Subjectively “light” bones	Gonadal insufficiency leading to: -decreased osteoclast apoptosis -decreased osteoblast lifespan, proliferation and differentiation -increased osteoclastogenesis due to increased inflammation	Thin cortex Old fractures of vertebrae -1 to -2.5 standard deviation on DEXA Lower trabeculae bone volume/total bone volume	Thinned trabeculae with poor connectivity Preferential loss of horizontal trabeculae	Most at risk: postmenopausal white women Men >75 years of age
Biparietal thinning	Thin, translucent, usually ovoid depressions found on the lateral and superior parietals. Erosion of the outer cortex sloping inward to the area of greater concavity. The contour of the inner table is preserved. Typically avoids involvement of the parietal foramina.	Etiology uncertain but may be related to senile osteoporosis, or have genetic or even biomechanical origins	Extreme radiolucency of the parietal Disrupted contours of the external parietal	Paradoxical lack of osteoclasts in some cases Evidence of woven bone in others, likely representing previous microfracture	More common in women than in men. Increasing incidence with age. Thought to affect 2-3% of the population.

Table 3 continued

<p>Enlarged parietal foramina</p>	<p>Enlarged holes surround the parietal foramina. May be circular, ovoid, or slit like.</p>	<p>Caused by complete are aberrant ossification of parietal fontanelles, may have genetic and environmental components</p>	<p>Observed as paired defects in the parietal. MRI is superior for the detection of any associated soft tissue anomalies</p>	<p>--</p>	<p>More common in males. Small (<2mm) foramina seen in ~65% of the population, while >5mm foramina are seen in ~1:20,000 and are usually hereditary</p>
<p>Scurvy</p>	<p>Hypertrophic bone of the orbits Abnormal porosity of the: anterior & posterior maxilla, infraorbital foramina, palate, horizontal ramus, greater wing of the sphenoid, lingual surface of the mandible Evidence of subperiosteal hemorrhage Antemortem tooth loss Evidence of intraarticular hemorrhage Cranial bossing due to new periosteal bone</p>	<p>Vitamin C deficiency leading to defects in the production of Type I Collagen (responsible for bone formation and blood vessel integrity)</p>	<p>White line of Fraenkel “Scurvy” line Dense line of calcification around epiphysis Metaphyseal spurs Subperiosteal hemorrhage/intracortical lacunae</p>	<p>Thickened zone of provisional calcification Decreased in trabeculae Evidence of new periosteal bone formation Disorganization of the growth plate</p>	<p>Historic- sailors and settlers without access to vitamin C Modern- elderly individuals with insufficient diets, children, typically in the setting of abuse/intentional malnourishment</p>
<p>Porotic cranial lesions</p>	<p>Presents primarily as either cribra orbitalia (CO) or porotic hyperostosis (PH). CO: small “sieve-like” lesions on the orbital roof, usually bilateral. Occasionally accompanied by cranial thinning. PH: 0.5mm to 2mm porous lesions on the cranial vault, accompanied by thickened bone. Primarily form between 6 months and 12 years of age. Adults with CO and PH will present with healed lesions.</p>	<p>Classically thought to be due to anemias of various origin, but now generally viewed as a manifestation of physical stress/disease in childhood e.g. infection, gastrointestinal illnesses, etc.</p>	<p>Both CO and PH may be viewed as they would macroscopically via CT 3D renderings CO: may present with thickened orbits PH: diplöic thickening, classic “Hair on end”</p>	<p>May show hypertrophic bone marrow with a reduction in red blood cells or hypertrophic bone with horizontally organized trabeculae</p>	<p>Common finding in archaeological populations from coastal Peru and the American Southwest Unknown incidence in contemporary populations, but noted to be as high as 24% (CO) and in a pediatric forensic sample</p>

Table 3 continued

<p>Arachnoid depressions and pacchionian pits</p>	<p>Varied in size form <2mm to >5mm. More common in the anterior frontal posterior to bregma (arachnoid). More common in the parietals and frontals (pacchionian)</p> <p>Smooth margins with no evidence of remodeling</p> <p>Erosion through outer table is extremely rare.</p>	<p>Normal variant, serve to filter and return CSF</p>	<p>Circumscribed pitting of the internal table of the skull, with no sclerotic or pathological changes to bone.</p>	<p>--</p>	<p>Common in all populations, but increase in size and frequency with age.</p>
<p>Intracranial hypertension</p>	<p>“Beaten copper” appearance of the cranium</p>	<p>Endocrine disorders such as Cushing Disease; hypervitaminosis A; chronic renal failure.</p> <p>May result from increased intravascular volume or increased CSF production</p>	<p>Prominent arachnoid pits, typically found within the temporal and greater wing of the sphenoid</p> <p>“Copper pound skull” appearance</p>	<p>--</p>	<p>Most commonly seen among middle aged obese women</p>
<p>Paget’s Disease</p>	<p>Inflamed, sclerotic bone</p> <p>Thick, heavy skull</p> <p>Lysis of subchondral bone</p>	<p>Likely a combination of environmental and genetic</p> <p>Disorder of the osteoclasts leading to increased resorption followed by increased abnormal osteoblastic activity.</p>	<p>Early stage- osteoporosis circumscripta of the cranium</p> <p>“Flame sign” denoting “V” shaped lysis of subchondral bone</p> <p>Thick trabeculae</p> <p>Sclerotic bone</p> <p>Cortical thickening</p>	<p>Disorganized bone formation</p>	<p>Most individuals over the age of 55. ~2% of the population of the UK.</p>

Table 3 continued

Mastoiditis	<p>Lytic destruction of the contour of the mastoid, particularly the later wall.</p> <p>Endocranially, inflammatory changes of the petrous may be present</p>	Acute infection of the middle ear that extends to the mastoid sinus	<p>Erosion of the bony septa of mastoid air cells</p> <p>Erosion of the lateral wall of mastoid</p> <p>Possible osteomyelitis of the petrous</p>	--	Instigating infections most common in infants. Rarely seen in all populations
Hyperparathyroidism	<p>Subperiosteal resorption is pathognomic</p> <p>Subchondral resorption around acromioclavicular and sternoclavicular joints</p> <p>Diffuse lytic lesions of the cranium</p> <p>Thinning cortex</p>	<p>Classic: Benign parathyroid adenoma</p> <p>Less common: secondary to kidney disease</p>	<p>General cortical thinning</p> <p>Focal lucent lesions with well-defined sclerotic margins and short transitions to normal bone</p> <p>Widening of articular surfaces with possible reactive sclerosis</p> <p>“Salt and pepper” appearance of the cranium with blurring of the trabecular and cortical layers</p>	Appearance similar to woven bone, with fibrous deposition under cartilage	<p>In the United States:</p> <p>Generally higher among Black individuals.</p> <p>Overall: 233/100,000 for women 85/100,000 for men</p> <p>High incidence among Black women 70-79 at 1,409/100,000</p>

Table References: Barnsely et al. (2021); Bennett et al. (2020); Bikel et al. (1993); Brickley et al. (2020); Burr and Allen (2019); Crist and Sorg (2014); Degnan and Levi (2011); Ittyachen and Anand (2019); Mafee et al. (1985); Mann et al. (2017); Mann and Hunt (2013); Marcocci et al. (2012); Marcu et al. (2011); O’Donnell et al. (2019); O’Donnell et al. (2020); O’Donnell et al. (2023); Rivera and Mirazón Lahr (2017); Rosen (2020); Sorg et al. (2004); Waldron (2009)

Summary of Cranial Osteoporosis and Cranial Pathology

Very few articles exist regarding cranial osteoporosis in general, and even fewer exist that examine cranial osteoporosis via computed tomography. However, other pathologic conditions affecting the cranium, including their radiographic features, have been well-studied. It is prudent that forensic anthropologists have an appreciation of cranial pathology to best discern its underlying cause. Furthermore, as substance and alcohol use become ever more prevalent in the forensic setting, anthropologists need to have an appreciation for how these conditions manifest skeletally. Advanced imaging modalities such as postmortem computed tomography offer novel opportunities to research their skeletal impacts.

Overview of Cranial Thickness

In contrast to the dearth of articles examining cranial osteoporosis, the studies of cranial thickness constitute a large body of work. Researchers from a wide array of scientific disciplines, including anthropology, engineering, and medicine, are interested in the implications and applications of cranial thickness measures (for example, Bourah et al., 2015; De Boer et al., 2016; Hatch et al., 2018; Lynnerup, 2001). While historically, cranial thickness was measured on dry bone, modern imaging techniques, such as computed tomography, have greatly expanded the methodologies by which the cranium can be measured.

Utility of Measuring Cranial Thickness via Computed Tomography

Newman et al. (1998) discuss the fact that manual CT measurements of structures less than 2.5mm may be overestimated due to the reconstruction algorithms creating blurred boundaries of cortical bone. In an attempt to overcome this obstacle, Treece et al. (2010)

developed a sophisticated method using a Gaussian point spread function 2 to increase the accuracy of cortical thickness measurements. Lillie et al. (2015) validated this methodology, finding it to be more accurate than measurements on untransformed clinical CT scans; however, the mean difference between standard CT measurements and the Treece et al. method was 0.078mm, well within tolerances for traditional osteometric measurements (Christensen et al., 2018; Lillie et al., 2015). Carew et al. (2019a) (2019b) found that computed tomography is accurate for standard forensic osteometrics. Additionally, Prevrhal et al. (1999) demonstrated that manual, local thickness measurements are accurate when the structure being measured is thicker than the slice thickness of the CT scan. This means in cases where CT slice thickness is <1mm, measurements of <1mm may be valid and accurate. Furthermore, this may not apply to higher-resolution post-mortem CT scans, where the radiation dose can be greater and scan times longer than in living patients, because there is little concern for increased radiation exposure compromising patient safety.

Some researchers, such as Boruah et al. (2015), Bourah et al. (2017), and Voie et al. (2014), have capitalized on the utility of computed tomography scans for advanced methodological approaches. For example, Boruah et al. (2015; 2017) measured cranial vault thickness by transferring cranial landmarks onto a cartesian plane and using Monte Carlo simulations to generate regional thickness heat maps. Voie et al. (2014) used software to measure calvaria thickness at 2,000 points across 51 skulls, similarly generating thickness maps without reporting specific anatomic thickness.

Overall, while more accurate or comprehensive algorithms exist for measuring the cranium via standard computed tomography, the error levels of manual, local thickness measures

have been demonstrated to fall within tolerable limits (Christensen et al., 2018; Lillie et al., 2015).

Standard References for Cranial Thickness

Several authors have attempted to create reference standards for cranial thickness (Adanty et al., 2021; De Boer et al., 2016; Eisova et al., 2016; Lille et al., 2015; Lynnerup, 2001; Rowbotham et al., 2022; Torimitsu et al., 2014a). Table 4 displays thicknesses reported by these studies, as well as definitions of where the measurements were taken.

Table 4 Measurements of cranial thickness reported in recent literature

Study	Population	Element	Measurement Site	Thickness Measurement in Millimeters and Standard Deviation		
				Male	Female	Overall
Adanty et al., 2021	13 males, 12 females from anatomic gift program, Canada	Frontal	Mid-frontal	6.98 ± 1.54	7.58 ± 1.94	7.26 ± 1.78
		Parietal	Left euryon	6.00 ± 1.49	7.00 ± 1.24	6.49 ± 1.46
De Boer et al., 2016	655 males, 339 females from a Dutch forensic sample	Frontal	Lateral to the crista frontalis	6.15 ± 1.91	7.13 ± 2.30*	--
		Parietal	Left or right euryon	4.22 ± 1.15	4.41 ± 1.15	--
		Occipital	Opistocranium	7.33 ± 2.01	6.89 ± 2.00*	--
Eisova et al., 2016	15 males, 11 females	Parietal, along a line delineating the parietal boss	Anterior 1	--	--	6.56 ± 1.76
			Anterior 2	--	--	6.36 ± 1.50
			Center point	--	--	5.56 ± 1.21
			Posterior 1	--	--	4.97 ± 0.87
			Posterior 2	--	--	6.67 ± 1.51
Lillie et al., 2015	2 males	Frontal	Not reported	--	--	2.26 ± 0.41
		Parietal	Not reported	--	--	1.24 ± 0.39
		Temporal	Temporal squamous	--	--	2.83 ± 0.77
		Occipital	Superior to the occipital protuberance	--	--	1.31 ± 0.38
Lynnerup, 2001	43 males, 21 females from a Dutch forensic sample	Frontal	1 cm in front of bregma	7.044 ± 1.273	6.678 ± 1.123	--
		Occipital	1 cm behind lambda	7.825 ± 1.657	7.603 ± 2.013	--
		Parietal	Right euryon	5.040 ± 1.250	5.635 ± 1.138	--
			Left euryon	5.034 ± 1.328	5.452 ± 1.419	--
Rowbotham et al., 2022	307 males, 237 females from an Australian forensic sample	Frontal	Mid-frontal	6.47	7.10*	--
			Frontal (L)	7.97	9.28*	--
			Frontal (R)	7.78	9.19*	--
		Parietal	Anterior parietal (L)	6.18	6.43	--
			Anterior parietal (R)	6.23	6.65*	--
			Mid-parietal (L)	7.01	8.05*	--
			Mid-parietal (R)	6.92	7.92*	--
			Posterior parietal (L)	7.29	8.32*	--
			Posterior parietal (R)	6.98	7.91*	--
		Occipital	Occipital protuberance	16.42	13.99*	--
			Superior occipital	7.33	7.30	--
			Mid-occipital (L)	4.73	4.25*	--
			Mid-occipital (R)	4.65	2.15*	--

Table 4 continued

			Basiocciput	8.80	8.01*	--
		Temporal	Temporal squama (L)	1.92	2.31*	--
			Temporal squama (R)	2.00	2.29*	--
			Mastoid (L)	16.28	14.79*	--
			Mastoid (R)	16.27	14.95*	--
			Petrous (L)	19.55	18.82*	--
			Petrous (R)	19.20	18.37*	--
Torimitsu et al., 2014a	54 males, 40 females from a Japanese forensic sample	Parietal	Along the right sagittal suture	6.7 ± 1.9	6.2 ± 1.5	--
		Occipital	Occipital protuberance	8.0 ± 1.7	7.2 ± 1.5*	--
		Temporal	Superior (L)	5.7 ± 1.1	6.6 ± 1.6*	--
			Superior (R)	5.5 ± 1.5	6.1 ± 1.4*	--

*denotes significant difference

The data from Table 4 show a wide range of reported thicknesses and significant differences between sexes. Measurements across the frontal ranged from 2.41mm to 9.19mm. Measurements of the occiput ranged from 1.31mm to 16.42mm at its thickest when measured at opistocranium. While the measurements of the parietal ranged from 1.24mm to 8.32mm, the 1.24mm measurement appeared to be an outlier as most measurements were in the 5mm to 8 mm range. Measurements of the temporal ranged greatly from 1.92mm at the squamous to nearly 2cm at the petrous.

Unfortunately, these studies sampled cranial thickness at different sites or simply measured the entire calvarium using thickness mapping techniques (such as Boruah et al., 2015; Bourah et al., 2017 and Voie et al., 2014), so direct comparisons are difficult to make. Despite their different methodologies, all studies found that cranial thickness is extremely heterogeneous. In fact, Voie et al. (2014) found statistically significant variations of thickness across the calvarium of a single individual. Furthermore, these authors found that the range and distribution of cranial thickness form a unique pattern for each individual, so cross-individual comparisons are even more difficult to make (Voie et al., 2014).

Cranial Thickness and Substance and Alcohol Use

In the course of this literature review, only two articles were identified that measured cranial thickness differences between groups of substance and alcohol users and non-users (Lynnerup, 2001; Lynnerup et al., 2005). Lynnerup (2001) and Lynnerup et al. (2005), measured four cranial core samples taken from the frontal, left and right parietals, and the occiput to examine the total cranial thickness (2001) and cranial diplöe (2005) in relationship to overall body build, age, and sex. Both studies utilized the same samples taken from 64 individuals in a

Danish forensic sample. They measured the overall and diplöic thickness between 27 individuals who had a substance or alcohol use history and 37 individuals who did not. No significant differences were found between the groups in either measurement. Neither article reported the measurements of the two groups.

Summary of Cranial Thickness Research

Measurement of cranial thickness has a long history, is of wide-ranging interest, and can be analyzed using simple to extremely complex techniques. As computed tomography has become more commonplace, more studies have relied on it for measuring cranial thickness. Two studies utilizing the same sample cursorily examined the relationship between substance and alcohol use and thickness and found no significant differences. No research was identified that utilized computed tomography scans to evaluate cranial thickness in heavy alcohol users.

Overview of Alcohol and Bone

As demonstrated above, more research is needed on the evaluation by computed tomography of the effects that heavy alcohol use may have on the skeleton in general and the cranium in particular. While data focusing on this specific research area is limited to non-existent, the effects that alcohol may have on bone are well documented, if not entirely understood. The interaction between bone and alcohol has been extensively studied and presents a picture of a complex and dynamic relationship. Alcohol appears to have both positive and negative effects in a dose-dependent manner.

Several studies have demonstrated that light to moderate alcohol intake, i.e., 8g – 28g/day (or 0.6 to ~2 standard drinks) may increase bone density (Ilich et al., 2002; Pedrera-Zamorano et

al., 2009; Williams et al., 2005; Tucker et al., 2009; Venkat et al., 2009). However, additional studies have soundly demonstrated that consumption of alcohol in excess of 28g/day is associated with negative skeletal effects (Alvisa-Negrin et al., 2009; Bikle et al., 1993; Cheraghi et al., 2019; Gaddini et al. 2016; Maurel et al., 2012a; Maddalozzo et al., 2009; Peris et al., 1994; Tucker et al., 2009).

Alcohol's Protective Effect on Bone

The current dietary guidelines from the United States Department of Agriculture recommend that women and men drink <1 and <2 standard drinks per day, respectively (Dietary Guidelines for Americans, 2020). Most research on the protective effects of alcohol on bone has studied markers of skeletal health, such as bone mineral density and serum markers of bone turnover, in individuals consuming between 8g and 28g per day of alcohol per day.

The protective effects of moderate alcohol consumption occur across the lifespan and are independent of sex. Venkat et al. (2009) and Sripanyakorn (2009) both demonstrated that younger individuals (20- to 40-year-olds) drinking up to 28 grams of alcohol per day have increased bone mineral density and decreased markers of bone turnover compared to peers who abstain. (2009) found Holbrook and Barrett-Connor (1993), Williams et al. (2005), and Pedrera-Zanmorano et al. (2009) demonstrated that men and women aged 45-60 who moderately consumed alcohol have increased bone mineral density (BMD) compared to abstaining peers. In each of these studies, alcohol consumption has led to a significant reduction in parathyroid hormone. Finally, Mostofsky et al. (2016) showed that elderly men and women who consumed at least 29g to 57g of alcohol per week all had greater BMD than peers who abstained.

Marrone et al. (2012) showed that among postmenopausal women who abstained from drinking for two weeks, there was an increase in serum markers of bone turnover. Upon resuming drinking alcohol, serum markers of bone turnover decreased overnight. Likewise, a study of younger men and women showed that moderate use of alcohol can cause a decrease in markers of resorption within mere hours after consumption (Sripanyakorn et al., 2009). Both studies showed an increase in calcitonin and the activation of estrogen receptors (Marrone et al., 2012; Sripanyakorn et al., 2009). The effects of calcitonin and estrogen are presented in Table 5. The relatively short period in which markers of bone turnover were affected by alcohol suggests that alcohol can have an immediate effect on osteoblasts and osteoclasts.

Furthermore, some studies have shown that bone turnover is globally suppressed in alcohol users. For example, it has been shown that serum markers of sclerostin and osteoprotegerin were increased, translating to low OB and OCL formation (Gaddini et al., 2016).

Alcohol's Negative Effects on Bone

Despite the possible benefits that moderate alcohol consumption may have on bone mineral density via a reduction of bone turnover, an enormous body of literature exists on the deleterious impact of heavy, chronic alcohol use (Alvisa-Negrin et al., 2009; Bikle et al., 1993; Cheraghi et al., Gaddini et al. 2016; Maurel et al., 2012a and 2012b; Maddalozzo et al., 2009; Peris et al., 1994; Tucker et al., 2009). For example, heavy alcohol consumption has been associated with a decrease in bone mineral density and an increased risk of fracture. A study of middle-aged male and female alcoholics showed that bone density T-scores of the total hip and spine were significantly lower than non-alcoholic controls. However, most were within normal limits (González-Reimers et al., 2015). In addition to the direct effects that alcohol has on bone,

lifestyle factors, such as tobacco use and degree of sedentism, of individuals with alcohol use disorder can also directly impact and potentiate the negative effects on bone. Gruchow et al. (1985) demonstrated that individuals with alcohol use disorder will forgo nutritionally substantive food and replace those calories with alcohol, leading to macro- and micro-nutrient deficiencies, lower body weight, and body fat. This preferential decision-making can cause reduced availability of substrates to form new bone, such as calcium and phosphate, leading to a net loss of bone density. Additionally, Turner and Iwaniec (2010) found there to be a dose-dependent relationship between caloric intake and alcohol. Rats fed 0.5% and 3% of their energy in alcohol ate more and gained more weight than controls, while rats given >12% of their energy requirements in alcohol ate less and gained less weight.

Tables 5 through 9 list common electrolytes, hormones, nutrients, metals, and cytokines that are involved in skeletal homeostasis or otherwise impact bone metabolism, as well as their relationships to alcohol and bone.

Table 5 Electrolytes and their role in human health, skeletal biology, and disruptions due to alcohol

Electrolyte	Use in Body	Impact on Bone	Alcohol	Summary
Calcium	Has roles in muscle contraction, enzyme reactions, coagulation, and skeletal architecture. ^a	Comprises significant portion of the osteoid matrix. ^b	Alcohol induces hypocalcemia. ^{c,d}	Results in increasing parathyroid secretion and OCL activity
Magnesium	Helps to regulate DNA synthesis, RNA translation, protein synthesis, ATP production, and the regulation of calcitonin. Required for parathyroid hormone and helps vitamin D absorb Ca in the gut. ^a	Required for proper mineralization of the matrix; helps promote OBs, suppresses OCLs. ^e	Lower serum levels in heavy alcohol users. ^f	Reduces OBs, increases OCLs.
Phosphate	Numerous metabolic functions and important for production of DNA, RNA, ATP, and ALP. ^a	Major component of alkaline phosphatase which is required for proper matrix mineralization. ^e	Low levels in heavy alcohol users. ^d	Disrupts normal mineralization
Potassium	Modulates cell membrane potential. ^a	Indirectly modulates bone resorption via controlling aldosterone, which in turn modulates PTH. ^{a,b}	Low levels in heavy alcohol users ^{c,d}	Low K increases aldosterone release, increasing levels of PTH and increases OCL activity
Sodium	Important for membrane potential and neural conductivity. ^a	Indirectly modulates RANKL and PTH via the renin-angiotensin-aldosterone system	Low levels in heavy alcohol users. ^{c,d}	Increases expression of RANKL and PTH, thereby increasing OCL activity

ALP= alkaline phosphatase; ATP= adenosine triphosphate; DNA= deoxyribonucleic acid; OB= osteoblast; OCL= osteoclast; PTH= parathyroid hormone; RANKL= receptor activator of nuclear factor kappa beta ligand; RNA= ribonucleic acid.

Table sources: Lazenby (2011)^a, Burr and Allen (2019)^b, Lieber (2000)^c, Palmer and Clegg (2017)^d, Gaddini et al. (2016)^e, Rink (1986)^f.

Table 5 displays common electrolytes, their role in normal physiology, how they interact with bone, how they are affected by alcohol and the resulting impact on bone. Long-standing evidence has shown that chronic alcohol abuse is associated with perturbed electrolyte balance, including low levels of calcium, magnesium, phosphate, potassium, and sodium (Gaddini et al., 2016; Lieber, 2000; Palmer and Clegg, 2017).

Ninety-nine percent of the body's calcium is stored in bone, with only 1% present in other cells. As such, when the body enters a state of hypocalcemia, parathyroid hormone is

released, inducing osteoclastogenesis and resorption to release calcium stored in the bony matrix to maintain the body's calcium homeostasis (Burr and Allen, 2019).

Magnesium is heavily involved in many functions of cells and tissues, not the least of which is the production of ATP (Lazenby, 2011). Regarding the skeleton, it is critical for proper mineralization and helps promote osteoblast differentiation and even decreases osteoclast differentiation, likely through the reduction of low-level inflammation and the reduction of pro-osteoclastogenic cytokines such as Interleukin-6 (Gaddini et al., 2016). Therefore, when magnesium is low, osteoblastogenesis is reduced, and osteoclastogenesis is increased. Additionally, it helps to regulate the body's levels of calcitonin (Gaddini et al., 2016; Rink, 1986).

Phosphate is required for the proper mineralization of bone, and the low levels of serum phosphate seen in chronic, heavy alcohol users can lead to poor mineralization of the bony matrix during remodeling (Gaddini et al., 2016). Additionally, approximately 85% of the body's phosphate is stored in the skeleton, so when low serum phosphate occurs, phosphate is liberated from the skeleton by the activation of parathyroid hormone (Burr and Allen, 2019).

Potassium indirectly influences bone. Potassium is regulated in the body by aldosterone, and when low serum levels are present, aldosterone is released to increase the renal retention of potassium (Lazenby, 2011). As previously mentioned, aldosterone increases bone resorption through the release of parathyroid hormone (Burr and Allen, 2019).

Sodium impacts the skeleton indirectly through the involvement of the renin-angiotensin-aldosterone system³ (Lazenby, 2011). Low serum sodium levels will release renin, which in turn

³ Renin is an enzyme produced by the kidneys and is responsible for catabolizing the precursor protein on angiotensin, which helps to maintain blood pressure (Lazenby, 2011). When blood pressure is high, renin is reduced; when blood pressure is low, renin is increased.

will release aldosterone and angiotensin, causing increased RANKL and parathyroid hormone release (Mo et al., 2020). RANKL and parathyroid hormone are both potent stimulants of osteoclastogenesis and activation (Burr and Allen, 2019; Lazenby, 2011; Mo et al., 2020).

Aldosterone is responsible for kidney retention of sodium, also helping to regulate blood pressure by increasing plasma volume (Lazenby, 2011).

Table 6 Selected hormones and their role in human health, skeletal biology, and effects due to alcohol

Hormones	Use in Body	Impact on Bone	Alcohol	Summary
Calcitonin	Ca metabolism ^a	Suppresses activity and differentiation of OCLs ^b Suppresses OC apoptosis ^b	Increases serum Calcitonin ^c	Decreases OCLs
Estrogen	Female sex hormone. Functions include development of female reproduction system, maintenance of reproductive cycle, and maintenance of bone density in men and women. ^a	Promotes OB proliferation, differentiation, and survival ^d Inhibits OCLs by limiting bone's response to PTH and increasing OB expression of OPG ^e	Ethanol may increase activation of estrogen receptors ^{c, f}	May provide moderate protective effect on bone in moderate drinkers.
Insulin-like Growth Factor-1	Glucose regulation, growth of bones and tissues during puberty, cell growth, survival, and differentiation ^{a, g}	Promotes OB proliferation, differentiation, and survival ^g	Markedly decreased in heavy alcohol use ^h	Decreases OBs
Leptin	Regulates appetite, neuroendocrine functions, energy and skeletal homeostasis ⁱ	Promotes OB, decreases OCL ^{b, i}	Decreased serum levels in alcohol use ^j Reduced production of adipocytes.	Reduces OB and increases OCL
Parathyroid Hormone	Ca metabolism ^a	Increases OCL activity to release Ca from bone, particularly intracortical remodeling. ^{b, k}	Increases serum PTH ^{c, j}	Increases OCLs
Testosterone	Male sex hormone, maintenance of male reproductive system, helps to regulate muscle mass and bone health in men and women ^a	Stimulates OBs, promotes mineralization ^b	Moderate consumption increase serum levels, while chronic, heavy consumption lowers serum levels ^{h, l}	Moderate consumption may have short-term benefits to bone health, while heavy use will reduce OB formation and mineralization and increase OC activity

Abbreviations: OB= osteoblast; OC= osteocyte; OCL= osteoclast; OPG= osteoprotegerin; PTH= parathyroid hormone

Table references: Lazenby (2011)^a, Burr and Allen (2019)^b, Sripanyakorn et al. (2009)^c, Rosen (2020)^d, Neve et al. (2011)^e, Marrone et al. (2012)^f, Wang et al. (2013)^g, Gaddini et al. (2016)^h, Holloway et al. (2002)ⁱ, Maurel et al. (2012a)^j, Rhee et al. (2011)^k, Smith et al. (2023)^l

Table 6 displays selected hormones, their role in normal physiology, how they interact with bone, how they are affected by alcohol, and the resulting impact on bone.

Produced by the thyroid, calcitonin helps, as its name suggests, to regulate calcium homeostasis by modulating parathyroid hormone, thereby reducing the osteoclastic release of calcium into the bloodstream (Burr and Allen, 2019; Lazenby, 2011). Serum levels of calcitonin increase during moderate drinking, suppressing osteoclastic activity and reducing bone turnover (Sripanyakorn et al., 2009). This increase in serum levels is thought to be one mechanism by which moderate drinking may protect bone.

Estrogen is a key protective hormone related to skeletal health. It is well established that the loss of estrogen in postmenopausal women increases osteoporosis and fracture risk and that estrogen supplementation increases bone mineral density (Rosen, 2020). This is due to the fact that estrogen has a positive effect on the survival of osteoblasts, helps bolster their differentiation, and inhibits osteoclast formation through the reduction of inflammatory cytokines, PTH, and T-cells (Neve et al., 2011). Moderate consumption may increase the activation of estrogen receptors, providing protective effects to bone (Marrone et al., 2012; Sripanyakorn et al., 2009).

Insulin-like Growth Factor-1 broadly affects normal growth, development, and energy metabolism (Lazenby, 2011; Wang et al., 2013). Skeletally, IGF-1 helps to increase osteoblast proliferation, differentiation, and survival, subsequently modulating osteoclastic activity (Wang et al., 2013). Levels of IGF-1 are significantly decreased in the setting of heavy alcohol use, thereby reducing osteoblasts and increasing bone turnover (Gaddini et al., 2016).

A critical hormone for skeletal homeostasis is leptin, which helps encourage MSCs to differentiate into osteoblasts by increasing osteoprotegerin, as well as inhibiting

osteoclastogenesis (Holloway et al., 2002). Maurel et al. (2012a) have shown that heavy alcohol users have lower serum levels of leptin, reducing osteoblast recruitment and subsequently increasing osteoclasts.

Parathyroid hormone is the antagonist of calcitonin, helping to stimulate osteoclastic activity in the setting of hypocalcemia (Burr and Allen, 2019; Lanzenby, 2011). Consumption of alcohol acutely increases levels of parathyroid hormone, immediately increasing osteoclasts beyond what is normally needed for skeletal homeostasis and causing a net loss in bone, particularly cortical (Maurel et al., 2012b; Rhee et al., 2011; Sripanyakorn et al., 2009).

Testosterone is the primary male sex hormone, but it also acts as a protective agent for bone in both men and women (Lazenby, 2011). It protects bone density by stimulating osteoblast formation, promoting mineralization, inhibiting osteoblast apoptosis, and increasing osteoclast apoptosis (Burr and Allen, 2019; Gaddini et al., 2016). Moderate consumption of alcohol has been shown to increase testosterone levels, possibly leading to an anabolic effect on bone (Gaddini et al., 2016; Smith, 2023). Conversely, chronic, heavy alcohol consumption leads to reduced levels of testosterone, leading to reduced osteoblast activity and increased osteoclastic activity (Smith, 2023).

Table 7 Selected vitamins and nutrients and their role in human health, skeletal biology, and disruptions due to alcohol

Vitamins and Nutrients	Use in Body	Impact on Bone	Alcohol	Summary
β-carotene	Potent anti-oxidant ^a	Actively scavenges free radicals and ROS ^a	Low levels in heavy alcohol users ^b	Deficiency would increase inflammation and increase OCL activity
Folate	Red blood cell function, cellular maturation, and metabolism of amino acids necessary for cell division ^c	Indirectly impacts bone by reducing circulating levels of homocysteine. Increased levels of homocysteine cause poor collagen cross-linkages necessary for bone strength ^{d,e}	Reduced in heavy alcohol users ^b	Increased levels of homocysteine would lead to a reduction in bone strength.
Riboflavin	Potent anti-inflammatory ^f	Potentiates the effect of Vitamin C on collagen production; promotes OB differentiation; reduces ROS ^g	Low levels in heavy alcohol users ^h	Deficiency would impair collagen production, reduce OBs, and reduce mitigation of ROS, causing an increase in OCL activity
Thiamine	Catabolizing sugars and amino acids ⁱ	Inhibits OCLs ^j	Low levels in heavy alcohol users ^b	Deficiency would cause a loss of the mitigating effect of thiamine on OCL activity in the setting of other inflammatory promoters of OCLs.
Vitamin A	Important of vision health and cell growth and development ^c	At normal levels promotes OB activity and inhibits OCL activity. ^k	Low levels in heavy alcohol users ^l	Heavy alcohol use reduces serum levels and may reduce promotion of OB activity and increase OCL activity
Vitamin C	Primary role in collagen synthesis, and anti-oxidant ^{m,n}	Produces collagen matrix ^m	Low levels in heavy alcohol users ^b	Low levels result in poor collagen synthesis, affecting bone strength, and may increase activity of OCLs
Vitamin D	As 1,25-dihydroxvitamin D, is responsible for proper absorption of Ca in the gut. ^o	Allows for proper uptake of dietary Ca ^o	Low levels in heavy alcohol users ^b	Low serum levels may lead to the development or exacerbation of hypocalcemia, triggering PTH release and increasing OCL activity
Vitamin K	Important for coagulation cascade and calcification processes, both normal and pathologic. ^p	Necessary for the production of Osteocalcin, an OB-specific protein that binds with hydroxyapatite to assist with proper mineralization. ^q	Reduced in heavy alcohol users ^b	Reduced Vitamin K levels would limit the production of Osteocalcin, impairing the proper mineralization of the osteoid matrix

Abbreviations: OB= osteoblast; OCL= osteoclast; PTH= parathyroid hormone; ROS= Reactive Oxygen Species
 Table sources: Gao and Zhao (2023)^a, Lieber (2000)^b, Lazenby (2011)^c, Kalimeri et al. (2020)^d, Van Meurs et al. (2004)^e, Suwannasom et al. (2020)^f, Chaves Neto et al. (2015)^g, Rosenthal et al. (1973)^h, Mkrtychyan et al. (2015)^l, Ma et al. (2020)^j, Yee et al. (2021)^k, Hoyumpa (1986)^l, Padayatty and Levine (2016)^m, Chin and Ima-Nirwana (2018)ⁿ, Gaddini et al. (2016)^o, Mladènka et al. (2021)^p, Neve et al. (2011)

Table 7 displays selected nutrients, their role in normal physiology, how they interact with bone, how they are affected by alcohol and the resulting impact on bone. In each case, alcohol use, particularly excessive or chronic alcohol use, disrupts these compounds by reducing them in the body, both through increased secretion and through lack of dietary intake. The nutrients and vitamins listed in Table 6 have broad implications for skeletal health, affecting every stage of skeletal homeostasis from osteoblastogenesis, matrix mineralization, and osteoclastic activity.

As a potent anti-oxidant, β -carotene actively scavenges free radicals and reactive oxygen species from the bloodstream (Gao and Zhao, 2023). The low-levels observed in heavy alcohol users would result in greater systemic inflammation, increasing osteoclastic activity (Lieber, 2000).

Folate indirectly impacts bone by modulating circulating levels of homocysteine (Kalimeri et al., 2020). Too much homocysteine results in poor collagen cross-linkages, causing decreased bone strength (Van Meurs et al., 2004). Folate levels are often noted to be low in heavy alcohol users, indirectly impacting proper collagen formation and bone strength.

Riboflavin is a powerful anti-inflammatory, which not only potentiates the effects of vitamin C but also promotes the differentiation of osteoblasts and reduces reactive oxygen species (Neto et al., 2015; Suwannasom et al., 2020). The reduced levels of riboflavin seen in heavy alcohol users can impair collagen synthesis, reduce osteoblastogenesis, and increase the ROS-mediated recruitment of osteoclasts (Rosenthal et al., 1973).

While primarily responsible for catabolizing sugars and amino acids, thiamine also inhibits the formation of osteoclasts (Ma et al., 2020; Mkrtychyan et al., 2015). The low levels of

thiamine found in heavy alcohol users would contribute to the pattern of increased bone turnover seen in this population (Lieber, 2000).

Vitamin A is critical to the normal growth and development of the cells, promotes osteoblast activity, and subsequently inhibits osteoclast activity (Lazenby, 2011; Yee et al., 2021). Serum levels of vitamin A are reduced in heavy alcohol users, leading to higher rates of bone turnover (Hoyumpa, 1986).

Vitamin C is a potent antioxidant, but most importantly, it is critical for the synthesis of collagen in the human body (Chin and Ima-Nirwana, 2018; Padayatty and Levine, 2016). When present in low levels, such as seen among heavy alcohol users, the bone becomes less dense more fragile due to the reduction in the collagen matrix (Garnero, 2012; Lieber, 2000). Additionally, the reduced anti-oxidant benefits may also increase the activity of inflammatory cytokines and reactive oxygen species. While the low levels seen in heavy alcohol users may diminish bone strength and increase fracture risk, these levels are still well above the threshold in which classic scorbutic lesions occur (Lieber, 2000). Scorbutic lesions are discussed in greater detail in Table 9.

Vitamin D, in its 1,25-dihydrox form, is responsible for the proper absorption of calcium in the gut. As with all vitamins, heavy alcohol users have lower levels of vitamin D, which may impair Ca absorption (Gaddini et al., 2016; Lieber, 2000). The role of vitamin D levels and their importance in skeletal health has recently been re-evaluated, showing that vitamin D supplementation may not be impactful for osteoporotic patients at high risk for fracture (Cummings and Rosen, 2022; Gallagher and Rosen, 2023). However, low levels may still exacerbate hypocalcemia in heavy alcohol users, causing an increasing parathyroid hormone and increased osteoclastic activity (Gaddini et al., 2016).

Vitamin K is primarily known as a critical component of the coagulation cascade; however, it also plays an important role in calcification (Mladènka et al., 2021). Vitamin K is necessary for the production of osteocalcin, an osteoblast-specific protein that binds with hydroxyapatite to ensure proper mineralization of the osteoid matrix (Neve et al., 2011). Low levels seen in heavy alcohol users limits the production of osteocalcin, impairing the integrity of the bony matrix (Liber, 2000).

Table 8 Selected metals and their role in human health, skeletal biology, and disruptions due to alcohol

Metals	Use in Body	Impact on Bone	Alcohol	Summary
Aluminum	None- generally considered a toxin ^a	Decreases Ca, Mg, and P ^b Inhibits OB differentiation ^c Inhibits mineralization ^c	Increased in heavy alcohol users ^d	Suppresses the number of OBs needed for normal skeletal homeostasis, and impairs the function of existing OBs leading to uncoupling and reduced bone strength.
Cadmium	None- generally considered a toxin ^a	Increase RANKL expression; preferentially directs MCS towards adipocyte lineage rather than OB lineage ^e	Increased levels in heavy alcohol users and potentiates the effect of alcohol on hepatocytes, increasing the risk of liver disease ^{d, f}	Increased levels would cause an increase in OCLs, while simultaneously decreasing OB production
Chromium	None- generally considered a toxin ^a	Taken up by OBs causing injury and the production of ROS while decreasing ALP secretion and increasing cytokines such as TNF- α and IL-6 ^{g, h}	Increased in heavy alcohol users ^d	Increased levels would increase the levels of ROS and inflammatory cytokines causing an increase in OCLs, while simultaneously causing poor mineralization and early OB apoptosis
Iron	Production of hemoglobin ^a Promotes release of TNF- α and IL-6 ⁱ	Increases OCL differentiation and activity ⁱ Decreases osteoblastogenesis ⁱ	Greater than 2 standard drinks per day can increase iron load ^d	Iron overload would cause increased OCL activity above that necessary for skeletal homeostasis, while simultaneously suppressing OBs.
Lead	None- generally considered a toxin ^a	Inhibits OPG, limiting OB regulation of OCLs ^b Effects are potentiated when co-administered with alcohol in mice ⁱ	Increased in heavy alcohol users ^d	Increased OCL activity via the disruption of OPG has been shown to decrease cortical width, bone mineral density, and increase fracture risk in mice. ⁱ
Nickel	Increases hormonal activity; plays a role in lipid metabolism ^a	Inhibits alkaline phosphatase, inhibiting bone mineralization; induces OC apoptosis ^{j, k}	Increased in heavy alcohol users ^d	Increased Nickel levels would cause poor bone mineralization and pre-mature death of OCs

Abbreviations: ALP= alkaline phosphatase, IL-6= Interleukin-6, MCS= mesenchymal stem cells, OB= osteoblast, OC= osteocyte, OCL= osteoclast, OPG= osteoprotegerin, RANK= Receptor Activator of Nuclear Factor kappa-B, ROS= reactive oxygen species, TNF- α = tumor necrosis factor alpha.

Table References: Lazenby (2011)^a, Rodríguez and Mandalunis (2018)^b, Song et al. (2017)^c, Lieber (2000)^d, Åkesson et al. (2006)^e, Kim et al. (2023)^f, Shah et al. (2015)^g, Genchi et al. (2020)^h, Kuprazewicz and Brzóška (2013)ⁱ, Wong et al. (2015)^j, Zdrojewicz et al. (2016)^k

Table 8 shows beneficial and toxic metals and how they interact with human biology, how they respond to alcohol, and how that response impacts bone. In all cases, heavy alcohol use increases the metal load in the body, typically increasing the activity of osteoclasts while inhibiting osteoblast formation and proper function, e.g., mineralization.

Aluminum does not have a known benefit for normal human physiology and is known to be toxic to human health (Lazenby, 2011). In higher amounts, aluminum reduces levels of calcium, magnesium, and phosphate and has also been shown to directly inhibit osteoblast formation and prevent proper mineralization of the osteoid matrix as a result of hypophosphatemia (Rodriguez and Mandalunis, 2018; Song et al., 2017). Serum levels of aluminum are frequently elevated in heavy alcohol users, leading to a reduction in new bone formation and poor matrix mineralization (Lieber, 2000).

Cadmium also does not have a known benefit for normal human physiology and is known to be toxic to human health (Lazenby, 2011). It has been demonstrated to increase RANKL expression and direct mesenchymal stem cells towards the adipocyte lineage (Åkesson et al., 2006). It also has potentiating effects when combined with ethanol, increasing hepatic cellular damage and increasing the risk for liver alcohol-related liver disease (Kim et al., 2023). Levels of cadmium are frequently elevated in heavy alcohol users, suggesting heavy alcohol users are yet again experiencing an increase in osteoclastic activity and a concomitant decrease in osteoblastic activity (Lieber, 2000).

Chromium similarly does not have a known benefit for normal human physiology and is known to be toxic to human health (Lazenby, 2011). Chromium is preferentially taken up by osteoblasts, causing severe cellular injury which not only causes poor production of ALP and reduced mineralization but also creates reactive oxygen species, triggering the release of

inflammatory cytokines such as IL-6 and TNF- α (Shah et al., 2015; Genchie et al., 2020).

Chromium levels are elevated in heavy alcohol users, suggesting that their osteoblasts are impaired, and osteoclastic activity is further increased (Lieber, 2000).

Even though it is a vital metal for human physiology, iron impacts the skeleton negatively when present in excessive amounts by promoting the release of TNF- α and IL-6 (Kuprazwicz and Brzóška, 2013; Lazenby, 2011). Iron increases monocyte differentiation to the osteoclastic lineage and decreases osteoblastogenesis (Kuprazwicz and Brzóška, 2013). Iron levels are frequently elevated in heavy alcohol users, with the risk of iron overload increasing significantly in individuals who consume more than two drinks per day (Lieber, 2000).

Widely known as a harmful substance, lead is often elevated in heavy alcohol users and inhibits osteoprotegerin, disrupting the OPG/RANKL/RANK cycle and limiting the regulatory effect osteoblasts have on osteoclasts (Lazenby, 2011; Lieber, 2000; Rodriguez and Mandalunis, 2018). In mice, iron overload potentiates the skeletal effects of alcohol and leads to decreased cortical width, lower bone mineral density, and increased fracture risk (Kuprazwicz and Brzóška, 2013).

Finally, nickel, which plays a vital role in hormone activity and lipid metabolism, also plays a role in skeletal homeostasis by inhibiting osteoblast activity and inducing apoptosis in osteocytes (Lazenby, 2011; Wong et al., 2015; Zdrojewicz et al., 2016). This effect is dose-dependent, and when nickel levels are increased beyond what is normally needed, as commonly seen in heavy alcohol users due to the presence of nickel in several types of alcoholic beverages, it inhibits osteoblast's production of ALP and causes early apoptosis of osteocytes (Lieber, 2000; Wong et al., 2015).

Table 9 Selected cytokines and their role in human health, skeletal biology, and disruptions due to alcohol

Selected Cytokines	Use in Body	Impact on Bone	Alcohol	Summary
Interleukin-6	Inflammatory cytokine ^a	Promotes recruitment and proliferation of OCLs ^b	Increases significantly during alcohol consumption ^c	Increases OCLs beyond what is needed for normal skeletal remodeling
Tumor Necrosis Factor-α	Part of macrophages and monocytes that triggers necrosis and apoptosis of cells as part of the acute inflammatory response ^{a, b}	Increases monocyte differentiation into OCLs ^b	Increased during alcohol consumption ^c	Increases OCLs beyond what is needed for normal skeletal remodeling

Abbreviations: OCL= osteoclast

Table references: Lazenby (2011)^a, Burr and Allen (2019)^b, Marrone et al. (2012)^c.

Table 9 displays selected cytokines significant to skeletal health, their role in normal physiology, their impact on bone, how they are affected by alcohol, and alcohol’s subsequent impact on bone. Cytokines are released as the result of a mild or acute inflammatory response, and serum levels of cytokines all significantly increase during any amount of alcohol consumption (Lazenby, 2011; Marrone et al., 2012). This, in turn, promotes osteoclastogenesis, leading to increased bone resorption (Burr and Allen, 2019).

When Tables 5 through 9 are viewed together, an appreciation of the complex and dynamic role alcohol can have on the human skeleton can be seen. Beyond the effects that alcohol use has on electrolytes, hormones, vitamins and nutrients, metals, and cytokines, alcohol has systemic negative effects on tissues and organs due to the production of acetaldehyde, reactive oxygen species, and increased permeability of the gut, which allows intestinal endotoxins to circulate in the bloodstream (Haber and Kortt, 2021; Lazenby, 2011).

The breakdown of alcohol in more harmful substances begins in the liver. Alcohol is metabolized in the liver via two specific metabolic pathways. The first pathway is mediated enzymatically by alcohol dehydrogenase and results in the production of acetaldehyde, acetate, and hydrogen ions (Lazenby, 2011). Acetate has been shown to increase bone remodeling, and

hydrogen ions can affect the acidity of blood and affect bone resorption (Lazenby, 2011; Mo et al., 2020; Saitta et al., 1989). A second pathway, almost exclusively used by individuals with a long history of alcohol use, is the microsomal ethanol oxidizing pathway, which produces acetaldehyde and free radicals (Lazenby, 2011). Acetaldehyde produced by either pathway is incredibly toxic to liver and other cells, and also directly inhibits osteoblastogenesis (Gaddini et al., 2016). Free radicals, as discussed, have been shown to directly affect osteoblasts, inducing early apoptosis. Free radicals and reactive oxygen species also increase osteoclastogenesis through the stimulation of Interleukin-6 and by increasing the responsiveness of osteoclastic precursor cells to RANKL (Burr and Allen, 2019; Gaddini et al., 2016). Additionally, the microsomal ethanol oxidizing pathway uses the enzyme cytochrome P450, which is necessary to break down other drugs and toxins in the liver (Lazenby, 2011). However, it is preferentially used by the liver to break down alcohol, inhibiting the liver's ability to handle other toxins and furthering the damage done to liver tissue (Lazenby, 2011).

The toxic effects of alcohol on the liver impair its normal function, including its ability to properly synthesize 25-hydroxylase. 25-hydroxylase is critical for the conversion of vitamin D into 1,25-dihydroxvitamin D, which is necessary for the proper absorption of calcium in the intestines (Burr and Allen, 2019). Taken together with an already potentially low dietary calcium intake, this could lead to severe hypocalcemia, triggering the release of parathyroid hormone and stimulating osteoclastic activity to maintain mineral homeostasis.

Additionally, alcohol has been shown to be globally harmful to other body systems as well. Discussing findings of the recent Global Burden of Disease study, Bryazka et al. (2022) report that alcohol use, at any level, even below one standard drink per day, has far-ranging

detrimental effects. Results found statistically significant increases in the risk of cardiovascular disease, breast cancer, tuberculosis, and accidental injury (Bryazka et al., 2022).

Reversal of Alcohol's Effects

Despite the wide-ranging negative effects alcohol consumption has on the skeleton, there is some evidence that reversal of these effects can be achieved with cessation of alcohol. Abstinence from alcohol has different effects depending on the population. For example, in a sample of postmenopausal women from the United States who drink moderately, two weeks of abstinence resulted in increased serum markers of bone turnover, likely due to the withdrawal of the positive effects that alcohol has on estrogen receptors and the subsequent inhibition of osteoclastogenesis (Marrone et al., 2012; Rosen, 2020). Conversely, short-term abstinence among alcohol abusers saw an increase in bone formation, which is likely due to the direct removal of the toxic effects alcohol has on osteoblasts as well as other effects, such as finally getting proper nutrition and regaining electrolyte balance (Marrone et al., 2012).

The positive skeletal effects of abstinence have been shown to only improve with time. Alvisa-Negrin et al. (2009) showed that after six months, bone mineral density and bone turnover were increased, and Peris et al. (1994) demonstrated that femoral neck and lumbar density increased over a two-year period despite initially being significantly lower than controls. Peris et al. (1994) also found that bone formation markers increased during prolonged abstinence. Despite abstaining, it is still unclear whether bone mineral density ever fully returns to normal limits. A return to normal bone density would entirely depend on factors such as the age at which they started and stopped drinking, the presence of alcoholic liver disease, and other lifestyle factors.

Summary Alcohol Use and Bone

Viewed as a whole, the studies referenced above point to alcohol being a substance that is widely detrimental to human health, even if there are small benefits to bone with moderate consumption. While Michael and Bengtson (2016) provided some discussion on the impact that heavy alcohol use can have on the skeleton, there is still a lack of information and understanding of alcohol's effects on the cranium. This knowledge gap may limit the understanding and appreciation that forensic anthropologists have when confronted with diffuse cranial thinning.

Radiography in Forensic Anthropology

Forensic anthropology is the application of biological anthropology methods to questions of medicolegal significance. Forensic anthropologists use knowledge of skeletal anatomy and biology to help assess characteristics of skeletal remains such as age, sex, population affinity, stature and pathological conditions. Additionally, forensic anthropologists help understand and explain the cause and timing of traumatic injuries and taphonomic changes to remains.

While examining skeletal remains is the ideal, it is not always feasible. As forensic anthropology adopts more advanced technology, the use of novel radiographic techniques is becoming more commonplace and can serve as an adjunctive method for case examinations and research.

Radiography⁴ in Forensic Anthropology

Forensic anthropology is the application of biological anthropology methods to questions of medicolegal significance. Forensic anthropologists use knowledge of skeletal anatomy and biology to help assess characteristics of skeletal remains such as age, sex, population affinity, stature and pathological conditions. Additionally, forensic anthropologists help understand and explain the cause and timing of traumatic injuries and taphonomic changes to remains.

While examining skeletal remains is the ideal, it is not always feasible. As forensic anthropology adopts more advanced technology, the use of novel radiographic techniques is becoming more commonplace and can serve as an adjunctive method for case examinations and research.

Forensic science has long been an early adopter, or at least an early attempter, of new technology. In 1839, Louis Daguerre introduced the first commercially available, practical photographic process (Hirsch, 2000). Just a few short years later, in 1843, Belgium began to use photography to document prisoners, opening the door to the application of the new technology to the legal system (Hirsch, 2000). Likewise, less than a year after the discovery of X-rays, König first utilized the novel technique to examine Egyptian mummies, and shortly thereafter, x-ray was used for the first time in the medicolegal setting to prove attempted murder (Buikstra, 2019; Lagalla, 2020). Since then, photography and X-rays have been commonly used in anthropology and medicolegal cases (Lagalla, 2020). More recently, however, anthropology and forensic science have slowly adopted newer, more advanced imaging modalities like computed tomography and magnetic resonance imaging (Garvin and Stock, 2016).

⁴ It is important to note here the difference between “radiography” and “radiology”. Radiography simply refers to a methodological approach, while radiology is branch of medicine concerned with using radiographic methods to treat and diagnose medical conditions.

As demonstrated by the relatively quick adoption of radiography in paleopathology, there are wide-ranging benefits to the use of radiography in anthropology. A skeletal survey done by either x-ray or computed tomography (CT) scan, upon initially receiving a set of remains, creates a permanent record of the remains, demonstrates their initial pre-processing condition (which is useful in cases of trauma), and the images may be re-examined or shared digitally with other experts for a second opinion (Garvin and Stock, 2016; Carew and Errickson, 2019).

Radiographic images may be used in court as part of testimony and, in some cases, may be 3-dimensionally rotated or sliced for the benefit of the jury (Franklin and Marks, 2022).

Furthermore, virtual/digital reconstructions have been shown to be accurate and less emotionally damaging to those in the courtroom (Franklin and Marks, 2022; Christensen et al., 2018). Lastly, radiography, particularly CT, can serve as a good proxy for examining dry bone when maceration of the remains is not feasible (Garvin and Stock, 2016).

Currently, various advanced imaging and radiographic techniques are employed in anthropology and are applied to both living and deceased individuals. X-rays, LODOX scanners, computed tomography (CT), and magnetic resonance imaging (MRI) are all in use. However, MRI is very uncommon in the post-mortem setting due to its long scan times and high costs (Mamabolo et al., 2020). These modalities can be employed to assist with the development of the biological profile, establish identification, diagnose skeletal pathology, evaluate trauma, and more recently, have demonstrated some utility in taphonomy beyond a gross inventory and condition of the remains (Garvin and Stock, 2016; Guareschi et al., 2023; Scheirs et al., 2020; Spies et al., 2020; Spies et al., 2021; Sorg et al., 2004).

Plain film x-ray, the classic radiographic technique, was first used in the forensic setting in 1895, and has been in constant use since (Lagalla, 2020). Today, it is the second most

common imaging technique, only after digital photography (Garvin and Stock, 2016). X-ray is fast, inexpensive, can be learned by technicians quickly, and applicable to a wide array of anthropological problems such as developing the biological profile, diagnosing pathology, and analyzing trauma (Garvin and Stock, 2016). Its major limitation is that due to the 2-dimensional nature of the image it produces, anatomic structures are superimposed upon one another and can be hard to distinguish. Additionally, basic X-rays are unsuitable for osteometric measurements due to a parallax effect (Christensen et al., 2018; Carew et al., 2019b).

Similar to plain film X-rays, a Lodox scanner uses X-rays to generate a 2-dimensional image. However, they utilize a “slot-scanning” method, which allows the entire body to be scanned in a very short amount of time, producing a head-to-toe image with less image distortion than plain film X-ray (Mamabolo et al., 2020; Marais, n.d.). However, as it is still 2-dimensional, superimposition remains a major problem (Mamabolo et al., 2020).

Computed tomography (CT) was introduced in clinical medicine in the 1970s, with its first documented use in forensic anthropology occurring in the 1980s by Reichs, who used it for a positive identification based on frontal sinus morphology (Uldin, 2017). There are many benefits of CT, as discussed below. However, the initial and ongoing costs associated with CT scanners are high, as is the technical know-how to properly run the machine (Aalders et al., 2017).

As previously discussed, due to its exceedingly high costs, long scan times, and the high technical skills required to operate, magnetic resonance imaging (MRI) is poorly suited to postmortem imaging. Furthermore, MRI relies on the presence of hydrogen ions in the body to produce an image. In life, bone barely contains enough hydrogen to produce a clear image signal, let alone after death when skeletal material becomes dehydrated. For all these reasons, MRI is

rarely to never used in death investigation (Mamabolo et al., 2020; National Institute of Biomedical Imaging and Bioengineering, n.d.).

Development of the Biological Profile

While more and more studies continue to demonstrate the efficacy of basic and advanced radiographic modalities in the development of the biological profile, significantly more research is necessary to generate appropriate population specific standards as well as to validate the application of methods developed on dry bone to radiographic data (Davies et al., 2015).

The feasibility of aging both adults and sub-adults has been soundly demonstrated using various skeletal features and imaging modalities. Sub-adult aging has long utilized radiography to help visualize unerupted dentition, the presence or absence of ossification centers, and the rate of epiphyseal union (Franklin et al., 2016; Sorg et al., 1989). For example, Sorg et al. (1989), demonstrated that you could use X-rays of the medial clavicle to accurately stage ossification centers. Likewise, various authors have shown that CT and MRI can be used to evaluate epiphyseal closure in other anatomic areas such as the humerus, radius, tibia, and calcaneus (Davies et al., 2015; Saint-Martin et al., 2013). It is important to note that stages or morphological evaluations of epiphyseal closure are not interchangeable between radiographs (of any modality) and macroscopic observations. This is because evidence of epiphyseal closure will be present on radiographs months or even years before they can be appreciated on dry bone (Saint-Martin et al., 2013).

Aging of the adult is more limited and relies mainly on degenerative changes to the skeleton. X-rays are a poor modality for aging adults, beyond gross age estimates derived from the degree of ossification of the laryngeal and costal cartilages (Garvin and Stock, 2016).

However, CT is increasingly demonstrating its utility in appropriately estimating structures such as sternal rib ends and the pubic symphysis (Garvin and Stock, 2016; Christensen et al., 2018). However, not every aging technique has, thus far, translated well to more advanced imaging modalities. For example, despite improved rates of resolution, estimation of cranial suture closure using Meindl and Lovejoy's method does not work because not enough of the cranial suture can be appreciated on 3-dimensional reconstructions (Garvin and Stock, 2016). Likewise, it has been demonstrated that traditional methods of aging the auricular surface did not work on CT scans as not all the features were shown on the scan (Villa et al., 2015). This study was promising though, as they were able to generate novel landmarks that produced reasonable age estimates. This is a good example of how forensic anthropology is just beginning to scratch the surface of potential new methodologies developed solely on radiographic images.

Estimation of sex, stature, and population affinity all rely heavily on metric traits. Though dry bone measurements are still considered the gold standard in the field, numerous studies have shown that standard osteometrics taken using CT scans are within the accepted 2-millimeter margin of error (Garvin and Stock, 2016). In some cases, computed tomography and MRI processing software can automate some measurements, such as maximum lengths or widths of bones, actually producing more accurate measurements than those taken from dry bone (Garvin and Stock, 2016). Digital measurements of bones have been shown to be accurate in the pelvis and the skull (Franklin et al., 2016; Colman et al., 2019). These measurements, as well as measurements of long bones, can help determine sex and stature. However, this is only true of CT scans. Studies have shown that magnification errors introduced during basic radiography (i.e., X-rays) can significantly skew estimates of stature and should not be used without a correction factor (Carew et al., 2019b). To date, no universal correction factor has been

established, so osteometric measurements of X-rays should not be carried out (Carew et al., 2019b).

Estimation of an individual's biological sex is possible using both metric and non-metric traits captured through radiography (Garvin and Stock, 2016). Studies of the pelvis and cranial have demonstrated high efficacy of non-metric traits such as the greater sciatic notch, sub-public angle, glabella, supra-orbital ridge, and the nuccal area in accurately estimating biological sex. CT is better at appreciating both metric and non-metric observations related to sex than is x-ray (Garvin and Stock, 2016).

Estimation of stature using postmortem computed tomography has been widely studied (see, for example, Baba et al., 2016; Colman et al., 2018; Giurazza et al., 2012; Winter et al., 2021). Regression formulae developed on dry bone have been applied to computed tomography scans with good results (Colman et al., 2018; Hasegawa et al., 2019; Kyllonen et al., 2017; Reynolds et al., 2014). Regression formulae have also been developed using CT scans only, though these have less utility to the average forensic anthropologist unless validated on dry bone (Baba et al., 2016; Giurazza et al., 2012; Torimitsu et al., 2014b; Zhang et al., 2015).

Estimation of population affinity has undergone a resurgence of methodological development in recent years, particularly regarding metric analysis. As discussed, osteometrics taken from X-rays cannot be used for accurate measurement. However, they can be for CT scans (Guareschi et al., 2023). Measurements taken from CT scans can be utilized in classic osteometric programs such as Fordisc (Garvin and Stock, 2016; Jantz and Ousley, 2005). Furthermore, using 3-dimensional reconstructions, non-metric traits, and advanced geomorphometric analyses can be performed with good results (Garvin and Stock, 2016).

Identification

Of course, the fundamental reason for producing a biological profile is to help identify an unknown individual. Beyond its applicability in estimating the biological profile, basic and advanced imaging modalities can be used to identify individuals based on unique dental and skeletal characteristics. Radiography has been employed for identification purposes for nearly a century. In 1926, the first documented case of postmortem radiography used for identification occurred when Culbert and Law compared antemortem radiographs a patient had undergone for chronic sinusitis, with postmortem X-rays of the frontal sinus and mastoid air cells (Brough et al., 2015; Lagalla, 2020).

In the years since 1926, numerous other anatomic areas and features have been discovered to be individuating. For instance, both basic and advanced imaging modalities have been used for positive identification of the sphenoid sinus, the margins of the thoracic vertebra, dentition, and even trabecular patterns (Brogdon et al., 2010; Brodgon et al., 2012; Franklin et al., 2016; Waldron, 2009; Watamaniuk and Rogers, 2010). Trabecular patterning can be especially individuating, even between identical twins, and can even be used in cases with complex taphonomy (Brogdon et al., 2010; Watamaniuk and Rogers, 2010). For example, Brogdon et al. (2010), were able to establish a positive identification of a homicide victim whose body had been severely burned and fragmented, using only the trabecular pattern of a few phalanges.

A major limitation of note in attempting to compare ante- and postmortem X-rays is the need to exactly replicate the angle of the antemortem image so that a true comparison can be made. This can be difficult when only skeletal remains are present and several attempts at correctly positioning remains may need to be made (Garvin and Stock, 2016).

Evaluating Trauma

Basic skeletal surveys done at the outset of an examination can reveal gross evidence of trauma, as well as document the fact that trauma was initially present and not the result of the examination (Franklin et al., 2016; Garvin and Stock, 2016.) While X-rays are classically used, it can be difficult to distinguish trauma due to the superimposition effect (Garvin and Stock, 2016). Studies have shown that CT is much better suited to the detection of fractures, including appreciation of fracture timing and directionality (Scheirs et al., 2020). Furthermore, CT has been demonstrated to have a significantly lower false positive rate than x-ray. Spies et al. (2021) demonstrated that non-experts, given even a modicum of training, are able to identify trauma on CT. Additionally, the 3-dimensional rendering capabilities of CT software can allow for the printing of true-to-life models of traumatic injuries, and even virtual reconstructions of comminuted fractures (Christensen et al., 2018). Computed tomography is also much more sensitive than X-rays for trauma identifications (Spies et al., 2020).

Assessing Taphonomic Change

Despite being a central area of forensic anthropology practice and research, there have been few studies examining the role of radiography in assessing taphonomy, and most of those are single case studies. For example, Moghaddam et al. (2023) used postmortem CT to help reconstruct a fragmented cranium that had been burned and were able to demonstrate the fragments had features associated with blunt force trauma, that was later confirmed by direct reconstruction of the cranium. Guareschi et al. (2023) discuss the use of CT to evaluate the presence or absence of the auditory ossicles. Their conclusion, however, was simply that the absence of the ossicles, which are very easily lost, simply may indicate the remains had been

moved at some point in time. Significantly more systematic research is needed in this area, particularly in regard to the utility, or lack thereof, in estimating the postmortem interval.

Summary of Imagining in Forensic Anthropology

While standard X-rays have been in use in forensic anthropology for decades, computed tomography represents a leading edge for both casework and research. Recently, it has been shown that computed tomography has a wide range of applications, from trauma analysis to assessing the biological profile to the interpretation and diagnosis of skeletal pathology. The rise of postmortem CT can give access to populations for which skeleton reference collections do not exist or are otherwise difficult to study, such as populations of modern, 21st-century individuals.

Conclusions

The above literature review provided an overview of issues related to skeletal health, cranial pathology and normal anatomic thickness, alcohol use, and the skeleton, and the promise of novel imagining modalities such as computed tomography in assessing bone density and bone quality in clinical and forensic settings. Three studies were identified that addressed cranial osteoporosis, two studies (using the same sample) were identified that examined cranial thickness in the setting of chronic substance and alcohol use, and one article was identified that demonstrated the impact alcohol use disorder can have on a forensic anthropology case. However, no studies were identified that specifically examined cranial thickness and bone quality among heavy alcohol users, let alone the implications any changes may have for forensic anthropologists. Therefore, this dissertation aims to begin bridging this knowledge gap by

examining cranial thickness and bone quality among heavy alcohol users via the promising modality of postmortem computed tomography.

Organization of the Chapters

Chapter II of this study describes the methodological approaches used, including discussion of sample selection, analysis software, and statistical analyses performed. Chapter III discusses the results of statistical analyses performed, including descriptive statistics of the study population and inferential statistical results. Chapter IV discusses the limitations of the study design, provides possible explanations for the study's results, and the importance of results to the medicolegal and clinical communities. Chapter V provides a brief summary of the study and discusses future research directions.

CHAPTER 2

METHODOLOGY

Introduction

The aim of this study was to determine whether there are significant differences in the crania of high-risk alcohol users compared to low-risk alcohol users; specifically, this study will focus on whether there are significant differences in cranial thickness, volume, and radiodensity as approximated by Hounsfield units between the high-risk and low-risk groups. One-hundred forty-four postmortem cranial computed tomography scans provided by the New Mexico Decedent Imaging Database were analyzed to measure these chosen parameters. This chapter describes the data source, sample selection process, data collection, and statistical methods used to address the hypotheses listed in Chapter 1.

New Mexico Decedent Image Database

Postmortem computed tomography scans utilized for this study were provided by the New Mexico Decedent Image Database, funded by the National Institute of Justice grant number 2016-DN-BX-0144 (Edgar et al. 2020). This dataset contains anonymized postmortem computed tomography scans of over 15,000 individuals whose deaths were investigated by the New Mexico Office of the Medical Investigator. NMDID contains up to 69 variables for each decedent, obtained from both the death investigation as well as next of kin interviews (Edgar et al., 2020). Variables range from basic demographic information to lifestyle factors such as eating habits, hobbies, and drug use. Variables included in NMDID that were pertinent to this study include a decedent's biological sex, age in years, primary cause of death, height, weight, and alcohol use status.

Alcohol use risk status used by NMDID may have one of six responses: never drank; low-risk; high-risk; previous high-risk; drinker, current status unknown; and unknown if ever drank. Those risk categories are modified from the definitions provided by the National Institute on Alcohol Abuse and Alcoholism. Generally speaking, however, “high-risk” alcohol use in men is defined as more than five standard drinks⁵ per day or more than 15 drinks per week, while “low-risk” alcohol use is defined as no more than three standard drinks per day and no more than seven drinks per week (NIAAA, N.D).

Determination of Effect Size, Sample Size, and Sample Selection

Study power was selected to be robust at $\beta = 0.9$ to reduce the likelihood of committing a Type II error, i.e., failing to reject the null hypothesis when it is, in fact, false.

A Cohen’s d was performed to measure the estimated effect size expected in the study (Cohen, 1988). Effect size was estimated based on data from Na et al. (2018). The difference between mean Hounsfield units measured at the anterior frontal bone between normal and osteoporotic patients, whose diagnosis was confirmed with dual-energy X-ray absorptiometry, were used.

Cohen’s d:

$$d = \frac{(M_1 - M_2)}{S_{\text{pooled}}}$$

Equation 1 Cohen's d for calculation of estimated study effect size

⁵ A standard drink is defined as either 12 ounces of beer, 5 ounces of wine, or 1.5 ounces of spirits (NIAAA, N.D.)

Where:

M_1 = Mean frontal bone HU of normal-density patients

M_2 = Mean frontal HU of osteoporotic patients

S_{pooled} = the pooled standard deviation of the samples, which is found by the following equation:

$$S_{pooled} = \sqrt{\frac{(S_1^2 + S_2^2)}{2}}$$

Equation 2 Calculation of S_{pooled} for Cohen's d

Na et al. (2018) reported that for the frontal bone as a whole:

- The mean and standard deviation Hounsfield units for normal density patients was $M_1 = 811.8$, and $SD_1 = 187.2$
- The mean and standard deviation for Hounsfield units for osteoporotic patients was $M_2 = 561.8$ and $SD_2 = 189.0$.

Given those figures, Cohen's d is calculated by:

$$S_{pooled} = \sqrt{\left[\frac{(187.2^2 + 189.0^2)}{2} \right]} = 188.1$$

$$d = \frac{811.8 - 561.8}{188.1} = 1.32$$

Equation 3 Calculation of Cohen's d to determine estimated effect size

An effect size greater than 0.8 is considered large, meaning that a smaller sample size is needed to determine whether an actual difference exists between two groups (Cohen, 1988).

Using sample size tables from Cohen (1988), when $p < 0.05$ is combined with an effect size of 1.32, a one-tailed t-test should have a minimum of ~11.5, or 12 individuals per group.

Sample Selection

Men of all population affinities and ethnicities between the ages of 21 and 55 were selected as the base population for this study. Twenty-one was chosen as the base age as it is above the legal drinking age in the United States. In contrast, 55 was selected as the upper bound for age as it is below the approximate age of onset of senescent osteoporosis in men (Walsh and Eastell, 2013). Women were deliberately not included in this pilot study to avoid potential confounding.

A search was performed on NMDID for all males between the ages of 21 and 55, and the metadata for 2,300 individuals was downloaded.

Body mass index was calculated based on the decedents' reported heights and weight. Individuals with body mass indices below 18.5 and above 34.9 were excluded from the sample because of the effects of body weight extremes on skeletal health (Rosen, 2020).

Individuals were excluded from the sample if their causes of death were related to intoxication of a substance other than alcohol alone, conditions that may affect bone quality, such as cancer or significant autoimmune conditions, or were indicative of significant cranial trauma, e.g., self-inflicted gunshot wounds. Individuals with a reported history of substance use disorder aside from alcohol use disorder were also excluded, regardless of their reported cause of death.

An individual was included in the high-risk group if they met the above criteria, had a high-risk alcohol use status reported in NMDID, and their cause of death was reported as “ethanolism” or “acute ethanol intoxication.” An individual was included in the low-risk group if

they met the above criteria, and their alcohol status was listed as low-risk or never drank. Causes of death for the low-risk group are reported in Chapter 3.

Based on the criteria above, a preliminary sample of 75 high-risk users and 71 low-risk alcohol users was selected. Scout images for each individual were then viewed on NMDID to ensure that the scans contained the cranium and that no cranial defects were present. No individuals in the preliminary high-risk group were eliminated based on scan exclusions, while two individuals from the low-risk group were excluded, both due to cranial trauma.

This left a final sample size of 75 high-risk and 69 low-risk male alcohol users. Even though the sample size calculation for this study was estimated to require only 12 individuals per group, all those meeting the sample selection criteria were included to increase statistical power.

Computed Tomography Settings

Tables 10 and 11 list the scan parameters used to acquire the scans included in this study, as reported by the NMDID data dictionary (Edgar et al., 2020). Scans were completed at a slice thickness of 0.5mm.

Table 10 Adult computed tomography scan protocol for the New Mexico Office of the Medical Investigator for non-decomposed cases

Scan Parameter	Setting
Energy	120 kVp
Milliamperere-seconds	300
Scan length	600-800 mm
Scan field of view	500-699 mm
Pitch	0.567
Collimation	16 x 0.75
Rotation time	1.0 seconds
Matrix	512 x 512

Table 11 Decomposed adult computed tomography protocol for the New Mexico Office of the Medical Investigator

Scan Parameter	Setting
Energy	120 kVp
Milliampere-seconds	300
Scan length	300 mm
Scan field of view	290 mm
Pitch	0.567
Collimation	16 x 0.75
Rotation time	1.0 seconds
Matrix	512 x 512

Data Collection

Segmentation and analyses were performed between November 2023 and April 2024. Before segmentation and measurement, individuals were dissociated from their alcohol status and analyzed blinded to avoid potential confirmation/investigator bias (Cooper et al., 2019; Dror, 2018).

Sixteen individuals were randomly selected for reanalysis to measure intra-observer reliability. Individuals in the total sample were numbered 1 to 144, and the Excel function RANDBETWEEN was run 16 times to return a random number between 1 and 144 (Microsoft Corporation, 2024). No two numbers appeared twice.

The number of individuals selected for reanalysis was calculated via Equation 4 after Walter et al. (1998).

$$n = \frac{2}{(1 - r)}$$

Equation 4 Equation to determine subsample needed for reliability testing

Where n equals the number of individuals needed for reanalysis and r represents the reliability coefficient predicted from the measurement.

Table 12 displays the interclass correlation coefficients for different levels of reliability. Interclass correlation coefficients are equivalent to the reliability coefficient (Liljequist et al., 2019).

Table 12 Level of agreement and reliability and associated interclass correlation coefficient

Level of Agreement/Reliability	Interclass/Reliability Coefficient
Poor agreement	<0.5
Moderate agreement	>0.5 to <0.75
Good agreement	>0.75 to <0.90
Excellent agreement	>0.90

A reliability value of 0.75 was selected to say with reasonable certainty a good level of agreement was achieved. Equation 5 shows the results of Equation 4. The number of individuals was doubled to increase statistical power.

$$n = \frac{2}{(1 - 0.75)} = 8$$

Equation 5 Calculation to determine subsample needed for reliability testing

Individuals were reanalyzed at least one month after the initial analysis to reduce memory bias.

3D Slicer

Computed tomography scans were analyzed using 3D Slicer, an open-source imaging software funded by the National Institutes of Health (Fedorov et al., 2012). Version 5.6.2 of 3D Slicer was run on a 2019 Apple MacBook Pro with 32 GB of RAM.

Pre-Segmentation Scan Processing

3D volume renderings of a computed tomography scan are comprised of 3-dimensional pixels called voxels (Thaler et al., 1978). To ensure isotropic spacing and that measurements were consistent across decedents, all scans were resampled to a voxel size of 0.5mm x 0.5mm x 0.5mm. In cases where the decedent's scan also included the full torso and upper extremities, the scan was first cropped to exclude all anatomy except the cranium to conserve computational resources and decrease processing time. For example, a scan involving the full torso would take approximately 3-5 minutes to load and render with each manipulation. In contrast, a cropped version of the same scan would take approximately <30 seconds to perform the same tasks.

Before segmentation, all scans were oriented to the Frankfurt plane⁶. The Frankfurt plane was established by creating a 3-D volume rendering of the scan and then using the Transform module in Slicer to adjust its orientation. Confirmation of the Frankfurt plane was made by creating a region of interest that was then cropped so the superior portion of the cranium from the vertex to Frankfurt plane was hidden. This created a perfectly horizontal line with which to align the inferior margin of the orbit and the superior margin of the external auditory meatus. Once the cranium was properly oriented, the transformation was registered to become the scan's new default orientation.

Determination of Segment Location

The location of the segments chosen for this study was based on observations made during several postmortem forensic anthropology examinations of individuals with a known history of alcohol use disorder. In these cases, thinning along with translucency was observed in

⁶ Frankfurt plane is an anatomic positional term that refers to aligning a skull such that the inferior margin of the orbit and the superior margin of the external auditory meatus are on the same horizontal plane (Virchow, 1891).

the lateral frontal, the squamous part of the temporal, and the cerebellar fossae of the occiput. Since thinning occurred over general anatomic regions, not at specific anatomical points, segments with a diameter of 20 millimeters were selected to best capture any regional morphologic changes. Segments were selected bilaterally at the orbital roof, the lateral frontal, the squamous part of the temporal, and the cerebellar fossae of the occiput. Table 13 describes segment placement in detail. Figures 8 to 10 demonstrate segment placement.

Table 13 Segment location

Segment	Location	Comments
Orbit roof	Center point of the orbital roof.	Best viewed inferiorly by cropping the 3D rendered volume of the cranium to hide the everything below the inferior margin of the orbit.
Lateral frontal	Centered between the sphenofrontal suture and the superior temporal ridge.	To confirm segment placement, the cranium may need to be viewed at an angle to achieve an oblique lighting effect which casts a shadow on the sphenofrontal suture.
Temporal squamous	Center point of the squamous part of the temporal, equidistant between from the anterior, superior, and posterior line of the squamosal suture.	Almost always located just superior and anterior to the external auditory meatus.
Cerebella fossa of the occiput	Centered on the deepest point of the cerebellar fossae of the when viewed endocranially.	Best viewed superiorly by cropping the 3D rendered volume of the cranium to hide the calvarium. Often the cranium needs to be rotated slightly along the sagittal axis and the cropping tool moved up and down to determine the deepest point of the bowl formed by the fossa.

Segment Selection

Segments were selected on a 3D volume rendered cranium using a 20mm spherical brush, with a thresholding limit of 200 Hounsfield units initially applied. Two hundred Hounsfield units were selected as the minimum threshold as it captured only voxels with Hounsfield units ≥ 200 , which captured most, if not all, osseous material. Without thresholding, a perfect sphere would be created, capturing the full spectrum of Hounsfield units.

Once each segment was selected, the Margin Tool was used to grow and then shrink the segment by 0.5mm, i.e., one voxel, with the threshold now set at -1,047 to 2,997 Hounsfield units. This process allowed any voxels below 200 Hounsfield units to be incorporated into the segment while maintaining the segment's original diameter and thickness.

To account for any noise that became incorporated during the selection process, the "Keep Selected Island" tool was used on each segment. This tool searches for groups of connected voxels and allows users to specify which group should be kept in the segment. If extraneous voxels were still present after this process, the scissor tool was used to trim them.

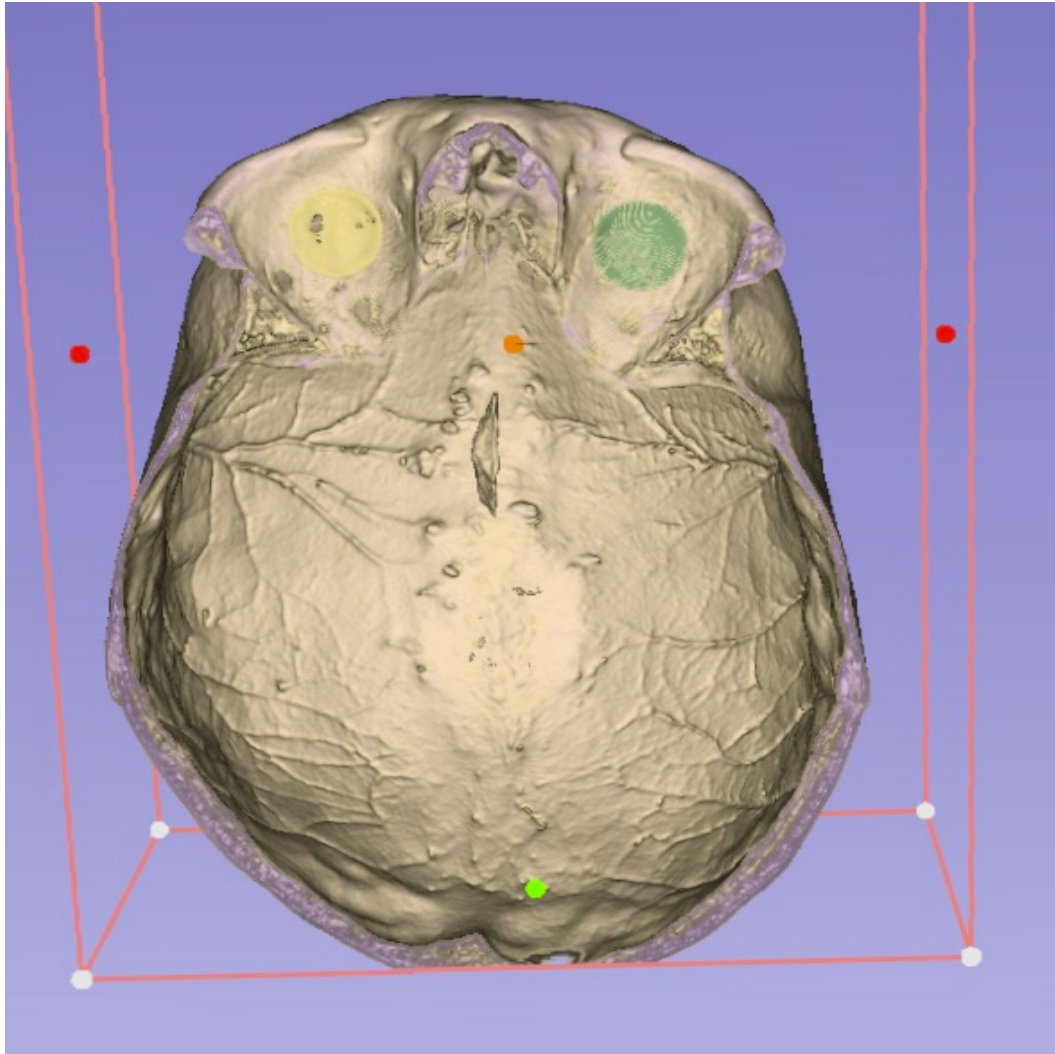


Figure 8 Inferior view of the cranium showing placement of the orbital segments. Anterior is up. Sectioning created virtually in 3D Slicer.

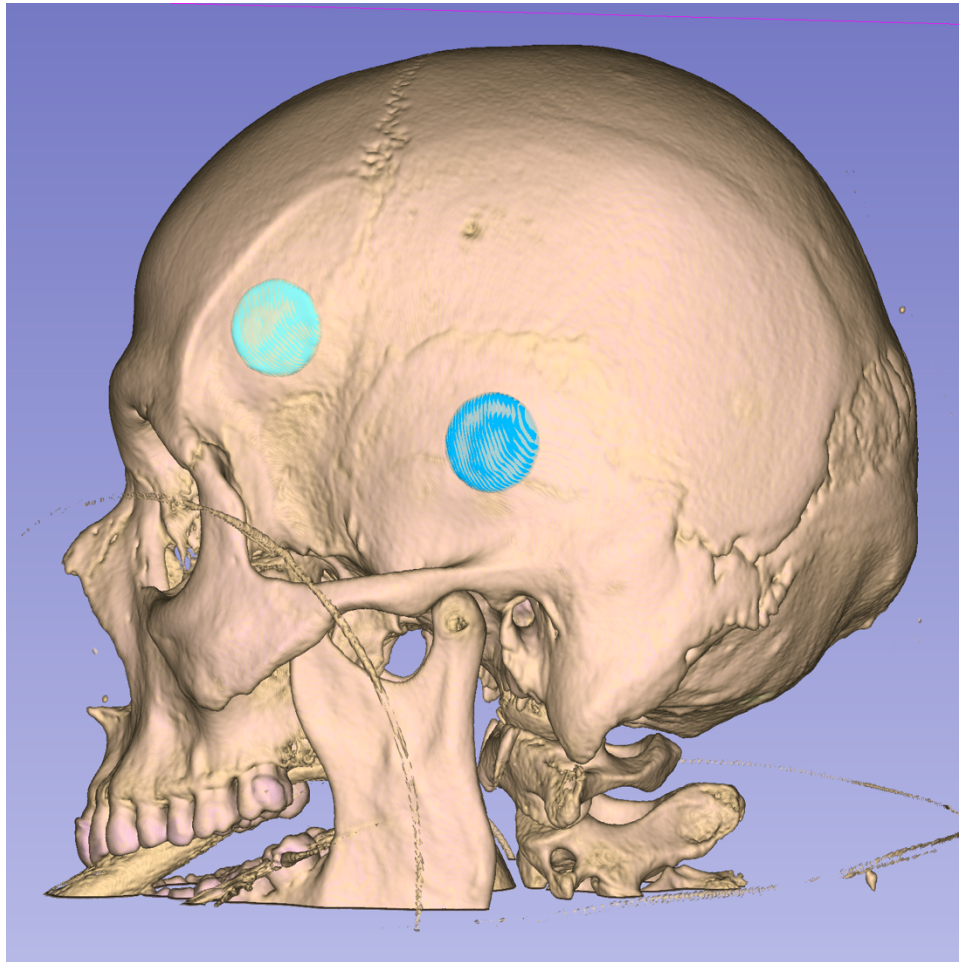


Figure 9 Lateral view of a decedent showing placement of the frontal and temporal segments

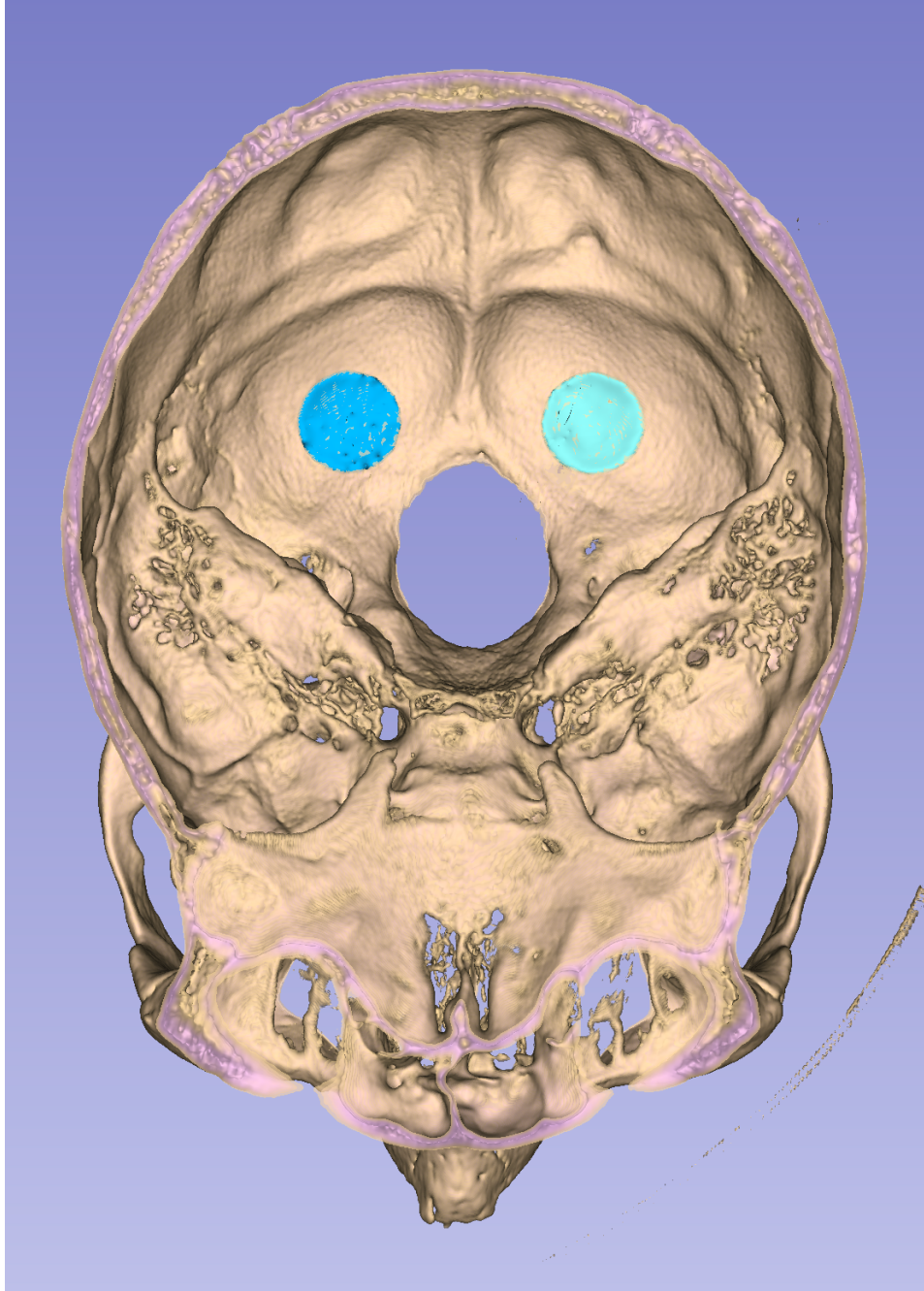


Figure 10 Endocranial view of the cranium showing placement of the cerebellar fossae segments.
Anterior is down. Sectioning created virtually with 3D Slicer

Slicer Statistics

Once segments were selected and cleaned, the Segment Statistics module automatically computed the number of voxels, volume in millimeters-cubed, and minimum, maximum, mean, and median Hounsfield units for each segment. Table 14 displays the definition of each variable computed by 3D Slicer as well as the minimum segment thickness, measured manually in 3D Slicer. The results of the Segment Statistics module were exported to an Excel spreadsheet for later analysis.

Table 14 Variable definition

Variable	Definition
Minimum segment thickness	The minimum thickness of each segment is defined as the shortest distance between the areas of greatest intensities representing the boundaries of the endocranial cortex and the ectocranial cortex. Minimum thickness is measured in the coronal plane.
Segment Volume	The volume of each segment in millimeters cubed
Minimum Hounsfield units	The minimum Hounsfield unit measured in each segment
Maximum Hounsfield units	The maximum Hounsfield unit measured in each segment
Mean Hounsfield units	The mean Hounsfield units of each segment
Median Hounsfield units	The median of the Hounsfield units of each segment

Measurement of Minimum Thickness

3D Slicer does not automatically compute the minimum thickness for segments; however, it can create manual line measurements between two or more user-selected points. Due to a lack of measurement automation, minimum segment thickness was performed manually. Fiducial markers were placed at the boundaries of the highest intensities at the point of minimum thickness of each segment to avoid any beam hardening artifacts present in the scan. Determination of fiducial placement was made under the guidance of a board-certified radiologist for several measurements until the author and the radiologist were in consistent agreement for placement. Minimum segment thickness was determined by viewing each segment

2-dimensionally in the coronal plane. Scans were initially viewed while the segment was visible, allowing a quick visual approximation of the location of segment thickness. Once the general area of minimum thinness was found visually, the segment marker was hidden to allow a clear view of the scan. Multiple measurements were taken, sometimes on multiple slices, to determine the actual area of minimum thinness. Once a minimum thickness was measured, the segment marker was unhidden to ensure the measurement fell within the segment bounds. Figures 11 to 14 demonstrate an example of minimum thickness measurement.

All manual measurements were entered into an Excel sheet and saved into the output files of each scan for redundancy and to check recording accuracy.

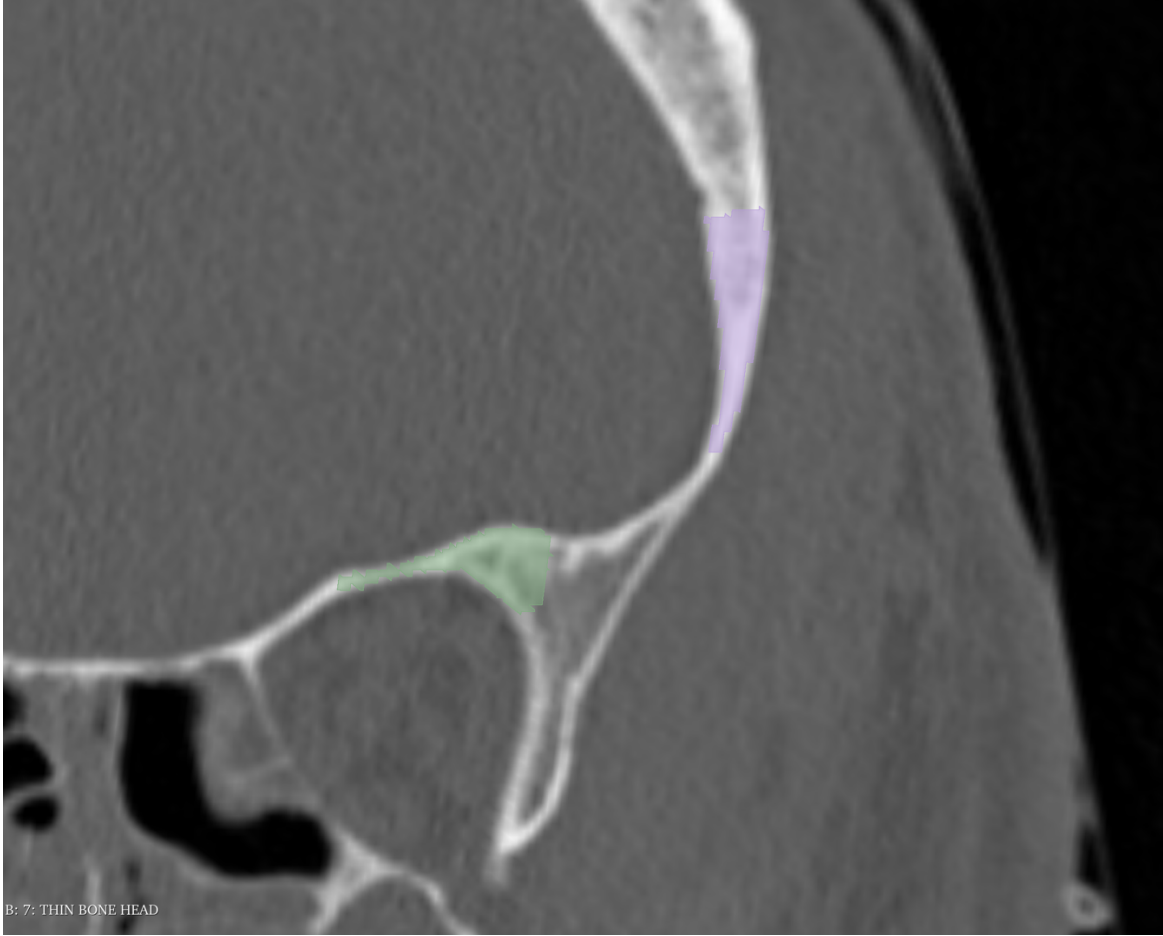


Figure 11 Coronal view of the left frontal segment



Figure 12 is the same slice as Figure 8, with the frontal segment hidden. Arrow points to the minimum segment thickness



Figure 13 Left frontal segment hidden, with minimum segment thickness measured

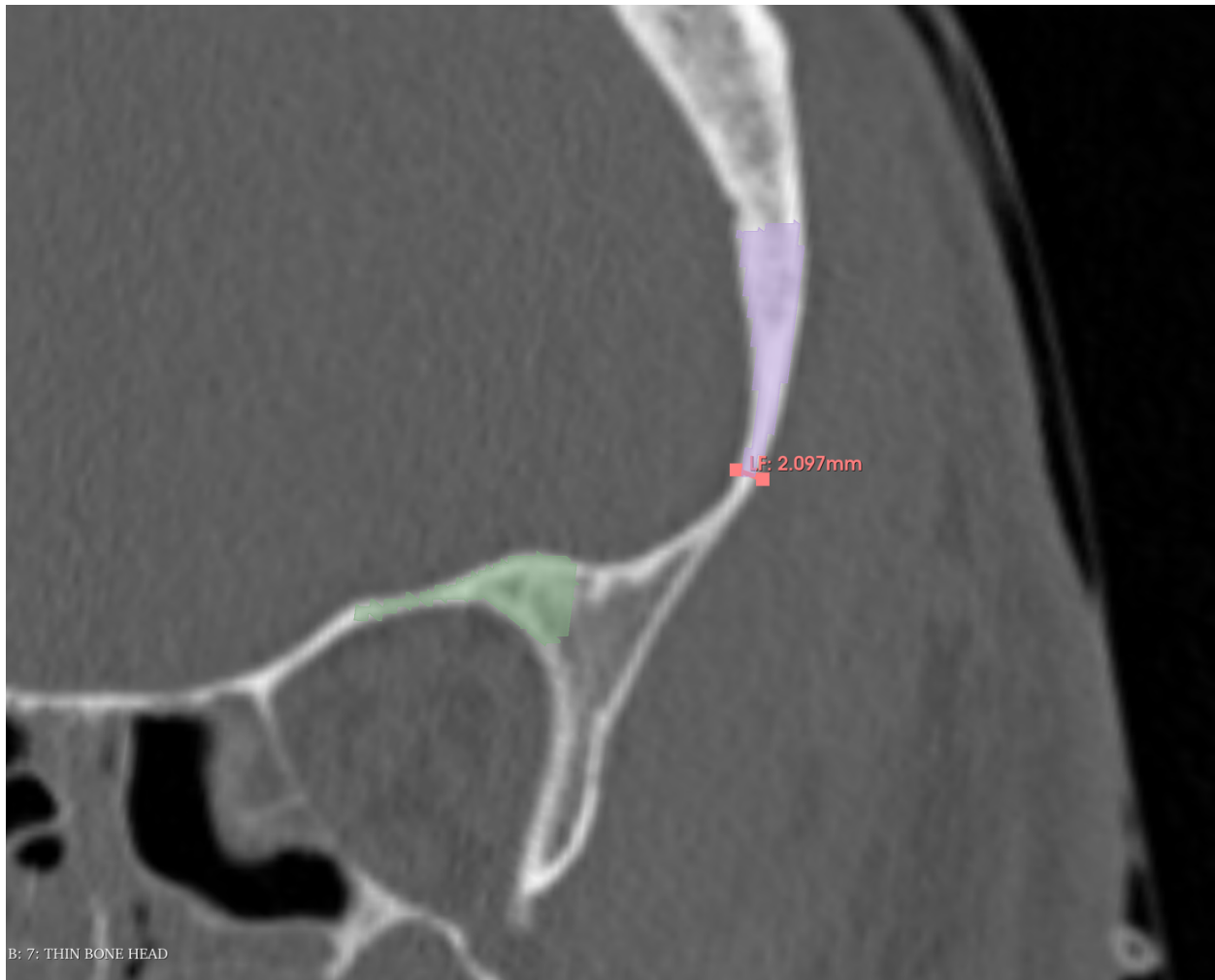


Figure 14 Frontal segment displayed showing minimum segment thickness

Statistical Analyses

Once all decedent scans were analyzed, a single dataset with the Slicer data, manual measurements, and decedent age, body mass index, population affinity, and alcohol status was compiled. All statistical analyses were performed using SPSS for Mac Version 29 (IBM, 2024).

Basic descriptive statistics (mean, minimum, maximum, range, standard deviation) were computed for each segment and variable. One-way t-tests for independent means were completed

to test the difference between risk groups. For t-tests, results were considered statistically significant when $p < 0.05$.

Analyses of covariances were performed for each variable to control for any interaction between the variable and decedent age and population affinity. Results were considered statistically significant if $p < 0.05$.

Pearson's correlations, with two-way p-values, were completed for the variables age, body mass index, minimum thickness, segment volume, and minimum, maximum, and mean Hounsfield units for each segment by risk group. A simple Bonferroni correction was applied to the p-value to reduce the likelihood of a Type I error, i.e., that significant correlations existed when, in fact, they did not. Equation 6 shows the calculation for the Bonferroni correction.

$$\text{Bonferroni correction} = \frac{\alpha}{n}$$

Equation 6 Equation for Bonferroni's correction

Where $\alpha = 0.05$ and $n =$ the number of comparisons. The correction significance for the Pearson's correlations is:

$$\text{Bonferroni correction} = \frac{0.05}{7} = 0.007$$

Equation 7 Calculation of Bonferroni correction

To assess intra-rater reliability, two-way mixed methods interclass correlation coefficients were calculated.

Results and interpretations of the study findings are reported in Chapter 3.

Chapter 3

RESULTS

Introduction

This chapter presents an overview of the sample used in this study, this study's results and some interpretations of the data. Results and interpretations are presented by the hypotheses listed in Chapter 1. For each hypothesis, a table with the mean, standard deviation, difference between the low-risk and high-risk groups, and the p-values for a one-tailed t-test for independent means are presented for each segment. Analysis of Covariances were run to test whether decedent age or decedent population affinity had a significant impact on the differences between the risk groups for each variable. Complete results of the Analysis of Covariances may be found in Appendix B. Additionally, Pearson's correlation coefficients for minimum segment thickness, segment volume, and mean Hounsfield units are discussed. Full Pearson's correlations may be found in Appendix B. Finally, interclass correlation coefficients are presented, assessing intraobserver agreement for the re-measurement of all variables.

Sample Overview

Based on the inclusion criteria listed in Chapter 2, 144 men between the ages of 21 and 55 were selected for this study. Table 15 shows the number of individuals in each risk group. Individuals classified as "low-risk" and "never drank" were combined into a single "low-risk" category for this study. Overall, 75 individuals were identified as high-risk alcohol users, and 69 were identified as low-risk alcohol users.

Table 15 Number of decedents in each alcohol use risk group

Risk Group	High-Risk	Low-Risk	
		Low- Risk	Never Drank
Number of individuals	75	50	19
Total	75	69	

Table 16 Reported causes of death for high-risk alcohol users

Reported Cause of Death Among High-Risk Alcohol Users	Count	Percent
Ethanol (alcohol) intoxication	23	31%
Ethanolism (chronic, alcoholism, alcoholic liver)	52	69%
Total	75	100%

Table 16 displays the reported causes of death for the high-risk group. As indicated in the methods section, individuals classified as high-risk were only included if their cause of death was related to ethanol. Thirty-one percent of decedents in the high-risk group had a reported cause of death of ethanol intoxication, whereas 69% had a reported cause of death of ethanolism.

Table 17 Reported causes of death for low-risk alcohol users

Reported Cause of Death Among Low-Risk Alcohol Users	Count	Percent
Asphyxia (suffocation, strangulation)	2	3%
Cardiac arrhythmia	26	38%
Drowning	2	3%
Emboli (thrombus, phlebitis)	1	1%
Exposure	2	3%
Gastrointestinal hemorrhage (gastroenteritis, ulcers, diverticulitis)	1	1%
Gunshot wound	7	10%
Hanging	5	7%
Hypertension (hypertensive cardiovascular disease)	4	6%
Multiple injuries (fractures, lacerations to internal organs)	13	19%
Accidental ligature strangulation	1	1%
Pneumonia (bronchitis)	1	1%
Respiratory Distress Syndrome (RDS, ARDS, IRDS, idiopathic pulmonary fibrosis, alveolar damage, insufficiency, Hanta viral)	1	1%
Sepsis	1	1%
Stab wound (slash, penetrating cut)	2	3%
Total	69	100%

Table 17 displays the reported causes of death for decedents in the low-risk category. Overall, cardiac arrhythmia was the most common cause of death, experienced by 38% of low-risk decedents.

Table 18 Decedent population affinity by risk group

Population Affinity	High-Risk n=75	Low-Risk n=69	Total
Black or African-American	0	4	4
Hispanic	5	10	15
Native American	18	6	24
Other	0	2	2
Other Asian	1	0	1
White	51	47	98
Total	75	69	144

Table 18 displays the number of individuals in each risk group by their reported population affinity. Individuals identified as White comprised the largest percentage of both risk groups at 68% in both groups.

Table 19 Average age and body mass index for the high-risk and low-risk alcohol user groups

Decedent Characteristic	High-Risk n=75	Low-Risk n=69	One-tailed Sig.
Age in years	43.85 (8.74)	41.19 (9.82)	0.044
Body mass index	26.96 (4.46)	27.67 (3.89)	0.150

Table 19 displays decedent age and body mass index for each risk group. The high-risk group was significantly older, with an average age of 43.85 years, compared to the low-risk group's average age of 41.19 years ($p < 0.05$). Body mass index was greater in the low-risk category than in the high-risk category, at 27.68 and 26.95, respectively. However, this difference was not statistically significant ($p > 0.05$)

Hypothesis 1- Minimum cranial thickness is lower in high-risk alcohol users than in low-risk alcohol users when measured at the cerebellar fossa of the occiput, the lateral frontal, the orbital roof, and the squamous part of the temporal

Table 20 Number of individuals analyzed for minimum segment thickness by segment and risk group

Segment	Risk Group	
	High	Low
Left cerebellar fossa	74	69
Left frontal	74	69
Left orbit	74	69
Left temporal	73	69
Right cerebellar fossa	74	69
Right frontal	74	69
Right orbit	74	69
Right temporal	74	69

Table 20 displays the number of decedents for whom minimum thickness was measured by segment and risk group. One individual was not measured due to segment corruption after segment statistics were computed. An additional individual was not measured at the left temporal, also due to segment corruption after statistics were computed.

One-Tail T-Tests for Independent Samples

Table 21 Average minimum segment thickness in millimeters as well as between-group differences and one-tail p-values for each segment and risk group

Segment	Risk Group Mean \pm Standard Deviation		Low-Risk Minus High-Risk Thickness in mm	One-tailed T- Test p-value
	High Risk	Low Risk		
Left cerebellar fossa	1.69 \pm 0.63	2.30 \pm 0.90	0.61	<0.001
Left frontal	2.75 \pm 1.18	2.86 \pm 0.92	0.11	0.262
Left orbit	1.64 \pm 0.74	1.96 \pm 0.64	0.32	0.003
Left temporal	1.75 \pm 0.50	2.29 \pm 0.60	0.54	<0.001
Right cerebellar fossa	1.63 \pm 0.54	2.17 \pm 0.71	0.54	<0.001
Right frontal	2.46 \pm 1.18	2.56 \pm 0.72	0.10	0.285
Right orbit	1.49 \pm 0.77	1.78 \pm 0.47	0.29	0.004
Right temporal	1.78 \pm 0.54	2.21 \pm 0.64	0.43	<0.001

Table 21 displays the mean and standard deviation for minimum segment thickness for each segment and risk group, as well as the difference in minimum thickness between the low-risk and high-risk groups and one-tailed p-values for the t-tests. The largest between-group difference in minimum thickness was seen in the left cerebellar fossa, while the least was seen in the right frontal. Minimum thickness was significantly less in the high-risk group compared to the low-risk group when measured at the left and right cerebellar fossa, the left and right temporal, and the left and right orbit ($p < 0.05$). While the left and right frontal segments were thinner in the high-risk group, the difference was not statistically significant ($p > 0.05$).

Figure 15 displays the range for minimum thickness for each segment by risk group. For each segment, the lowest minimum thickness recorded for the low-risk group was higher than that of the high-risk group. However, the range of thicknesses varied more in the high-risk group. For the left frontal, left orbit, right frontal, and right orbit, the upper bound of minimum thickness was greater in the high-risk group compared to the low-risk group.

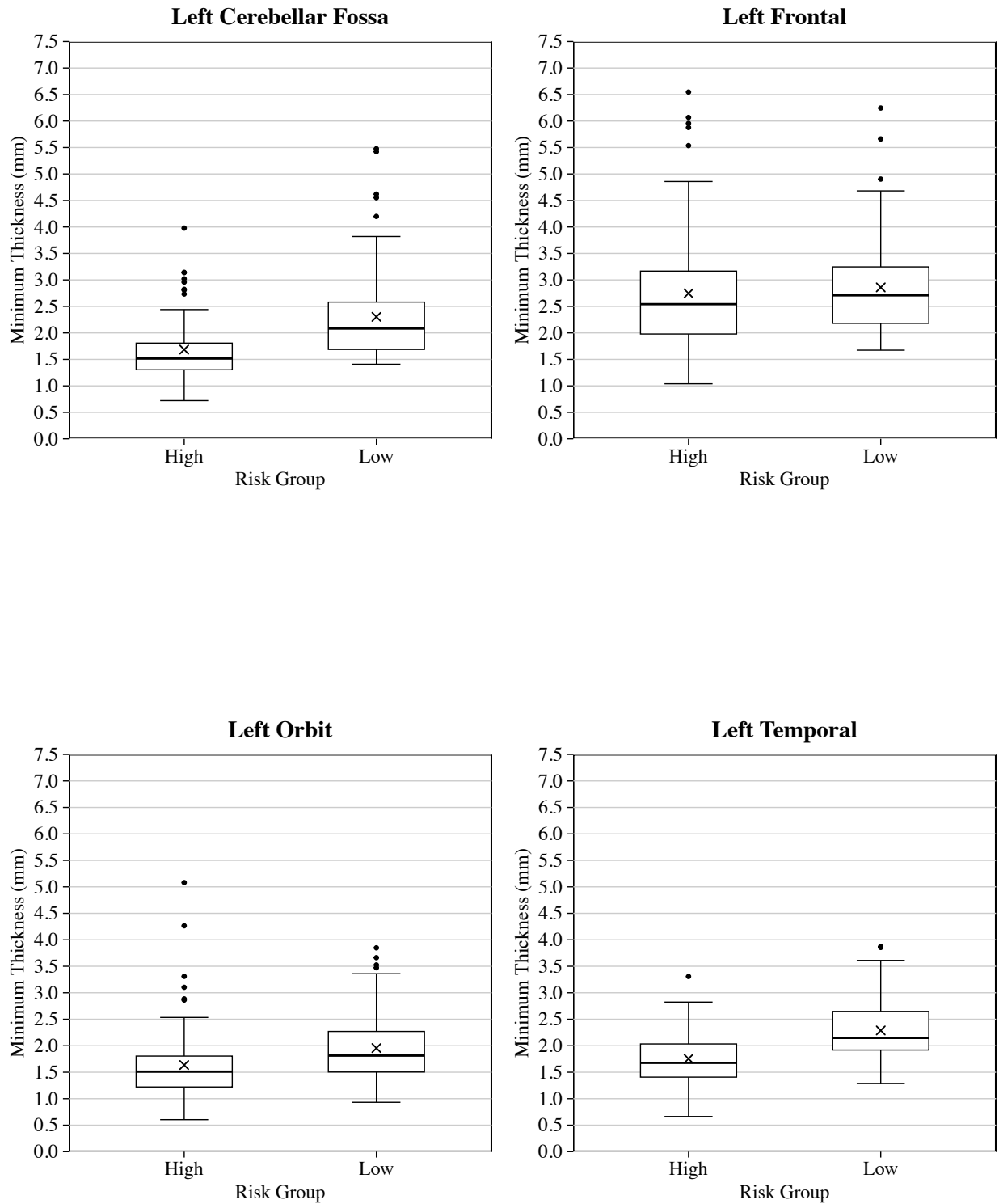


Figure 15 Range of minimum thickness by segment and risk group

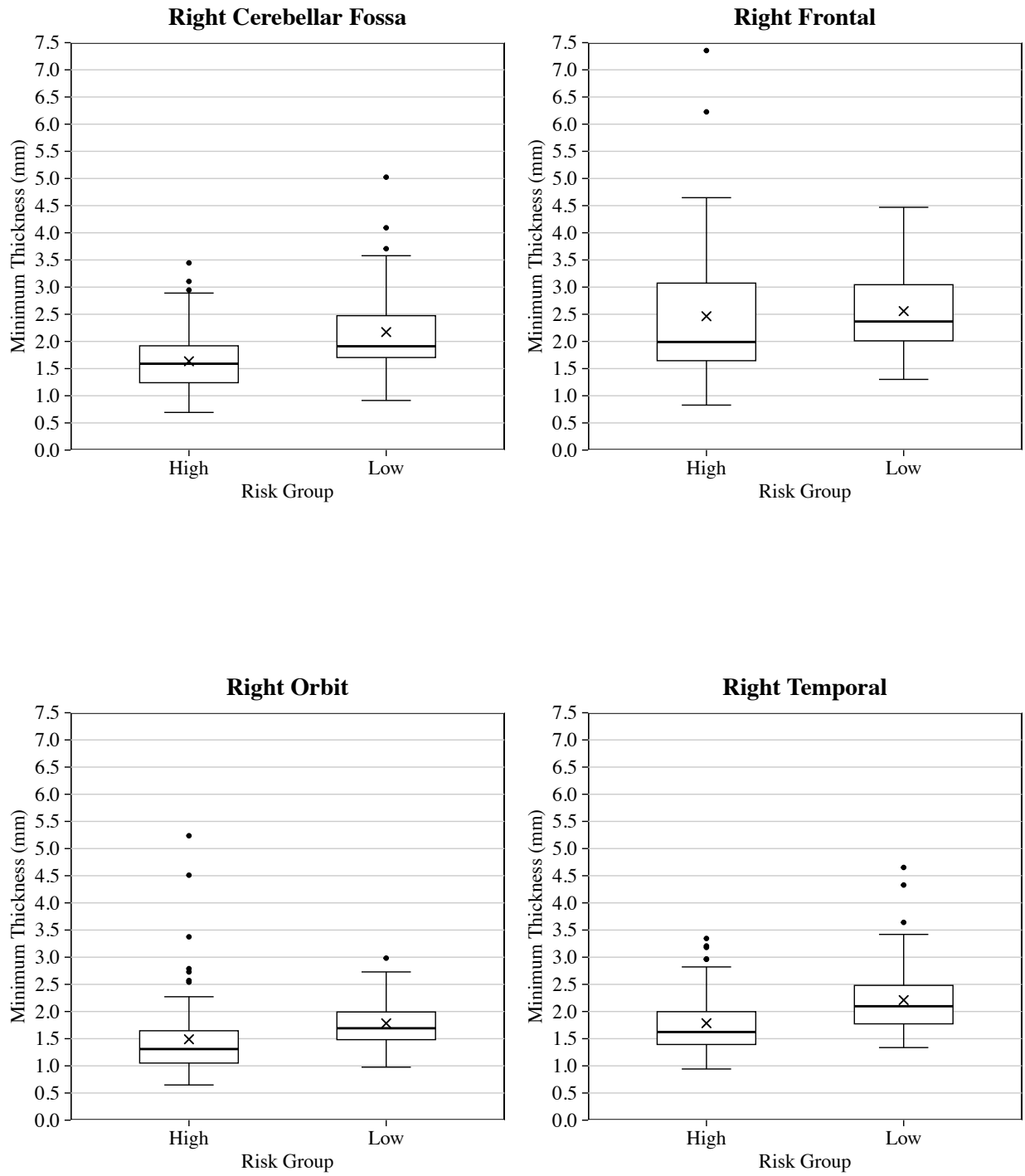


Figure 15 continued Range of minimum thickness by segment and risk group

Analysis of Covariance

Table 22 Results of Analysis of Covariances for minimum segment thickness controlling for decedent age and population affinity

Segment	Significance Level for the Difference in Minimum Segment Thickness	
	Controlling for Age	Controlling for Population Affinity
Left cerebellar fossa	<0.001	<0.001
Left frontal	0.417	0.369
Left orbit	0.007	0.005
Left temporal	<0.001	<0.001
Right cerebellar fossa	<0.001	<0.001
Right frontal	0.519	0.342
Right orbit	0.011	.005
Right temporal	<0.001	<0.001

Table 22 displays the p-values associated with the analysis of covariances controlling for decedent age and population affinity.

When the means of minimum segment thickness were adjusted for decedent age, individuals in the high-risk group still had significantly thinner crania when measured at the left and right cerebellar fossae, the left and right orbit, and the left and right temporal ($p < 0.05$). The difference in thickness at the left and right frontal remained non-significant ($p > 0.05$). The same pattern held true when the means of segment thickness were adjusted for decedent population affinity. Individuals in the high-risk group still had significantly thinner crania when measured at the left and right cerebellar fossa, the left and right orbit, and the left and right temporal ($p < 0.05$). The difference in thickness at the left and right frontal remained non-significant ($p > 0.05$).

Binary Logistic Regression

A binary logistic regression was performed to determine if a cutoff value for risk group membership by minimum thickness could be reliably established for each segment, i.e., could

minimum segment thickness correctly predict whether a decedent was high-risk or low-risk. A probability cutoff value of 0.5 was used to determine group membership.

Table 23 displays the percentage of cases correctly categorized into their respective group. In general, the high-risk group was more likely to be correctly classified as high-risk than the low-risk group was to be correctly classified as low-risk. The best agreement for the high-risk group was for the left frontal at 83.8%, while the worst was for the left orbit at 48.4%. The best agreement for the low-risk group was for the left temporal at 59.4%, while the worst agreement was at the left frontal at 17.4%. These results indicate that the calculated cutoff values are generally better than chance for correctly classifying an individual as a high-risk alcohol user, except at the left orbit, where classification is worse than chance alone.

Table 24 displays the 50th percentile cutoff value for minimum thickness, and the sensitivity, and positive predicted value of the model. Sensitivity measures the percentage of high-risk alcohol users the model correctly identified as being high-risk, whereas positive predictive value measures the percent of individuals the model identified as being high-risk who were actually high-risk. For example, for the left cerebellar segment, the model correctly identified 75.7% of all high-risk decedents as being high-risk, whereas among all the individuals the model identified as being high-risk, 62.9% were actually high-risk.

While the model was sensitive enough to correctly identify high-risk decedents about 75% of the time, it showed poor positive predictive value, indicating it over-identified decedents as being high-risk. This suggests that the 50th percentile value calculated by the model would erroneously classify too many individuals as high-risk for it to have real-world utility. Additionally, there are many causes of cranial thinning, and the prevalence of alcohol-induced cranial thinning within all cases of cranial thinning is not currently known.

Figures 16 through 23 display the predicted classification plots for each segment.

Table 23 Classification of risk group membership based on the 50th percentile value for minimum segment thickness

Segment	Observed	Predicted		Percent Correct
		High Risk	Low risk	
Left cerebellar fossa	High risk	56	18	75.7
	Low risk	33	36	52.2
	Overall Percentage			64.3
Left frontal	High risk	62	12	83.8
	Low risk	57	12	17.4
	Overall Percentage			51.7
Left orbit	High risk	58	16	78.4
	Low risk	37	32	46.4
	Overall Percentage			62.9
Left temporal	High risk	54	19	74.0
	Low risk	28	41	59.4
	Overall Percentage			66.9
Right cerebellar fossa	High risk	55	19	74.3
	Low risk	32	37	53.6
	Overall Percentage			64.3
Right frontal	High risk	58	16	78.4
	Low risk	56	13	18.8
	Overall Percentage			49.7
Right orbit	High risk	59	15	79.7
	Low risk	36	33	47.8
	Overall Percentage			64.3
Right temporal	High risk	56	18	75.7
	Low risk	32	37	53.6
	Overall Percentage			65.0

Table 24 Fiftieth percentile cranial thickness measurements, sensitivity, and positive predictive value of the model for each segment

Segment	50 th Percentile Cutoff Value in millimeters	Sensitivity	Positive Predictive Value
Left cerebellar fossa	1.984	75.7%	62.9%
Left frontal	3.490	83.8%	52.1%
Left orbit	1.875	78.4%	61.1%
Left temporal	2.023	74.0%	65.9%
Right cerebellar fossa	1.905	74.3%	63.2%
Right frontal	3.235	78.4%	50.9%
Right orbit	1.703	79.7%	62.1%
Right temporal	2.021	75.7%	63.6%

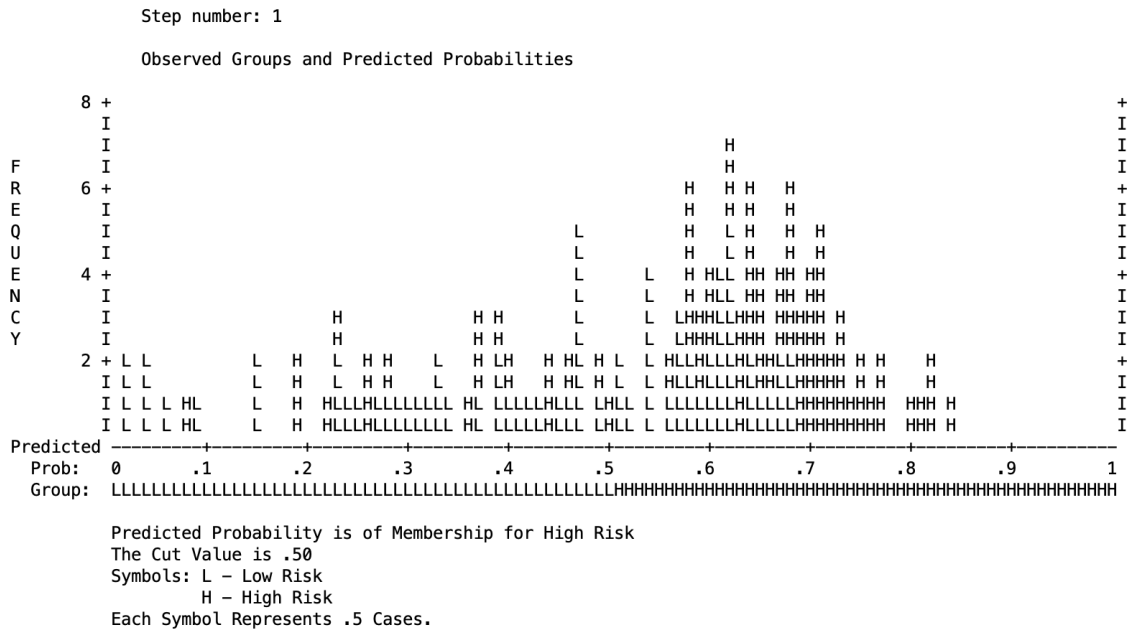


Figure 16 Predicted probability of group membership for the left cerebellar fossa

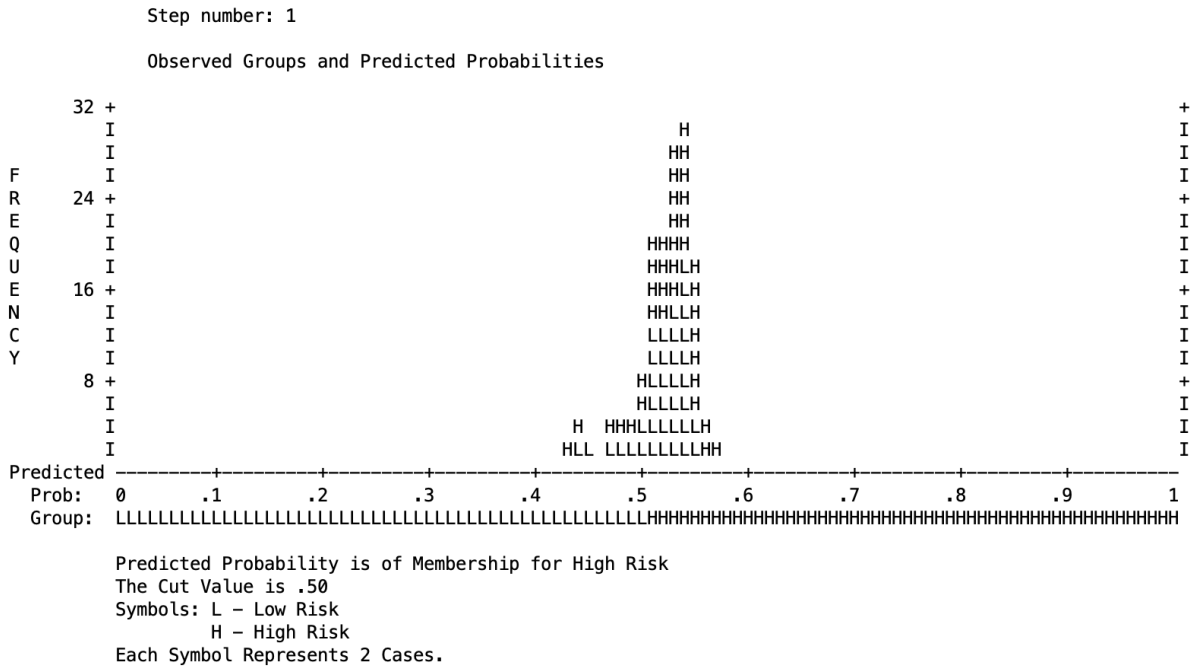


Figure 17 Predicted probability of group membership for the left frontal

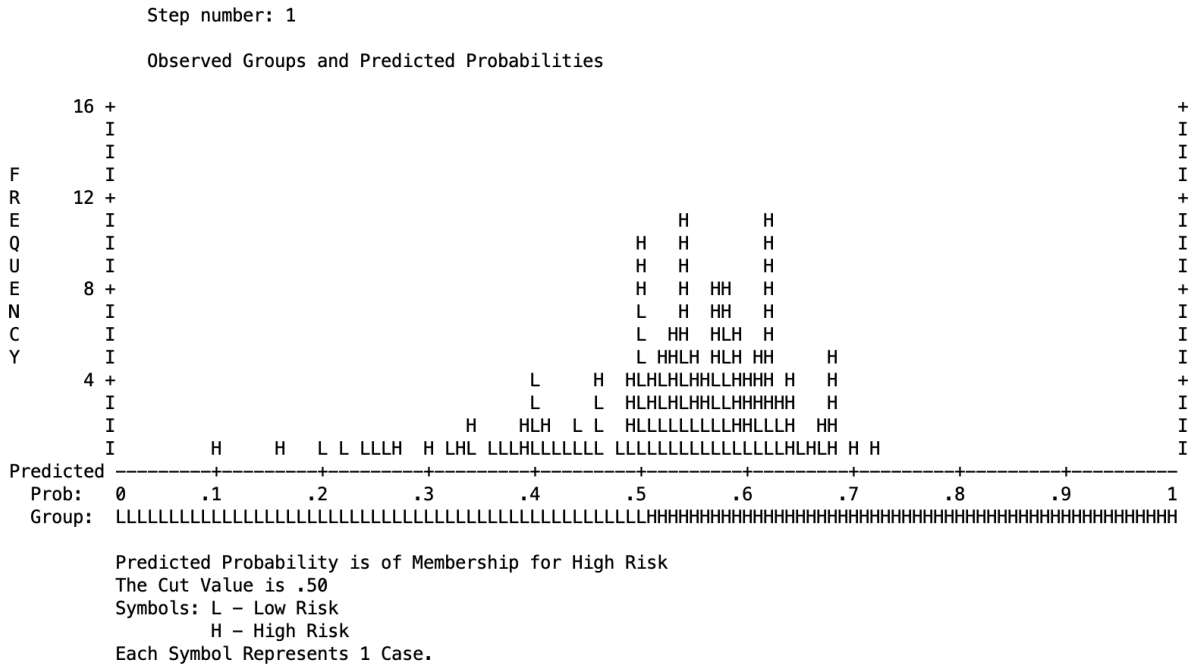


Figure 18 Predicted probability of group membership for the left orbit

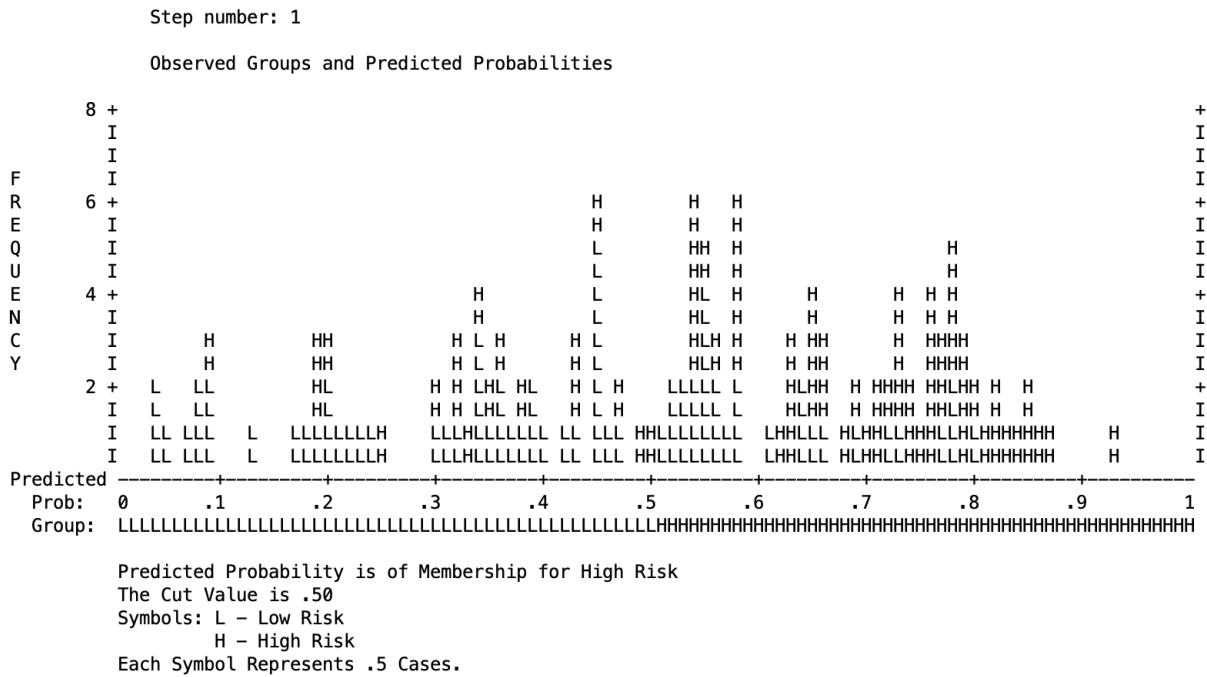


Figure 19 Predicted probability of group membership for the left temporal

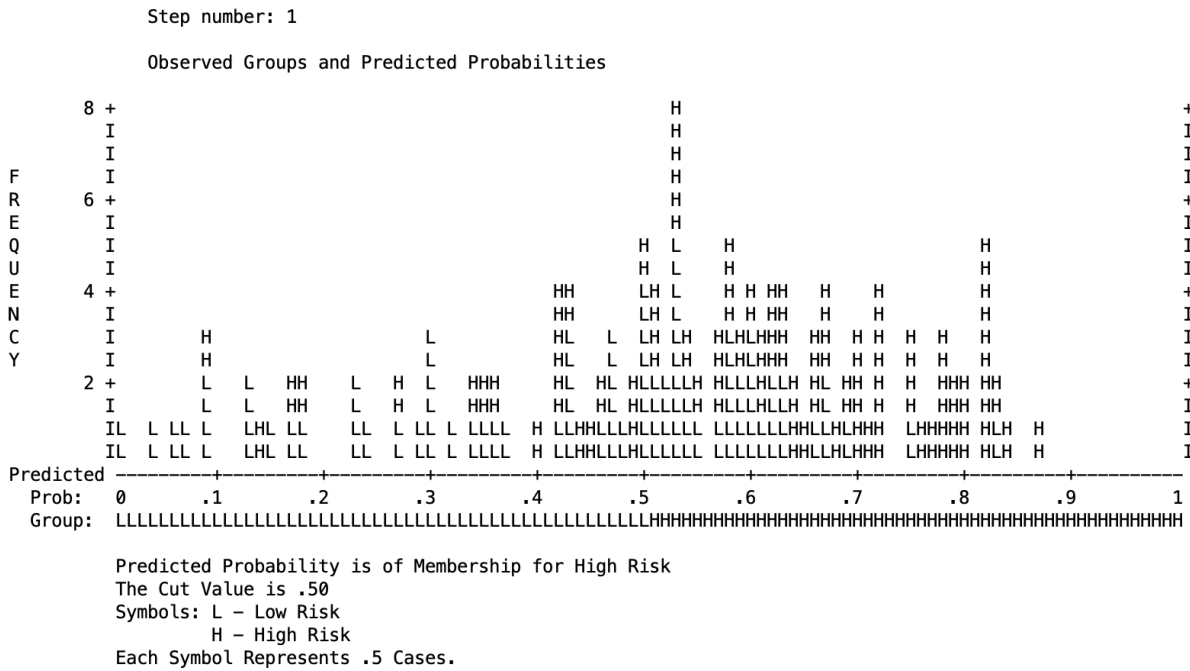


Figure 20 Predicted probability of group membership for the right cerebellar fossa

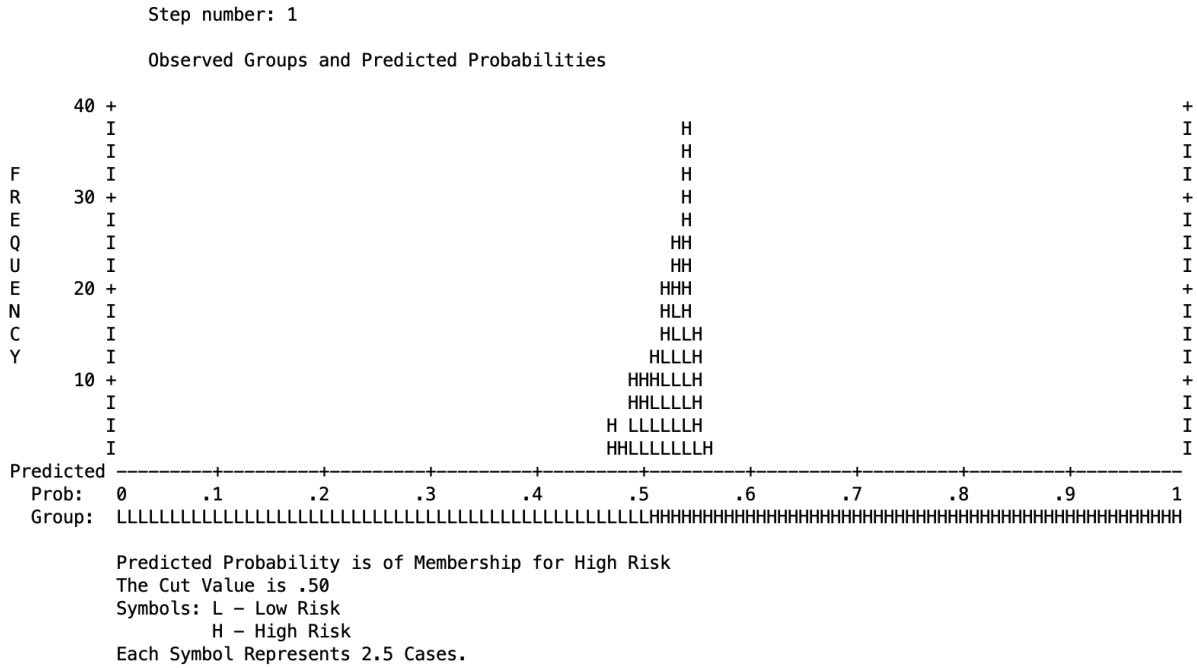


Figure 21 Predicted probability of group membership for the right frontal

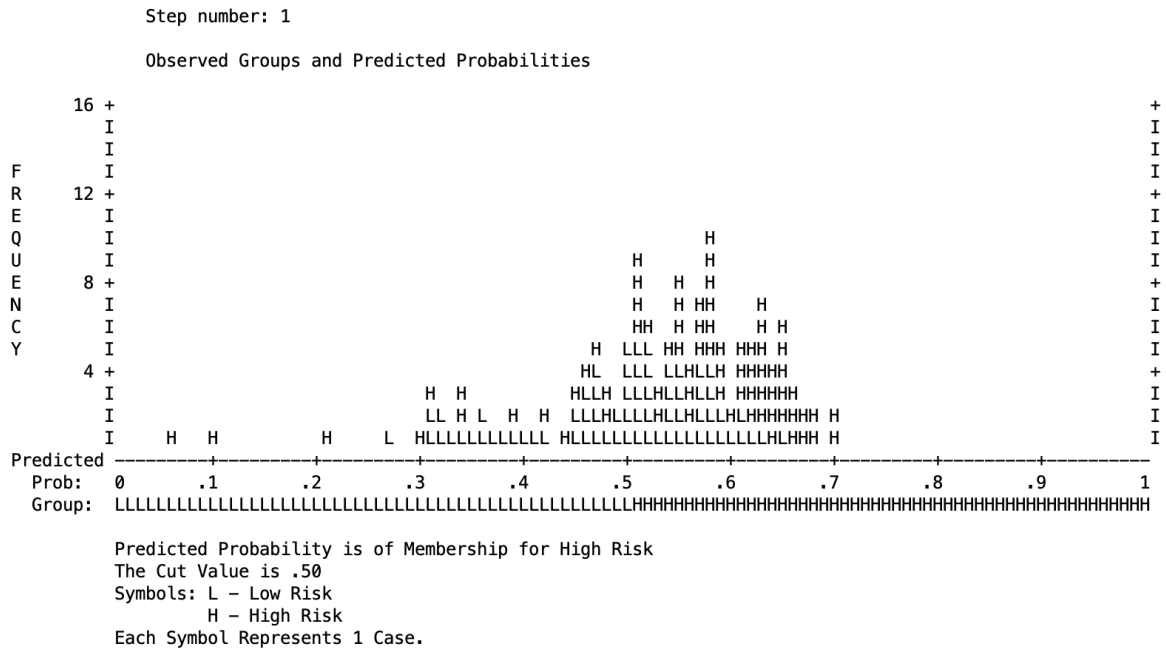


Figure 22 Predicted probability of group membership for the right orbit

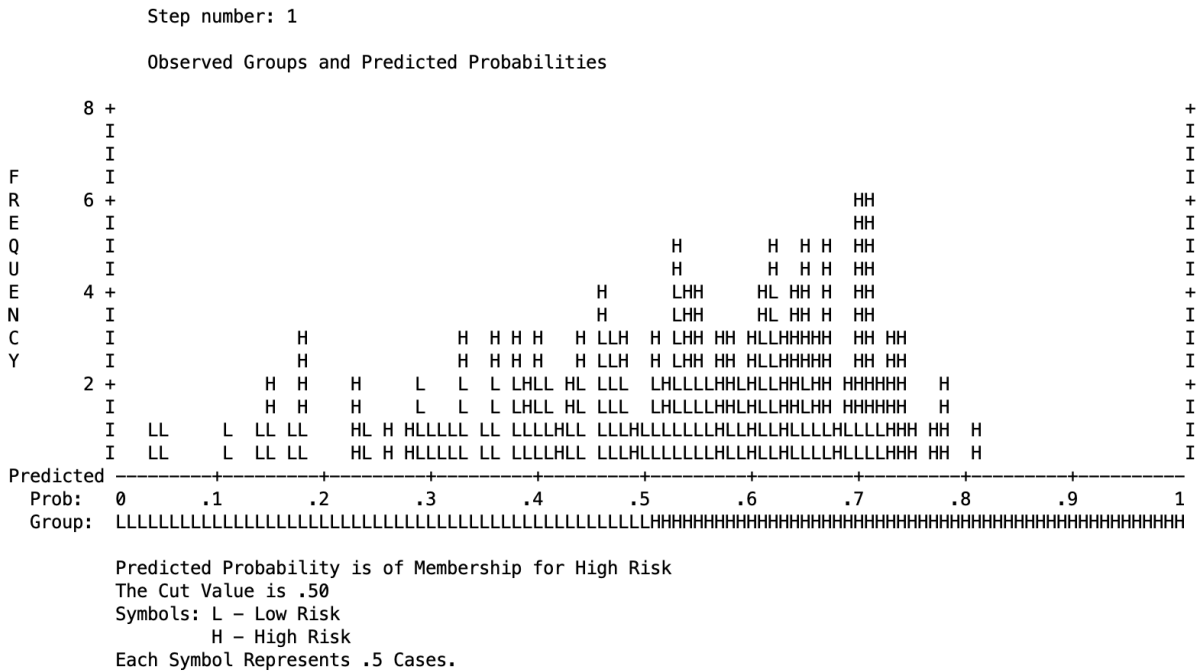


Figure 23 Predicted probability of group membership for the right temporal

Summary of Hypothesis One

These results give mixed support to the hypothesis that high-risk alcohol users have significantly thinner crania than low-risk alcohol users. Minimum cranial thickness in high-risk alcohol users is significantly thinner than in low-risk alcohol users when measured at the left and right cerebellar fossae, the left and right orbit, and the left and right temporal. The data does not support the hypothesis that high-risk alcohol users have significantly thinner crania when measured at the left and right lateral frontal. Analysis of Covariance was performed, controlling for decedent age and population affinity. Minimum segment thickness remained significant between the two risk groups when these factors were controlled for, indicating that the observed difference in segment thickness was related to alcohol use alone.

While a binary logistic regression was performed in an attempt to establish a cutoff value for minimum thickness, which would discriminate between high-risk and low-risk alcohol users,

the model was overly sensitive and had poor positive predictive values. Additionally, even if a reliable cutoff value were found, its efficacy would be limited since a myriad of conditions could account for cranial thinning, and our current lack of knowledge of what percent of cases of cranial thinning seen in the general population are caused by high-risk alcohol use.

Hypothesis Two: Cranial segment volume is significantly lower in high-risk alcohol users than in low-risk users

One-Tail T-Tests for Independent Samples

Table 25 Average minimum segment volume in millimeters cubed as well as between-group differences and one-tail p-values for each segment and risk group

Segment	Risk Group Mean \pm Standard Deviation		Low-Risk Minus High-Risk Volume in mm ³	One-tailed T- Test p-value
	High-Risk n=75	Low-Risk n=69		
Left cerebellar fossa	1,021.71 \pm 329.07	1,039.29 \pm 304.61	17.58	0.370
Left frontal	1,143.38 \pm 269.39	1,107.42 \pm 226.23	(35.96)	0.195
Left orbit	792.37 \pm 319.19	740.5 \pm 320.10	(51.83)	0.166
Left temporal	851.31 \pm 206.89	842.39 \pm 190.93	(8.92)	0.395
Right cerebellar fossa	1,015.71 \pm 298.36	1,042.75 \pm 303.32	27.04	0.295
Right frontal	1,094.18 \pm 264.94	1,040.66 \pm 211.39	(53.52)	0.092
Right orbit	785.85 \pm 325.42	741.82 \pm 324.66	(44.03)	0.210
Right temporal	839.76 \pm 208.91	839.21 \pm 218.01	(0.55)	0.494

Table 25 displays the mean and standard deviation of segment volume in millimeters cubed for each segment by risk group, as well as the difference between the low-risk and high-risk groups and p-values for the t-test for two independent means. Segment volume was paradoxically greater in the high-risk group for all segments but the left and right cerebellar fossae, however, none of these differences were statistically significant ($p > 0.05$).

Figure 24 displays the range volume for each segment by risk group. As shown, the means of risk group volume is very close for each segment, with substantial overlap in the range of values. Additionally, the range of volumes recorded for each segment varied widely, with only the right cerebellar fossa showing the hypothesized relationship between the two groups, i.e., that segment volume was greater in low-risk alcohol users than in high-risk alcohol users.

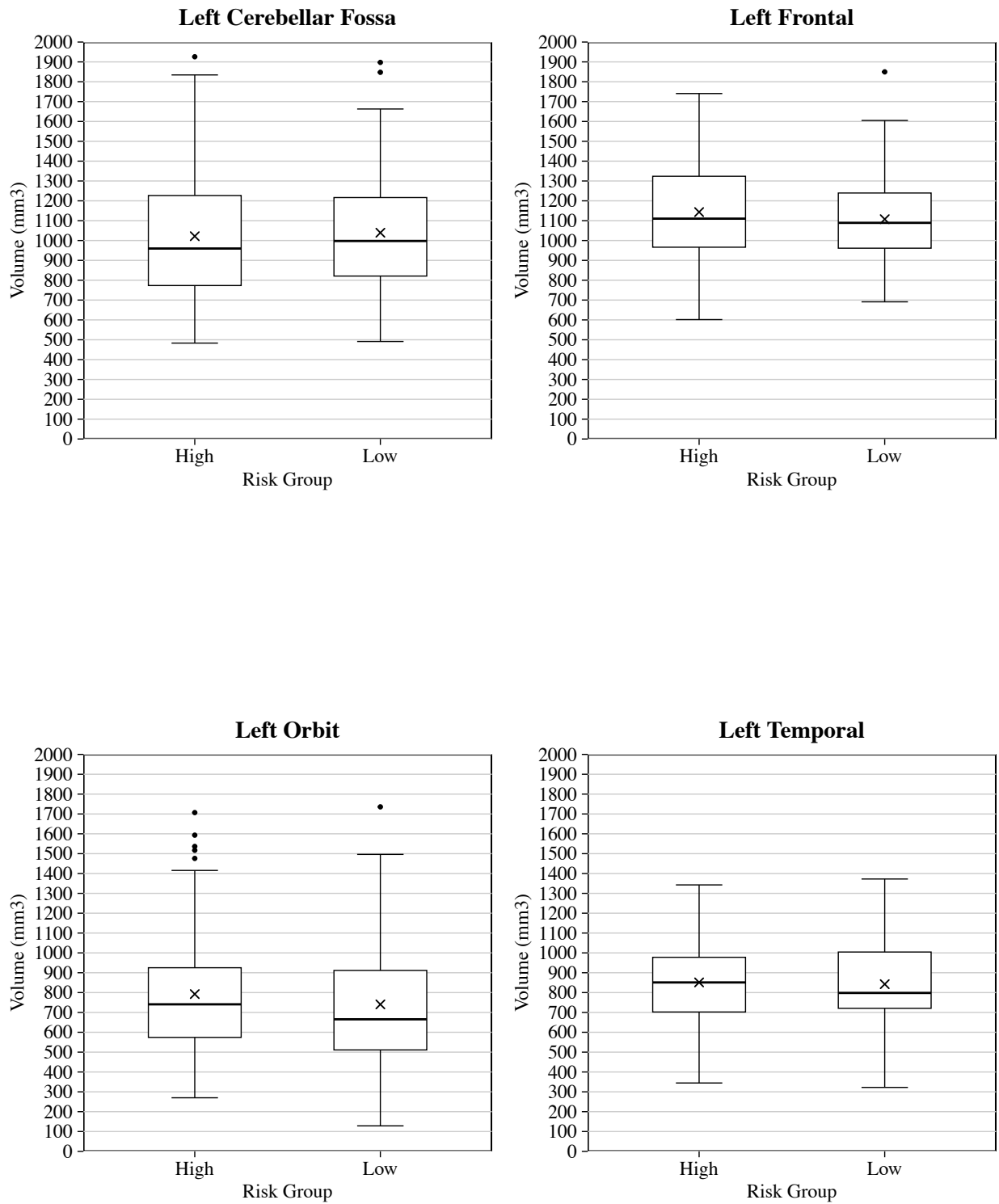


Figure 24 Range of segment volume by segment and risk group

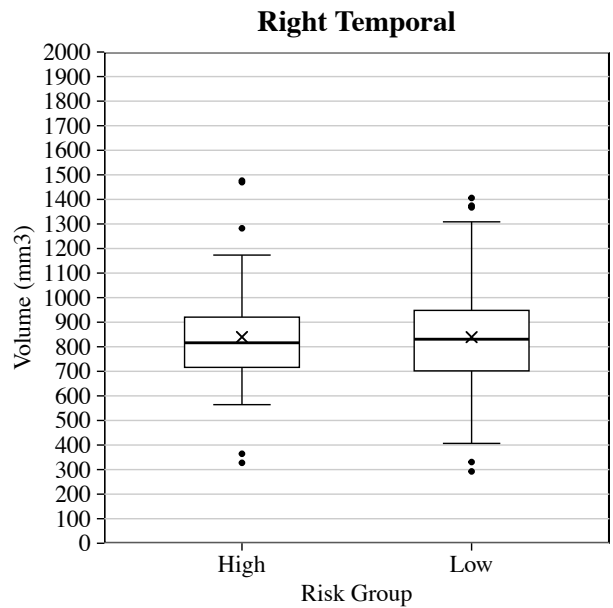
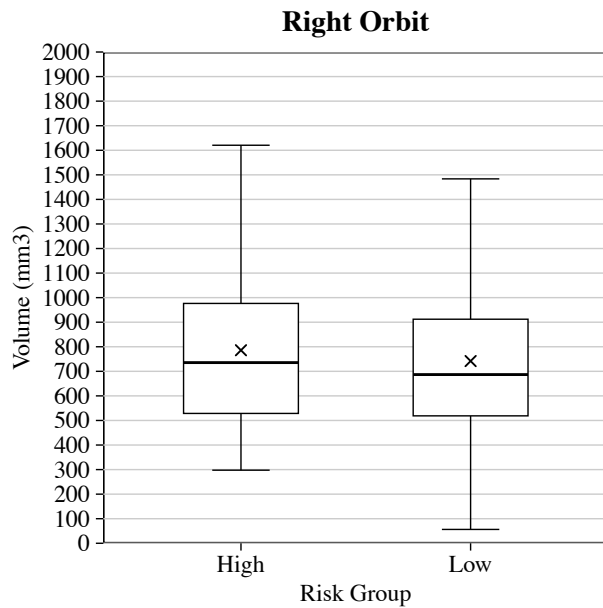
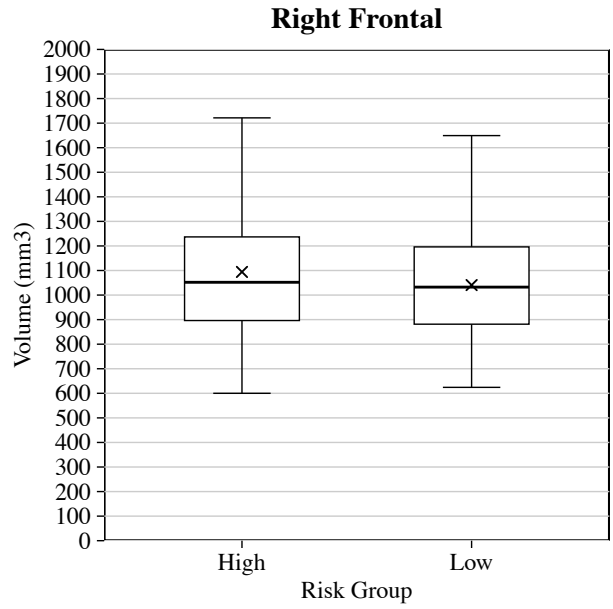
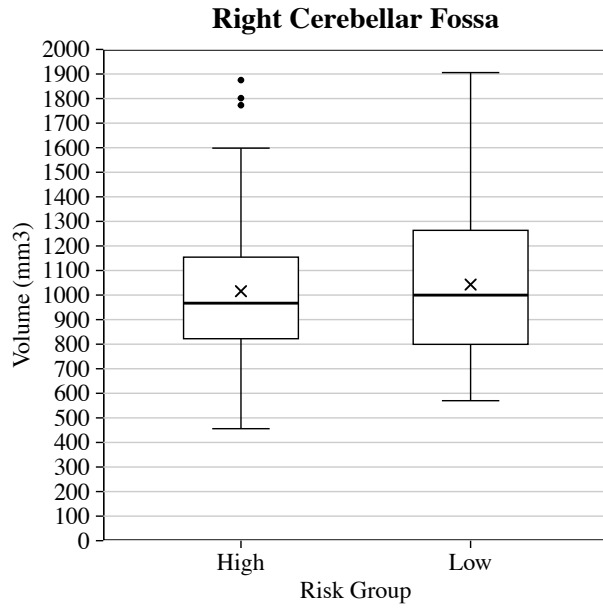


Figure 24 continued Range of segment volume by segment and risk group

Analysis of Covariance

Table 26 Results of Analysis of Covariances for segment volume controlling for decedent age and population affinity

Segment	Significance Level for the Difference in Segment Volume	
	Controlling for Age	Controlling for Population Affinity
Left cerebellar fossa	0.453	0.832
Left frontal	0.497	0.465
Left orbit	0.204	0.351
Left temporal	0.879	0.905
Right cerebellar fossa	0.414	0.648
Right frontal	0.208	0.248
Right orbit	0.242	0.411
Right temporal	0.987	0.890

Table 26 displays the p-values associated with the analysis of covariances controlling for decedent age and population affinity.

When the mean volume of each segment was adjusted for decedent age, differences in segment volume remained non-significant between the two risk groups. This indicates that age does not impact segment volume between the risk groups ($p > 0.05$).

When the mean volume of each segment was adjusted for decedent population affinity, differences in segment volume remained non-significant between the two risk groups. This indicates that population affinity does not significantly affect segment volume ($p > 0.05$).

Summary of Hypothesis Two

These results do not support the hypothesis that segment volume is lower in high-risk alcohol users compared to low-risk alcohol users. The fact that some cranial segments are significantly thinner in high-risk alcohol users with no change in overall segment volume could suggest that high-risk alcohol users have areas with compensatory thickening, resulting in similar segment volume to low-risk users.

Hypothesis 3a: Minimum Hounsfield units are lower in high-risk alcohol users than in low-risk alcohol users

One-Tail T-Tests for Independent Samples

Table 27 Average minimum Hounsfield units detected as well as between-group differences and one-tail p-values by segment and risk group

Segment	Risk Group Mean \pm Standard Deviation		Low-Risk Minus High-Risk Hounsfield Units	One-tailed T-Test p- value
	High-Risk n=75	Low-Risk n=69		
Left cerebellar fossa	-21.25 \pm 166.11	32.16 \pm 120.35	53.41	0.015
Left frontal	-65.99 \pm 210.82	-20.67 \pm 177.89	45.32	0.084
Left orbit	-40.4 \pm 160.66	29.51 \pm 153.64	69.91	0.004
Left temporal	40.12 \pm 266.48	121.04 \pm 207.56	80.92	0.023
Right cerebellar fossa	2.15 \pm 124.29	46.75 \pm 106.9	44.60	0.011
Right frontal	-97.55 \pm 202.03	2.45 \pm 168.59	100.10	<.001
Right orbit	-40.64 \pm 167.51	26.96 \pm 127.60	67.60	0.004
Right temporal	68.72 \pm 234.5	122.01 \pm 222.37	53.29	0.082

Table 27 displays the mean and standard deviation of the minimum Hounsfield units for each segment by risk group, as well as the difference between the low-risk and high-risk groups and p-values for the t-test for two independent means. The segment with the lowest average minimum Hounsfield units for the high-risk group was the right frontal at -97.55, while for the low-risk group, it was the left frontal at -20.67. The temporal segments of both groups had the highest average minimum Hounsfield units.

In support of Hypothesis 3a, minimum Hounsfield units for each segment, except the left frontal and right temporal, were significantly lower in the high-risk group compared to the low-risk group ($p < 0.05$).

Figure 25 displays the range for minimum Hounsfield units for each segment by risk group. The left and right frontals' non-significance can be appreciated due to the wide and overlapping spread of the data.

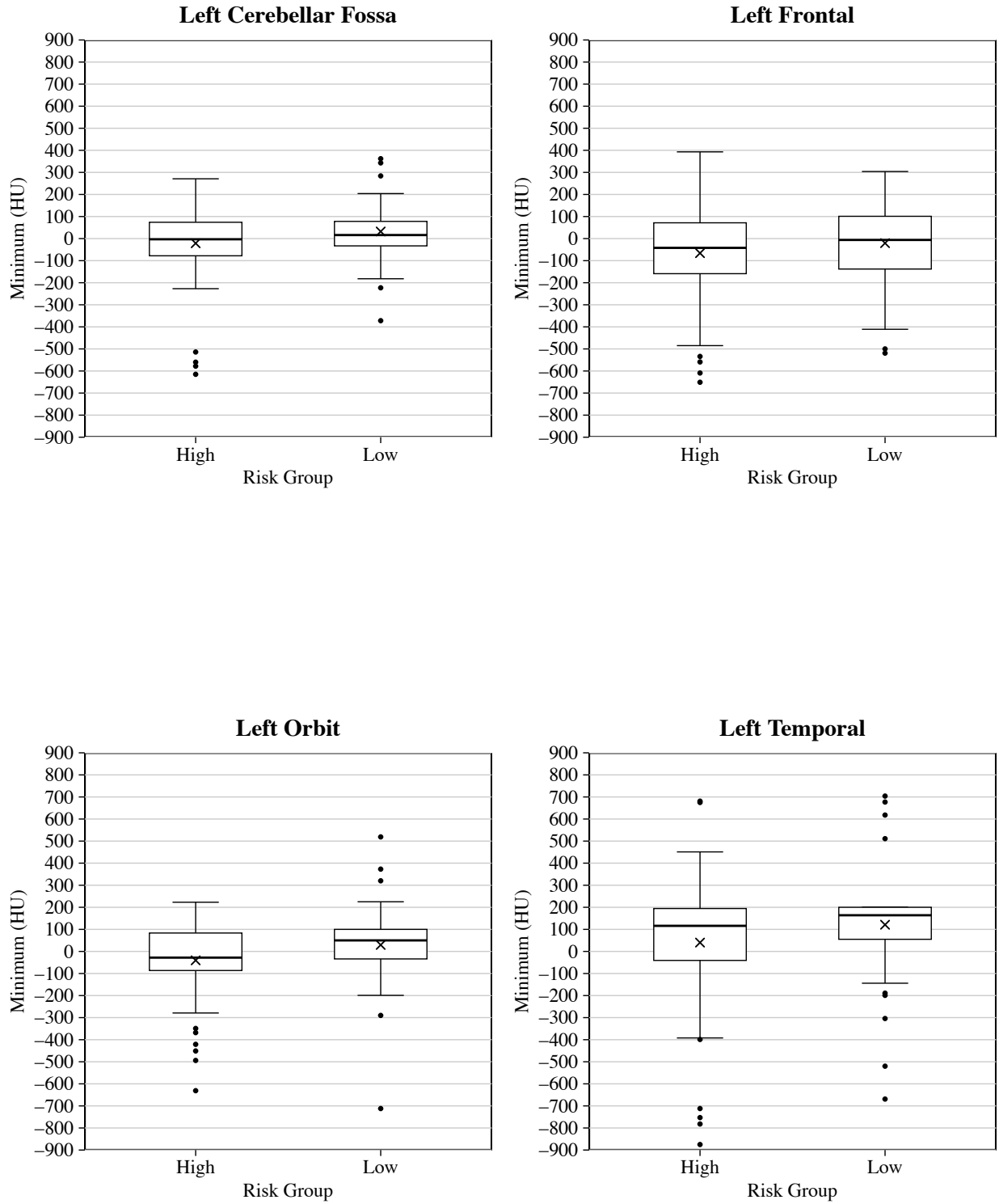


Figure 25 Range of minimum Hounsfield units by segment and risk group

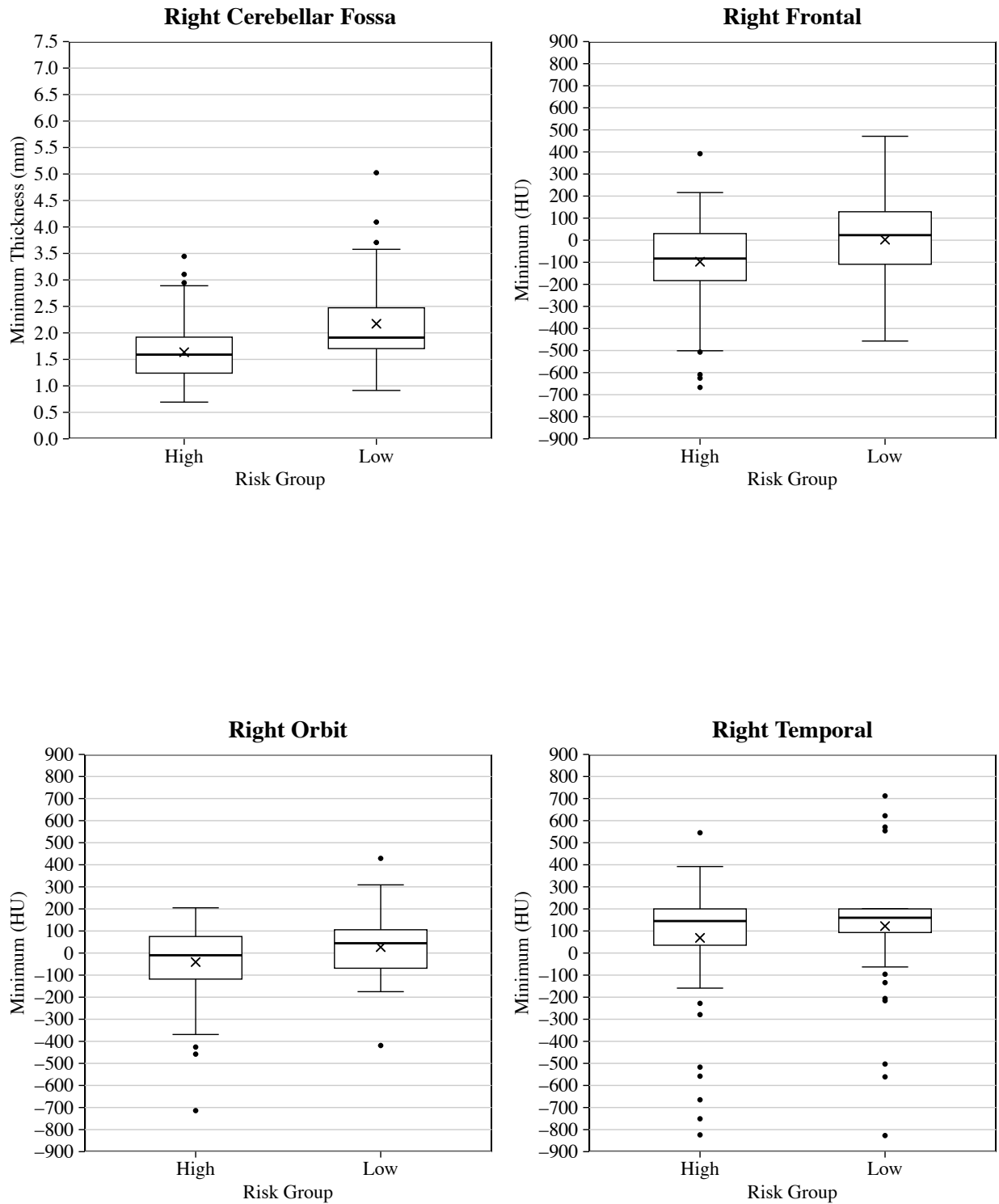


Figure 25 continued Range of minimum Hounsfield by segment and risk group

Analysis of Covariance

Table 28 Results of Analysis of Covariances for minimum Hounsfield units controlling for decedent age and population affinity

Segment	Significance Level for the Difference in Minimum Hounsfield Units	
	Controlling for Age	Controlling for Population Affinity
Left cerebellar fossa	0.052	0.023
Left frontal	0.208	0.209
Left orbit	0.007	0.010
Left temporal	0.050	0.068
Right cerebellar fossa	0.026	0.025
Right frontal	<.001	0.002
Right orbit	0.006	0.008
Right temporal	0.149	0.199

Table 28 displays the p-values associated with the analysis of covariances controlling for decedent age and population affinity.

When minimum Hounsfield units of each segment were adjusted for decedent age, the difference between the two risk groups became non-significant in the left cerebellar fossa and left temporal ($p > 0.05$). This indicates that age significantly impacts the difference in minimum Hounsfield units between the groups for these two segments. The remaining segments retained their prior levels of significance. This indicates that age does not significantly impact the difference in minimum Hounsfield units between the two groups for these segments.

When the minimum Hounsfield units of each segment were adjusted for decedent population affinity, the difference between the two groups became non-significant at the left temporal ($p > 0.05$). This indicates that population affinity significantly impacts the difference in minimum Hounsfield units between the two groups for this segment. The remaining segments had no change in their significance, indicating that population affinity does not significantly impact the difference in minimum Hounsfield units between the two groups.

Summary of Hypothesis 3a

These findings give mixed support to Hypothesis 3a and suggest that, overall, high-risk alcohol users have areas of significantly less radiodensity in the left and right cerebellar fossa, the right frontal, the left and right orbits, and the left temporal. However, when age is accounted for, the significance between the two groups disappears for the left cerebellar fossa and left temporal. Likewise, the significance disappears in the left temporal when decedent population affinity is accounted for. These changes suggest that decedent age and population affinity can affect the minimum Hounsfield units measured in high-risk decedents.

Hypothesis 3b: Maximum Hounsfield units are greater in high-risk users than in low-risk users

One-Tail T-Tests for Independent Samples

Table 29 Average maximum Hounsfield units detected, between-group differences, and one-tail p-values by segment and risk group

Segment	Risk Group Mean \pm Standard Deviation		Low-Risk Minus High-Risk Hounsfield Units	One-tailed T- Test p-value
	High-Risk n=75	Low-Risk n=69		
Left cerebellar fossa	1,819.87 \pm 115.06	1,783.7 \pm 98.73	(36.17)	0.023*
Left frontal	2,019.32 \pm 160.97	2,006.09 \pm 120.19	(13.23)	0.290
Left orbit	1,907.17 \pm 197.61	1,875.43 \pm 132.74	(31.74)	0.132
Left temporal	2,144.07 \pm 156.25	2,122.06 \pm 135.21	(22.01)	0.185
Right cerebellar fossa	1,814.07 \pm 115.64	1,778.94 \pm 86.39	(35.13)	0.021*
Right frontal	1,992.21 \pm 145.31	2,003.3 \pm 140.72	11.09	0.321
Right orbit	1,891.51 \pm 184.75	1,851.41 \pm 143.55	(40.10)	0.076
Right temporal	2,146.13 \pm 150.16	2,119.19 \pm 145.49	(26.94)	0.138

Table 29 displays the mean and standard deviation of the maximum Hounsfield units for each segment by risk group, as well as the difference between the low-risk and high-risk groups and p-values for the t-test for two independent means. Each segment of the high-risk group, except for the right frontal, achieved greater maximum Hounsfield units than their counterparts in the low-risk group. The left and right temporals in both groups achieved the highest maximum Hounsfield units, while the left and right cerebellar fossae achieved the lowest for both groups. However, between-group differences were only statistically significant for the left and right cerebellar fossae ($p < 0.05$).

Figure 26 displays the range of maximum Hounsfield units for each segment by risk group. For all segments except the right frontal, the maximum recorded Hounsfield unit was higher in the high-risk group than in the low-risk group.

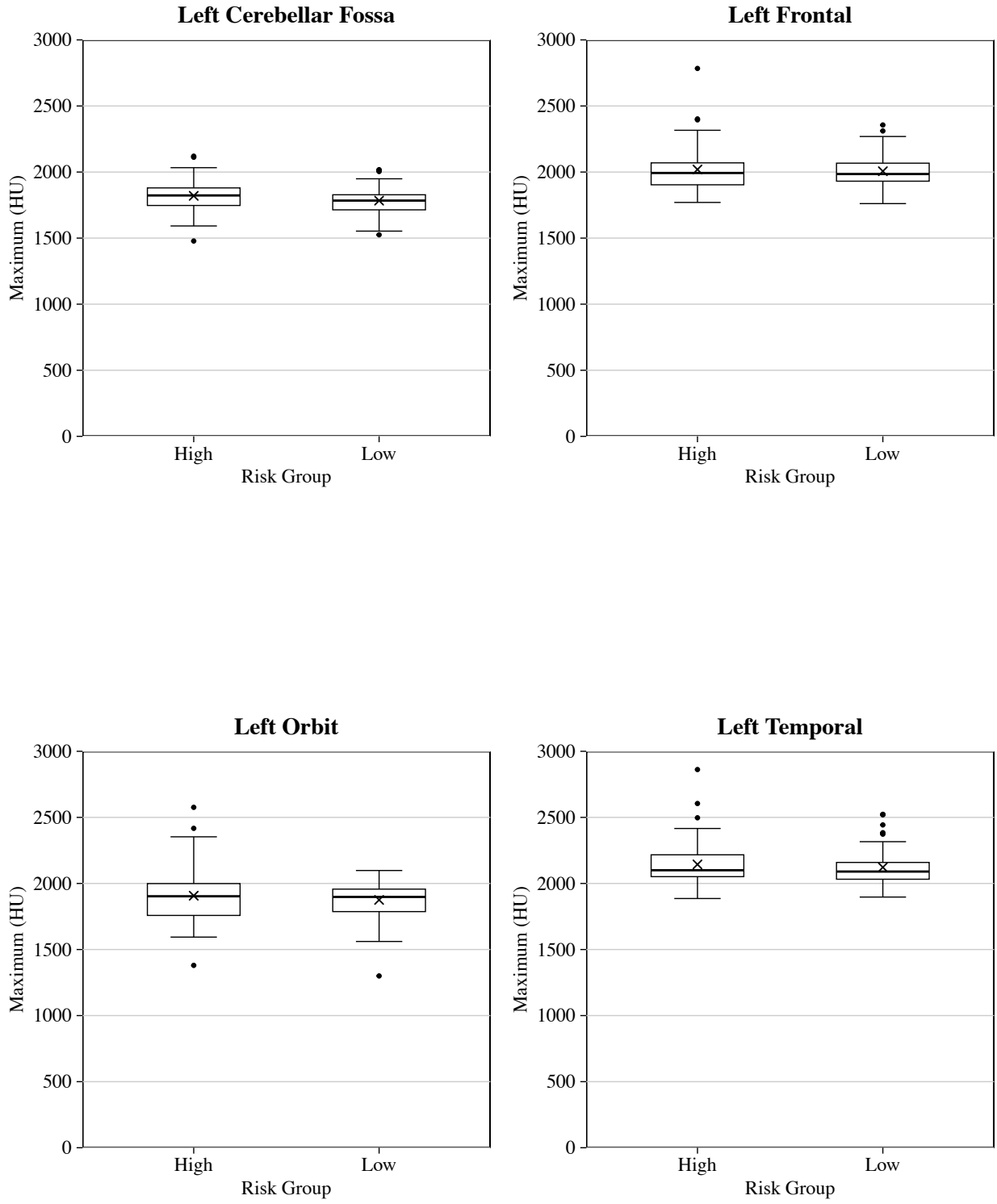


Figure 26 Range of maximum Hounsfield units by segment and risk group

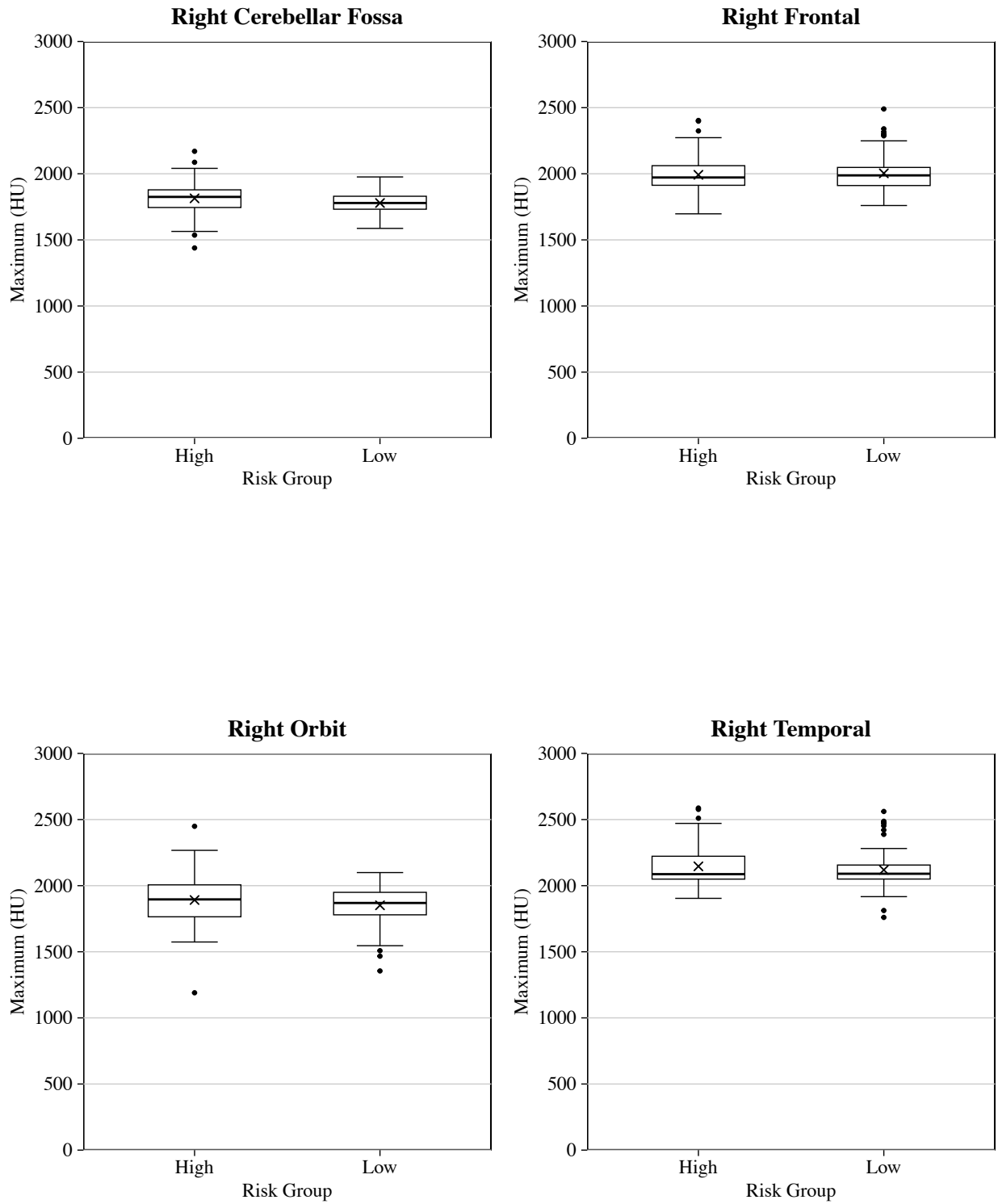


Figure 26 continued Range of maximum Hounsfield units by segment and risk group

Analysis of Covariance

Table 30 Results of Analysis of Covariances for maximum Hounsfield units controlling for decedent age and population affinity

Segment	Significance Level for the Difference in Maximum Hounsfield Units	
	Controlling for Age	Controlling for Population Affinity
Left cerebellar fossa	0.084	0.042
Left frontal	0.504	0.527
Left orbit	0.267	0.242
Left temporal	0.308	0.376
Right cerebellar fossa	0.072	0.030
Right frontal	0.726	0.724
Right orbit	0.132	0.121
Right temporal	0.214	0.253

Table 30 displays the p-values associated with the analysis of covariances controlling for decedent age and population affinity.

When maximum Hounsfield units of each segment were adjusted for decedent age, the difference between the risk groups became non-significant in the left and right cerebellar fossa ($p > 0.05$). This indicates that for these two segments, age significantly impacts the difference in maximum Hounsfield units between the groups. The remaining segments stayed non-significant, suggesting that age does not significantly affect the difference in minimum Hounsfield units between the two groups for these segments ($p > 0.05$).

When the maximum Hounsfield units of each segment were adjusted for decedent population affinity, the differences between the groups had no change in their respective significance, indicating that population affinity does not significantly impact the difference in maximum Hounsfield units between the two groups.

Summary of Hypothesis 3b

These findings suggest that even though the high-risk alcohol users have areas that are significantly less radiodense than the low-risk group, they also have areas that are more radiodense than the low-risk group.

Hypothesis 3c: Mean Hounsfield units are greater among high-risk alcohol users than low-risk alcohol users

One-Tail T-Tests for Independent Samples

Table 31 Average mean Hounsfield units detected as well as between-group differences and one-tail p-values by segment and risk group

Segment	Risk Group Mean ± Standard Deviation		Low-Risk Minus High-Risk Hounsfield Units	One-tailed T-Test p-value
	High-Risk n=75	Low-Risk n=69		
Left cerebellar fossa	926.1 ± 135.82	947.66 ± 156.47	21.56	0.189
Left frontal	1,048.34 ± 166.21	1,112.46 ± 134.80	64.12	0.006*
Left orbit	819.46 ± 158.47	810.66 ± 163.02	(8.80)	0.372
Left temporal	1,181.59 ± 128.19	1,193.82 ± 128.89	12.23	0.285
Right cerebellar fossa	953.4 ± 140.31	963.01 ± 147.53	9.61	0.345
Right frontal	1,049.33 ± 157.10	1,103.74 ± 137.81	54.41	0.015*
Right orbit	802.35 ± 142.03	786.72 ± 148.95	(15.63)	0.261
Right temporal	1,177.05 ± 134.23	1,197.99 ± 137.11	20.94	0.178

Table 31 displays the mean and standard deviation of the mean Hounsfield units for each segment by risk group, as well as the difference between the low-risk and high-risk groups and p-values for the t-test for two independent means. The mean Hounsfield units for the left and right cerebellar fossae, the left and right frontals, and the left and right temporals were all greater in the low-risk group compared to the high-risk group. The left and right temporals had the highest mean for each group, while the left and right orbits had the lowest. Between-group differences were only significant for the left and right temporals ($p < 0.05$).

Figure 27 displays the range of mean Hounsfield units for each segment by risk group. The left orbit saw the greatest spread of mean values for both groups, while the right temporal saw the closest grouping of values.

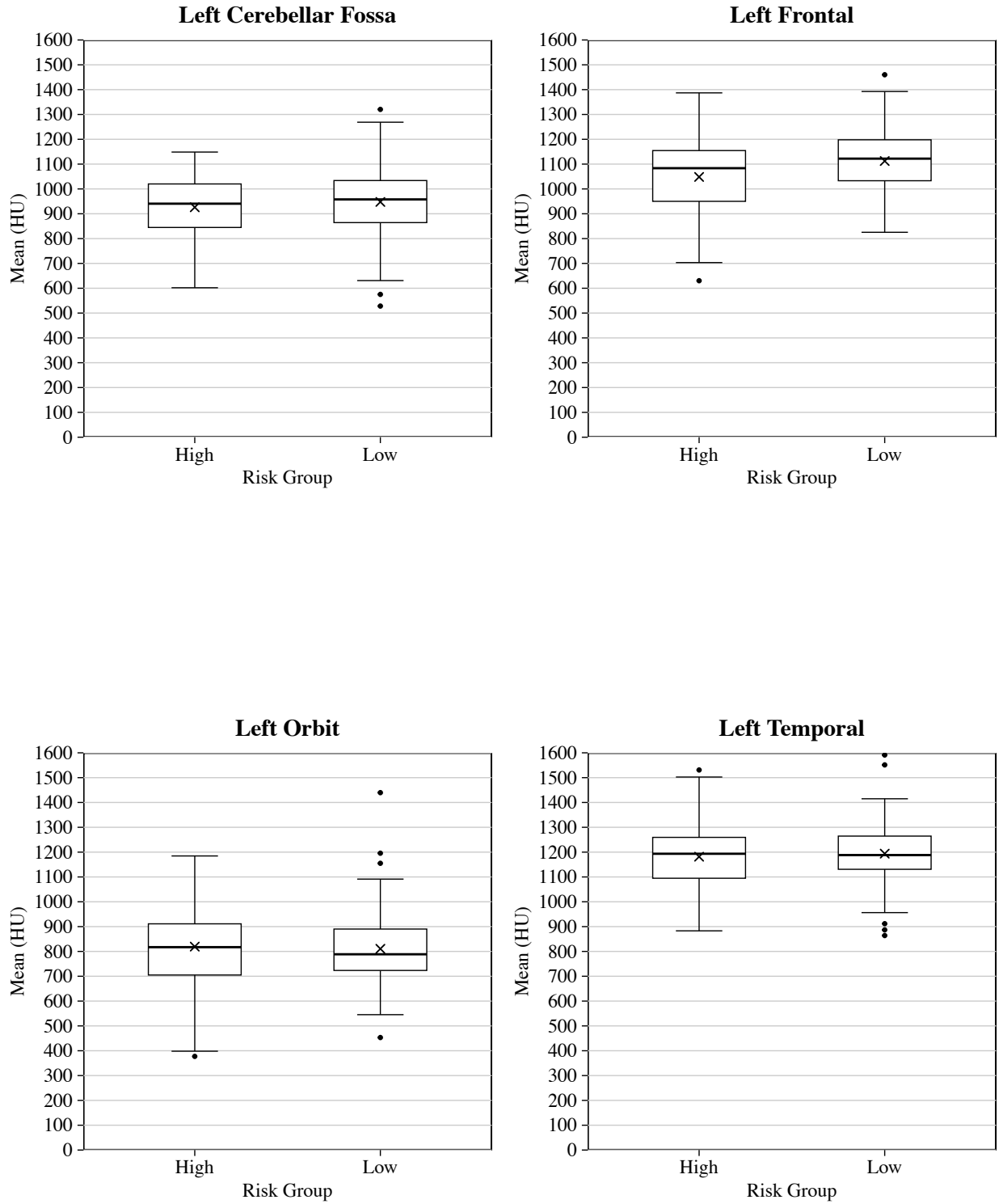


Figure 27 Range of mean Hounsfield units by segment and risk group

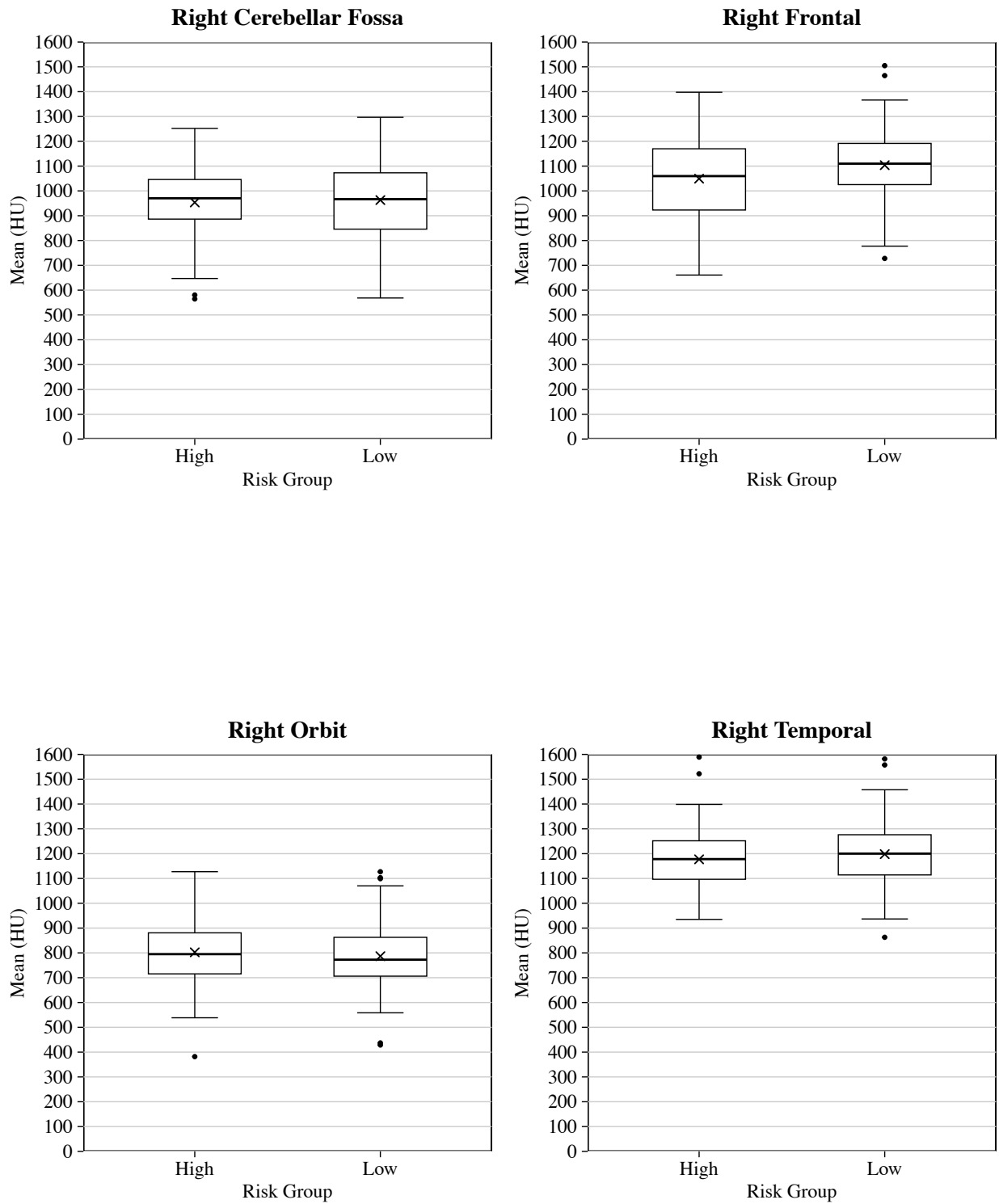


Figure 27 continued Range of mean Hounsfield units by segment and risk group

Analysis of Covariance

Table 32 Results of Analysis of Covariances for mean Hounsfield units controlling for decedent age and population affinity

Segment	Significance Level for the Difference in Mean Hounsfield Units	
	Controlling for Age	Controlling for Population Affinity
Left cerebellar fossa	0.029	0.483
Left frontal	0.020	0.019
Left orbit	0.650	0.658
Left temporal	0.530	0.663
Right cerebellar fossa	0.438	0.862
Right frontal	0.039	0.045
Right orbit	0.394	0.429
Right temporal	0.350	0.426

Table 32 displays the p-values associated with the analysis of covariances controlling for decedent age and population affinity.

When the mean Hounsfield units of each segment were adjusted for decedent age, the difference between the two risk groups became significant in the left orbit ($p < 0.05$). This indicates that age significantly impacts the difference in maximum Hounsfield units between the groups for this segment. The remaining segments retained their respective significance, indicating that age does not significantly impact the difference in mean Hounsfield units between the two groups for these segments.

When the mean Hounsfield units of each segment were adjusted for decedent population affinity, the differences between the groups had no change in their respective significance, indicating that population affinity does not significantly impact the difference in mean Hounsfield units between the two groups.

Pearson's Correlation Coefficients

Table 33 Pearson's correlation coefficients between minimum segment thickness and mean Hounsfield units

Segment	Minimum Segment Thickness and Mean Hounsfield	
	High-Risk	Low-Risk
Left cerebellar fossa	.377**	.423**
Left frontal	-.386**	-.166
Left orbit	-.094	.048
Left temporal	-.105	-.145
Right cerebellar fossa	.455**	.478**
Right frontal	-.445**	-.210
Right orbit	-.054	-0.25
Right temporal	-.164	-.202

Note: $p < 0.001$ **

Table 33 displays the two-tailed Pearson's correlation coefficients between minimum segment thickness and mean Hounsfield units. For minimum segment thickness and mean Hounsfield units, the left and right cerebellar fossae demonstrated significant weak to moderate positive correlation between the variables in both the high-risk and low-risk groups, i.e., as segment thickness increases, mean Hounsfield units increase ($p < 0.001$). Conversely, the left and right frontal segments have a significant weak to moderate negative correlation between these variables, i.e., as segment thickness increases, mean Hounsfield units decrease ($p < 0.001$). While these results initially appear to be at odds with one another, these findings become logical when the general anatomic makeup of the segments is considered. The basal region of the occiput is comprised of primarily dense cortical bone, so as this area increases in thickness, more cortical bone is deposited, increasing radiodensity. The lateral frontal region, on the other hand, has more diploic bone, so as this segment increases in thickness, the more trabecular and air cells are present, lowering the mean density (Boruah et al., 2015).

Table 34 Pearson's correlation coefficients for segment volume and mean Hounsfield units

Segment	Mean Hounsfield	
	High	Low
Left cerebellar fossa	.548**	.577**
Left frontal	-.386**	-.324
Left orbit	.069	.015
Left temporal	-.175	-.132
Right cerebellar fossa	.594**	.593**
Right frontal	-.388*	-.387*
Right orbit	.169	.164
Right temporal	-.150	-.323

Note: $p < 0.007^*$, $p < 0.001^{**}$

Table 34 displays the Pearson's correlation coefficients for segment volume and mean Hounsfield units. As with minimum segment thickness and mean Hounsfield units, segment volume and mean Hounsfield units exhibited a significant moderate positive correlation in both risk groups' left and right cerebellar fossae ($p < 0.001$). Similarly, the left and right frontal exhibited a weak negative correlation between these two variables. For the left frontal, the correlation was only significant in the high-risk group ($p < 0.001$). For the right frontal, the correlation was significant in both risk groups ($p < 0.007$).

Summary of Hypothesis 3c

These findings do not support hypothesis 3c and, contrary to the hypothesis, suggest that high-risk segments tend to be less radiodense than low-risk segments. Though only significantly so the temporals. However, when decedent age is accounted for, the difference between the two risk groups becomes significant in the left orbit as well. This suggests that age may affect mean Hounsfield units. Results of the Pearson's correlation coefficients demonstrate that different cranial segments have different proportions of cortical and trabecular bone.

Hypothesis 3d: Median Hounsfield units are greater in high-risk alcohol users than in low-risk alcohol users

One-Tail T-Tests for Independent Samples

Table 35 Average median Hounsfield units detected as well as between-group differences and one-tail p-values by segment and risk group

Segment	Risk Group Mean ± Standard Deviation		Low-Risk Minus High-Risk in Hounsfield Units	Sig.
	High-Risk n=75	Low-Risk n=69		
Left cerebellar fossa	971.95 ± 193.29	1,006.91 ± 217	34.96	0.154
Left frontal	1,088.27 ± 221.29	1,177.16 ± 178.41	88.89	0.005*
Left orbit	778.24 ± 195.43	764.65 ± 199.71	(13.59)	0.340
Left temporal	1,252.93 ± 174.27	1,272.29 ± 171.17	19.36	0.252
Right cerebellar fossa	1,007.57 ± 198.09	1,027.35 ± 208.61	19.78	0.280
Right frontal	1,101.43 ± 210.36	1,164.97 ± 176.79	63.54	0.026*
Right orbit	754.68 ± 164.71	739.68 ± 188.24	(15.00)	0.306
Right temporal	1,243.29 ± 180.89	1,284.1 ± 177.38	40.81	0.087

Table 35 displays the mean and standard deviation of the median Hounsfield units for each segment by risk group, as well as the difference between the low-risk and high-risk groups. Median Hounsfield units are greater in the low-risk group than in the high-risk group for all segments except the left and right orbits. However, the differences between the two groups are only significant for the left and right frontal ($p < 0.05$).

Figure 28 displays the range of median Hounsfield units for each segment by risk group.

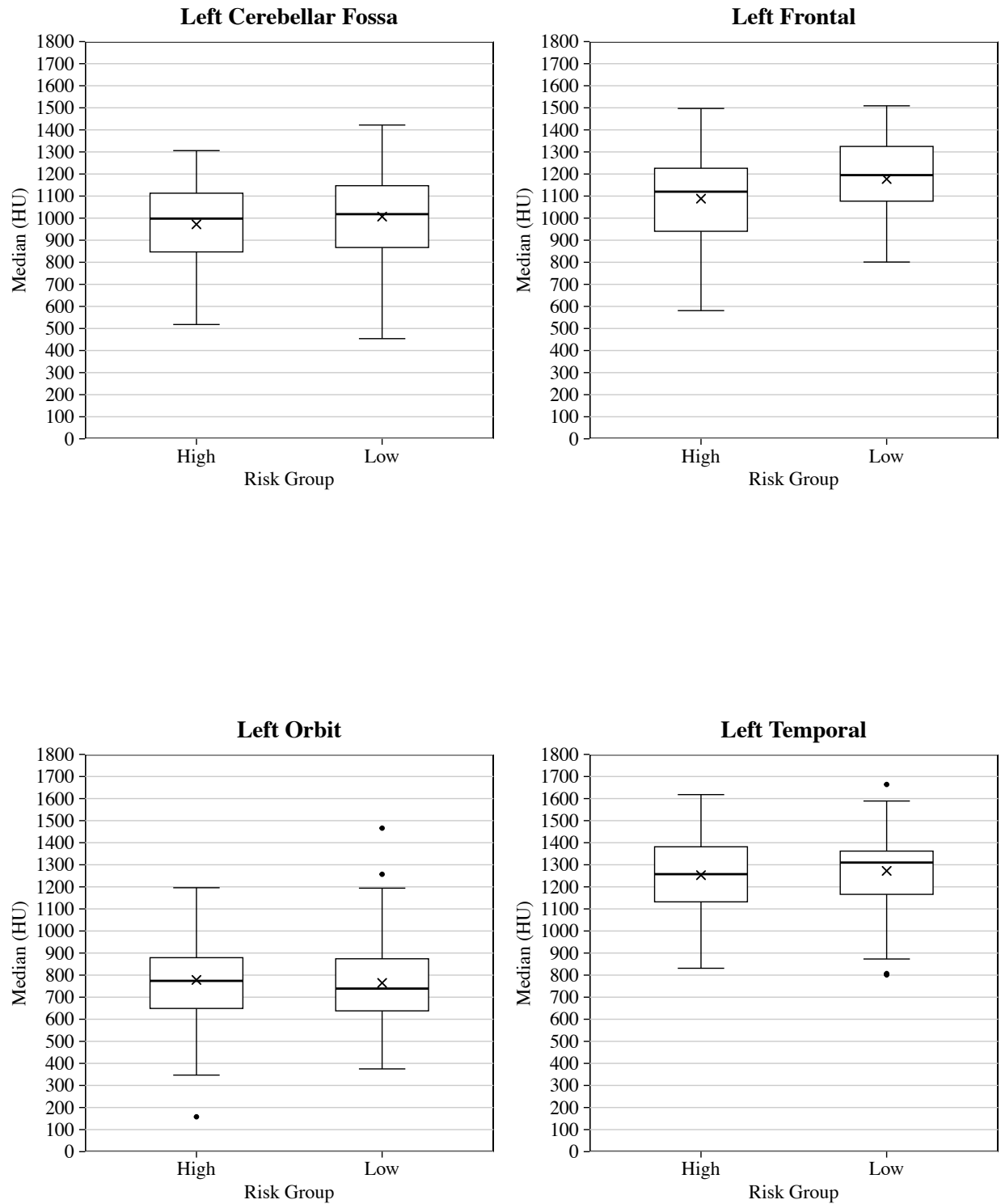


Figure 28 Range of median Hounsfield units by segment and risk group

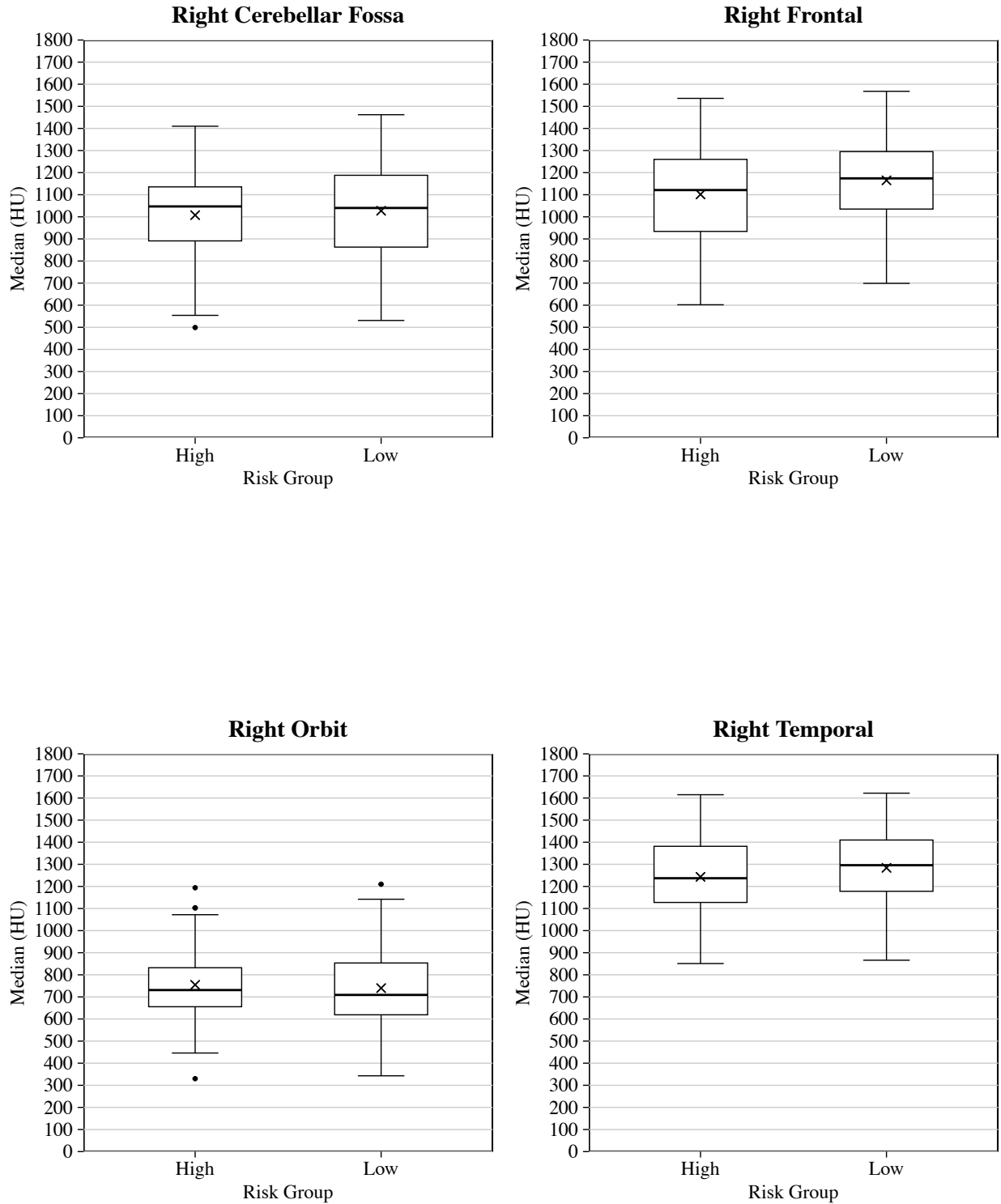


Figure 28 continued Range of median Hounsfield units by segment and risk group

Analysis of Covariance

Table 36 Results of Analysis of Covariances for median Hounsfield units controlling for decedent age and population affinity

Segment	Significance Level for the Difference in Median Hounsfield Units	
	Controlling for Age	Controlling for Population Affinity
Left cerebellar fossa	0.168	0.402
Left frontal	0.016	0.014
Left orbit	0.582	0.597
Left temporal	0.457	0.632
Right cerebellar fossa	0.338	0.732
Right frontal	0.068	0.083
Right orbit	0.455	0.508
Right temporal	0.169	0.266

Table 36 displays the p-values associated with the analysis of covariances controlling for decedent age and population affinity.

When the median Hounsfield units of each segment were adjusted for decedent age, the right frontal became non-significant ($p > 0.05$). This suggests that age significantly impacted the median Hounsfield units for this segment. The remaining segments had no changes in their respective significance. This indicates that age does not significantly impact the difference in median Hounsfield units between the groups for these segments.

When the median Hounsfield units of each segment were adjusted for decedent population affinity, the right frontal became non-significant ($p > 0.05$). This suggests that population affinity significantly impacted the median Hounsfield units for this segment. The remaining segments had no changes in their respective significance. This indicates that population affinity does not significantly impact the difference in median Hounsfield units between the groups for these segments.

Summary of Hypothesis 3d

These findings do not support the hypothesis that median Hounsfield units would be significantly greater in high-risk alcohol users than in low-risk alcohol users. Overall, median Hounsfield units were lower in the high-risk group, albeit the difference was only significant in left and right frontal segments. However, when age and population affinity are accounted for, the difference in median Hounsfield units becomes non-significant for the right frontal, suggesting that these variables affect median Hounsfield units.

Intraobserver Error

The 16 cases whose numbers appeared were selected for reanalysis. Due to small sample sizes, cases were not segregated by risk group. Two-way mixed methods interclass coefficients were calculated for each variable. Interclass correlation coefficients range from -1 to 1, with 1 being perfect agreement and <0.5 suggesting agreement is no better than chance. Table 37 lists intraclass correlation coefficients and their corresponding level of agreement after Liljequist et al. (2019).

Tables 38 to 43 display the interclass correlation coefficients, 95% confidence levels, and p-values for measurement agreement between original and reanalyzed cases for minimum segment thickness, segment volume, and minimum, maximum, mean, and median Hounsfield units.

Table 37 Level of agreement for interclass coefficients

Level of Agreement	Interclass Coefficient
Poor agreement	<0.5
Moderate agreement	>0.5 to <0.75
Good agreement	>0.75 to <0.90
Excellent agreement	>0.90

Table 38 Interclass correlation coefficient for minimum segment thickness

Segment	Interclass Correlation Coefficient (95% CI)	Sig.
Left cerebellar fossa	0.999 (0.996 - 1.000)	<.001
Left frontal	0.869 (0.642 - 0.956)	<.001
Left orbit	0.852 (0.601 - 0.950)	<.001
Left temporal	0.980 (0.937 - 0.993)	<.001
Right cerebellar fossa	0.902 (0.725 - 0.968)	<.001
Right frontal	0.949 (0.840 - 0.984)	<.001
Right orbit	0.982 (0.946 - 0.994)	<.001
Right temporal	0.864 (0.629 - 0.954)	<.001

Table 38 displays the interclass coefficients for measurements of minimum segment thickness. Intraobserver agreement for minimum segment thickness measured good to excellent, with all agreements being highly significant ($p < 0.001$). This suggests that minimum segment thickness could be reliably located in the region of interest.

Table 39 Interclass correlation coefficients for segment volume

Segment	Interclass Correlation Coefficient (95% CI)	Sig.
Left cerebellar fossa	0.929 (0.778 - 0.977)	<.001
Left frontal	0.865 (0.579 - 0.957)	<.001
Left orbit	0.950 (0.843 - 0.984)	<.001
Left temporal	0.846 (0.520 - 0.951)	<.001
Right cerebellar fossa	0.645 (0.107 - 0.886)	0.037
Right frontal	0.769 (0.281 - 0.926)	0.006
Right orbit	0.942 (0.820 - 0.981)	<.001
Right temporal	0.713 (0.106 - 0.908)	0.016

Table 39 displays the interclass coefficient for the remeasurement of segment volume. The right cerebellar fossa and right temporal had moderate but significant agreement between the

two measures ($p < 0.05$). The left frontal, left temporal, and right frontal all had good agreement between the two measures ($p < 0.05$). The left cerebellar fossa and left and right orbit all had excellent agreement between the measures ($p < 0.001$).

Table 40 Interclass correlation coefficients for minimum Hounsfield units

Segment	Interclass Correlation Coefficient (95% CI)	Sig.
Left cerebellar fossa	0.396 (-0.881 - 0.806)	0.187
Left frontal	0.669 (-0.03 - 0.894)	0.028
Left orbit	0.389 (-0.902 - 0.804)	0.193
Left temporal	0.895 (0.674 - 0.966)	<.001
Right cerebellar fossa	0.489 (-0.59 - 0.836)	0.119
Right frontal	0.857 (0.556 - 0.954)	<.001
Right orbit	0.806 (0.395 - 0.938)	0.003
Right temporal	0.782 (0.321 - 0.93)	0.005

Table 40 displays the interclass coefficient of measurement of minimum Hounsfield units. The left cerebellar fossa, left orbit, and right cerebellar fossa saw poor agreement between the two measures ($p > 0.05$). The left frontal saw moderate but significant agreement between the two measures ($p < 0.028$). The left temporal, right frontal, right orbit, and right temporal all had good agreement between the two measurements ($p < 0.05$).

Table 41 Interclass correlation coefficients for maximum Hounsfield Units

Segment	Interclass Correlation Coefficient (95% CI)	Sig.
Left cerebellar fossa	0.954 (0.857 - 0.985)	<.001
Left frontal	0.682 (0.008 - 0.898)	0.024
Left orbit	0.948 (0.838 - 0.983)	<.001
Left temporal	0.954 (0.856 - 0.985)	<.001
Right cerebellar fossa	0.687 (0.026 - 0.900)	0.023
Right frontal	0.953 (0.852 - 0.985)	<.001
Right orbit	0.960 (0.877 - 0.987)	<.001
Right temporal	0.970 (0.906 - 0.990)	<.001

Table 41 displays the interclass coefficient for measurements of maximum Hounsfield units. The left frontal and right cerebellar fossa had moderate but significant agreement between the two measurements ($p < 0.05$). The remaining segments saw excellent and highly significant agreement between the two measurements ($p < 0.001$).

Table 42 Interclass correlation coefficients for mean Hounsfield units

Segment	Interclass Correlation Coefficient (95% CI)	Sig.
Left cerebellar fossa	0.750 (0.220 - 0.920)	0.009
Left frontal	0.695 (0.049 - 0.902)	0.021
Left orbit	0.737 (0.181 - 0.916)	0.011
Left temporal	0.530 (-0.464 - 0.849)	0.093
Right cerebellar fossa	0.751 (0.224 - 0.920)	0.009
Right frontal	0.579 (-0.312 - 0.865)	0.066
Right orbit	0.770 (0.284 - 0.926)	0.006
Right temporal	0.704 (0.077 - 0.905)	0.018

Table 42 displays the interclass coefficient for measurements of mean Hounsfield units. The left temporal and right frontal had moderate but insignificant agreement between the two

measurements ($p>0.05$). The left frontal, left orbit, and right temporal had moderate but significant agreement between the measurements ($p<0.05$). The left and right cerebellar fossae, and right orbit all exhibited good agreement between the measurements ($p<0.05$).

Table 43 Interclass correlation coefficients for median Hounsfield units

Segment	Interclass Correlation Coefficient (95% CI)	Sig.
Left cerebellar fossa	0.800 (0.376 - 0.936)	0.003
Left frontal	0.740 (0.189 - 0.916)	0.011
Left orbit	0.763 (0.263 - 0.924)	0.007
Left temporal	0.626 (0.166 - 0.880)	0.044
Right cerebellar fossa	0.822 (0.445 - 0.943)	0.002
Right frontal	0.750 (0.223 - 0.920)	0.009
Right orbit	0.744 (0.202 - 0.918)	0.01
Right temporal	0.851 (0.535 - 0.952)	<.001

Table 43 displays the interclass coefficient for measurements of median Hounsfield units. The left frontal, left temporal, and right orbit all had moderate but significant agreement between the measurements ($p<0.05$). The remaining segments all saw significant, good agreement between the measurements ($p>0.05$).

Interpretation of Interclass Correlation Coefficients

Overall, the interclass correlation coefficients demonstrate good to excellent agreement for most measures, suggesting that the cranial segments selected during reanalysis were in similar locations to the ones selected during the original analysis.

Conclusions

This study assessed minimum thickness, volume, and markers of radiodensity in cranial segments sampled from high and low-risk alcohol-using men between the ages of 21 and 55. Cranial segments were selected at the left and right cerebellar fossae, the left and right lateral frontal, the left and right orbital roofs, and the left and right temporal squamous.

The findings presented above demonstrate that high-risk alcohol users have thinner cranial segments than low-risk alcohol users, and the difference was statistically significant at the left and right cerebellar fossae, the left and right orbital roofs, and the left and right temporal squamous. Importantly, the significant differences in thickness between high-risk alcohol users and low-risk alcohol users remain significant when decedent age and population affinity are controlled for.

Segment volume was not significantly different between the two risk groups, though paradoxically, the average segment volume was greater in the high-risk group despite the differences in minimum thickness between the risk groups. This suggests that high-risk alcohol users may have areas of maximum thickness greater than low-risk alcohol users, perhaps due to a local inflammatory response.

Markers of radiodensity, as measured in Hounsfield units, showed that in this study, high-risk alcohol users had cranial segments that exhibited areas of significantly lower and significantly higher radiodensity and had overall lower mean density. While the finding of greater radiodensity is paradoxical, the findings of lower mean density suggest that the high-risk segments are more porous.

When linear relationships between variables are explored, the left and right cerebellar fossa demonstrate positive correlations between minimum segment thickness, mean Hounsfield

units, and segment volume, while the left and right frontal exhibit negative correlations between these variables, further supporting the findings of radiodensity markers.

Finally, interclass correlation coefficients showed that the author was consistent in selecting cranial segments and could reliably measure the variables in question.

CHAPTER 4

DISCUSSION

Introduction

This chapter addresses the limitations of the study's methodological approach, possible physiological explanations for alcohol-induced bone disease, and discusses the importance of the study's findings to death investigation, forensic anthropology, and clinical medicine.

Limitations of the Research Design and Methodology

This study used a novel research design and methodology to answer the questions of whether high-risk alcohol users had thinner crania, lower cranial volume, and lower radiodensity as measured in Hounsfield units when compared to low-risk alcohol users. As with any research project, the design and methodological approach have limitations.

Limitations of the Research Design

The current study relied on previously collected data to select a study sample. As with any secondary data collection, the information available for this study was limited to what was reported in the underlying dataset. For example, only an individual's drinking status was listed, but with no quantification of how much they drank, how often they drank, or for how long they had been exhibiting behavior associated with high-risk alcohol use.

This study focused solely on men aged 21-55, so its findings only currently apply to this population. Incorporating women and increasing the age range would have made the results more applicable to the general population.

When comparing minimum cranial thickness between high-risk and low-risk alcohol users, the assumption is that high-risk alcohol users may have thinner crania due to alcohol-induced pathological changes. However, observed differences between the groups may be occurring in the opposite direction; that is to say, low-risk alcohol users may have greater minimum thickness because they are benefiting from the positive skeletal effects of moderate alcohol use.

Finally, the estimated effect size for this study was based on the results of Na et al. (2018), who measured Hounsfield units on a single slice of a computed tomography scan of the anterior frontal. This study, however, measured Hounsfield units across the full thickness of the cranium and in different anatomic regions. Even though this study's sample size was over five times greater than that calculated using data from Na et al. (2018), it may still have been too small to detect a true difference.

Limitations of the Methodology

Body Mass Index

Body mass index (BMI) was used to include or exclude individuals from this study. Calculation of BMI was done using the living height and weight of decedents, as reported in the New Mexico Decedent Image Database. These data were gathered during the death investigation and through next-of-kin interviews, as such there may be issues with the accuracy of the height and weight inputs in the BMI calculation, causing erroneous inclusion or exclusion of individuals.

Nutritional Status

While NMDID collects data related to a decedent's usual dietary patterns, this data is reported categorically as either convenience food, eating disorder, normal, overeating, unknown, vegan, vegetarian, or weight reduction without further definition of these categories (Edgar et al., 2020). Additionally, this information is collected through next-of-kin interviews and is not available for every case. In this study, only 44 individuals had their usual dietary patterns reported, and as such, this variable could not be analyzed.

Scan resolution

The computed tomography scans used in this study were resampled to a 0.5mm x 0.5mm x 0.5mm voxel size, which was an insufficient resolution to measure the width of individual layers of cortical bone and diploe and only allowed for measurement of full cranial thickness. Additionally, this resolution did not allow for the analysis of markers of bone density, such as trabecular number, thickness, and separation or bone volume by total volume.

Hounsfield Units

Hounsfield units, by definition, are a measure of radiodensity and have been repeatedly shown in clinical literature to be an excellent proxy for bone density and a reliable opportunistic screening tool for osteoporosis (For example, Buckens et al., 2015; Christensen et al., 2020; Colantonio et al., 2020; Elarjani et al., 2021; Hendrickson et al., 2018; Lee et al., 2017). However, Hounsfield units' relationship to osteoporosis t-scores has predominately been studied in the trabeculae of long bones and not in the cortex of flat bones. Only one study was identified that measured Hounsfield units in the cranium; however, Hounsfield units were measured in the

anterior frontal, which has a much thicker layer of trabeculae than the sites analyzed in this study (Na et al., 2018). Na et al. (2018) also took a different methodological approach than this study, measuring Hounsfield units on a single slice of a computed tomography scan and only along a small line. This study examined Hounsfield units over a much broader area, across all layers of bone, and in areas of the cranium that are compositionally much different from the anterior frontal. Since this study examined Hounsfield units using a novel methodology, the findings cannot be compared to prior research.

Segment Selection and Reporting

The areas of the cranium that were chosen for study (the cerebellar fossa of the occiput, lateral frontal, the orbital roof, and the temporal squamous) were selected based on observations made during forensic anthropology examinations of individuals with known alcohol use disorder. There may be additional areas of the cranium that should have been included in this study or areas that may have been more appropriate to include.

The decision to report the left and right-sided segments independent of one another was made in an attempt to account for intra-individual variation in the morphology of the endocranial surface. For instance, while the left segment taken from a given area may exhibit severe thinning, the right-sided pair of that segment may not exhibit thinning in that particular area due to endocranial undulations. If aggregating the measurements of minimum cranial thickness for the left and right segments still showed a significant difference between high-risk and low-risk alcohol users, this would strengthen the argument that alcohol has an effect on cranial thickness and reduce the chance that this study's findings represent a Type I statistical error. Furthermore, by aggregating the left and right sides, it could be said that alcohol significantly thins entire

regions of the cranium, i.e. the orbital roofs, the temporal squamous, and the cerebellar fossa of the occiput, without having to qualify the thinning may occur in only one side.

Replicability

The author was the only individual to select the location of the cranial segments and measure their minimum thickness. However, measurements of minimum thickness were initially performed under the guidance of a board-certified radiologist, and interclass correlation coefficients showed that the author had very good agreement for repeated measures of the same individuals. The definitions of segment placements listed in Chapter 2 should be verified to ensure accuracy.

Pathophysiology of Alcohol-Induced Bone Disease

Numerous metabolic disturbances unrelated to alcohol can cause changes to the human skeleton, primarily arising from nutritional or hormone perturbations (Burr and Allen, 2019). Also, despite seemingly infinite causes of skeletal disease, there are finite ways these diseases can manifest in the skeleton, i.e., abnormal growth, destruction, size, or shape (Waldron, 2009). As such, it can be exceedingly difficult to diagnose a disease based on the skeleton alone, especially when soft tissue manifestations of the suspected disease are required for diagnostic certainty. Therefore, anthropological diagnoses of skeletal pathology are usually probabilistic (Waldron, 2009).

The body of research demonstrating that heavy alcohol use is detrimental to skeletal health is substantial (For example, Alvisa-Negrin et al., 2009; Bikle et al., 1993; Cheraghi et al., Gaddini et al. 2016; Maurel et al., 2012a; Maddalozzo et al., Peris et al., 1994; Tucker et al.,

2009). Grossly, alcohol has negative effects on osteoblast formation and lifespan while simultaneously increasing osteoclast activity. Heavy alcohol use is associated with global cortical thinning, lower bone mineral density, and lower DEXA t-scores (Gonzalez-Reimers et al., 2015; Michael and Bengtson, 2016).

Macroscopically, alcohol-induced osteopenia or osteoporosis may not necessarily be differentiated from other diseases resulting in reduced bone mass, except, as hypothesized in this study, by the presence of widespread, abnormally thin cortex, particularly in flat bones such as the cranium and the scapulae. Whereas postmenopausal osteoporosis predominantly occurs in and affects trabecular bone, alcohol-induced bone loss takes place in both cortical and trabecular bone (Chakkalakal, 2005). Rhee et al. (2011) have demonstrated that parathyroid hormone increases intracortical remodeling. Cortical bone comprises 80% of the bone mass of the human skeleton and serves as the major repository for stored minerals such as calcium, phosphate, and magnesium; it follows then that cortical bone would be preferentially mined to regain homeostasis (Burr and Allen, 2019).

Additionally, unlike trabecular bone, cortical bone has Haversian Canals, which function to support the osteocyte (Burr and Allen, 2019). Haversian canals contain small blood vessels that carry nutrients to the osteocyte. The presence of these small blood vessels could be significant in that they provide a direct pathway for alcohol and its toxic metabolites to exert negative apoptotic effects directly on cortical bone cells as well as increase local inflammation, leading to the increased recruitment of osteoclasts (Burr and Allen, 2019; Chakkalakal, 2005).

In the cortex, bone formation usually exceeds bone resorption on the periosteal surface. In contrast, bone resorption usually is higher on the endosteal surface, likely due to the proximity and higher exposure to inflammatory cytokines found in the bone marrow cavity (Burr and

Allen, 2019). The reduction in osteoblast activity due to alcohol may limit the periosteal apposition of bone. Likewise, the already increased osteoclastic activity of the endosteal surface would likely be further increased by the presence of alcohol. Taken together, this may suggest that cortical thinning occurs from the endosteal surface outward. This has been seen in other forms of osteoporosis, where there is trabecularization of the endocortical surface as it erodes during resorption (Bikle et al., 1993).

Finally, where macroscopic changes associated with heavy alcohol use may be difficult to differentiate from other conditions, Bikle et al. (1993) suggest that it may be possible to differentiate alcohol-induced osteopenia and osteoporosis from other disease states via histology. Specifically, these authors posit that alcohol-induced bone loss may be differentiated if the ratio between total and active remodeling surfaces is below 60% of the total cross-sectional area and there are decreased formation surfaces present (Bikle et al., 1993).

Importance to Medicolegal Death Investigation and Public Health

By recognizing that cranial thinning may occur in the setting of heavy alcohol use, medicolegal death investigators might better understand and explain fatalities among individuals with a known history of alcohol use disorder when blunt force trauma of the head contributes to their death. Furthermore, recognition of the role heavy alcohol use can have in cranial trauma deaths may increase the documentation of alcohol use/alcohol use disorder on the death certificate, leading to better public health statistics and a better understanding of the far-reaching effects of alcohol use.

Importance to Forensic Anthropology

In the United States, where an estimated 1 in 10 individuals over the age of 18 meet the criteria for alcohol use disorder, it is highly probable that at some point in their career, a forensic anthropologist will encounter a decedent who may be at risk for and/or exhibit signs of alcohol-induced bone disease (US Department of Health and Human Services, 2018). The negative skeletal effects of heavy alcohol use discussed above can affect a forensic anthropological examination in a myriad of ways, namely by altering estimates of age, interpretation of antemortem and perimortem trauma, and assisting with differential diagnosis of observed pathology, e.g. cranial thinning. As such, it is critical that forensic anthropologists have an appreciation of alcohol-induced bone disease.

A case report by Michael and Bengtson (2016) demonstrates the effects that heavy alcohol use can have on a forensic anthropology case. In their report of a 42-year-old male who was known to consume alcohol heavily, they report severe cortical thinning observed radiographically and a gross underestimate of age at death (average of 31.5 years) when measured histologically. The histological underestimate of this case is likely due to the decrease in osteoblastic activity seen in alcohol abuse, a reduction that would subsequently cause a decrease in osteon formation (Maurel et al., 2012a). Reduced bone mass and increased porosity may cause remains to appear macroscopically older than the individual actually is. When viewed together, the conflicting data would make an accurate age estimation more difficult.

Heavy alcohol use is associated with an increased fracture rate, as well as a decrease in the timing and proper healing of fractures (Chakkalakal, 2005). Improper healing of fractures in heavy alcohol users exists even in the setting of proper medical care and treatment. The delay in fracture healing can likely be attributed to the reduction in bone formation seen in heavy alcohol

use. Similar to the importance of appreciating alcohol's role in cranial blunt force trauma deaths, the cortical thinning observed among heavy alcohol users may alter the interpretation of perimortem trauma. For example, cortical thinning increases fragility, so blunt force traumatic injuries of the cranium may be disproportionate to the actual force involved, i.e., less force would be required to cause significant trauma. The higher-than-average rate of accidental fracture and altered timing of fracture healing could impact cases where there are questions regarding the timing of antemortem injuries.

Regarding the development of a differential diagnosis in cases with macroscopic skeletal features associated with heavy alcohol use may include cortical thinning and increased translucency of flat bones, decreased bone density, increased porosity, and an increase in pathological and poorly healed fractures. Histologically, age may be discrepant from macroscopic estimates, and bone formation may be decreased. When these findings are present, especially in populations not traditionally at risk for osteopenia or osteoporosis, such as younger men, and there is no other discernible underlying cause, alcohol-induced bone disease should be considered. While this constellation of symptoms is not pathognomonic for heavy alcohol use, they are, at minimum, indicative of an underlying systemic problem, the recognition of which could be useful in helping to individuate a set of unknown remains. For example, the findings of this study could be helpful for entering unknown decedents into missing persons datasets such as the National Missing and Unidentified Persons System. While findings of cranial thinning cannot be conclusively linked to high-risk alcohol use, the behavior could be mentioned as a possible descriptor of an unidentified decedent, increasing the probability of identification.

Importance to Clinical Communities

If clinicians have an understanding that high-risk alcohol use behavior impacts the cranium, it can impact patient care in two major ways. Firstly, clinicians could provide head injury prevention education, such as helmet safety and fall prevention strategies. Secondly, recognition that cranial osteoporosis may occur in this population provides an opportunity for screen and treatment if appropriate.

Segment Volume

Paradoxically, this study found that segment volume was greater in high-risk alcohol users than in low-risk alcohol users. However, the differences observed were not statistically significant. Possibly, explanations for this finding may include local inflammation or variation in underlying cranial morphology.

Computed Tomography in Forensic Casework and Research

This study's findings build on ever-growing evidence that postmortem computed tomography is a valid, rich, and important modality for gaining new insights into anthropological questions. Overall, computed tomography greatly benefits anthropological casework and research and pairs well with macroscopic analysis. For example, it can document remains as they appear prior to examination and for future reanalysis and can also serve as a reasonable proxy for dry remains when maceration is not feasible. Computed tomography is also accurate when performing osteometrics, identifying fractures, and aging both sub-adults and adults (Garvin and Stock, 2016; Scheirs et al., 2020; Spies et al., 2020; Spies et al., 2021). Furthermore, by allowing

anthropologists to view internal structures, computed tomography helps create more robust differential diagnoses of pathological changes observed macroscopically (Buikstra, 2019)

In some instances, computed tomography is superior to macroscopic analysis. As the present study shows, computed tomography can detect bony changes that may not be apparent macroscopically. The differences seen in cranial thickness between high-risk and low-risk alcohol users were in the submillimeter range, not a difference that is likely appreciable to the human eye. This finding demonstrates that computed tomography can give novel insights into biological problems that are not readily apparent via macroscopic analysis and opens new avenues for future areas of research.

Computed tomography, however, is not without its limitations. As useful as computed tomography is for assessing skeletal pathology, it can also be very limiting depending on the type of bony change being assessed. For example, as discussed by Anderson et al. (2021), in cases where cranial lesions were smaller than the resolution of the scan, computed tomography was worse at detecting lesions than traditional macroscopic assessment. Similarly, cortical translucency resulting from thinning is not readily apparent on 3D volume renderings of a computed tomography scan because of the solid surface algorithms used.

As computed tomography becomes increasingly common in forensic anthropology, it opens the door to new research questions and novel methodologies, giving anthropologists new and more powerful insights into the human skeleton. Though this is an exciting new frontier, anthropologists need to recognize that computed tomography is not always a superior method to, or blanket substitution for, traditional macroscopic analysis but rather a separate and very powerful additional modality.

Moving forward, forensic anthropology training programs should further incorporate radiographic training into their programs to prepare the next generation of forensic anthropologists. Additionally, governing bodies should create standards for radiography in forensic anthropology, which outline the scope of practice for forensic anthropologists and establish consensus on methodological best practices.

Alcohol-Induced Bone Disease and Hounsfield Units

In this study, Hounsfield units were used as a proxy for bone density and measured across the full thickness of the cranium, capturing values from both cortical and trabecular bone. Table 44 shows the relationship between Hounsfield units in high-risk alcohol users and low-risk alcohol users.

Table 44 Hounsfield units in high-risk alcohol users compared to Hounsfield units of low-risk users by segment

Segment	Minimum	Maximum	Mean	Median
LC	Lower	Higher	Lower	Lower
LF	Lower	Higher	Lower	Lower
LO	Lower	Higher	Higher	Higher
LT	Lower	Higher	Lower	Lower
RC	Lower	Higher	Lower	Lower
RF	Lower	Lower	Lower	Lower
RO	Lower	Higher	Higher	Higher
RT	Lower	Higher	Lower	Lower

Note: **Bolded** differences are statistically significant

Overall, high-risk alcohol users had lower minimum, mean, and median Hounsfield units, suggesting that they were less dense than low-risk alcohol users; however, the high-risk users also showed higher maximum Hounsfield units, suggesting these individuals also had areas of greater density.

The lower Hounsfield units seen in high-risk alcohol users are expected and may be explained by a combination of the underlying physiology of alcohol-induced bone disease and the anatomic composition of flat bone. A major factor in alcohol-induced bone disease is parathyroid hormone, which preferentially resorbs cortical bone, reduces cortical thickness, and increases cortical porosity. Parathyroid hormone significantly increases during the consumption of alcohol. In flat bone such as the cranium, which is predominately cortical bone, the impact of increased parathyroid hormone can be especially pronounced, causing increased resorption and a blurring of the bony layers of the cranium, as seen in classic hyperparathyroidism (Maurel et al., 2012b; Rhee et al., 2011; Bennett et a., 2020).

Conversely, the finding that high-risk alcohol users had higher maximum Hounsfield units than low-risk alcohol users is paradoxical and needs further study.

Despite the fact that cranial segments of high-risk alcohol users were less dense overall, the differences were minor and only statistically significant for some segments. This suggests that using Hounsfield units as a proxy for bone density in cortical bone is not as useful as in trabecular bone due to the more uniform densities seen across cortical bone when measured at the current resolution.

Summary

The present study demonstrated the utility of postmortem computed tomography for assessing measures of cranial thickness and radiodensity. Of this study's findings, the most significant for death investigation, forensic anthropology, and clinical medicine is that the crania of high-risk alcohol users are indeed thinner than those of low-risk alcohol users. This finding has the potential to enhance public health statistics around fatal head injuries in heavy alcohol

users, help forensic anthropologists better interpret skeletal remains, and help clinicians prevent head injuries and treat secondary osteoporosis in patients with high-risk alcohol use.

CHAPTER 5

CONCLUSIONS

Introduction

This study demonstrated that high-risk alcohol users had significantly thinner crania than low-risk alcohol users when measured at the cerebellar fossa of the occiput, the orbital roof, and the squamous part of the temporal but not at the lateral frontal. This study also showed that using Hounsfield units to approximate bone density in cortical bone needs further research.

Future Research

While there is much more research to be done to fully understand the impact of alcohol on the cranium and its related morbidity and mortality, this study provides a solid foundation from which to start. Future studies should incorporate women, compare cranial segments with other anatomic areas with established correlates between Hounsfield units and bone density, correlate cranial Hounsfield units with DEXA-derived bone density values, correlate cranial findings with known soft tissue makers of heavy alcohol use such as liver cirrhosis and hypertrophic parotid glands, and use a mixed methods approach to analyze computed tomography scans of crania with observed macroscopic translucency. Additionally, once the area of minimal cranial thickness was identified, performing an additional segmentation centered on that point may provide a more accurate picture of the bone quality and volume of the area of thinning. Finally, the paradoxical findings that high-risk alcohol users have greater segment volume and higher maximum Hounsfield units need to be explored further to determine if they are spurious or valid findings.

Final Remarks

This study demonstrated that the crania of high-risk alcohol users are significantly thinner than those of low-risk alcohol users. Though the observed differences were in the sub-millimeter range, that may be enough to appreciate cortical translucency in thin areas of the cranium macroscopically. This study may help medicolegal death investigators, forensic anthropologists, and clinicians further appreciate the impact that heavy alcohol use can have on the skeleton. Finally, this study demonstrates the utility of postmortem computed tomography in exploring biological questions not appreciable macroscopically and provides a solid foundation from which to continue exploring alcohol-induced changes to the cranium.

REFERENCES

- Aalders, M. C., Adolphi, N. L., Daly, B., Davis, G. G., de Boer, H. H., Decker, S. J., ... Wozniak, K. (2017). Research in forensic radiology and imaging; Identifying the most important issues. *Journal of Forensic Radiology and Imaging*, 8, 1–8. <https://doi.org/10.1016/j.jofri.2017.01.004>
- Adanty, K., Rabey, K. N., Doschak, M. R., Bhagavathula, K. B., Hogan, J. D., Romanyk, D. L., ... Dennison, C. R. (2021). Cortical and trabecular morphometric properties of the human calvarium. *Bone*, 148, 115931. <https://doi.org/10.1016/j.bone.2021.115931>
- Åkesson, A., Bjellerup, P., Lundh, T., Lidfeldt, J., Nerbrand, C., Samsioe, G., ... Vahter, M. (2006). Cadmium-Induced Effects on Bone in a Population-Based Study of Women. *Environmental Health Perspectives*, 114(6), 830–834.
- Alvisa-Negrín, J., González-Reimers, E., Santolaria-Fernández, F., García-Valdecasas-Campelo, E., Valls, M. R. A., Pelazas-González, R., ... de los Ángeles Gómez-Rodríguez, M. (2009). Osteopenia in Alcoholics: Effect of Alcohol Abstinence. *Alcohol and Alcoholism*, 44(5), 468–475. <https://doi.org/10.1093/alcalc/agp038>
- Anderson, B. W., Kortz, M. W., Black, A. C., & Kharazi, K. A. A. (2023). *Anatomy, Head and Neck, Skull*. StatPearls Publishing. Retrieved from <https://www.ncbi.nlm.nih.gov/books/NBK499834/>
- Anderson, R. J. (1882). Observations on the thickness of the human skull. *The Dublin Journal of Medical Science*, 74(4), 270–280. <https://doi.org/10.1007/BF02967147>
- Ansari, S., Ito, K., & Hofmann, S. (2022). Alkaline Phosphatase Activity of Serum Affects Osteogenic Differentiation Cultures. *ACS Omega*, 7(15), 12724–12733. <https://doi.org/10.1021/acsomega.1c07225>
- Asrani, S. K., Mellinger, J., Arab, J. P., & Shah, V. H. (2021). Reducing the Global Burden of Alcohol-Associated Liver Disease: A Blueprint for Action. *Hepatology*, 73(5), 2039–2050. <https://doi.org/10.1002/hep.31583>
- Baba, M., Hyodoh, H., Okazaki, S., Shimizu, J., Mizuo, K., Rokukawa, M., ... Inoue, H. (2016). Stature estimation from anatomical landmarks in femur using postmortem CT. *Journal of Forensic Radiology and Imaging*, 7, 28–32. <https://doi.org/10.1016/j.jofri.2016.11.002>
- Bennett, J., Suliburk, J. W., & Morón, F. E. (2020). Osseous Manifestations of Primary Hyperparathyroidism: Imaging Findings. *International Journal of Endocrinology*, 2020, 3146535. <https://doi.org/10.1155/2020/3146535>
- Berger, A. (2002). Bone mineral density scans. *BMJ: British Medical Journal*, 325(7362), 484.

- Bialer, O. Y., Rueda, M. P., Bruce, B. B., Newman, N. J., Biousse, V., & Saindane, A. M. (2014). Meningoceles in Idiopathic Intracranial Hypertension. *American Journal of Roentgenology*, 202(3), 608–613. <https://doi.org/10.2214/AJR.13.10874>
- Bikle, D. D., Stesin, A., Halloran, B., Steinbach, L., & Recker, R. (1993). Alcohol-Induced Bone Disease: Relationship to Age and Parathyroid Hormone Levels. *Alcoholism: Clinical and Experimental Research*, 17(3), 690–695. <https://doi.org/10.1111/j.1530-0277.1993.tb00821.x>
- Boruah, S., Paskoff, G. R., Shender, B. S., Subit, D. L., Salzar, R. S., & Crandall, J. R. (2015). Variation of bone layer thicknesses and trabecular volume fraction in the adult male human calvarium. *Bone*, 77, 120–134. <https://doi.org/10.1016/j.bone.2015.04.031>
- Boruah, S., Subit, D. L., Paskoff, G. R., Shender, B. S., Crandall, J. R., & Salzar, R. S. (2017). Influence of bone microstructure on the mechanical properties of skull cortical bone – A combined experimental and computational approach. *Journal of the Mechanical Behavior of Biomedical Materials*, 65, 688–704. <https://doi.org/10.1016/j.jmbbm.2016.09.041>
- Brickley, M. B., Ives, R., & Mays, S. (2020). *The Bioarchaeology of Metabolic Bone Disease*. Academic Press.
- Brismar, T. B., & Ringertz, H. (1996). Effect of Bone Density of the Head on Total Body DEXA Measurements in 100 Healthy Swedish Women. *Acta Radiologica*, 37(1), 101–106. <https://doi.org/10.1080/02841859609174368>
- Brogdon, B. G., Sorg, M. H., & Marden, K. (2010). Fingering a Murderer: A Successful Anthropological and Radiological Collaboration*. *Journal of Forensic Sciences*, 55(1), 248–250. <https://doi.org/10.1111/j.1556-4029.2009.01229.x>
- Brogdon BG, Sorg MH, Elifritz J, Brown HG, & Wren JA. (2012). Multidisciplinary Combination of Traditional and New Techniques in the Determination of Identity: The Utility of the Sphenoid Sinus Rediscovered. *Proceedings of the American Academy of Forensic Sciences*. Presented at the American Academy of Forensic Sciences, Atlanta, GA. Atlanta, GA.
- Brough, A. L., Morgan, B., & Ruttly, G. N. (2015). The basics of disaster victim identification. *Journal of Forensic Radiology and Imaging*, 3(1), 29–37. <https://doi.org/10.1016/j.jofri.2015.01.002>
- Bryazka, D., Reitsma, M. B., Griswold, M. G., Abate, K. H., Abbafati, C., Abbasi-Kangevari, M., ... Gakidou, E. (2022). Population-level risks of alcohol consumption by amount, geography, age, sex, and year: A systematic analysis for the Global Burden of Disease Study 2020. *The Lancet*, 400(10347), 185–235. [https://doi.org/10.1016/S0140-6736\(22\)00847-9](https://doi.org/10.1016/S0140-6736(22)00847-9)

- Brzóska, M. M., Galażyn-Sidoreczuk, M., & Dzwilewska, I. (2013). Ethanol consumption modifies the body turnover of cadmium: A study in a rat model of human exposure. *Journal of Applied Toxicology: JAT*, 33(8), 784–798. <https://doi.org/10.1002/jat.2734>
- Buckens, C. F., Dijkhuis, G., de Keizer, B., Verhaar, H. J., & de Jong, P. A. (2015). Opportunistic screening for osteoporosis on routine computed tomography? An external validation study. *European Radiology*, 25(7), 2074–2079. <https://doi.org/10.1007/s00330-014-3584-0>
- Buikstra, J. (2019). *Ortner's Identification of Pathological Conditions in Human Skeletal Remains*. Academic Press.
- Burge, R., Dawson-Hughes, B., Solomon, D. H., Wong, J. B., King, A., & Tosteson, A. (2007). Incidence and Economic Burden of Osteoporosis-Related Fractures in the United States, 2005–2025. *Journal of Bone and Mineral Research*, 22(3), 465–475. <https://doi.org/10.1359/jbmr.061113>
- Burr, D. B., & Allen, M. R. (2019). *Basic and Applied Bone Biology*. Academic Press.
- Carew, R. M., & Errickson, D. (2019). Imaging in forensic science: Five years on. *Journal of Forensic Radiology and Imaging*, 16, 24–33. <https://doi.org/10.1016/j.jofri.2019.01.002>
- Carew, R. M., Morgan, R. M., & Rando, C. (2019a). A Preliminary Investigation into the Accuracy of 3D Modeling and 3D Printing in Forensic Anthropology Evidence Reconstruction. *Journal of Forensic Sciences*, 64(2), 342–352. <https://doi.org/10.1111/1556-4029.13917>
- Carew, R. M., Viner, M. D., Conlogue, G., Márquez-Grant, N., & Beckett, S. (2019b). Accuracy of computed radiography in osteometry: A comparison of digital imaging techniques and the effect of magnification. *Journal of Forensic Radiology and Imaging*, 19, 100348. <https://doi.org/10.1016/j.jofri.2019.100348>
- Centers for Disease Control and Prevention, National Center for Health Statistics. National Vital Statistics System, Mortality 2018-2022 on CDC WONDER Online Database, released in 2024. Accessed at <http://wonder.cdc.gov/mcd-icd10-expanded.html> on Jul 7, 2024 8:55:41 PM
- Chakkalakal, D. (2005). Alcohol-Induced Bone Loss and Deficient Bone Repair. *Alcoholism: Clinical and Experimental Research*, 29(12), 2077–2090.
- Chaves Neto, A. H., Yano, C. L., Paredes-Gamero, E. J., Machado, D., Justo, G. Z., Peppelenbosch, M. P., & Ferreira, C. V. (2010). Riboflavin and photoproducts in MC3T3-E1 differentiation. *Toxicology in Vitro: An International Journal Published in Association with BIBRA*, 24(7), 1911–1919. <https://doi.org/10.1016/j.tiv.2010.07.026>

- Cheraghi, Z., Doosti-Irani, A., Almasi-Hashiani, A., Baigi, V., Mansournia, N., Etminan, M., & Mansournia, M. A. (2019). The effect of alcohol on osteoporosis: A systematic review and meta-analysis. *Drug and Alcohol Dependence*, *197*, 197–202. <https://doi.org/10.1016/j.drugalcdep.2019.01.025>
- Chin, K.-Y. (2017). A Review on the Relationship between Aspirin and Bone Health. *Journal of Osteoporosis*, *2017*, e3710959. <https://doi.org/10.1155/2017/3710959>
- Chin, K.-Y., & Ima-Nirwana, S. (2018). The Role of Vitamin E in Preventing and Treating Osteoarthritis—A Review of the Current Evidence. *Frontiers in Pharmacology*, *9*, 946. <https://doi.org/10.3389/fphar.2018.00946>
- Christensen, A. M., Smith, M. A., Gleiber, D. S., Cunningham, D. L., & Wescott, D. J. (2018). The Use of X-ray Computed Tomography Technologies in Forensic Anthropology. *Forensic Anthropology*, *1*(2), 124–141. <https://doi.org/10.5744/fa.2018.0013>
- Christensen, D. L., Nappo, K. E., Wolfe, J. A., Tropf, J. G., Berge, M. J., Wheatley, B. M., ... Tintle, S. M. (2020). Ten-year fracture risk predicted by proximal femur Hounsfield units. *Osteoporosis International*, *31*(11), 2123–2130. <https://doi.org/10.1007/s00198-020-05477-y>
- Cohen, J. (1988). *Statistical Power Analysis for the Behavioral Sciences* (2nd ed.). Hillsdale, NJ: Lawrence Erlbaum Associates.
- Colantonio, D. F., Saxena, S. K., Vanier, A., Rodkey, D., Tintle, S., & Wagner, S. C. (2020). Cervical Spine Computed Tomography Hounsfield Units Accurately Predict Low Bone Mineral Density of the Femoral Neck. *Clinical Spine Surgery*, *33*(2), E58–E62. <https://doi.org/10.1097/BSD.0000000000000879>
- Coley, B. D. (2018). *Caffey's Pediatric Diagnostic Imaging E-Book*. Elsevier Health Sciences.
- Colman, K. L., Janssen, M.C., Stull, C. L., Van Rijn, R. R., Oostra, R. J., De Boer, H. H., & Van Der Merwe, A. E. (2018). Dutch population specific sex estimation formulae using the proximal femur. *Forensic Science International*, 268-e1.
- Colman, K. L., de Boer, H. H., Dobbe, J. G. G., Liberton, N. P. T. J., Stull, K. E., van Eijnatten, M., ... van der Merwe, A. E. (2019). Virtual forensic anthropology: The accuracy of osteometric analysis of 3D bone models derived from clinical computed tomography (CT) scans. *Forensic Science International*, *304*, 109963. <https://doi.org/10.1016/j.forsciint.2019.109963>
- Computed Tomography (CT). (n.d.). Retrieved May 29, 2024, from National Institute of Biomedical Imaging and Bioengineering website: <https://www.nibib.nih.gov/science-education/science-topics/computed-tomography-ct>

- Cooper, G. S., & Meterko, V. (2019). Cognitive bias research in forensic science: A systematic review. *Forensic Science International*, 297, 35–46. <https://doi.org/10.1016/j.forsciint.2019.01.016>
- Crist, T. A., & Sorg, M. H. (2014). Adult scurvy in New France: Samuel de Champlain’s “Mal de la terre” at Saint Croix Island, 1604–1605. *International Journal of Paleopathology*, 5, 95–105. <https://doi.org/10.1016/j.ijpp.2014.04.002>
- Crist, Thomas A.J., Washburn, A., Park, H., Hood, I., & Hickey, M.A. (1997). Cranial Bone Displacement as a Taphonomic Process in Potential Child Abuse Cases. In *Forensic Taphonomy: The postmortem fate of human remains*. CRC Press.
- Cummings, S. R., & Rosen, C. (2022). VITAL Findings—A Decisive Verdict on Vitamin D Supplementation. *New England Journal of Medicine*, 387(4), 368–370. <https://doi.org/10.1056/NEJMe2205993>
- Dall’Ara, E., & Cheong, V. S. (2022). Chapter 6—Bone biomechanics. In B. Innocenti & F. Galbusera (Eds.), *Human Orthopaedic Biomechanics* (pp. 97–120). Academic Press. <https://doi.org/10.1016/B978-0-12-824481-4.00007-X>
- Davies, C. M. (2013). *Skeletal Age Estimation and the Epiphyseal Scar: Challenging the status quo* (Dissertation). University of Dundee.
- De Boer, H. H. (Hans), Van der Merwe, A. E. (Lida), & Soerdjbalie-Maikoe, V. (Vidija). (2016). Human cranial vault thickness in a contemporary sample of 1097 autopsy cases: Relation to body weight, stature, age, sex and ancestry. *International Journal of Legal Medicine*, 130(5), 1371–1377. <https://doi.org/10.1007/s00414-016-1324-5>
- Degnan, A. J., & Levy, L. M. (2011). Pseudotumor Cerebri: Brief Review of Clinical Syndrome and Imaging Findings. *American Journal of Neuroradiology*, 32(11), 1986–1993. <https://doi.org/10.3174/ajnr.A2404>
- Delgado-Calle, J., Sato, A. Y., & Bellido, T. (2017). Role and mechanism of action of sclerostin in bone. *Bone*, 96, 29–37. <https://doi.org/10.1016/j.bone.2016.10.007>
- Delphin-Rittmon, M. E. (2022). *The National Survey on Drug Use and Health: 2020*. Retrieved from <https://www.samhsa.gov/data/sites/default/files/reports/slides-2020-nsduh/2020NSDUHNationalSlides072522.pdf>
- Drinking Levels Defined | National Institute on Alcohol Abuse and Alcoholism (NIAAA). (n.d.). Retrieved September 8, 2022, from <https://www.niaaa.nih.gov/alcohol-health/overview-alcohol-consumption/moderate-binge-drinking>
- Dror, I. (2018, April 20). Biases in Forensic Experts. *Science*, 360(6386), 243.

- Edgar, HJH; Daneshvari Berry, S; Moes, E; Adolphi, NL; Bridges, P; Nolte, KB (2020). New Mexico Decedent Image Database. Office of the Medical Investigator, University of New Mexico. doi.org/10.25827/5s8c-n515.
- Eisová, S., Rangel de Lázaro, G., Pířová, H., Pereira-Pedro, S., & Bruner, E. (2016). Parietal Bone Thickness and Vascular Diameters in Adult Modern Humans: A Survey on Cranial Remains. *The Anatomical Record*, 299(7), 888–896. <https://doi.org/10.1002/ar.23348>
- el Demellawy, D., Davila, J., Shaw, A., & Nasr, Y. (2018). Brief Review on Metabolic Bone Disease. *Academic Forensic Pathology*, 8(3), 611–640. <https://doi.org/10.1177/1925362118797737>
- Elarjani, T., Warner, T., Nguyen, K., Nguyen, S., & Urakov, T. M. (2021). Quantifying Bone Quality Using Computed Tomography Hounsfield Units in the Mid-sagittal View of the Lumbar Spine. *World Neurosurgery*, 151, e418–e425. <https://doi.org/10.1016/j.wneu.2021.04.051>
- Excel*. (2023). Microsoft Corporation.
- Fedorov, A., Beichel, R., Kalpathy-Cramer, J., Finet, J., Fillion-Robin, J.-C., Pujol, S., ... Kikinis, R. (2012). 3D Slicer as an image computing platform for the Quantitative Imaging Network. *Magnetic Resonance Imaging*, 30(9), 1323–1341. <https://doi.org/10.1016/j.mri.2012.05.001>
- Franklin, D., & Flavel, A. (2015). CT evaluation of timing for ossification of the medial clavicular epiphysis in a contemporary Western Australian population. *International Journal of Legal Medicine*, 129(3), 583–594. <https://doi.org/10.1007/s00414-014-1116-8>
- Franklin, D., & Marks, M. K. (2022). The professional practice of forensic anthropology: Contemporary developments and cross-disciplinary applications. *WIREs Forensic Science*, 4(2), e1442. <https://doi.org/10.1002/wfs2.1442>
- Franklin, D., Swift, L., & Flavel, A. (2016). ‘Virtual anthropology’ and radiographic imaging in the Forensic Medical Sciences. *Egyptian Journal of Forensic Sciences*, 6(2), 31–43. <https://doi.org/10.1016/j.ejfs.2016.05.011>
- Gaddini, G. W., Turner, R. T., Grant, K. A., & Iwaniec, U. T. (2016). Alcohol: A Simple Nutrient with Complex Actions on Bone in the Adult Skeleton. *Alcoholism: Clinical and Experimental Research*, 40(4), 657–671. <https://doi.org/10.1111/acer.13000>
- Gallagher, J. C., & Rosen, C. J. (2023). Vitamin D: 100 years of discoveries, yet controversy continues. *The Lancet Diabetes & Endocrinology*, 11(5), 362–374. [https://doi.org/10.1016/S2213-8587\(23\)00060-8](https://doi.org/10.1016/S2213-8587(23)00060-8)

- Gao, S. S., & Zhao, Y. (2023). The effects of β -carotene on osteoporosis: A systematic review and meta-analysis of observational studies. *Osteoporosis International: A Journal Established as Result of Cooperation between the European Foundation for Osteoporosis and the National Osteoporosis Foundation of the USA*, 34(4), 627–639. <https://doi.org/10.1007/s00198-022-06593-7>
- Garnero, P. (2012). The contribution of collagen crosslinks to bone strength. *BoneKEy Reports*, 1, 182. <https://doi.org/10.1038/bonekey.2012.182>
- Garvin, H. M., & Stock, M. K. (2016). The Utility of Advanced Imaging in Forensic Anthropology. *Academic Forensic Pathology*, 6(3), 499–516. <https://doi.org/10.23907/2016.050>
- Gaudsen EB, Nwachukwu BU, Schreiber JJ, Lorch DG, & Lane JM. (2017). Opportunistic Use of CT Imaging for Osteoporosis Screening and Bone Density Assessment: A Qualitative Systemic Review. *J Bone Joint Sur Am.*, (99), 1580–1590.
- Genchi, G., Sinicropi, M. S., Lauria, G., Carocci, A., & Catalano, A. (2020). The Effects of Cadmium Toxicity. *International Journal of Environmental Research and Public Health*, 17(11), 3782. <https://doi.org/10.3390/ijerph17113782>
- Giurazza, F., Del Vescovo, R., Schena, E., Battisti, S., Cazzato, R. L., Grasso, F. R., ... Zobel, B. B. (2012). Determination of stature from skeletal and skull measurements by CT scan evaluation. *Forensic Science International*, 222(1), 398.e1-398.e9. <https://doi.org/10.1016/j.forsciint.2012.06.008>
- Griessenauer, C. J., Veith, P., Mortazavi, M. M., Stewart, C., Grochowsky, A., Loukas, M., & Tubbs, R. S. (2013). Enlarged parietal foramina: A review of genetics, prognosis, radiology, and treatment. *Child's Nervous System: ChNS: Official Journal of the International Society for Pediatric Neurosurgery*, 29(4), 543–547. <https://doi.org/10.1007/s00381-012-1982-7>
- Gruchow, H. W., Sobocinski, K. A., Barboriak, J. J., & Scheller, J. G. (1985). Alcohol consumption, nutrient intake and relative body weight among US adults. *The American Journal of Clinical Nutrition*, 42(2), 289–295. <https://doi.org/10.1093/ajcn/42.2.289>
- Haber, P. S., & Kortt, N. C. (2021). Alcohol use disorder and the gut. *Addiction*, 116(3), 658–667. <https://doi.org/10.1111/add.15147>
- Hatch, J. L., Schopper, H., Boersma, I. M., Rizk, H. G., Nguyen, S. A., Lambert, P. R., ... Meyer, T. A. (2018). The bone mineral density of the lateral skull base and its relation to obesity and spontaneous CSF leaks. *Otology & Neurotology: Official Publication of the American Otological Society, American Neurotology Society [and] European Academy of Otology and Neurotology*, 39(9), e831–e836. <https://doi.org/10.1097/MAO.0000000000001969>

- Hasegawa, I., Uenishi, K., Fukunaga, T., Kimura, R., & Osawa, M. (2009). Stature estimation formulae from radiographically determined limb bone length in a modern Japanese population. *Legal Medicine, 11*(6), 260–266.
- Hatipoglu, H. G., Ozcan, H. N., Hatipoglu, U. S., & Yuksel, E. (2008). Age, sex and body mass index in relation to calvarial diploe thickness and craniometric data on MRI. *Forensic Science International, 182*(1), 46–51. <https://doi.org/10.1016/j.forsciint.2008.09.014>
- Hendrickson, N. R., Pickhardt, P. J., del Rio, A. M., Rosas, H. G., & Anderson, P. A. (2018). Bone Mineral Density T-Scores Derived from CT Attenuation Numbers (Hounsfield Units): Clinical Utility and Correlation with Dual-energy X-ray Absorptiometry. *The Iowa Orthopaedic Journal, 38*, 25–31.
- Heuzé, Y., Boyadjiev, S. A., Marsh, J. L., Kane, A. A., Cherkez, E., Boggan, J. E., & Richtsmeier, J. T. (2010). New insights into the relationship between suture closure and craniofacial dysmorphology in sagittal nonsyndromic craniosynostosis. *Journal of Anatomy, 217*(2), 85–96. <https://doi.org/10.1111/j.1469-7580.2010.01258.x>
- Hingson, R. W., Heeren, T., Edwards, E. M., & Saitz, R. (2012). Young Adults at Risk for Excess Alcohol Consumption Are Often Not Asked or Counseled About Drinking Alcohol. *Journal of General Internal Medicine, 27*(2), 179–184. <https://doi.org/10.1007/s11606-011-1851-1>
- Hirsch, R. (2000). *Seizing the Light: A History of Photography*. McGraw-Hill.
- Holbrook, T. L., & Barrett-Connor, E. (1993). A prospective study of alcohol consumption and bone mineral density. *BMJ: British Medical Journal, 306*(6891), 1506–1509.
- Holloway, W. R., Collier, F. M., Aitken, C. J., Myers, D. E., Hodge, J. M., Malakellis, M., ... Nicholson, G. C. (2002). Leptin Inhibits Osteoclast Generation. *Journal of Bone and Mineral Research, 17*(2), 200–209. <https://doi.org/10.1359/jbmr.2002.17.2.200>
- Home | Dietary Guidelines for Americans. (n.d.). Retrieved March 2, 2024, from <https://www.dietaryguidelines.gov/>
- Hounsfield, G. N. (1980). Computed medical imaging. Nobel lecture, December 8, 1979. *Journal of Computer Assisted Tomography, 4*(5), 665–674. <https://doi.org/10.1097/00004728-198010000-00017>
- Hoyumpa, A. M. (1986). Mechanisms of vitamin deficiencies in alcoholism. *Alcoholism, Clinical and Experimental Research, 10*(6), 573–581. <https://doi.org/10.1111/j.1530-0277.1986.tb05147.x>
- Idriss, H. T., & Naismith, J. H. (2000). TNF alpha and the TNF receptor superfamily: Structure-function relationship(s). *Microscopy Research and Technique, 50*(3), 184–195. [https://doi.org/10.1002/1097-0029\(20000801\)50:3<184::AID-JEMT2>3.0.CO;2-H](https://doi.org/10.1002/1097-0029(20000801)50:3<184::AID-JEMT2>3.0.CO;2-H)

- Ilich, J. Z., Brownbill, R. A., Tamborini, L., & Crncevic-Orlic, Z. (2002). To Drink or Not to Drink: How Are Alcohol, Caffeine and Past Smoking Related to Bone Mineral Density in Elderly Women? *Journal of the American College of Nutrition*, 21(6), 536–544. <https://doi.org/10.1080/07315724.2002.10719252>
- Ittyachen, A. M., & Anand, R. (2019). Copper beaten skull. *BMJ Case Reports*, 12(8), e230916. <https://doi.org/10.1136/bcr-2019-230916>
- Jantz, R. L., & Ousley S.D. (n.d.). *FORDISC 3.1 Personal Computer Forensic Discriminant Functions*. Retrieved from <https://fac.utk.edu/fordisc-3-1-personal-computer-forensic-discriminant-functions/>
- Jonathan Ford. (2018). An Analysis of Computerized Tomography (CT) -Derived Bone Density Values and Volumetrics for Age and Sex Estimation From the Proximal Femur. *Proceedings of the American Academy of Forensic Sciences, 2018*, 185. Seattle, WA. Retrieved from https://www.aafs.org/wp-content/uploads/2018_Complete_Proceedings.pdf
- Kalimeri, M., Leek, F., Wang, N. X., Koh, H. R., Roy, N. C., Cameron-Smith, D., ... Totman, J. J. (2020). Folate and Vitamin B-12 Status Is Associated With Bone Mineral Density and Hip Strength of Postmenopausal Chinese-Singaporean Women. *JBMR Plus*, 4(10), e10399. <https://doi.org/10.1002/jbm4.10399>
- Kanis, J. A., McCloskey, E. V., Johansson, H., Oden, A., Melton, L. J., & Khaltsev, N. (2008). A reference standard for the description of osteoporosis. *Bone*, 42(3), 467–475. <https://doi.org/10.1016/j.bone.2007.11.001>
- Kartsogiannis, V., & Ng, K. W. (2004). Cell lines and primary cell cultures in the study of bone cell biology. *Molecular and Cellular Endocrinology*, 228(1–2), 79–102. <https://doi.org/10.1016/j.mce.2003.06.002>
- Kaufman, J.-M. (2021). Management of osteoporosis in older men. *Aging Clinical and Experimental Research*, 33(6), 1439–1452. <https://doi.org/10.1007/s40520-021-01845-8>
- Kawashima, Y., Fujita, A., Buch, K., Li, B., Qureshi, M. M., Chapman, M. N., & Sakai, O. (2019). Using texture analysis of head CT images to differentiate osteoporosis from normal bone density. *European Journal of Radiology*, 116, 212–218. <https://doi.org/10.1016/j.ejrad.2019.05.009>
- Khamaysi, Z., Bergman, R., Telman, G., & Goldsher, D. (2014). Clinical and imaging findings in patients with neurosyphilis: A study of a cohort and review of the literature. *International Journal of Dermatology*, 53(7), 812–819. <https://doi.org/10.1111/ijd.12095>

- Kim, J. H., Na, J. E., Lee, J., Park, Y. E., Lee, J., Choi, J. H., ... Park, S. H. (2023). Blood Concentrations of Lead, Cadmium, and Mercury Are Associated With Alcohol-Related Liver Disease. *Journal of Korean Medical Science*, 38(49), e412. <https://doi.org/10.3346/jkms.2023.38.e412>
- Kivekäs, I., Vasama, J.-P., & Hakomäki, J. (2014). Bilateral Temporal Bone Otosyphilis. *Otology & Neurotology*, 35(2), e90. <https://doi.org/10.1097/MAO.0b013e3182a3603f>
- Kupraszewicz, E., & Brzóska, M. M. (2013). Excessive ethanol consumption under exposure to lead intensifies disorders in bone metabolism: A study in a rat model. *Chemico-Biological Interactions*, 203(2), 486–501. <https://doi.org/10.1016/j.cbi.2013.01.002>
- Lagalla, Roberto. (2020). A Brief History of Forensic Radiology. In G. Lo Re, A. Argo, M. Midiri, & C. Cattaneo (Eds.), *Radiology in Forensic Medicine: From Identification to Post-mortem Imaging* (pp. 1–2). Cham: Springer International Publishing. <https://doi.org/10.1007/978-3-319-96737-0>
- Lazenby, R. B. (2011). *Handbook of Pathophysiology*. Wolters Kluwer/Lippincott Williams & Wilkins Health.
- Learn What Osteoporosis Is and What It's Caused by. (n.d.). Retrieved October 15, 2018, from National Osteoporosis Foundation website: <https://www.nof.org/patients/what-is-osteoporosis/>
- Lee, D. C., Hoffmann, P. F., Kopperdahl, D. L., & Keaveny, T. M. (2017). Phantomless calibration of CT scans for measurement of BMD and bone strength—Inter-operator reanalysis precision. *Bone*, 103, 325–333. <https://doi.org/10.1016/j.bone.2017.07.029>
- Lee, S. J., Binkley, N., Lubner, M. G., Bruce, R. J., Ziemlewicz, T. J., & Pickhardt, P. J. (2016). Opportunistic screening for osteoporosis using the sagittal reconstruction from routine abdominal CT for combined assessment of vertebral fractures and density. *Osteoporosis International*, 27(3), 1131–1136. <https://doi.org/10.1007/s00198-015-3318-4>
- Li, J., Chen, X., Lu, L., & Yu, X. (2020). The relationship between bone marrow adipose tissue and bone metabolism in postmenopausal osteoporosis. *Cytokine & Growth Factor Reviews*, 52, 88–98. <https://doi.org/10.1016/j.cytogfr.2020.02.003>
- Lieber, C. S. (2000). Alcohol: Its Metabolism and Interaction With Nutrients. *Annual Review of Nutrition*, 20(Volume 20, 2000), 395–430. <https://doi.org/10.1146/annurev.nutr.20.1.395>
- Liljequist, D., Elfving, B., & Skavberg Roaldsen, K. (2019). Intra-class correlation – A discussion and demonstration of basic features. *PLoS ONE*, 14(7), e0219854. <https://doi.org/10.1371/journal.pone.0219854>

- Lillie, E. M., Urban, J. E., Lynch, S. K., Weaver, A. A., & Stitzel, J. D. (2016). Evaluation of Skull Cortical Thickness Changes With Age and Sex From Computed Tomography Scans. *Journal of Bone and Mineral Research*, 31(2), 299–307. <https://doi.org/10.1002/jbmr.2613>
- Lillie, E. M., Urban, J. E., Weaver, A. A., Powers, A. K., & Stitzel, J. D. (2015). Estimation of skull table thickness with clinical CT and validation with microCT. *Journal of Anatomy*, 226(1), 73–80. <https://doi.org/10.1111/joa.12259>
- Lynnerup, N. (2001). Cranial thickness in relation to age, sex and general body build in a Danish forensic sample. *Forensic Science International*, 117(1), 45–51. [https://doi.org/10.1016/S0379-0738\(00\)00447-3](https://doi.org/10.1016/S0379-0738(00)00447-3)
- Lynnerup, N., Astrup, J. G., & Sejrsen, B. (2005). Thickness of the human cranial diploe in relation to age, sex and general body build. *Head & Face Medicine*, 1, 13. <https://doi.org/10.1186/1746-160X-1-13>
- Ma, Q., Liang, M., Wang, Y., Ding, N., Wu, Y., Duan, L., ... Dou, C. (2020). Non-coenzyme role of vitamin B1 in RANKL-induced osteoclastogenesis and ovariectomy induced osteoporosis. *Journal of Cellular Biochemistry*, 121(7), 3526–3536. <https://doi.org/10.1002/jcb.29632>
- Maddalozzo, G. F., Turner, R. T., Edwards, C. H. T., Howe, K. S., Widrick, J. J., Rosen, C. J., & Iwaniec, U. T. (2009). Alcohol alters whole body composition, inhibits bone formation, and increases bone marrow adiposity in rats. *Osteoporosis International*, 20(9), 1529–1538. <https://doi.org/10.1007/s00198-009-0836-y>
- Mafee, M. F., Singleton, E. L., Valvassori, G. E., Espinosa, G. A., Kumar, A., & Aimi, K. (1985). Acute otomastoiditis and its complications: Role of CT. *Radiology*, 155(2), 391–397. <https://doi.org/10.1148/radiology.155.2.3983389>
- Magnetic Resonance Imaging (MRI). (n.d.). Retrieved December 16, 2023, from National Institute of Biomedical Imaging and Bioengineering website: <https://www.nibib.nih.gov/science-education/science-topics/magnetic-resonance-imaging-mri>
- Mamabolo, B., Alblas, A., & Brits, D. (2020). Modern imaging modalities in forensic anthropology and the potential of low-dose X-rays. *Forensic Imaging*, 23, 200406. <https://doi.org/10.1016/j.fri.2020.200406>
- Mann, R. W., & Hunt, D. R. (2013). *Photographic Regional Atlas of Bone Disease: A Guide to Pathologic and Normal Variation in the Human Skeleton (3rd Ed.)*. Charles C Thomas Publisher.
- Mann, R. W., Kobayashi, M., & Schiller, A. L. (2017). Biparietal Thinning: Accidental Death by a Fall from Standing Height. *Journal of Forensic Sciences*, 62(5), 1406–1409. <https://doi.org/10.1111/1556-4029.13425>

- Marais, C. (n.d.). Lodox Critical Imaging Technology. Retrieved July 17, 2024, from Lodox Systems website: <https://lodox.com/>
- Marcocci, C., Cianferotti, L., & Cetani, F. (2012). Bone disease in primary hyperparathyroidism. *Therapeutic Advances in Musculoskeletal Disease*, 4(5), 357–368. <https://doi.org/10.1177/1759720X12441869>
- Marcu, F., Bogdan, F., Muțiu, G., & Lazăr, L. (2011). The histopathological study of osteoporosis. *Romanian Journal of Morphology and Embryology = Revue Roumaine De Morphologie Et Embryologie*, 52(1 Suppl), 321–325.
- Marrone, J. A., Maddalozzo, G. F., Branscum, A. J., Hardin, K., Cialdella-Kam, L., Philbrick, K. A., ... Iwaniec, U. T. (2012). Moderate alcohol intake lowers biochemical markers of bone turnover in postmenopausal women. *Menopause (New York, N.Y.)*, 19(9), 974–979. <https://doi.org/10.1097/GME.0b013e31824ac071>
- Matsuo, K., & Otaki, N. (2012). Bone cell interactions through Eph/ephrin: Bone modeling, remodeling and associated diseases. *Cell Adhesion & Migration*, 6(2), 148–156. <https://doi.org/10.4161/cam.20888>
- Maurel, D.B., Boisseau, N., Benhamou, C. L., & Jaffre, C. (2012a). Alcohol and bone: Review of dose effects and mechanisms. *Osteoporosis International*, 23(1), 1–16. <https://doi.org/10.1007/s00198-011-1787-7>
- Maurel, D.B., Boisseau, N., Benhamou, C.L., & Jaffré, C. (2012b). Cortical bone is more sensitive to alcohol dose effects than trabecular bone in the rat. *Joint Bone Spine*, 79(5), 492–499. <https://doi.org/10.1016/j.jbspin.2011.10.004>
- Melton III, J. L. (1995). Perspectives: How many women have osteoporosis now? *Journal of Bone and Mineral Research*, 10(2), 175–177. <https://doi.org/10.1002/jbmr.5650100202>
- Michael, A. R., & Bengtson, J. D. (2016). Chronic alcoholism and bone remodeling processes: Caveats and considerations for the forensic anthropologist. *Journal of Forensic and Legal Medicine*, 38, 87–92. <https://doi.org/10.1016/j.jflm.2015.11.022>
- Miller, S. C. (1989). Bone Lining Cells: Structure and Function. *Scanning Microscopy*, 3(3), 953–961.
- Minisola, S., Arnold, A., Belaya, Z., Brandi, M. L., Clarke, B. L., Hannan, F. M., ... Thakker, R. V. (2022). Epidemiology, Pathophysiology, and Genetics of Primary Hyperparathyroidism. *Journal of Bone and Mineral Research*, 37(11), 2315–2329. <https://doi.org/10.1002/jbmr.4665>

- Mkrtchyan, G., Aleshin, V., Parkhomenko, Y., Kaehne, T., Luigi Di Salvo, M., Parroni, A., ... Bunik, V. (2015). Molecular mechanisms of the non-coenzyme action of thiamin in brain: Biochemical, structural and pathway analysis. *Scientific Reports*, 5, 12583. <https://doi.org/10.1038/srep12583>
- Mladěnka, P., Macáková, K., Kujovská Krčmová, L., Javorská, L., Mrštná, K., Carazo, A., ... Nováková, L. (2021). Vitamin K – sources, physiological role, kinetics, deficiency, detection, therapeutic use, and toxicity. *Nutrition Reviews*, 80(4), 677–698. <https://doi.org/10.1093/nutrit/nuab061>
- Mo, C., Ke, J., Zhao, D., & Zhang, B. (2020). Role of the renin–angiotensin–aldosterone system in bone metabolism. *Journal of Bone and Mineral Metabolism*, 38(6), 772–779. <https://doi.org/10.1007/s00774-020-01132-y>
- Moghaddam, N., Campana, L., Abegg, C., Vilarino, R., Volland, C., Dedouit, F., ... Fracasso, T. (2023). Hidden lesions: A case of burnt remains. *Forensic Sciences Research*, 8(2), 163–169. <https://doi.org/10.1093/fsr/owad019>
- Na, M. K., Won, Y. D., Kim, C. H., Kim, J. M., Cheong, J. H., Ryu, J. I., & Han, M.H. (2018). Opportunistic osteoporosis screening via the measurement of frontal skull Hounsfield units derived from brain computed tomography images. *PLoS ONE*, 13(5). <https://doi.org/10.1371/journal.pone.0197336>
- Neve, A., Corrado, A., & Cantatore, F. P. (2011). Osteoblast physiology in normal and pathological conditions. *Cell and Tissue Research*, 343(2), 289–302. <https://doi.org/10.1007/s00441-010-1086-1>
- Newman, D. L., Dougherty, G., Obaid, A. A., & Hajrasy, H. A. (1998). Limitations of clinical CT in assessing cortical thickness and density. *Physics in Medicine and Biology*, 43(3), 619–626. <https://doi.org/10.1088/0031-9155/43/3/013>
- O'Donnell, L. (2019). Indicators of stress and their association with frailty in the precontact Southwestern United States. *American Journal of Physical Anthropology*, 170(3), 404–417. <https://doi.org/10.1002/ajpa.23902>
- O'Donnell, L., Buikstra, J. E., Hill, E. C., Anderson, A. S., & O'Donnell Jr, M. J. (2023). Skeletal manifestations of disease experience: Length of illness and porous cranial lesion formation in a contemporary juvenile mortality sample. *American Journal of Human Biology*, 35(8), e23896. <https://doi.org/10.1002/ajhb.23896>
- O'Donnell, L., Hill, E. C., Anderson, A. S. A., & Edgar, H. J. H. (2020). Cribra orbitalia and porotic hyperostosis are associated with respiratory infections in a contemporary mortality sample from New Mexico. *American Journal of Physical Anthropology*, 173(4), 721–733. <https://doi.org/10.1002/ajpa.24131>

- Padayatty, S. J., & Levine, M. (2016). Vitamin C physiology: The known and the unknown and Goldilocks. *Oral Diseases*, 22(6), 463–493. <https://doi.org/10.1111/odi.12446>
- Palmer, B. F., & Clegg, D. J. (2017). Electrolyte Disturbances in Patients with Chronic Alcohol-Use Disorder. *New England Journal of Medicine*, 377(14), 1368–1377. <https://doi.org/10.1056/NEJMra1704724>
- Pedreira-Zamorano, J. D., Lavado-Garcia, J. M., Roncero-Martin, R., Calderon-Garcia, J. F., Rodriguez-Dominguez, T., & Canal-Macias, M. L. (2009). Effect of beer drinking on ultrasound bone mass in women. *Nutrition*, 25(10), 1057–1063. <https://doi.org/10.1016/j.nut.2009.02.007>
- Peris, P., Parés, A., Guañabens, N., Del Río, L., Pons, F., Martínez de Osaba, M. J., ... Muñoz-Gómez, J. (1994). Bone mass improves in alcoholics after 2 years of abstinence. *Journal of Bone and Mineral Research: The Official Journal of the American Society for Bone and Mineral Research*, 9(10), 1607–1612. <https://doi.org/10.1002/jbmr.5650091014>
- Pervaiz, K., Cabezas, A., Downes, K., Santoni, B. G., & Frankle, M. A. (2013). Osteoporosis and shoulder osteoarthritis: Incidence, risk factors, and surgical implications. *Journal of Shoulder and Elbow Surgery*, 22(3), e1–e8. <https://doi.org/10.1016/j.jse.2012.05.029>
- Pickhardt, P. J., Pooler, B. D., Lauder, T., del Rio, A. M., Bruce, R. J., & Binkley, N. (2013). Opportunistic Screening for Osteoporosis Using Abdominal Computed Tomography Scans Obtained for Other Indications. *Annals of Internal Medicine*, 158(8), 588–595. <https://doi.org/10.7326/0003-4819-158-8-201304160-00003>
- Prevrhal, S., Engelke, K., & Kalender, W. A. (1999). Accuracy limits for the determination of cortical width and density: The influence of object size and CT imaging parameters. *Physics in Medicine and Biology*, 44(3), 751–764. <https://doi.org/10.1088/0031-9155/44/3/017>
- Ranke, J. (1884). Verständigung gber ein gemeinsames cranio–metrisches Verfahren (Frankfurter Verständigung). *Archiver Anthropologie*, 15, 1-8.
- Reynolds, M. S. (2014). *Stature estimation of a contemporary Australian sub-population: An evaluation of the Trotter and Gleser method using computed tomography of the femur* (Masters_by_research, Queensland University of Technology). Queensland University of Technology. Retrieved from <https://eprints.qut.edu.au/75735/>
- Rhee, Y., Allen, M. R., Condon, K., Lezcano, V., Ronda, A. C., Galli, C., ... Bellido, T. (2011). PTH receptor signaling in osteocytes governs periosteal bone formation and intracortical remodeling. *Journal of Bone and Mineral Research*, 26(5), 1035–1046. <https://doi.org/10.1002/jbmr.304>

- Rico, H. (1990). Alcohol and Bone Disease. *Alcohol and Alcoholism*, 25(4), 345–352. <https://doi.org/10.1093/oxfordjournals.alcalc.a045014>
- Rink, E. B. (1986). Magnesium Deficiency in Alcoholism. *Alcoholism: Clinical and Experimental Research*, 10(6), 590–594. <https://doi.org/10.1111/j.1530-0277.1986.tb05150.x>
- Rivera, F., & Mirazón Lahr, M. (2017). New evidence suggesting a dissociated etiology for cribra orbitalia and porotic hyperostosis. *American Journal of Physical Anthropology*, 164(1), 76–96. <https://doi.org/10.1002/ajpa.23258>
- Robling, A. G., & Bonewald, L. F. (2020). The Osteocyte: New Insights. *Annual Review of Physiology*, 82(1), 485–506. <https://doi.org/10.1146/annurev-physiol-021119-034332>
- Roche, A. F. (1953). Increase in Cranial Thickness During Growth. *Human Biology*, 25(2), 81–92.
- Rodríguez, J., & Mandalunis, P. M. (2018). A Review of Metal Exposure and Its Effects on Bone Health. *Journal of Toxicology*, 2018, 4854152. <https://doi.org/10.1155/2018/4854152>
- Romme, E. A., Murchison, J. T., Phang, K. F., Jansen, F. H., Rutten, E. P., Wouters, E. F., ... MacNee, W. (2012). Bone attenuation on routine chest CT correlates with bone mineral density on DXA in patients with COPD. *Journal of Bone and Mineral Research*, 27(11), 2338–2343. <https://doi.org/10.1002/jbmr.1678>
- Rosen, C. J. (2020). The Epidemiology and Pathogenesis of Osteoporosis. In *Endotext [Internet]*. MDText.com, Inc. Retrieved from <https://www.ncbi.nlm.nih.gov/sites/books/NBK279134/>
- Rosenthal, W. S., Adham, N. F., Lopez, R., & Cooperman, J. M. (1973). Riboflavin deficiency in complicated chronic alcoholism. *The American Journal of Clinical Nutrition*, 26(8), 858–860. <https://doi.org/10.1093/ajcn/26.8.858>
- Rothschild, B. M. (2022). The bare bones appearance of hyperparathyroidism: Distinguishing subperiosteal bone resorption from periosteal reaction. *International Journal of Osteoarchaeology*, 32(1), 276–282. <https://doi.org/10.1002/oa.3063>
- Ross, A. H., Jantz, R. L., & McCormick, W. F. (1998). Cranial Thickness in American Females and Males. *Journal of Forensic Sciences*, 43(2), 267–272. <https://doi.org/10.1520/JFS16218J>
- Rowbotham, S. K., Mole, C. G., Tieppo, D., Blaszkowska, M., Cordner, S. M., & Blau, S. (2022). Average thickness of the bones of the human neurocranium: Development of reference measurements to assist with blunt force trauma interpretations. *International Journal of Legal Medicine*. <https://doi.org/10.1007/s00414-022-02824-y>

- Saint-Martin, P., Rérolle, C., Dedouit, F., Bouilleau, L., Rousseau, H., Rougé, D., & Telmon, N. (2013). Age estimation by magnetic resonance imaging of the distal tibial epiphysis and the calcaneum. *International Journal of Legal Medicine*, 127(5), 1023–1030. <https://doi.org/10.1007/s00414-013-0844-5>
- Saitta, J. C., Lipkin, E. W., & Howard, G. A. (1989). Acetate inhibition of chick bone cell proliferation and bone growth in vitro. *Journal of Bone and Mineral Research*, 4(3), 379–386. <https://doi.org/10.1002/jbmr.5650040312>
- Sandiofrt, E. (1783). Caput quintum. De sinusati profundo, in utroque osse verticis obervato. In *Exercitationes Acadmiceae*.
- Scheirs, S., Cos, M., McGlynn, H., Ortega-Sánchez, M., Malgosa, A., & Galtés, I. (2020). Visualization and documentation of perimortem traits in long bone fractures using computed tomography. *Forensic Science, Medicine and Pathology*, 16(2), 281–286. <https://doi.org/10.1007/s12024-020-00237-0>
- Schreiber, J. J., Anderson, P. A., & Hsu, W. K. (2014). Use of computed tomography for assessing bone mineral density. *Neurosurgical Focus*, 37(1), E4. <https://doi.org/10.3171/2014.5.FOCUS1483>
- Schreiber, J. J., Anderson, P. A., Rosas, H. G., Buchholz, A. L., & Au, A. G. (2011). Hounsfield Units for Assessing Bone Mineral Density and Strength: A Tool for Osteoporosis Management. *JBJS*, 93(11), 1057–1063. <https://doi.org/10.2106/JBJS.J.00160>
- Shah, K. M., Wilkinson, J. M., & Gartland, A. (2015). Cobalt and chromium exposure affects osteoblast function and impairs the mineralization of prosthesis surfaces in vitro. *Journal of Orthopaedic Research: Official Publication of the Orthopaedic Research Society*, 33(11), 1663–1670. <https://doi.org/10.1002/jor.22932>
- Smith, G. E. (1907). The Causation of the Symmetrical Thinning of the Parietal Bones in Ancient Egyptians. *Journal of Anatomy and Physiology*, 41(Pt 3), 232–233.
- Smith, S. J., Lopresti, A. L., & Fairchild, T. J. (2023). The effects of alcohol on testosterone synthesis in men: A review. *Expert Review of Endocrinology & Metabolism*, 18(2), 155–166. <https://doi.org/10.1080/17446651.2023.2184797>
- Song, M., Huo, H., Cao, Z., Han, Y., & Gao, L. (2017). Aluminum Trichloride Inhibits the Rat Osteoblasts Mineralization In Vitro. *Biological Trace Element Research*, 175(1), 186–193. <https://doi.org/10.1007/s12011-016-0761-9>
- Sorg M, Hunter L, & Benson J. (2004). The Use of Computerized Tomography and Radiography in Examining Colonists of Samuel de Champlain’s 1604 Settlement of Isle de Ste. Croix. *Proceedings of the Society for Historical Archaeology*. Presented at the 37th Annual Conference on Historical and Underwater Archaeology, St. Louis, MO. St. Louis, MO.

- Spencer, H., Rubio, N., Rubio, E., Indreika, M., & Seitam, A. (1986). Chronic alcoholism. Frequently overlooked cause of osteoporosis in men. *The American Journal of Medicine*, 80(3), 393–397. [https://doi.org/10.1016/0002-9343\(86\)90712-6](https://doi.org/10.1016/0002-9343(86)90712-6)
- Spies, A. J., Steyn, M., Bussy, E., & Brits, D. (2020). Forensic imaging: The sensitivities of various imaging modalities in detecting skeletal trauma in simulated cases of child abuse using a pig model. *Journal of Forensic and Legal Medicine*, 76, 102034. <https://doi.org/10.1016/j.jflm.2020.102034>
- Spies, A. J., Steyn, M., Prince, D. N., & Brits, D. (2021). Can forensic anthropologists accurately detect skeletal trauma using radiological imaging? *Forensic Imaging*, 24, 200424. <https://doi.org/10.1016/j.fri.2020.200424>
- Sripanyakorn, S., Jugdaohsingh, R., Mander, A., Davidson, S. L., Thompson, R. P., & Powell, J. J. (2009). Moderate ingestion of alcohol is associated with acute ethanol-induced suppression of circulating CTX in a PTH-independent fashion. *Journal of Bone and Mineral Research: The Official Journal of the American Society for Bone and Mineral Research*, 24(8), 1380–1388. <https://doi.org/10.1359/jbmr.090222>
- Suwannasom, N., Kao, I., Pruß, A., Georgieva, R., & Bäumlner, H. (2020). Riboflavin: The Health Benefits of a Forgotten Natural Vitamin. *International Journal of Molecular Sciences*, 21(3), 950. <https://doi.org/10.3390/ijms21030950>
- Takeuchi, S., Takasato, Y., Masaoka, H., Hayakawa, T., Otani, N., Yoshino, Y., & Yatsushige, H. (2008). [3D CT findings of biparietal thinning]. *Brain and Nerve = Shinkei Kenkyu No Shinpo*, 60(3), 296–297.
- Thaler, H. T., Ferber, P. W., & Rottenberg, D. A. (1978). A statistical method for determining the proportions of gray matter, white matter, and CSF using computed tomography. *Neuroradiology*, 16, 133–135. <https://doi.org/10.1007/BF00395227>
- Titorencu, I., Pruna, V., Jinga, V. V., & Simionescu, M. (2014). Osteoblast ontogeny and implications for bone pathology: An overview. *Cell and Tissue Research*, 355(1), 23–33. <https://doi.org/10.1007/s00441-013-1750-3>
- Torimitsu, S., Nishida, Y., Takano, T., Koizumi, Y., Makino, Y., Yajima, D., ... Iwase, H. (2014)a. Statistical analysis of biomechanical properties of the adult skull and age-related structural changes by sex in a Japanese forensic sample. *Forensic Science International*, 234, 185.e1-185.e9. <https://doi.org/10.1016/j.forsciint.2013.10.001>
- Torimitsu, S., Makino, Y., Saitoh, H., Sakuma, A., Ishii, N., Hayakawa, M., ... Iwase, H. (2014)b. Stature estimation based on radial and ulnar lengths using three-dimensional images from multidetector computed tomography in a Japanese population. *Legal Medicine*, 16(4), 181–186. <https://doi.org/10.1016/j.legalmed.2014.03.001>

- Treecce, G. M., Gee, A. H., Mayhew, P. M., & Poole, K. E. S. (2010). High resolution cortical bone thickness measurement from clinical CT data. *Medical Image Analysis, 14*(3), 276–290. <https://doi.org/10.1016/j.media.2010.01.003>
- Tucker, K. L., Jugdaohsingh, R., Powell, J. J., Qiao, N., Hannan, M. T., Sripanyakorn, S., ... Kiel, D. P. (2009). Effects of beer, wine, and liquor intakes on bone mineral density in older men and women. *The American Journal of Clinical Nutrition, 89*(4), 1188–1196. <https://doi.org/10.3945/ajcn.2008.26765>
- Turner, R. T., & Iwaniec, U. T. (2010). Moderate weight gain does not influence bone metabolism in skeletally mature female rats. *Bone, 47*(3), 631–635. <https://doi.org/10.1016/j.bone.2010.06.010>
- Turner, Russell T. (2000). Skeletal Response to Alcohol. *Alcoholism: Clinical and Experimental Research, 24*(11), 1693–1701. <https://doi.org/10.1111/j.1530-0277.2000.tb01971.x>
- Uldin, T. (2017). Virtual anthropology – a brief review of the literature and history of computed tomography. *Forensic Sciences Research, 2*(4), 165–173. <https://doi.org/10.1080/20961790.2017.1369621>
- U.S. Department of Health and Human Services, Substance Abuse and Mental Health Services Administration, Center for Behavioral Health Statistics and Quality. (2018). *National Survey on Drug Use and Health 2016* (NSDUH-2016-DS0001). Retrieved from <https://datafiles.samhsa.gov/>
- Van Dort, M. J., Driessen, J. H. M., Geusens, P., Romme, E. A. P. M., Smeenk, F. W. J. M., Wouters, E. F. M., & Van Den Bergh, J. P. W. (2019). Vertebral bone attenuation in Hounsfield Units and prevalent vertebral fractures are associated with the short-term risk of vertebral fractures in current and ex-smokers with and without COPD: A 3-year chest CT follow-up study. *Osteoporosis International, 30*(8), 1561–1571. <https://doi.org/10.1007/s00198-019-04977-w>
- van Meurs Joyce B.J., Dhonukshe-Rutten Rosalie A.M., Pluijm Saskia M.F., van der Klift Marjolein, de Jonge Robert, Lindemans Jan, ... Uitterlinden André G. (2004). Homocysteine Levels and the Risk of Osteoporotic Fracture. *New England Journal of Medicine, 350*(20), 2033–2041. <https://doi.org/10.1056/NEJMoa032546>
- Venkat, K. K., Arora, M. M., Singh, P., Desai, M., & Khatkhatay, I. (2009). Effect of alcohol consumption on bone mineral density and hormonal parameters in physically active male soldiers. *Bone, 45*(3), 449–454. <https://doi.org/10.1016/j.bone.2009.05.005>
- Villa, C., Buckberry, J., Cattaneo, C., Frohlich, B., & Lynnerup, N. (2015). Quantitative analysis of the morphological changes of the pubic symphyseal face and the auricular surface and implications for age at death estimation. *Journal of Forensic Sciences, 60*(3), 556–565. <https://doi.org/10.1111/1556-4029.12689>

- Virchow, R. Zur Frankfurter Verstäädigung. XXII Versammlung der Deutschen Anthropologischen Gesellschaft, Danzig, CBDAG 22 (1891): 121-124.
- Voie, A., Dirnbacher, M., Fisher, D., & Hölscher, T. (2014). Parametric mapping and quantitative analysis of the human calvarium. *Computerized Medical Imaging and Graphics*, 38(8), 675–682. <https://doi.org/10.1016/j.compmedimag.2014.06.022>
- Waldron, T. (2009). *Paleopathology*. Cambridge University Press.
- Walter, S. D., Eliasziw, M., & Donner, A. (1998). Sample size and optimal designs for reliability studies. *Statistics in Medicine*, 17(1), 101–110. [https://doi.org/10.1002/\(sici\)1097-0258\(19980115\)17:1<101::aid-sim727>3.0.co;2-e](https://doi.org/10.1002/(sici)1097-0258(19980115)17:1<101::aid-sim727>3.0.co;2-e)
- Wang, Y., Bikle, D. D., & Chang, W. (2013). Autocrine and Paracrine Actions of IGF-I Signaling in Skeletal Development. *Bone Research*, 1(1), 249–259. <https://doi.org/10.4248/BR201303003>
- Watamaniuk, L., & Rogers, T. (2010). Positive Personal Identification of Human Remains Based on Thoracic Vertebral Margin Morphology. *Journal of Forensic Sciences*, 55(5), 1162–1170. <https://doi.org/10.1111/j.1556-4029.2010.01447.x>
- Weber, N. K., Fidler, J. L., Keaveny, T. M., Clarke, B. L., Khosla, S., Fletcher, J. G., ... Bruining, D. H. (2014). Validation of a CT-Derived Method for Osteoporosis Screening in IBD Patients Undergoing Contrast-Enhanced CT Enterography. *The American Journal of Gastroenterology*, 109(3), 401–408. <https://doi.org/10.1038/ajg.2013.478>
- What Is A Standard Drink? | National Institute on Alcohol Abuse and Alcoholism (NIAAA). (n.d.). Retrieved May 26, 2024, from <https://www.niaaa.nih.gov/alcohols-effects-health/overview-alcohol-consumption/what-standard-drink#>
- Williams, F., Cherkas, L., Spector, T., & MacGregor, A. (2005). The effect of moderate alcohol consumption on bone mineral density: A study of female twins. *Annals of the Rheumatic Diseases*, 64(2), 309–310. <https://doi.org/10.1136/ard.2004.022269>
- Winter, K. A., Alston-Knox, C., Meredith, M., & MacGregor, D. (2021). Estimating biological sex and stature from the humerus: A pilot study using a contemporary Australian sub-population using computed tomography. *Forensic Science International: Reports*, 4, 100227. <https://doi.org/10.1016/j.fsir.2021.100227>
- Wong, A. K. O., Beattie, K. A., Bhargava, A., Cheung, M., Webber, C. E., Chettle, D. R., ... Adachi, J. D. (2015). Bone lead (Pb) content at the tibia is associated with thinner distal tibia cortices and lower volumetric bone density in postmenopausal women. *Bone*, 79, 58–64. <https://doi.org/10.1016/j.bone.2015.05.010>

- Yamada, M., Briot, J., Pedrono, A., Sans, N., Mansat, P., Mansat, M., & Swider, P. (2007). Age- and gender-related distribution of bone tissue of osteoporotic humeral head using computed tomography. *Journal of Shoulder and Elbow Surgery*, *16*(5), 596–602. <https://doi.org/10.1016/j.jse.2007.01.006>
- Yee, M. M. F., Chin, K.-Y., Ima-Nirwana, S., & Wong, S. K. (2021). Vitamin A and Bone Health: A Review on Current Evidence. *Molecules*, *26*(6), 1757. <https://doi.org/10.3390/molecules26061757>
- Yiu Luk, S., Fai Shum, J. S., Wai Chan, J. K., & San Khoo, J. L. (2010). Bilateral thinning of the parietal bones: A case report and review of radiological features. *The Pan African Medical Journal*, *4*. Retrieved from <https://www.ncbi.nlm.nih.gov/pmc/articles/PMC2984314/>
- Yoganandan, N., Pintar, F. A., Sances, A., Walsh, P. R., Ewing, C. L., Thomas, D. J., & Snyder, R. G. (1995). Biomechanics of Skull Fracture. *Journal of Neurotrauma*, *12*(4), 659–668. <https://doi.org/10.1089/neu.1995.12.659>
- Zaidi, Q., Danisa, O., & Cheng, W. (2018). Measurement Techniques and Utility of Hounsfield Unit Values for Assessment of Bone Quality Prior to Spinal Instrumentation: A Review of Current Literature. *Spine*. <https://doi.org/10.1097/BRS.0000000000002813>
- Zdrojewicz, Z., Popowicz, E., & Winiarski, J. (2016). [Nickel—Role in human organism and toxic effects]. *Polski Mercuriusz Lekarski: Organ Polskiego Towarzystwa Lekarskiego*, *41*(242), 115–118.
- Zhang, K., Luo, Y., Fan, F., Zheng, J., Yang, M., Li, T., ... Deng, Z. (2015). Stature estimation from sternum length using computed tomography–volume rendering technique images of western Chinese. *Journal of Forensic and Legal Medicine*, *35*, 40–44. <https://doi.org/10.1016/j.jflm.2015.07.003>

APPENDIX A

PERMISSION TO USE PHOTOGRAPHS

ATTORNEY GENERAL
DEPARTMENT OF JUSTICE

OFFICE OF THE CHIEF MEDICAL EXAMINER

JOHN M. FORMELLA
ATTORNEY GENERAL



JAMES T. BOFFETTI
DEPUTY ATTORNEY GENERAL

July 13, 2024

Jamie A. Wren, MPH
Research Associate
Margaret Chase Smith Policy Center
University of Maine

Dear Mr. Wren:

You have my permission to use de-identified photos taken during the examination of case [REDACTED] for your doctoral dissertation.

Sincerely,

A handwritten signature in cursive script, appearing to read "Jennie V. Duval".

Jennie V. Duval, M.D.
Chief Medical Examiner

APPENDIX B

ANALYSIS OF COVARIANCE AND PEARSON CORRELATION TABLES

Table 45 Analysis of Covariance for minimum segment thickness controlling for decedent age

Tests of Between-Subjects Effects

Dependent Variable: Minimum Thickness

Segment	Source	Type III Sum of			F	Sig.
		Squares	df	Mean Square		
LC	Corrected Model	15.231 ^a	2	7.615	13.050	<.001
	Intercept	14.610	1	14.610	25.037	<.001
	Age	1.608	1	1.608	2.756	.099
	RiskGroup	14.703	1	14.703	25.197	<.001
	Error	81.695	140	.584		
	Total	659.287	143			
	Corrected Total	96.926	142			
LF	Corrected Model	2.249 ^b	2	1.124	1.003	.369
	Intercept	33.717	1	33.717	30.078	<.001
	Age	1.790	1	1.790	1.597	.208
	RiskGroup	.743	1	.743	.663	.417
	Error	156.937	140	1.121		
	Total	1280.621	143			
	Corrected Total	159.185	142			
LO	Corrected Model	3.664 ^c	2	1.832	3.788	.025
	Intercept	20.365	1	20.365	42.099	<.001
	Age	.002	1	.002	.005	.945
	RiskGroup	3.613	1	3.613	7.469	.007
	Error	67.724	140	.484		
	Total	529.811	143			
	Corrected Total	71.388	142			
LT	Corrected Model	10.323 ^d	2	5.161	17.145	<.001
	Intercept	22.092	1	22.092	73.384	<.001
	Age	.189	1	.189	.628	.430
	RiskGroup	10.323	1	10.323	34.290	<.001
	Error	41.844	139	.301		
	Total	628.378	142			
	Corrected Total	52.167	141			

Table 45 continued

RC	Corrected Model	10.668 ^e	2	5.334	13.430	<.001
	Intercept	18.098	1	18.098	45.566	<.001
	Age	.350	1	.350	.882	.349
	RiskGroup	10.652	1	10.652	26.820	<.001
	Error	55.604	140	.397		
	Total	579.383	143			
	Corrected Total	66.272	142			
RF	Corrected Model	.649 ^f	2	.325	.333	.717
	Intercept	33.749	1	33.749	34.611	<.001
	Age	.333	1	.333	.342	.560
	RiskGroup	.408	1	.408	.419	.519
	Error	136.514	140	.975		
	Total	1037.412	143			
	Corrected Total	137.163	142			
RO	Corrected Model	3.319 ^g	2	1.659	4.001	.020
	Intercept	21.379	1	21.379	51.554	<.001
	Age	.232	1	.232	.559	.456
	RiskGroup	2.788	1	2.788	6.723	.011
	Error	58.057	140	.415		
	Total	441.717	143			
	Corrected Total	61.376	142			
RT	Corrected Model	6.561 ^h	2	3.281	9.248	<.001
	Intercept	22.684	1	22.684	63.944	<.001
	Age	.099	1	.099	.280	.597
	RiskGroup	6.559	1	6.559	18.488	<.001
	Error	49.665	140	.355		
	Total	622.597	143			
	Corrected Total	56.227	142			

a. R Squared = .157 (Adjusted R Squared = .145)

b. R Squared = .014 (Adjusted R Squared = .000)

c. R Squared = .051 (Adjusted R Squared = .038)

d. R Squared = .198 (Adjusted R Squared = .186)

e. R Squared = .161 (Adjusted R Squared = .149)

f. R Squared = .005 (Adjusted R Squared = -.009)

g. R Squared = .054 (Adjusted R Squared = .041)

h. R Squared = .117 (Adjusted R Squared = .104)

Table 46 Analysis of Covariance for minimum segment thickness controlling for decedent population affinity

Tests of Between-Subjects Effects

Dependent Variable: Minimum Thickness

Segment	Source	Type III Sum of			F	Sig.
		Squares	df	Mean Square		
LC	Corrected Model	14.464 ^a	2	7.232	12.279	<.001
	Intercept	206.174	1	206.174	350.034	<.001
	PopAff	.842	1	.842	1.429	.234
	RiskGroup	13.032	1	13.032	22.125	<.001
	Error	82.462	140	.589		
	Total	659.287	143			
	Corrected Total	96.926	142			
LF	Corrected Model	11.281 ^b	2	5.640	5.339	.006
	Intercept	269.672	1	269.672	255.259	<.001
	PopAff	10.822	1	10.822	10.244	.002
	RiskGroup	.859	1	.859	.813	.369
	Error	147.905	140	1.056		
	Total	1280.621	143			
	Corrected Total	159.185	142			
LO	Corrected Model	4.464 ^c	2	2.232	4.669	.011
	Intercept	132.726	1	132.726	277.652	<.001
	PopAff	.802	1	.802	1.677	.197
	RiskGroup	3.907	1	3.907	8.172	.005
	Error	66.925	140	.478		
	Total	529.811	143			
	Corrected Total	71.388	142			
LT	Corrected Model	11.250 ^d	2	5.625	19.109	<.001
	Intercept	165.501	1	165.501	562.229	<.001
	PopAff	1.117	1	1.117	3.793	.053
	RiskGroup	10.619	1	10.619	36.074	<.001
	Error	40.917	139	.294		
	Total	628.378	142			
	Corrected Total	52.167	141			

Table 46 continued

RC	Corrected Model	10.490 ^e	2	5.245	13.164	<.001
	Intercept	177.711	1	177.711	446.017	<.001
	PopAff	.173	1	.173	.433	.512
	RiskGroup	10.055	1	10.055	25.235	<.001
	Error	55.782	140	.398		
	Total	579.383	143			
	Corrected Total	66.272	142			
RF	Corrected Model	17.820 ^f	2	8.910	10.452	<.001
	Intercept	187.620	1	187.620	220.095	<.001
	PopAff	17.504	1	17.504	20.534	<.001
	RiskGroup	.775	1	.775	.909	.342
	Error	119.343	140	.852		
	Total	1037.412	143			
	Corrected Total	137.163	142			
RO	Corrected Model	3.941 ^g	2	1.970	4.803	.010
	Intercept	108.262	1	108.262	263.892	<.001
	PopAff	.854	1	.854	2.081	.151
	RiskGroup	3.321	1	3.321	8.095	.005
	Error	57.435	140	.410		
	Total	441.717	143			
	Corrected Total	61.376	142			
RT	Corrected Model	8.485 ^h	2	4.243	12.442	<.001
	Intercept	155.324	1	155.324	455.482	<.001
	PopAff	2.023	1	2.023	5.934	.016
	RiskGroup	6.987	1	6.987	20.490	<.001
	Error	47.741	140	.341		
	Total	622.597	143			
	Corrected Total	56.227	142			

a. R Squared = .149 (Adjusted R Squared = .137)

b. R Squared = .071 (Adjusted R Squared = .058)

c. R Squared = .063 (Adjusted R Squared = .049)

d. R Squared = .216 (Adjusted R Squared = .204)

e. R Squared = .158 (Adjusted R Squared = .146)

f. R Squared = .130 (Adjusted R Squared = .117)

g. R Squared = .064 (Adjusted R Squared = .051)

h. R Squared = .151 (Adjusted R Squared = .139)

Table 47 Analysis of Covariance for segment volume controlling for decedent age

Tests of Between-Subjects Effects

Dependent Variable: Volume [mm3] (1)

Segment	Source	Type III Sum of			F	Sig.
		Squares	df	Mean Square		
LC	Corrected Model	818330.872 ^a	2	409165.436	4.269	.016
	Intercept	3023093.102	1	3023093.102	31.538	<.001
	Age	807215.265	1	807215.265	8.421	.004
	RiskGroup	54254.387	1	54254.387	.566	.453
	Error	13515739.120	141	95856.306		
	Total	167143679.871	144			
	Corrected Total	14334069.991	143			
LF	Corrected Model	139991.409 ^b	2	69995.705	1.127	.327
	Intercept	6547794.082	1	6547794.082	105.430	<.001
	Age	93524.622	1	93524.622	1.506	.222
	RiskGroup	28756.023	1	28756.023	.463	.497
	Error	8756924.438	141	62105.847		
	Total	191518607.166	144			
	Corrected Total	8896915.847	143			
LO	Corrected Model	540415.741 ^c	2	270207.870	2.709	.070
	Intercept	6746400.385	1	6746400.385	67.641	<.001
	Age	443854.808	1	443854.808	4.450	.037
	RiskGroup	162319.903	1	162319.903	1.627	.204
	Error	14063140.981	141	99738.589		
	Total	99435124.662	144			
	Corrected Total	14603556.722	143			
LT	Corrected Model	29478.156 ^d	2	14739.078	.370	.691
	Intercept	3950600.172	1	3950600.172	99.175	<.001
	Age	26637.736	1	26637.736	.669	.415
	RiskGroup	923.560	1	923.560	.023	.879
	Error	5576870.570	140	39834.790		
	Total	108197877.006	143			
	Corrected Total	5606348.726	142			

Table 47 continued

RC	Corrected Model	366006.238 ^e	2	183003.119	2.064	.131
	Intercept	4177496.746	1	4177496.746	47.108	<.001
	Age	339739.803	1	339739.803	3.831	.052
	RiskGroup	59447.070	1	59447.070	.670	.414
	Error	12503882.462	141	88680.017		
	Total	165243770.030	144			
	Corrected Total	12869888.700	143			
RF	Corrected Model	109748.977 ^f	2	54874.488	.941	.393
	Intercept	6916308.552	1	6916308.552	118.553	<.001
	Age	6806.381	1	6806.381	.117	.733
	RiskGroup	93475.128	1	93475.128	1.602	.208
	Error	8225849.702	141	58339.360		
	Total	172749354.514	144			
	Corrected Total	8335598.679	143			
RO	Corrected Model	637076.286 ^g	2	318538.143	3.112	.048
	Intercept	7105011.255	1	7105011.255	69.412	<.001
	Age	567946.371	1	567946.371	5.548	.020
	RiskGroup	141475.528	1	141475.528	1.382	.242
	Error	14330500.425	140	102360.717		
	Total	98635230.049	143			
	Corrected Total	14967576.711	142			
RT	Corrected Model	2204.897 ^h	2	1102.449	.024	.976
	Intercept	4351178.717	1	4351178.717	94.981	<.001
	Age	2193.941	1	2193.941	.048	.827
	RiskGroup	11.748	1	11.748	.000	.987
	Error	6459388.376	141	45811.265		
	Total	107946464.834	144			
	Corrected Total	6461593.273	143			

a. R Squared = .057 (Adjusted R Squared = .044)

b. R Squared = .016 (Adjusted R Squared = .002)

c. R Squared = .037 (Adjusted R Squared = .023)

d. R Squared = .005 (Adjusted R Squared = -.009)

e. R Squared = .028 (Adjusted R Squared = .015)

f. R Squared = .013 (Adjusted R Squared = -.001)

g. R Squared = .043 (Adjusted R Squared = .029)

h. R Squared = .000 (Adjusted R Squared = -.014)

Table 48 Analysis of Covariance for segment volume controlling for decedent population affinity

Tests of Between-Subjects Effects

Dependent Variable: Volume [mm3] (1)

Segment	Source	Type III Sum of Squares	df	Mean Square	F	Sig.
LC	Corrected Model	294509.259 ^a	2	147254.630	1.479	.231
	Intercept	56258435.165	1	56258435.165	565.006	<.001
	PopAff	283393.653	1	283393.653	2.846	.094
	RiskGroup	4484.039	1	4484.039	.045	.832
	Error	14039560.732	141	99571.353		
	Total	167143679.871	144			
	Corrected Total	14334069.991	143			
LF	Corrected Model	268194.956 ^b	2	134097.478	2.191	.116
	Intercept	53698925.400	1	53698925.400	877.482	<.001
	PopAff	221728.169	1	221728.169	3.623	.059
	RiskGroup	32840.821	1	32840.821	.537	.465
	Error	8628720.891	141	61196.602		
	Total	191518607.166	144			
	Corrected Total	8896915.847	143			
LO	Corrected Model	115412.243 ^c	2	57706.121	.562	.572
	Intercept	26431742.425	1	26431742.425	257.236	<.001
	PopAff	18851.310	1	18851.310	.183	.669
	RiskGroup	90054.241	1	90054.241	.876	.351
	Error	14488144.480	141	102752.798		
	Total	99435124.662	144			
	Corrected Total	14603556.722	143			
LT	Corrected Model	152953.417 ^d	2	76476.709	1.963	.144
	Intercept	29817513.826	1	29817513.826	765.478	<.001
	PopAff	150112.997	1	150112.997	3.854	.052
	RiskGroup	553.270	1	553.270	.014	.905
	Error	5453395.309	140	38952.824		
	Total	108197877.006	143			
	Corrected Total	5606348.726	142			
RC	Corrected Model	140682.681 ^e	2	70341.341	.779	.461

Table 48 continued

	Intercept	53766939.733	1	53766939.733	595.570	<.001
	PopAff	114416.247	1	114416.247	1.267	.262
	RiskGroup	18873.751	1	18873.751	.209	.648
	Error	12729206.019	141	90278.057		
	Total	165243770.030	144			
	Corrected Total	12869888.700	143			
RF	Corrected Model	528889.032 ^f	2	264444.516	4.776	.010
	Intercept	45987263.261	1	45987263.261	830.594	<.001
	PopAff	425946.436	1	425946.436	7.693	.006
	RiskGroup	74634.126	1	74634.126	1.348	.248
	Error	7806709.647	141	55366.735		
	Total	172749354.514	144			
	Corrected Total	8335598.679	143			
RO	Corrected Model	78951.476 ^g	2	39475.738	.371	.691
	Intercept	28050589.677	1	28050589.677	263.764	<.001
	PopAff	9821.562	1	9821.562	.092	.762
	RiskGroup	72364.578	1	72364.578	.680	.411
	Error	14888625.235	140	106347.323		
	Total	98635230.049	143			
	Corrected Total	14967576.711	142			
RT	Corrected Model	205093.888 ^h	2	102546.944	2.311	.103
	Intercept	28975560.709	1	28975560.709	653.010	<.001
	PopAff	205082.933	1	205082.933	4.622	.033
	RiskGroup	852.132	1	852.132	.019	.890
	Error	6256499.384	141	44372.336		
	Total	107946464.834	144			
	Corrected Total	6461593.273	143			

a. R Squared = .021 (Adjusted R Squared = .007)

b. R Squared = .030 (Adjusted R Squared = .016)

c. R Squared = .008 (Adjusted R Squared = -.006)

d. R Squared = .027 (Adjusted R Squared = .013)

e. R Squared = .011 (Adjusted R Squared = -.003)

f. R Squared = .063 (Adjusted R Squared = .050)

g. R Squared = .005 (Adjusted R Squared = -.009)

h. R Squared = .032 (Adjusted R Squared = .018)

Table 49 Analysis of Covariance for minimum Hounsfield units controlling for decedent age

Tests of Between-Subjects Effects

Dependent Variable: Minimum [hnsfU]

Segment	Source	Type III Sum of			F	Sig.
		Squares	df	Mean Square		
LC	Corrected Model	152874.285 ^a	2	76437.143	3.621	.029
	Intercept	54353.799	1	54353.799	2.575	.111
	Age	50347.392	1	50347.392	2.385	.125
	RiskGroup	81105.399	1	81105.399	3.842	.052
	Error	2976316.041	141	21108.624		
	Total	3131903.000	144			
	Corrected Total	3129190.326	143			
LF	Corrected Model	94728.368 ^b	2	47364.184	1.232	.295
	Intercept	981.148	1	981.148	.026	.873
	Age	20916.251	1	20916.251	.544	.462
	RiskGroup	61598.042	1	61598.042	1.603	.208
	Error	5419822.069	141	38438.454		
	Total	5796777.000	144			
	Corrected Total	5514550.438	143			
LO	Corrected Model	184959.986 ^c	2	92479.993	3.719	.027
	Intercept	11716.740	1	11716.740	.471	.494
	Age	9332.594	1	9332.594	.375	.541
	RiskGroup	183690.126	1	183690.126	7.388	.007
	Error	3505952.653	141	24864.912		
	Total	3697774.000	144			
	Corrected Total	3690912.639	143			
LT	Corrected Model	234417.425 ^d	2	117208.713	2.023	.136
	Intercept	52098.348	1	52098.348	.899	.345
	Age	600.228	1	600.228	.010	.919
	RiskGroup	226202.600	1	226202.600	3.904	.050
	Error	8112740.547	140	57948.147		
	Total	9243417.000	143			
	Corrected Total	8347157.972	142			
RC	Corrected Model	71590.848 ^e	2	35795.424	2.628	.076

Table 49 continued

	Intercept	5040.484	1	5040.484	.370	.544
	Age	83.109	1	83.109	.006	.938
	RiskGroup	69354.278	1	69354.278	5.093	.026
	Error	1920219.090	141	13618.575		
	Total	2071475.000	144			
	Corrected Total	1991809.938	143			
RF	Corrected Model	375947.540 ^f	2	187973.770	5.369	.006
	Intercept	60844.134	1	60844.134	1.738	.190
	Age	16601.706	1	16601.706	.474	.492
	RiskGroup	374206.035	1	374206.035	10.688	.001
	Error	4936481.953	141	35010.510		
	Total	5667149.000	144			
	Corrected Total	5312429.493	143			
RO	Corrected Model	176650.023 ^g	2	88325.011	3.921	.022
	Intercept	17331.126	1	17331.126	.769	.382
	Age	13692.422	1	13692.422	.608	.437
	RiskGroup	173810.938	1	173810.938	7.716	.006
	Error	3153585.726	140	22525.612		
	Total	3340559.000	143			
	Corrected Total	3330235.748	142			
RT	Corrected Model	115600.870 ^h	2	57800.435	1.099	.336
	Intercept	16511.971	1	16511.971	.314	.576
	Age	13527.482	1	13527.482	.257	.613
	RiskGroup	110786.273	1	110786.273	2.106	.149
	Error	7418228.623	141	52611.551		
	Total	8813179.000	144			
	Corrected Total	7533829.493	143			

a. R Squared = .049 (Adjusted R Squared = .035)

b. R Squared = .017 (Adjusted R Squared = .003)

c. R Squared = .050 (Adjusted R Squared = .037)

d. R Squared = .028 (Adjusted R Squared = .014)

e. R Squared = .036 (Adjusted R Squared = .022)

f. R Squared = .071 (Adjusted R Squared = .058)

g. R Squared = .053 (Adjusted R Squared = .040)

h. R Squared = .015 (Adjusted R Squared = .001)

Table 50 Analysis of Covariance for minimum Hounsfeld units controlling for decedent population affinity

Tests of Between-Subjects Effects

Dependent Variable: Minimum [hnsfU]

Segment	Source	Type III Sum of			F	Sig.
		Squares	df	Mean Square		
LC	Corrected Model	148916.610 ^a	2	74458.305	3.523	.032
	Intercept	19413.098	1	19413.098	.918	.340
	PopAff	46389.716	1	46389.716	2.195	.141
	RiskGroup	112108.880	1	112108.880	5.304	.023
	Error	2980273.717	141	21136.693		
	Total	3131903.000	144			
	Corrected Total	3129190.326	143			
LF	Corrected Model	207745.132 ^b	2	103872.566	2.760	.067
	Intercept	10.663	1	10.663	.000	.987
	PopAff	133933.014	1	133933.014	3.559	.061
	RiskGroup	59890.528	1	59890.528	1.591	.209
	Error	5306805.306	141	37636.917		
	Total	5796777.000	144			
	Corrected Total	5514550.438	143			
LO	Corrected Model	182939.526 ^c	2	91469.763	3.677	.028
	Intercept	1077.403	1	1077.403	.043	.835
	PopAff	7312.134	1	7312.134	.294	.589
	RiskGroup	169631.706	1	169631.706	6.818	.010
	Error	3507973.113	141	24879.242		
	Total	3697774.000	144			
	Corrected Total	3690912.639	143			
LT	Corrected Model	696203.840 ^d	2	348101.920	6.370	.002
	Intercept	1227926.504	1	1227926.504	22.469	<.001
	PopAff	462386.642	1	462386.642	8.461	.004
	RiskGroup	185029.085	1	185029.085	3.386	.068
	Error	7650954.133	140	54649.672		
	Total	9243417.000	143			
	Corrected Total	8347157.972	142			

Table 50 continued

RC	Corrected Model	73404.464 ^e	2	36702.232	2.698	.071
	Intercept	41343.310	1	41343.310	3.039	.083
	PopAff	1896.725	1	1896.725	.139	.709
	RiskGroup	69482.479	1	69482.479	5.107	.025
	Error	1918405.474	141	13605.713		
	Total	2071475.000	144			
	Corrected Total	1991809.938	143			
RF	Corrected Model	423668.706 ^f	2	211834.353	6.110	.003
	Intercept	13889.056	1	13889.056	.401	.528
	PopAff	64322.872	1	64322.872	1.855	.175
	RiskGroup	336066.499	1	336066.499	9.693	.002
	Error	4888760.787	141	34672.062		
	Total	5667149.000	144			
	Corrected Total	5312429.493	143			
RO	Corrected Model	162976.732 ^g	2	81488.366	3.602	.030
	Intercept	1859.703	1	1859.703	.082	.775
	PopAff	19.132	1	19.132	.001	.977
	RiskGroup	161980.170	1	161980.170	7.160	.008
	Error	3167259.016	140	22623.279		
	Total	3340559.000	143			
	Corrected Total	3330235.748	142			
RT	Corrected Model	217540.866 ^h	2	108770.433	2.096	.127
	Intercept	869570.870	1	869570.870	16.758	<.001
	PopAff	115467.479	1	115467.479	2.225	.138
	RiskGroup	86603.566	1	86603.566	1.669	.199
	Error	7316288.627	141	51888.572		
	Total	8813179.000	144			
	Corrected Total	7533829.493	143			

a. R Squared = .048 (Adjusted R Squared = .034)

b. R Squared = .038 (Adjusted R Squared = .024)

c. R Squared = .050 (Adjusted R Squared = .036)

d. R Squared = .083 (Adjusted R Squared = .070)

e. R Squared = .037 (Adjusted R Squared = .023)

f. R Squared = .080 (Adjusted R Squared = .067)

g. R Squared = .049 (Adjusted R Squared = .035)

h. R Squared = .029 (Adjusted R Squared = .015)

Table 51 Analysis of Covariance for maximum Hounsfield units controlling for decedent age

Tests of Between-Subjects Effects

Dependent Variable: Maximum [hnsFU]

Segment	Source	Type III Sum of			F	Sig.
		Squares	df	Mean Square		
LC	Corrected Model	88297.225 ^a	2	44148.612	3.888	.023
	Intercept	19155846.213	1	19155846.213	1686.917	<.001
	Age	41278.674	1	41278.674	3.635	.059
	RiskGroup	34421.009	1	34421.009	3.031	.084
	Error	1601130.602	141	11355.536		
	Total	469564353.000	144			
	Corrected Total	1689427.826	143			
LF	Corrected Model	21104.328 ^b	2	10552.164	.516	.598
	Intercept	27351243.257	1	27351243.257	1336.848	<.001
	Age	14811.189	1	14811.189	.724	.396
	RiskGroup	9202.524	1	9202.524	.450	.504
	Error	2884788.610	141	20459.494		
	Total	586406151.000	144			
	Corrected Total	2905892.938	143			
LO	Corrected Model	36301.112 ^c	2	18150.556	.626	.536
	Intercept	23159210.272	1	23159210.272	798.831	<.001
	Age	99.989	1	99.989	.003	.953
	RiskGroup	36000.677	1	36000.677	1.242	.267
	Error	4087781.714	141	28991.360		
	Total	519576779.000	144			
	Corrected Total	4124082.826	143			
LT	Corrected Model	37516.459 ^d	2	18758.229	.874	.420
	Intercept	30770533.851	1	30770533.851	1433.548	<.001
	Age	20219.532	1	20219.532	.942	.333
	RiskGroup	22436.980	1	22436.980	1.045	.308
	Error	3005044.898	140	21464.606		
	Total	653921141.000	143			
	Corrected Total	3042561.357	142			
RC	Corrected Model	70253.085 ^e	2	35126.542	3.367	.037

Table 51 continued

	Intercept	19400246.564	1	19400246.564	1859.407	<.001
	Age	25915.547	1	25915.547	2.484	.117
	RiskGroup	34357.771	1	34357.771	3.293	.072
	Error	1471132.888	141	10433.567		
	Total	466669686.000	144			
	Corrected Total	1541385.972	143			
RF	Corrected Model	16174.247 ^f	2	8087.124	.394	.675
	Intercept	26821071.328	1	26821071.328	1305.283	<.001
	Age	11753.553	1	11753.553	.572	.451
	RiskGroup	2528.926	1	2528.926	.123	.726
	Error	2897281.642	141	20548.097		
	Total	577490336.000	144			
	Corrected Total	2913455.889	143			
RO	Corrected Model	67967.693 ^g	2	33983.846	1.221	.298
	Intercept	23298558.547	1	23298558.547	837.242	<.001
	Age	10633.665	1	10633.665	.382	.537
	RiskGroup	63754.040	1	63754.040	2.291	.132
	Error	3895885.552	140	27827.754		
	Total	505326665.000	143			
	Corrected Total	3963853.245	142			
RT	Corrected Model	55180.629 ^h	2	27590.314	1.264	.286
	Intercept	31160927.166	1	31160927.166	1427.071	<.001
	Age	29088.957	1	29088.957	1.332	.250
	RiskGroup	33957.315	1	33957.315	1.555	.214
	Error	3078816.260	141	21835.576		
	Total	658425732.000	144			
	Corrected Total	3133996.889	143			

a. R Squared = .052 (Adjusted R Squared = .039)

b. R Squared = .007 (Adjusted R Squared = -.007)

c. R Squared = .009 (Adjusted R Squared = -.005)

d. R Squared = .012 (Adjusted R Squared = -.002)

e. R Squared = .046 (Adjusted R Squared = .032)

f. R Squared = .006 (Adjusted R Squared = -.009)

g. R Squared = .017 (Adjusted R Squared = .003)

h. R Squared = .018 (Adjusted R Squared = .004)

Table 52 Analysis of Covariance for maximum Hounsfeld units controlling for decedent population affinity

Tests of Between-Subjects Effects

Dependent Variable: Maximum [hnsfU]

Segment	Source	Type III Sum of			F	Sig.
		Squares	df	Mean Square		
LC	Corrected Model	52245.446 ^a	2	26122.723	2.250	.109
	Intercept	154008727.530	1	154008727.530	13263.782	<.001
	PopAff	5226.895	1	5226.895	.450	.503
	RiskGroup	49047.221	1	49047.221	4.224	.042
	Error	1637182.380	141	11611.223		
	Total	469564353.000	144			
	Corrected Total	1689427.826	143			
LF	Corrected Model	31871.675 ^b	2	15935.837	.782	.460
	Intercept	193981928.365	1	193981928.365	9516.788	<.001
	PopAff	25578.536	1	25578.536	1.255	.265
	RiskGroup	8208.364	1	8208.364	.403	.527
	Error	2874021.263	141	20383.130		
	Total	586406151.000	144			
	Corrected Total	2905892.938	143			
LO	Corrected Model	55247.489 ^c	2	27623.744	.957	.386
	Intercept	171023425.192	1	171023425.192	5926.586	<.001
	PopAff	19046.366	1	19046.366	.660	.418
	RiskGroup	39871.164	1	39871.164	1.382	.242
	Error	4068835.338	141	28856.988		
	Total	519576779.000	144			
	Corrected Total	4124082.826	143			
LT	Corrected Model	17354.113 ^d	2	8677.056	.402	.670
	Intercept	211675056.100	1	211675056.100	9795.860	<.001
	PopAff	57.187	1	57.187	.003	.959
	RiskGroup	17044.569	1	17044.569	.789	.376
	Error	3025207.244	140	21608.623		
	Total	653921141.000	143			
	Corrected Total	3042561.357	142			

Table 52 continued

RC	Corrected Model	77097.321 ^e	2	38548.660	3.712	.027
	Intercept	155327271.797	1	155327271.797	14956.850	<.001
	PopAff	32759.783	1	32759.783	3.155	.078
	RiskGroup	49732.837	1	49732.837	4.789	.030
	Error	1464288.652	141	10385.026		
	Total	466669686.000	144			
	Corrected Total	1541385.972	143			
RF	Corrected Model	53765.808 ^f	2	26882.904	1.325	.269
	Intercept	192552639.979	1	192552639.979	9494.009	<.001
	PopAff	49345.114	1	49345.114	2.433	.121
	RiskGroup	2538.001	1	2538.001	.125	.724
	Error	2859690.081	141	20281.490		
	Total	577490336.000	144			
	Corrected Total	2913455.889	143			
RO	Corrected Model	137648.670 ^g	2	68824.335	2.518	.084
	Intercept	169251243.005	1	169251243.005	6192.866	<.001
	PopAff	80314.642	1	80314.642	2.939	.089
	RiskGroup	66563.674	1	66563.674	2.436	.121
	Error	3826204.575	140	27330.033		
	Total	505326665.000	143			
	Corrected Total	3963853.245	142			
RT	Corrected Model	41903.374 ^h	2	20951.687	.955	.387
	Intercept	216736236.745	1	216736236.745	9883.210	<.001
	PopAff	15811.703	1	15811.703	.721	.397
	RiskGroup	28945.923	1	28945.923	1.320	.253
	Error	3092093.515	141	21929.741		
	Total	658425732.000	144			
	Corrected Total	3133996.889	143			

a. R Squared = .031 (Adjusted R Squared = .017)

b. R Squared = .011 (Adjusted R Squared = -.003)

c. R Squared = .013 (Adjusted R Squared = -.001)

d. R Squared = .006 (Adjusted R Squared = -.009)

e. R Squared = .050 (Adjusted R Squared = .037)

f. R Squared = .018 (Adjusted R Squared = .005)

g. R Squared = .035 (Adjusted R Squared = .021)

h. R Squared = .013 (Adjusted R Squared = -.001)

Table 53 Analysis of Covariance for mean Hounsfield units controlling for decedent age

Tests of Between-Subjects Effects

Dependent Variable: Mean [hnsfU]

Segment	Source	Type III Sum of			F	Sig.
		Squares	df	Mean Square		
LC	Corrected Model	148526.211 ^a	2	74263.105	3.613	.029
	Intercept	4097424.412	1	4097424.412	199.352	<.001
	Age	131822.202	1	131822.202	6.414	.012
	RiskGroup	32354.735	1	32354.735	1.574	.212
	Error	2898068.645	141	20553.678		
	Total	129321303.644	144			
	Corrected Total	3046594.855	143			
LF	Corrected Model	175326.394 ^b	2	87663.197	3.800	.025
	Intercept	8443766.084	1	8443766.084	366.058	<.001
	Age	27589.211	1	27589.211	1.196	.276
	RiskGroup	127190.861	1	127190.861	5.514	.020
	Error	3252410.153	141	23066.739		
	Total	171098527.813	144			
	Corrected Total	3427736.547	143			
LO	Corrected Model	24009.221 ^c	2	12004.611	.464	.629
	Intercept	4893382.560	1	4893382.560	189.335	<.001
	Age	21228.232	1	21228.232	.821	.366
	RiskGroup	5335.387	1	5335.387	.206	.650
	Error	3644167.009	141	25845.156		
	Total	99374229.866	144			
	Corrected Total	3668176.231	143			
LT	Corrected Model	9454.699 ^d	2	4727.350	.285	.753
	Intercept	8694322.937	1	8694322.937	523.505	<.001
	Age	4114.981	1	4114.981	.248	.619
	RiskGroup	6591.217	1	6591.217	.397	.530
	Error	2325107.293	140	16607.909		
	Total	203983656.756	143			
	Corrected Total	2334561.993	142			

Table 53 continued

RC	Corrected Model	139150.620 ^e	2	69575.310	3.502	.033
	Intercept	4297295.259	1	4297295.259	216.324	<.001
	Age	135834.326	1	135834.326	6.838	.010
	RiskGroup	12042.849	1	12042.849	.606	.438
	Error	2800975.497	141	19865.074		
	Total	135099203.583	144			
	Corrected Total	2940126.117	143			
RF	Corrected Model	114786.617 ^f	2	57393.308	2.603	.078
	Intercept	7971039.461	1	7971039.461	361.459	<.001
	Age	8412.314	1	8412.314	.381	.538
	RiskGroup	95893.822	1	95893.822	4.348	.039
	Error	3109388.979	141	22052.404		
	Total	169758088.105	144			
	Corrected Total	3224175.596	143			
RO	Corrected Model	50693.712 ^g	2	25346.856	1.208	.302
	Intercept	4869625.693	1	4869625.693	232.096	<.001
	Age	41976.573	1	41976.573	2.001	.159
	RiskGroup	15346.218	1	15346.218	.731	.394
	Error	2937355.986	140	20981.114		
	Total	93349111.686	143			
	Corrected Total	2988049.698	142			
RT	Corrected Model	16348.504 ^h	2	8174.252	.441	.644
	Intercept	8950884.375	1	8950884.375	483.353	<.001
	Age	587.513	1	587.513	.032	.859
	RiskGroup	16312.236	1	16312.236	.881	.350
	Error	2611085.130	141	18518.334		
	Total	205547123.877	144			
	Corrected Total	2627433.634	143			

a. R Squared = .049 (Adjusted R Squared = .035)

b. R Squared = .051 (Adjusted R Squared = .038)

c. R Squared = .007 (Adjusted R Squared = -.008)

d. R Squared = .004 (Adjusted R Squared = -.010)

e. R Squared = .047 (Adjusted R Squared = .034)

f. R Squared = .036 (Adjusted R Squared = .022)

g. R Squared = .017 (Adjusted R Squared = .003)

h. R Squared = .006 (Adjusted R Squared = -.008)

Table 54 Analysis of Covariance for mean Hounsfeld units controlling for decedent population affinity

Tests of Between-Subjects Effects

Dependent Variable: Mean [hnsfU]

Segment	Source	Type III Sum of Squares	df	Mean Square	F	Sig.
LC	Corrected Model	173382.671 ^a	2	86691.336	4.254	.016
	Intercept	45519644.763	1	45519644.763	2233.831	<.001
	PopAff	156678.662	1	156678.662	7.689	.006
	RiskGroup	10102.332	1	10102.332	.496	.483
	Error	2873212.184	141	20377.391		
	Total	129321303.644	144			
	Corrected Total	3046594.855	143			
LF	Corrected Model	686723.820 ^b	2	343361.910	17.663	<.001
	Intercept	64130965.824	1	64130965.824	3298.951	<.001
	PopAff	538986.637	1	538986.637	27.726	<.001
	RiskGroup	109362.218	1	109362.218	5.626	.019
	Error	2741012.727	141	19439.807		
	Total	171098527.813	144			
	Corrected Total	3427736.547	143			
LO	Corrected Model	67981.374 ^c	2	33990.687	1.331	.267
	Intercept	33599662.368	1	33599662.368	1315.916	<.001
	PopAff	65200.385	1	65200.385	2.554	.112
	RiskGroup	5029.654	1	5029.654	.197	.658
	Error	3600194.857	141	25533.297		
	Total	99374229.866	144			
	Corrected Total	3668176.231	143			
LT	Corrected Model	55555.366 ^d	2	27777.683	1.706	.185
	Intercept	68698289.504	1	68698289.504	4220.155	<.001
	PopAff	50215.648	1	50215.648	3.085	.081
	RiskGroup	3105.747	1	3105.747	.191	.663
	Error	2279006.627	140	16278.619		
	Total	203983656.756	143			
	Corrected Total	2334561.993	142			
RC	Corrected Model	218058.353 ^e	2	109029.176	5.648	.004
	Intercept	48280528.571	1	48280528.571	2500.876	<.001
	PopAff	214742.059	1	214742.059	11.123	.001
	RiskGroup	585.143	1	585.143	.030	.862

Table 54 continued

	Error	2722067.764	141	19305.445		
	Total	135099203.583	144			
	Corrected Total	2940126.117	143			
RF	Corrected Model	723230.603 ^f	2	361615.302	20.387	<.001
	Intercept	64380068.275	1	64380068.275	3629.664	<.001
	PopAff	616856.300	1	616856.300	34.778	<.001
	RiskGroup	72338.190	1	72338.190	4.078	.045
	Error	2500944.993	141	17737.199		
	Total	169758088.105	144			
	Corrected Total	3224175.596	143			
RO	Corrected Model	102888.573 ^g	2	51444.287	2.496	.086
	Intercept	32221274.603	1	32221274.603	1563.510	<.001
	PopAff	94171.434	1	94171.434	4.570	.034
	RiskGroup	12958.145	1	12958.145	.629	.429
	Error	2885161.125	140	20608.294		
	Total	93349111.686	143			
	Corrected Total	2988049.698	142			
RT	Corrected Model	78408.302 ^h	2	39204.151	2.169	.118
	Intercept	69646762.245	1	69646762.245	3852.529	<.001
	PopAff	62647.311	1	62647.311	3.465	.065
	RiskGroup	11504.839	1	11504.839	.636	.426
	Error	2549025.332	141	18078.194		
	Total	205547123.877	144			
	Corrected Total	2627433.634	143			

a. R Squared = .057 (Adjusted R Squared = .044)

b. R Squared = .200 (Adjusted R Squared = .189)

c. R Squared = .019 (Adjusted R Squared = .005)

d. R Squared = .024 (Adjusted R Squared = .010)

e. R Squared = .074 (Adjusted R Squared = .061)

f. R Squared = .224 (Adjusted R Squared = .213)

g. R Squared = .034 (Adjusted R Squared = .021)

h. R Squared = .030 (Adjusted R Squared = .016)

Table 55 Analysis of Covariance for median Hounsfeld units controlling for decedent population affinity

Tests of Between-Subjects Effects

Dependent Variable: Median [hnsfU]

Segment	Source	Type III Sum of			F	Sig.
		Squares	df	Mean Square		
LC	Corrected Model	295264.879 ^a	2	147632.440	3.642	.029
	Intercept	4090624.265	1	4090624.265	100.914	<.001
	Age	251325.984	1	251325.984	6.200	.014
	RiskGroup	77955.167	1	77955.167	1.923	.168
	Error	5715557.281	141	40535.867		
	Total	146775205.000	144			
	Corrected Total	6010822.160	143			
LF	Corrected Model	342206.234 ^b	2	171103.117	4.210	.017
	Intercept	9685534.598	1	9685534.598	238.335	<.001
	Age	58230.924	1	58230.924	1.433	.233
	RiskGroup	242923.890	1	242923.890	5.978	.016
	Error	5729994.989	141	40638.262		
	Total	190226148.000	144			
	Corrected Total	6072201.222	143			
LO	Corrected Model	46197.287 ^c	2	23098.644	.592	.554
	Intercept	4636872.540	1	4636872.540	118.903	<.001
	Age	39562.182	1	39562.182	1.014	.316
	RiskGroup	11899.158	1	11899.158	.305	.582
	Error	5498603.150	141	38997.185		
	Total	91306291.000	144			
	Corrected Total	5544800.437	143			
LT	Corrected Model	24668.148 ^d	2	12334.074	.411	.664
	Intercept	9593830.278	1	9593830.278	319.940	<.001
	Age	11288.650	1	11288.650	.376	.540
	RiskGroup	16681.765	1	16681.765	.556	.457
	Error	4198084.215	140	29986.316		
	Total	232069291.000	143			
	Corrected Total	4222752.364	142			

Table 55 continued

RC	Corrected Model	282553.864 ^e	2	141276.932	3.561	.031
	Intercept	4314940.939	1	4314940.939	108.748	<.001
	Age	268501.203	1	268501.203	6.767	.010
	RiskGroup	36664.915	1	36664.915	.924	.338
	Error	5594660.795	141	39678.445		
	Total	154829069.000	144			
	Corrected Total	5877214.660	143			
RF	Corrected Model	160922.268 ^f	2	80461.134	2.107	.125
	Intercept	9002668.472	1	9002668.472	235.768	<.001
	Age	15810.807	1	15810.807	.414	.521
	RiskGroup	128894.310	1	128894.310	3.376	.068
	Error	5384011.482	141	38184.479		
	Total	190029240.000	144			
	Corrected Total	5544933.750	143			
RO	Corrected Model	85108.326 ^g	2	42554.163	1.384	.254
	Intercept	4657978.394	1	4657978.394	151.494	<.001
	Age	77080.074	1	77080.074	2.507	.116
	RiskGroup	17264.041	1	17264.041	.561	.455
	Error	4304587.128	140	30747.051		
	Total	84301557.000	143			
	Corrected Total	4389695.455	142			
RT	Corrected Model	61969.307 ^h	2	30984.654	.958	.386
	Intercept	10010316.838	1	10010316.838	309.614	<.001
	Age	2122.505	1	2122.505	.066	.798
	RiskGroup	61857.250	1	61857.250	1.913	.169
	Error	4558757.332	141	32331.612		
	Total	234269494.000	144			
	Corrected Total	4620726.639	143			

a. R Squared = .049 (Adjusted R Squared = .036)

b. R Squared = .056 (Adjusted R Squared = .043)

c. R Squared = .008 (Adjusted R Squared = -.006)

d. R Squared = .006 (Adjusted R Squared = -.008)

e. R Squared = .048 (Adjusted R Squared = .035)

f. R Squared = .029 (Adjusted R Squared = .015)

g. R Squared = .019 (Adjusted R Squared = .005)

h. R Squared = .013 (Adjusted R Squared = -.001)

Table 56 Analysis of Covariance for median Hounsfeld units controlling for decedent population affinity

Tests of Between-Subjects Effects

Dependent Variable: Median [hnsfU]

Segment	Source	Type III Sum of				
		Squares	df	Mean Square	F	Sig.
LC	Corrected Model	368192.225 ^a	2	184096.113	4.600	.012
	Intercept	52554606.635	1	52554606.635	1313.253	<.001
	PopAff	324253.331	1	324253.331	8.103	.005
	RiskGroup	28297.657	1	28297.657	.707	.402
	Error	5642629.934	141	40018.652		
	Total	146775205.000	144			
	Corrected Total	6010822.160	143			
LF	Corrected Model	1233419.075 ^b	2	616709.537	17.971	<.001
	Intercept	73339892.692	1	73339892.692	2137.092	<.001
	PopAff	949443.766	1	949443.766	27.666	<.001
	RiskGroup	213081.195	1	213081.195	6.209	.014
	Error	4838782.147	141	34317.604		
	Total	190226148.000	144			
	Corrected Total	6072201.222	143			
LO	Corrected Model	108810.677 ^c	2	54405.339	1.411	.247
	Intercept	30805870.009	1	30805870.009	799.050	<.001
	PopAff	102175.572	1	102175.572	2.650	.106
	RiskGroup	10853.684	1	10853.684	.282	.597
	Error	5435989.760	141	38553.119		
	Total	91306291.000	144			
	Corrected Total	5544800.437	143			
LT	Corrected Model	212622.257 ^d	2	106311.129	3.711	.027
	Intercept	80677487.667	1	80677487.667	2816.579	<.001
	PopAff	199242.758	1	199242.758	6.956	.009
	RiskGroup	6594.918	1	6594.918	.230	.632
	Error	4010130.107	140	28643.786		
	Total	232069291.000	143			
	Corrected Total	4222752.364	142			
RC	Corrected Model	525198.542 ^e	2	262599.271	6.918	.001
	Intercept	57168470.205	1	57168470.205	1506.115	<.001
	PopAff	511145.881	1	511145.881	13.466	<.001

Table 56 continued

	RiskGroup	4481.120	1	4481.120	.118	.732
	Error	5352016.118	141	37957.561		
	Total	154829069.000	144			
	Corrected Total	5877214.660	143			
RF	Corrected Model	1289188.022 ^f	2	644594.011	21.356	<.001
	Intercept	74741647.418	1	74741647.418	2476.316	<.001
	PopAff	1144076.560	1	1144076.560	37.905	<.001
	RiskGroup	91935.319	1	91935.319	3.046	.083
	Error	4255745.728	141	30182.594		
	Total	190029240.000	144			
	Corrected Total	5544933.750	143			
RO	Corrected Model	157095.902 ^g	2	78547.951	2.598	.078
	Intercept	29355282.888	1	29355282.888	970.973	<.001
	PopAff	149067.650	1	149067.650	4.931	.028
	RiskGroup	13320.841	1	13320.841	.441	.508
	Error	4232599.553	140	30232.854		
	Total	84301557.000	143			
	Corrected Total	4389695.455	142			
RT	Corrected Model	227920.311 ^h	2	113960.156	3.658	.028
	Intercept	80975720.894	1	80975720.894	2599.153	<.001
	PopAff	168073.509	1	168073.509	5.395	.022
	RiskGroup	46049.039	1	46049.039	1.478	.226
	Error	4392806.328	141	31154.655		
	Total	234269494.000	144			
	Corrected Total	4620726.639	143			

a. R Squared = .061 (Adjusted R Squared = .048)

b. R Squared = .203 (Adjusted R Squared = .192)

c. R Squared = .020 (Adjusted R Squared = .006)

d. R Squared = .050 (Adjusted R Squared = .037)

e. R Squared = .089 (Adjusted R Squared = .076)

f. R Squared = .232 (Adjusted R Squared = .222)

g. R Squared = .036 (Adjusted R Squared = .022)

h. R Squared = .049 (Adjusted R Squared = .036)

Table 57 Two-tailed Pearson's correlation coefficients for the left cruciform by risk-group

Left Cruciform Correlations			Age	BMI	Minimum Thickness	Volume [mm3] (1)	Minimum [hnsfU]	Maximum [hnsfU]	Mean [hnsfU]	Median [hnsfU]	
High	Age	Pearson Correlation	--								
		N	75								
		<hr/>									
	BMI	Pearson Correlation	-.246	--							
		Sig. (2-tailed)	.033								
		N	75	75							
	<hr/>										
	Minimum Thickness	Pearson Correlation	.176	-.136	--						
		Sig. (2-tailed)	.133	.247							
		N	74	74	74						
	<hr/>										
	Volume [mm3] (1)	Pearson Correlation	.292	-.113	.734	--					
		Sig. (2-tailed)	.011	.332	<.001						
		N	75	75	74	75					
	<hr/>										
	Minimum [hnsfU]	Pearson Correlation	-.154	.093	-.346	-.475	--				
		Sig. (2-tailed)	.188	.426	.003	<.001					
		N	75	75	74	75	75				
<hr/>											
Maximum [hnsfU]	Pearson Correlation	.216	-.221	.185	.279	-.140	--				
	Sig. (2-tailed)	.062	.057	.115	.016	.231					
	N	75	75	74	75	75	75				
<hr/>											
Mean [hnsfU]	Pearson Correlation	.217	-.318	.377	.548	.017	.571	--			
	Sig. (2-tailed)	.061	.005	<.001	<.001	.888	<.001				
	N	75	75	74	75	75	75	75			
<hr/>											
Median [hnsfU]	Pearson Correlation	.197	-.282	.372	.583	-.047	.535	.981	--		
	Sig. (2-tailed)	.090	.014	.001	<.001	.689	<.001	<.001			

Table 57 continued

	N	75	75	74	75	75	75	75	75
Low Age	Pearson Correlation	--							
	N	69							
BMI	Pearson Correlation	-.194	--						
	Sig. (2-tailed)	.111							
	N	69	69						
Minimum Thickness	Pearson Correlation	.116	-.091	--					
	Sig. (2-tailed)	.344	.456						
	N	69	69	69					
Volume [mm3] (1)	Pearson Correlation	.182	-.058	.833	--				
	Sig. (2-tailed)	.134	.638	<.001					
	N	69	69	69	69				
Minimum [hnsfU]	Pearson Correlation	-.103	-.134	-.048	-.165	--			
	Sig. (2-tailed)	.399	.272	.693	.175				
	N	69	69	69	69	69			
Maximum [hnsfU]	Pearson Correlation	.096	-.121	.047	.206	-.219	--		
	Sig. (2-tailed)	.431	.321	.703	.089	.071			
	N	69	69	69	69	69	69		
Mean [hnsfU]	Pearson Correlation	.201	-.192	.423	.577	.330	.365	--	
	Sig. (2-tailed)	.097	.114	<.001	<.001	.006	.002		
	N	69	69	69	69	69	69	69	
Median [hnsfU]	Pearson Correlation	.212	-.168	.446	.635	.266	.341	.983	--
	Sig. (2-tailed)	.080	.166	<.001	<.001	.027	.004	<.001	
	N	69	69	69	69	69	69	69	69

Table 58 Two-tailed Pearson's correlation coefficients for the left frontal by risk-group

Left frontal correlations										
Risk Group	Segment		Age	BMI	Minimum Thickness	Volume [mm3] (1)	Minimum [hnsfU]	Maximum [hnsfU]	Mean [hnsfU]	Median [hnsfU]
High	LF	Age	Pearson Correlation	--						
		N	75							
	BMI	Pearson Correlation	-.246	--						
		Sig. (2-tailed)	.033							
		N	75	75						
	Minimum Thickness	Pearson Correlation	.046	.181	--					
		Sig. (2-tailed)	.698	.124						
		N	74	74	74					
	Volume [mm3] (1)	Pearson Correlation	.065	.222	.753	--				
		Sig. (2-tailed)	.577	.056	<.001					
		N	75	75	74	75				
	Minimum [hnsfU]	Pearson Correlation	-.146	.051	.032	-.144	--			
		Sig. (2-tailed)	.211	.663	.784	.216				
		N	75	75	74	75	75			
	Maximum [hnsfU]	Pearson Correlation	.011	-.202	-.260	-.308	-.122	--		
		Sig. (2-tailed)	.926	.083	.025	.007	.297			
		N	75	75	74	75	75	75		
	Mean [hnsfU]	Pearson Correlation	-.137	-.189	-.386	-.344	.093	.385	--	
		Sig. (2-tailed)	.242	.105	<.001	.003	.427	<.001		
		N	75	75	74	75	75	75	75	
Median [hnsfU]	Pearson Correlation	-.138	-.157	-.375	-.328	.089	.330	.988	--	
	Sig. (2-tailed)	.238	.178	<.001	.004	.447	.004	<.001		

Table 58 continued

		N	75	75	74	75	75	75	75	75
Low	LF	Age	Pearson Correlation	--						
		N	69							
BMI		Pearson Correlation	-.194	--						
		Sig. (2-tailed)	.111							
		N	69	69						
Minimum Thickness		Pearson Correlation	.184	.183	--					
		Sig. (2-tailed)	.130	.133						
		N	69	69	69					
Volume [mm3] (1)		Pearson Correlation	.148	.208	.559	--				
		Sig. (2-tailed)	.224	.087	<.001					
		N	69	69	69	69				
Minimum [hnsfU]		Pearson Correlation	.033	.015	.021	-.440	--			
		Sig. (2-tailed)	.788	.904	.863	<.001				
		N	69	69	69	69	69			
Maximum [hnsfU]		Pearson Correlation	-.182	.107	-.086	-.401	.188	--		
		Sig. (2-tailed)	.135	.384	.484	<.001	.123			
		N	69	69	69	69	69	69		
Mean [hnsfU]		Pearson Correlation	-.040	-.005	-.166	-.324	.478	.242	--	
		Sig. (2-tailed)	.741	.968	.174	.007	<.001	.046		
		N	69	69	69	69	69	69	69	
Median [hnsfU]		Pearson Correlation	-.058	.015	-.215	-.297	.424	.184	.975	--
		Sig. (2-tailed)	.634	.903	.075	.013	<.001	.129	<.001	
		N	69	69	69	69	69	69	69	69

Table 59 Two-tailed Pearson's correlation coefficients for the left orbit by risk-group

Left Orbit Correlations										
Risk Group	Segment		Age	BMI	Minimum Thickness	Volume [mm3] (1)	Minimum [hnsfU]	Maximum [hnsfU]	Mean [hnsfU]	Median [hnsfU]
High	LO	Age	Pearson Correlation	--						
			N	75						
	BMI	Pearson Correlation	-.246	--						
		Sig. (2-tailed)	.033							
		N	75	75						
	Minimum Thickness	Pearson Correlation	-.099	-.017	--					
		Sig. (2-tailed)	.400	.888						
		N	74	74	74					
	Volume [mm3] (1)	Pearson Correlation	-.185	.202	.530	--				
		Sig. (2-tailed)	.111	.083	<.001					
		N	75	75	74	75				
	Minimum [hnsfU]	Pearson Correlation	-.024	.166	.034	-.212	--			
		Sig. (2-tailed)	.841	.155	.774	.068				
		N	75	75	74	75	75			
	Maximum [hnsfU]	Pearson Correlation	.042	-.258	-.073	.005	-.365	--		
		Sig. (2-tailed)	.721	.026	.537	.967	.001			
		N	75	75	74	75	75	75		
	Mean [hnsfU]	Pearson Correlation	-.161	-.120	-.094	.069	-.224	.627	--	
		Sig. (2-tailed)	.169	.303	.428	.554	.053	<.001		
		N	75	75	74	75	75	75	75	
Median [hnsfU]	Pearson Correlation	-.161	-.105	-.102	.065	-.222	.538	.986	--	
	Sig. (2-tailed)	.168	.368	.389	.582	.056	<.001	<.001		

Table 59 continued

		N	75	75	74	75	75	75	75	75
Low	LO	Age	Pearson Correlation	--						
		N	69							
BMI		Pearson Correlation	-.194	--						
		Sig. (2-tailed)	.111							
		N	69	69						
Minimum Thickness		Pearson Correlation	.123	.106	--					
		Sig. (2-tailed)	.314	.386						
		N	69	69	69					
Volume [mm3] (1)		Pearson Correlation	-.165	.195	.399	--				
		Sig. (2-tailed)	.175	.109	<.001					
		N	69	69	69	69				
Minimum [hnsfU]		Pearson Correlation	.128	-.050	-.040	-.633	--			
		Sig. (2-tailed)	.295	.681	.744	<.001				
		N	69	69	69	69	69			
Maximum [hnsfU]		Pearson Correlation	-.073	-.043	-.173	.115	-.014	--		
		Sig. (2-tailed)	.552	.723	.155	.348	.906			
		N	69	69	69	69	69	69		
Mean [hnsfU]		Pearson Correlation	.003	-.009	.048	.015	.280	.491	--	
		Sig. (2-tailed)	.979	.940	.694	.904	.020	<.001		
		N	69	69	69	69	69	69	69	
Median [hnsfU]		Pearson Correlation	-.013	.023	.062	.043	.256	.438	.989	--
		Sig. (2-tailed)	.919	.850	.613	.724	.034	<.001	<.001	
		N	69	69	69	69	69	69	69	69

Table 60 Two-tailed Pearson's correlation coefficients for the left temporal by risk-group

Left Temporal Correlations												
Risk Group	Segment		Age	BMI	Minimum Thickness	Volume [mm3] (1)	Minimum [hnsfU]	Maximum [hnsfU]	Mean [hnsfU]	Median [hnsfU]		
High	LT	Age	Pearson Correlation	--								
			N	75								
			<hr/>									
		BMI	Pearson Correlation	-.246	--							
			Sig. (2-tailed)	.033								
			N	75	75							
		<hr/>										
		Minimum Thickness	Pearson Correlation	.103	.165	--						
			Sig. (2-tailed)	.385	.162							
			N	73	73	73						
		<hr/>										
		Volume [mm3] (1)	Pearson Correlation	.045	.269	.650	--					
			Sig. (2-tailed)	.702	.020	<.001						
			N	74	74	73	74					
		<hr/>										
		Minimum [hnsfU]	Pearson Correlation	-.067	-.019	-.427	-.520	--				
			Sig. (2-tailed)	.573	.874	<.001	<.001					
			N	74	74	73	74	74				
		<hr/>										
		Maximum [hnsfU]	Pearson Correlation	-.057	-.230	.237	.230	-.323	--			
			Sig. (2-tailed)	.632	.049	.044	.048	.005				
			N	74	74	73	74	74	74			
		<hr/>										
		Mean [hnsfU]	Pearson Correlation	-.016	-.134	-.105	-.175	.337	.301	--		
Sig. (2-tailed)	.892		.255	.377	.135	.003	.009					
N	74		74	73	74	74	74	74				
<hr/>												
Median [hnsfU]	Pearson Correlation	.022	-.079	-.139	-.118	.326	.211	.959	--			
	Sig. (2-tailed)	.853	.504	.240	.315	.005	.071	<.001				

Table 60 continued

		N	74	74	73	74	74	74	74	74
Low	LT	Age	Pearson Correlation	--						
		N	69							
	BMI	Pearson Correlation	-.194	--						
		Sig. (2-tailed)	.111							
		N	69	69						
	Minimum Thickness	Pearson Correlation	.039	.013	--					
		Sig. (2-tailed)	.752	.918						
		N	69	69	69					
	Volume [mm3] (1)	Pearson Correlation	.094	.230	.504	--				
		Sig. (2-tailed)	.441	.057	<.001					
		N	69	69	69	69				
	Minimum [hnsfU]	Pearson Correlation	.062	-.103	.008	-.398	--			
		Sig. (2-tailed)	.611	.399	.948	<.001				
		N	69	69	69	69	69			
	Maximum [hnsfU]	Pearson Correlation	-.111	.115	.139	-.059	-.101	--		
		Sig. (2-tailed)	.364	.347	.254	.629	.410			
		N	69	69	69	69	69	69		
	Mean [hnsfU]	Pearson Correlation	.097	-.067	-.145	-.132	.340	.079	--	
		Sig. (2-tailed)	.426	.582	.234	.281	.004	.520		
		N	69	69	69	69	69	69	69	
	Median [hnsfU]	Pearson Correlation	.081	-.027	-.107	.008	.183	-.023	.949	--
		Sig. (2-tailed)	.508	.829	.380	.945	.133	.850	<.001	
		N	69	69	69	69	69	69	69	69

Table 61 Two-tailed Pearson's correlation coefficients for the right cruciform by risk-group

Right Cruciform Correlations										
Risk Group	Segment		Age	BMI	Minimum Thickness	Volume [mm3] (1)	Minimum [hnsfU]	Maximum [hnsfU]	Mean [hnsfU]	Median [hnsfU]
High	RC	Age	Pearson Correlation	--						
			N	75						
	BMI	Pearson Correlation	-.246	--						
		Sig. (2-tailed)	.033							
		N	75	75						
	Minimum Thickness	Pearson Correlation	.174	-.082	--					
		Sig. (2-tailed)	.137	.486						
		N	74	74	74					
	Volume [mm3] (1)	Pearson Correlation	.214	-.040	.670	--				
		Sig. (2-tailed)	.065	.737	<.001					
		N	75	75	74	75				
	Minimum [hnsfU]	Pearson Correlation	-.049	-.115	-.094	-.266	--			
		Sig. (2-tailed)	.677	.326	.426	.021				
		N	75	75	74	75	75			
	Maximum [hnsfU]	Pearson Correlation	.106	-.078	.245	.182	-.202	--		
		Sig. (2-tailed)	.367	.505	.036	.118	.083			
		N	75	75	74	75	75	75		
	Mean [hnsfU]	Pearson Correlation	.120	-.228	.455	.594	.023	.517	--	
		Sig. (2-tailed)	.304	.049	<.001	<.001	.844	<.001		
		N	75	75	74	75	75	75	75	
Median [hnsfU]	Pearson Correlation	.108	-.210	.442	.628	-.007	.431	.982	--	
	Sig. (2-tailed)	.357	.070	<.001	<.001	.951	<.001	<.001		

Table 61 continued

		N	75	75	74	75	75	75	75	75
Low	RC	Age	Pearson Correlation	--						
		N	69							
BMI		Pearson Correlation	-.194	--						
		Sig. (2-tailed)	.111							
		N	69	69						
Minimum Thickness		Pearson Correlation	.010	-.083	--					
		Sig. (2-tailed)	.937	.499						
		N	69	69	69					
Volume [mm3] (1)		Pearson Correlation	.114	-.011	.805	--				
		Sig. (2-tailed)	.350	.931	<.001					
		N	69	69	69	69				
Minimum [hnsfU]		Pearson Correlation	.041	-.185	.033	-.134	--			
		Sig. (2-tailed)	.739	.127	.789	.271				
		N	69	69	69	69	69			
Maximum [hnsfU]		Pearson Correlation	.171	.021	.154	.303	-.215	--		
		Sig. (2-tailed)	.159	.862	.206	.011	.076			
		N	69	69	69	69	69	69		
Mean [hnsfU]		Pearson Correlation	.303	-.162	.478	.593	.278	.469	--	
		Sig. (2-tailed)	.012	.184	<.001	<.001	.021	<.001		
		N	69	69	69	69	69	69	69	
Median [hnsfU]		Pearson Correlation	.312	-.137	.490	.645	.186	.446	.983	--
		Sig. (2-tailed)	.009	.262	<.001	<.001	.125	<.001	<.001	
		N	69	69	69	69	69	69	69	69

Table 62 Two-tailed Pearson's correlation coefficients for the right frontal by risk-group

Right Frontal Correlations											
Risk Group	Segment		Age	BMI	Minimum Thickness	Volume [mm3] (1)	Minimum [hnsfU]	Maximum [hnsfU]	Mean [hnsfU]	Median [hnsfU]	
High	RF	Age	Pearson Correlation	--							
			N	75							
		BMI	Pearson Correlation	-.246	--						
			Sig. (2-tailed)	.033							
			N	75	75						
		Minimum Thickness	Pearson Correlation	.021	.099	--					
			Sig. (2-tailed)	.858	.403						
			N	74	74	74					
		Volume [mm3] (1)	Pearson Correlation	-.010	.258	.758	--				
			Sig. (2-tailed)	.931	.026	<.001					
			N	75	75	74	75				
		Minimum [hnsfU]	Pearson Correlation	-.041	.172	-.030	-.110	--			
			Sig. (2-tailed)	.727	.141	.803	.349				
			N	75	75	74	75	75			
		Maximum [hnsfU]	Pearson Correlation	.056	-.217	-.251	-.174	-.064	--		
			Sig. (2-tailed)	.635	.061	.031	.135	.586			
			N	75	75	74	75	75	75		
		Mean [hnsfU]	Pearson Correlation	-.068	-.234	-.445	-.338	.167	.453	--	
			Sig. (2-tailed)	.562	.043	<.001	.003	.152	<.001		
			N	75	75	74	75	75	75	75	
		Median [hnsfU]	Pearson Correlation	-.084	-.214	-.455	-.353	.127	.386	.986	--
			Sig. (2-tailed)	.476	.065	<.001	.002	.279	<.001	<.001	

Table 62 continued

		N	75	75	74	75	75	75	75	75
Low	RF	Age	Pearson Correlation	--						
		N	69							
BMI		Pearson Correlation	-.194	--						
		Sig. (2-tailed)	.111							
		N	69	69						
Minimum Thickness		Pearson Correlation	.099	.152	--					
		Sig. (2-tailed)	.418	.212						
		N	69	69	69					
Volume [mm3] (1)		Pearson Correlation	.077	.240	.584	--				
		Sig. (2-tailed)	.530	.047	<.001					
		N	69	69	69	69				
Minimum [hnsfU]		Pearson Correlation	.174	-.180	.094	-.386	--			
		Sig. (2-tailed)	.153	.138	.441	.001				
		N	69	69	69	69	69			
Maximum [hnsfU]		Pearson Correlation	-.183	.154	-.015	-.178	.096	--		
		Sig. (2-tailed)	.132	.207	.901	.144	.433			
		N	69	69	69	69	69	69		
Mean [hnsfU]		Pearson Correlation	-.035	.005	-.210	-.387	.515	.198	--	
		Sig. (2-tailed)	.775	.965	.083	.001	<.001	.102		
		N	69	69	69	69	69	69	69	
Median [hnsfU]		Pearson Correlation	-.021	.061	-.239	-.352	.488	.128	.977	--
		Sig. (2-tailed)	.861	.620	.048	.003	<.001	.294	<.001	
		N	69	69	69	69	69	69	69	69

Table 63 Two-tailed Pearson's correlation coefficients for the right orbit by risk-group

Right Orbit Correlations											
Risk Group	Segment		Age	BMI	Minimum Thickness	Volume [mm3] (1)	Minimum [hnsfU]	Maximum [hnsfU]	Mean [hnsfU]	Median [hnsfU]	
High	RO	Age	Pearson Correlation	--							
			N	75							
			<hr/>								
		BMI	Pearson Correlation	-.246	--						
			Sig. (2-tailed)	.033							
			N	75	75						
	<hr/>										
		Minimum Thickness	Pearson Correlation	-.154	.020	--					
			Sig. (2-tailed)	.191	.865						
			N	74	74	74					
	<hr/>										
		Volume [mm3] (1)	Pearson Correlation	-.264	.188	.616	--				
			Sig. (2-tailed)	.022	.107	<.001					
			N	75	75	74	75				
	<hr/>										
		Minimum [hnsfU]	Pearson Correlation	.010	.056	-.130	-.220	--			
			Sig. (2-tailed)	.932	.636	.269	.058				
			N	75	75	74	75	75			
	<hr/>										
		Maximum [hnsfU]	Pearson Correlation	-.124	-.202	-.031	.155	-.264	--		
			Sig. (2-tailed)	.288	.082	.795	.184	.022			
			N	75	75	74	75	75	75		
	<hr/>										
		Mean [hnsfU]	Pearson Correlation	-.223	-.086	-.054	.169	-.092	.703	--	
Sig. (2-tailed)			.054	.464	.648	.148	.432	<.001			
N			75	75	74	75	75	75	75		
<hr/>											
	Median [hnsfU]	Pearson Correlation	-.240	-.059	-.064	.175	-.082	.614	.984	--	
		Sig. (2-tailed)	.038	.615	.588	.132	.483	<.001	<.001		

Table 63 continued

		N	75	75	74	75	75	75	75	75
Low	RO	Age	Pearson Correlation	--						
		N	69							
BMI		Pearson Correlation	-.194	--						
		Sig. (2-tailed)	.111							
		N	69	69						
Minimum Thickness		Pearson Correlation	.074	-.005	--					
		Sig. (2-tailed)	.548	.970						
		N	69	69	69					
Volume [mm3] (1)		Pearson Correlation	-.128	.142	.436	--				
		Sig. (2-tailed)	.299	.248	<.001					
		N	68	68	68	68				
Minimum [hnsfU]		Pearson Correlation	.141	-.189	-.061	-.601	--			
		Sig. (2-tailed)	.252	.122	.623	<.001				
		N	68	68	68	68	68			
Maximum [hnsfU]		Pearson Correlation	.038	.054	-.133	.237	-.256	--		
		Sig. (2-tailed)	.760	.663	.280	.052	.035			
		N	68	68	68	68	68	68		
Mean [hnsfU]		Pearson Correlation	-.020	.076	-.025	.164	-.009	.425	--	
		Sig. (2-tailed)	.871	.539	.839	.181	.943	<.001		
		N	68	68	68	68	68	68	68	
Median [hnsfU]		Pearson Correlation	-.039	.134	.009	.180	-.025	.330	.985	--
		Sig. (2-tailed)	.749	.277	.942	.143	.838	.006	<.001	
		N	68	68	68	68	68	68	68	68

Table 64 Two-tailed Pearson's correlation coefficients for the right temporal by risk-group

Right Temporal Correlations											
Risk Group	Segment		Age	BMI	Minimum Thickness	Volume [mm3] (1)	Minimum [hnsfU]	Maximum [hnsfU]	Mean [hnsfU]	Median [hnsfU]	
High	RT	Age	Pearson Correlation	--							
			N	75							
		BMI	Pearson Correlation	-.246	--						
			Sig. (2-tailed)	.033							
			N	75	75						
		Minimum Thickness	Pearson Correlation	.147	.059	--					
			Sig. (2-tailed)	.210	.620						
			N	74	74	74					
		Volume [mm3] (1)	Pearson Correlation	.072	.269	.646	--				
			Sig. (2-tailed)	.537	.020	<.001					
			N	75	75	74	75				
		Minimum [hnsfU]	Pearson Correlation	-.114	.147	-.145	-.196	--			
			Sig. (2-tailed)	.332	.209	.216	.093				
			N	75	75	74	75	75			
		Maximum [hnsfU]	Pearson Correlation	-.054	-.290	.079	.051	-.166	--		
			Sig. (2-tailed)	.647	.012	.505	.667	.154			
			N	75	75	74	75	75	75		
		Mean [hnsfU]	Pearson Correlation	-.036	-.101	-.164	-.150	.350	.226	--	
			Sig. (2-tailed)	.761	.390	.163	.200	.002	.052		
			N	75	75	74	75	75	75	75	
		Median [hnsfU]	Pearson Correlation	-.021	-.026	-.194	-.093	.315	.132	.957	--
			Sig. (2-tailed)	.858	.823	.098	.429	.006	.261	<.001	

Table 64 continued

		N	75	75	74	75	75	75	75	75	
Low	RT	Age	Pearson Correlation	--							
			N	69							
		BMI	Pearson Correlation	-.194	--						
			Sig. (2-tailed)	.111							
			N	69	69						
		Minimum Thickness	Pearson Correlation	-.039	.110	--					
			Sig. (2-tailed)	.753	.367						
			N	69	69	69					
		Volume [mm3] (1)	Pearson Correlation	-.032	.157	.654	--				
			Sig. (2-tailed)	.796	.196	<.001					
			N	69	69	69	69				
		Minimum [hnsfU]	Pearson Correlation	.202	-.175	-.137	-.348	--			
			Sig. (2-tailed)	.095	.150	.262	.003				
			N	69	69	69	69	69			
		Maximum [hnsfU]	Pearson Correlation	-.140	.177	.165	-.042	-.039	--		
			Sig. (2-tailed)	.250	.146	.175	.733	.753			
			N	69	69	69	69	69	69		
		Mean [hnsfU]	Pearson Correlation	.063	-.071	-.202	-.323	.460	.292	--	
			Sig. (2-tailed)	.607	.564	.096	.007	<.001	.015		
			N	69	69	69	69	69	69	69	
		Median [hnsfU]	Pearson Correlation	.064	-.008	-.190	-.186	.349	.208	.952	--
			Sig. (2-tailed)	.603	.951	.118	.127	.003	.086	<.001	
			N	69	69	69	69	69	69	69	69

BIOGRAPHY OF THE AUTHOR

Jamie Allen Wren was born in Bangor, Maine, on June 19th, 1989. He was raised in Bangor and graduated from Bangor High School in 2008. He attended the University of Maine, graduating in 2012 with a Bachelor's degree in Anthropology. Afterward, he attended the University of New England, earning a Master's in Public Health in 2015.

In 2010, he began working at the University of Maine's Margaret Chase Smith Policy Center, assisting Dr. Marcella H. Sorg with public health research projects and a taphonomic study on scavenger behavior in northern New England. After receiving his master's degree, he joined the Margaret Chase Smith Policy Center staff full-time as a Research Associate. He currently serves as the project director for the Maine Violent Death Reporting System and Maine's State Unintentional Drug Overdose Reporting System. His research interests include medicolegal death investigation, the forensic epidemiology of suicide and fatal drug overdoses, the skeletal impacts of substance use disorder, and imaging in forensic anthropology.

In addition to his work in the field of public health, he has assisted board-certified forensic anthropologist Dr. Marcella H. Sorg with forensic anthropology cases since 2011.

He lives in Orono, Maine, with his husband, Thomas Mitchell.

Jamie is a candidate for the degree of Doctor of Philosophy in Interdisciplinary Studies from the University of Maine in August 2024.